On the transition from two- to three-dimensional turbulence in the presence of background rotation

A THESIS SUBMITTED IN FULFILMENT OF THE REQUIREMENTS FOR THE DEGREE OF
DOCTOR OF PHILOSOPHY IN ENGINEERING

Author
Jonathan A. BRONS

Supervisors
Prof. Alban POTHÉRAT
Prof. Peter J. THOMAS

October 21, 2019

Contents

List of Figures

List of Tables

Abbreviations

2D	Two-Dimensional
3D	Three-Dimensional
APA	Advanced Phase Averaging
MHD	MagnetoHydroDynamics
IW	Inertial Wave(s)
Q2D	Quasi-Two-Dimensional

Abstract

We explore the transition from three-dimensional to two-dimensional turbulence in rotating turbulent flows. Inertial waves are thought of as the main mechanism driving physical processes in rotating turbulent flows. However, they can only exist in a limited flow regime and some steady anisotropic phenomena, such as Taylor columns, are driven by wave-free mechanisms. We identify these flow regimes and conditions under which inertial waves play no part with regards to formation of columnar structures, the promotion of anisotropy and the development of a transient turbulent flow field. A new mechanism is proposed by which columnar structures and anisotropy in general develop in rotating flows, which is based on a balance between the Coriolis force and the viscous or inertial forces operating in the flow field. These theories are validated experimentally using a setup where turbulence is forced through fluid injection/withdrawal and both 3D and quasi-2D flow structures develop. In line with the proposed mechanism, the columnar structures are found to scale as $\sim Ro^{-1}$ showing they form as a consequence of a balance between the Coriolis force and the flow's inertial forces. Surprisingly, in the fast-rotating limit ($Ro \rightarrow 0$) it is found that the anisotropy of the average turbulent flow develops not because of the interactions of inertial waves but rather from an interplay between the Coriolis force and the average advection. The mechanism governing the spatial development of a transient turbulent flow field is shown to transition from being advection driven to being driven by linear inertial waves. This transition is shown to be scale-dependent with large scale motions being more susceptible to the influence of the Coriolis force. The wave-free mechanisms identified here reveal an entirely new aspect of rotating turbulence and challenge the current paradigm that place inertial waves at the heart of its dynamics.

Acknowledgements

The research conducted over the last four years has culminated in me writing this thesis. Though it bears my name as its sole author, it, and the work that bore it, cannot be attributed to the efforts of one person. Over the past few years I've been supported in these efforts by numerous people in many ways and here I would like to give them my thanks. In my experience doing a PhD is a lonely job and it is easy to make yourself feel worse than you probably should. I was fortunate enough to have many friends and colleagues around who kept this from happening. By keeping me on my skates, in the gym or at a table playing boardgames they saw to it that my time outside the lab or in the office was well spent. Of all my friends and colleagues' special thanks must go to Bogdan Teaca. From the first day I met him he has been incredibly supportive and a great friend... albeit in his own way. Without him my stay a Coventry would have been lesser for it... probably.
Projects like this one are for a large part theoretical in nature, but when push comes to shove you need the help of a practically minded people to help you through. A great deal of gratitude goes out to Ian Bates and Martin Holdsworth, who would always lend a helping hand when needed. But of all the people that I had the pleasure of working with special thanks must go to Paul Hackett. Even when teaching duties ought to have kept him, he would always find time to help me out and build the parts necessary every time I came up with another crazy idea. If he had not been there the experiments would not have turned out as well as they did... if at all.
I would also like to thank both Prof. Gert-jan van Heijst and Prof. Peter Read for the fruitful discussions we had during the examination of this thesis. Thanks to their input I was able to address a number of weaknesses in my story and the thesis has turned out better for it.

Finally, we come to the two people without whom this sproject would not have been possible and who helped me become the researcher I am today, Prof. Peter Thomas and Prof. Alban Pothérat. Peter's approach to supervision is very hands-off. He gave me the freedom to fail and helped me back up when I did. Being an experimentalist at heart, Peter was a great help at guiding me throughout my experiments. He also showed some great techniques in how to effectively deal

with a university's bureaucracy. His best teaching moments however came when we reviewed my work, not because Peter would ask the difficult question, but because he has the uncanny ability to ask the important question you did not think about. This showed me the importance of every now and then taking a step back and looking at my problems from a broader perspective. Alban's approach to is far more hands-on. At times this made him the most frustrating and infuriating person to work with, but when you take a closer look there definitely is a method to his madness...and he is quite mad. He has guided me along almost every avenue of my academic career and taught me a great deal. In all my time I have never had a better teacher. I am forever grateful to both these men for giving me the opportunity to pursue this PhD and all the help they have given me over the past four years.

General introduction

The physics of flows subject to background rotation lays at the heart of a wide range of disciplines, ranging from astrophysics and atmospheric sciences [47] down to the engineering of rotating machines and material processing [63]. The Coriolis force, associated to this background rotation, can have wide-ranging effects on the physics of a flow as compared to its non-rotating counterpart. When a turbulent flow field is subject to a Coriolis force strong enough to overcome the local inertial forces the flow field can become almost fully invariant along the direction of the Coriolis force [22]. This places turbulent flow fields subject to background rotating (rotating turbulence) in the quasi-two-dimensional (Q2D) turbulent flow regime. In this regime dynamics of both three-dimensional (3D) and two-dimensional (2D) turbulent flows are active. In 3D turbulent flows energy directly cascades down from larger scale structures to smaller ones until viscosity can dissipate a flow's energy [20], while in 2D turbulent flows energy inversely cascades into increasingly larger structures [16, 32]. This difference severely impacts a flow's ability to dissipate energy [43]. While 3D and 2D turbulent flows separately are relatively well understood the state between these two regimes, where seemingly contradicting dynamics can potentially be present simultaneously, is far less clear.

A phenomenon seen in these Q2D turbulent flows is the emergence of anisotropic elongated columnar structures [25, 36]. A famous example of this is the Great Red Spot on Jupiter, which is an anticyclonic storm about 1.3 times the size of the Earth which has raged on for at least 200 years. This shows that these columnar structures can grow to enormous sizes, be highly energetic and persist for great lengths of time. Though phenomena such as the Great Red Spot may seem rare they are more common than one may initially think. As such an understanding of how such structures come about and how they are maintained is crucial. This thesis aims to contribute to this understanding, exploring the mechanism which drives the formation of columnar structures, or promotion of anisotropy, in rotating turbulence.

In addition to columnar structures flows subject to background rotation support the existence of a form of internal waves known as inertial waves [14, 24]. This sets rotating turbulence apart from

other Q2D turbulent flows. These inertial waves are excited by inertia while the Coriolis force acts as the restoring force. They are known to be an efficient mechanism by which energy is transported in rotating flows [33, 67]. This places them at the heart of numerous theories describing physical processes in rotational turbulence, such as the promotion of anisotropy. Two main theories, supported by strong numerical and experimental evidence, account for the promotion of anisotropy in rotating turbulence. The first states that the mechanism by which columnar structures emerge is the consequence of non-linear inertial wave interactions, which cause energy to preferably be transferred to modes aligned with the axis of rotation [54]. The second argues that the mechanism is governed by linear inertial waves preferentially propagating energy along the axis of rotation [15]. However anisotropic columnar structures, known as Taylor columns [61], have been observed in flow regimes where inertia is negligible. Analytical solution show that these structures are steady and free from inertial waves [40, 41]. Though inertia cannot be neglected under turbulent flow conditions, the existence of these Taylor columns does suggest the possibility of another mechanism promoting anisotropy in rotating turbulence which is wave-free. The interplay between inertial waves and turbulence is a central thread which runs through this thesis and is summarized by the following question:

To what extent do inertial waves influence the development of the flow structures that form in rotating turbulent flow fields, where both 3D and 2D turbulent dynamics are active?

This question is addressed experimentally using a setup where an inhomogeneous turbulent flow field is continuously forced through fluid injection and withdrawal at the bottom wall of a tank filled with fluid whilst it is subject to background rotation. The inhomogeneity is caused by the gradual decay of the applied inertial forces along the axis of rotation. This ensures that the flow supports the simultaneous existence of both Q2D columnar flow structures and local 3D turbulent flow structures that are capable of exciting inertial waves.
For inspiration as to what a wave-free mechanism for the promotion of anisotropy may look like we turn to another field of Q2D turbulent flows known as magnetohydrodynamic (MHD) flows [16]. Similar to the Coriolis force the Lorentz force associated to MHD flows is known to promote anisotropy [49]. Two studies by Sommeria *et al*. (1982) [55] and Pothérat & Klein (2014) [50] found that a diffusive mechanism, based on a balance between the Lorentz force and viscous or inertial forces, promotes anisotropy and is wave-free.

This thesis is divided into six chapters. In the first chapter we review several key concepts of rotating turbulence in general. Doing so will give us an insight into the important physical pro-

cesses thought to be at the heart of rotating turbulence. In the second chapter a new mechanism driving formation of the columnar structure is proposed. This mechanism, inspired by those seen in MHD turbulence, is similarly based on a balance between the Coriolis force and viscous/inertial forces opposing it. By examining the governing equations in the context of average flow quantities a method is introduced by which the influence of static forces and fluctuating forces, such as those due to inertial waves, can be evaluated separately. In the third chapter the experimental setup designed and used in this study is described. In addition, the experimental protocol and important analysis techniques are discussed.

In the fourth and fifth chapter the dynamics of the flow are studied under statistically steady conditions, with the fourth chapter dedicated to describing fundamental results regarding the flow's topology, such as flow structures and the identification of inertial waves. In the fifth chapter the validity of the new mechanism is tested. Flow regimes are identified where different balances of forces influence the promotion of anisotropy in rotating turbulence, including a flow regime where anisotropy is promoted because of a balance between the average flow's inertia and the Coriolis force, but not inertial waves. In the sixth chapter the transient state between an initially still flow field, under solid-body rotation, and the statistically steady flow field of chapters four and five is explored. It is found that in the early stages of the flow build-up the motion of the turbulent front transitions from a scale-independent advection driven mechanism, like a single turbulent jet, to a mechanism that is driven by linear inertial waves.

Chapter 1

Fundamentals of rotating turbulent flows

Rotating turbulent flows are ubiquitous in both nature and industry and are of great interest in geophysical and astrophysical flows. Elongated coherent columnar structures form in such flow fields and they are the consequence of interactions between waves and turbulence [16]. These structures, how they are formed and how they relate to the overall anisotropy of the flow field are of key interest in this thesis. We begin this chapter by discussing rotating flows in the absence of turbulence and a number of key phenomena that arise, in particular inertial waves, which are thought to be at the heart of rotating turbulence.

We then turn to the subject of turbulence itself. We focus on the two states of three-dimensional and two-dimensional turbulence, how energy cascades across the scales of the flow and why different flow structures are preferred for either of the two states. The resultant of both rotating and turbulent flows, namely rotating turbulence, is discussed in the context of the leading theories behind the mechanism driving the formation of columnar structures. In addition a brief review is given of historical and recent experimental studies on the subject. Both rotating turbulence and magnetohydrodynamic (MHD) turbulence are similar in a number of respects, but the mechanism driving the structure formation in MHD turbulence is significantly different. Here we review this mechanism as the theory behind it can be applied to rotating turbulence and forms the basis forms the basis for a number of theories formulated later in this thesis.

1.1 Rotational flows

We consider an incompressible fluid of density ρ and kinematic viscosity ν which rotates as a rigid body at a rate $\mathbf{\Omega}$. For convenience we adopt a frame of reference which rotates with the fluid. The Navier-Stokes equation in this frame becomes,

$$\partial_t \mathbf{u} + (\mathbf{u}\cdot\nabla)\mathbf{u} = -\nabla[p/\rho - \frac{1}{2}(\mathbf{\Omega}\times\mathbf{x})^2] + 2\mathbf{u}\times\mathbf{\Omega} + \nu\nabla^2\mathbf{u} \ , \tag{1.1}$$

where $\partial_t = \frac{\partial}{\partial t}$, $\mathbf{x}$ is the positional vector, $\mathbf{u}$ is the velocity vector representing the velocity fields and p is the pressure. Here $-\nabla[\frac{1}{2}(\mathbf{\Omega}\times\mathbf{x})^2]$ represents the centrifugal force acting on the fluid and $2\mathbf{u}\times\mathbf{\Omega}$ represents the Coriolis force. Furthermore we assume continuity

$$\nabla\cdot\mathbf{u} = 0 \ .$$

If, in this system rotating at a rate Ω, there is a motion of characteristic length ℓ and velocity U, the relative ratios between inertial forces, viscous forces and the Coriolis force are given by three dimensionless numbers. The Reynolds number (Re) which gives the ratio between inertial and viscous forces, the Rossby number (Ro) which gives the ratio between inertial forces and the Coriolis force and the Ekman number (Ek), which gives the ratio between the viscous forces and the Coriolis force, these are given by

$$Re = \frac{U\ell}{\nu} \ , \ Ro = \frac{U}{2\Omega\ell} \ , \ Ek = \frac{\nu}{2\Omega\ell^2} \ .$$

For the moment we assume $Re \gg 1$, which implies that the viscous forces are negligible. The equations of motion then simplify to

$$\partial_t \mathbf{u} + (\mathbf{u}\cdot\nabla)\mathbf{u} = -\nabla(p^*/\rho) + 2\mathbf{u}\times\mathbf{\Omega} \ , \tag{1.2}$$

where p^* is the reduced pressure given by $p^* = p - \frac{1}{2}\rho(\mathbf{\Omega}\times\mathbf{u})^2$. Note the Coriolis force cannot do work on the fluid, $(2\mathbf{u}\times\mathbf{\Omega})\cdot\mathbf{u} = 0$. Now assume $\mathbf{\Omega} = \Omega\mathbf{e}_z$ and there is a particle that is moving radially at a velocity $\mathbf{u} = u_r\mathbf{e}_r$ in cylindrical (r,θ,z) coordinates. The Coriolis force acting on the particle , $-2\Omega u_r\mathbf{e}_\theta$, will cause a co-rotating motion (i.e. same direction as $\mathbf{\Omega}$) if the particle is moving radially inward and a counter-rotating motion if it is moving radially outward. From an inertial frame of reference this can be seen as a conservation of angular momentum.

1.1.1 Taylor-Proudman theorem and Taylor columns

Equation (1.2) can be simplified even further if it is assumed that $Ro \ll 1$ and $Re \gg 1$ (which implies $Ek \ll 1$.) Equation (1.2) then becomes a linear equation.

$$\partial_t \mathbf{u} = 2\mathbf{u} \times \mathbf{\Omega} - \nabla(p^*/\rho) \ . \tag{1.3}$$

By taking the curl of this equation we get,

$$\partial_t \boldsymbol{\omega} = 2(\mathbf{\Omega} \cdot \nabla)\mathbf{u} \ , \tag{1.4}$$

where $\boldsymbol{\omega} = \nabla \times \mathbf{u}$. If the motion is steady $\partial_t \boldsymbol{\omega} = 0$ and we are left with

$$(\mathbf{\Omega} \cdot \nabla)\mathbf{u} = 0 \ . \tag{1.5}$$

This implies that $\mathbf{u}$ is two-dimensional, or to put it differently, it is independent of the coordinate parallel to $\mathbf{\Omega}$. This is called the Taylor-Proudman theorem. This theorem has important consequences. If, for example, we have an object placed inside a large tank filled with water rotating steadily at $\mathbf{\Omega} = \Omega \mathbf{e}_z$ and we slowly tow this object across said tank, the fluid located between the object, the bottom of the tank and the surface of the water will move as well, as if attached to the object. Because (1.5) states that $\partial_z u_z = 0$ no flow over the object is allowed and any fluid outside of the column over the object has to move around it. This example almost exactly describes the experiments conducted by G.I. Taylor (1922) [61] whom first published on this phenomenon. By placing some dye both over and ahead of the object Taylor observed that both would travel with the object as if rigidly attached. These structures are known as *Taylor columns*.

This raises two important questions; How are these Taylor columns formed and how does the fluid within the column know to move with the object? Though not explicitly stated in their study of Stewartson layers, Moore and Saffman (1969) [40, 41] showed analytically that Taylor columns are both steady in time and must form under the combined influence of viscous forces and the Coriolis force. Another explanation is given by Davidson (2013, p.53) [16], where Taylor columns form as a consequence of low-frequency inertial waves being emitted by the moving object

1.1.2 Inertial waves

Due to the presence of the Coriolis force a rotating, incompressible fluid can support a form of internal waves called inertial waves. Suppose we have a system where $\mathbf{\Omega} = \Omega \mathbf{e}_z$ and $Ro \ll 1$, $Re \gg 1$, then the Taylor-Proudman theorem states that $\partial_z u_z = 0$, which due to $\nabla \cdot \mathbf{u} = 0$ means

that $\nabla_\perp \cdot \mathbf{u}_\perp = -\partial_z u_z = 0$, where $\mathbf{u}_\perp = (u_x, u_y, 0)$.

If now we have a ring of fluid around the axis of rotation that moves radially outward, then the Coriolis force ($2\mathbf{u} \times \mathbf{\Omega}$) will act on this motion and generate a negative (i.e. counter to the background rotation) circulation. This circulation in turn generates a Coriolis force that contracts the ring of fluid which will generate a positive circulation and so on and so forth. In effect the Coriolis force acts as a restoring force, returning the flow to its original state, but due to inertia it will overshoot and as a result oscillations will ensue [38],[35]. These oscillations are what we call inertial waves.

It is not immediately obvious how (1.4) can support wave like motions as it does not appear as a standard wave-like equation. By applying the operator $\nabla \times \partial_t$ to (1.4) we find:

$$\partial_{tt}(\nabla^2 \mathbf{u}) + 4(\mathbf{\Omega} \cdot \nabla)^2 \mathbf{u} = 0 \,. \tag{1.6}$$

This equation supports plane waves of the form

$$\mathbf{u} = \hat{\mathbf{u}}\, exp[i(\mathbf{k} \cdot \mathbf{x} - \sigma t)] \;, \tag{1.7}$$

where $\hat{\mathbf{u}}$ is a constant complex vector normal to the wave vector $\mathbf{k}$ (i.e. $\mathbf{u} \cdot \mathbf{k} = 0$) and σ is the wave frequency. Inserting (1.7) into (1.6) reveals the relation between $\mathbf{k}$ and σ, commonly referred to as the dispersion relation for inertial waves, which is given by:

$$\sigma = 2(\mathbf{\Omega} \cdot \mathbf{k})/|\mathbf{k}|. \tag{1.8}$$

If $\mathbf{\Omega} = \Omega \mathbf{e}_z$ then (1.8) yields:

$$\sigma = 2\Omega \frac{k_z}{|\mathbf{k}|} = 2\Omega \cos\theta \;, \tag{1.9}$$

where θ is the angle between $\mathbf{\Omega}$ and $\mathbf{k}$. From (1.9) the phase velocity c_p and group velocity c_g can be derived,

$$c_p = \frac{\sigma}{\mathbf{k}} = 2\Omega \cos\theta \frac{\mathbf{k}}{k^2} \;, \tag{1.10a}$$

$$c_g = \frac{\partial \sigma}{\partial \mathbf{k}} = \frac{2\Omega}{k} \sin\theta \;. \tag{1.10b}$$

Inertial waves have a number of important features. First, their phase velocity is perpendicular to their group velocity, which differs from most waves where these are parallel to one another. Second, their frequency σ depends on the relative angle between $\mathbf{\Omega}$ and $\mathbf{k}$, varying from $\sigma = 0$ to $\sigma = 2|\mathbf{\Omega}|$, but does not depend on the magnitude of $\mathbf{k}$. This implies that the wave length of

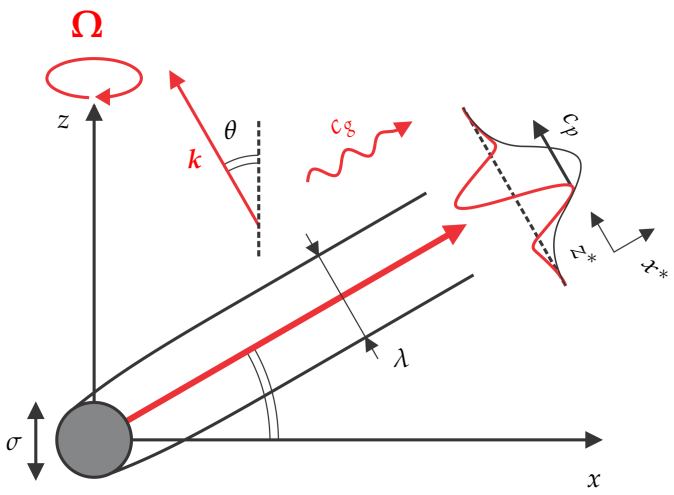

Figure 1.1: A two-dimensional sketch of an inertial wavepacket generated by oscillating a rod at a frequency σ.

a wave is determined by some external length scale. One of the first experimental observations of these waves and the relation between θ and σ were made by Görtler (1957) and Oser (1958) by oscillating a disk in a rotating tank [24]. More recently this was illustrated in great detail by Cortet *et al*. [14] where a rod submerged in a rotating tank was oscillated at a frequency $\sigma < 2\Omega$. Packets of inertial waves could be seen being emitted from the rod at exactly the angle θ. Figure 1.1 shows the anatomy of such an inertial wave packet, generated by oscillating a rod at frequency σ.

If we now go back to the example of an object slowly being dragged across a rotating tank, this slow motion could be seen as akin to a low frequency oscillation. This low frequency oscillation causes inertial waves to be emitted which are aligned almost exactly with the axis of rotation, $\sigma \approx 0 \;\rightarrow\; \theta \approx 90°$, carrying energy away at a speed $c_g \sim 2\Omega/k$. This velocity is likely to be far greater than the velocity at which the object is being dragged. As the inertial waves travel upward they carry with them the information that the object is moving horizontally, in pace with the towed object. And so the Taylor column is constantly formed and reformed by a train of inertial waves emitted by the object. The problem with this explanation is that Taylor columns are in fact steady flow structures, making it difficult to justify them as a consequence of a transient phenomenon such as low-frequency inertial waves.

1.2 Turbulence

We now turn to the subject of turbulence. Turbulence is a complex topic that tends to produce multiple questions for each answer found. The leading cause of this is the seemingly chaotic nature of turbulent flow fields. The randomness that is often associated with these flows is caused,

in part, by the non-linear coupling between the velocity field and the vorticity field.

1.2.1 Vorticity equation

A vorticity field can be calculated by $\boldsymbol{\omega} = \nabla \times \mathbf{u}$. This relation can be applied to the equations of motion as well. By taking the curl of the Navier-Stokes equation, the so-called vorticity equation is found.

$$\frac{D\boldsymbol{\omega}}{Dt} = (\boldsymbol{\omega} \cdot \nabla)\mathbf{u} + \nu \nabla^2 \boldsymbol{\omega} \ . \tag{1.11}$$

Here $\frac{D}{Dt} = \partial_t + \mathbf{u} \cdot \nabla$ is the material derivative. An important term in (1.11) is $(\boldsymbol{\omega} \cdot \nabla)\mathbf{u}$, which is known as the vortex stretching term. In the inviscid limit the stretching (or compression) of fluid elements will cause vorticity to rise (or fall) in order to conserve angular momentum, this in turn causes a rise (or fall) in kinetic energy. If, for example, our fluid element is a vortex tube, then stretching this tube would cause it to narrow. In order to conserve angular momentum the vorticity would need to increase, which in turn increases the angular speed of the fluid and thus a rise in kinetic energy.

Equation (1.11) shows that vorticity can only change through advection or diffusion, it cannot be spontaneously created within the flow field. In the absence of body forces vorticity must originate from solid surfaces where it then gets diffused into the flow field.

The relation $\boldsymbol{\omega} = \nabla \times \mathbf{u}$ may also be inverted, through what is known as the Biot-Savart law. In the case of infinite domains, provided the flow field is at rest at infinity, the Biot-Savart law is given as,

$$\mathbf{u}(\mathbf{x}) = \frac{1}{4\pi} \int \frac{\mathbf{r} \times \boldsymbol{\omega}(\mathbf{x}')}{r^3} d\mathbf{x}', \quad \mathbf{r} = \mathbf{x}' - \mathbf{x} \tag{1.12}$$

Equations (1.11) and (1.12) show the non-linear coupling between $\mathbf{u}(\mathbf{x})$ and $\boldsymbol{\omega}(\mathbf{x})$, and highlights the chaotic nature of turbulent flows. According to (1.11) a velocity field $\mathbf{u}(\mathbf{x})$ advects and distorts the vorticity field $\boldsymbol{\omega}(\mathbf{x})$, which in turn changes $\mathbf{u}(\mathbf{x})$ in accordance with (1.12).

1.2.2 The cascade of energy

We are interested in the formation of structures in rotating turbulent flows. In turbulence there exists an important link between the scales of the flow and the propagation of energy through the flow. For three-dimensional (3D) turbulence energy cascades down from the larger scales of the flow down to increasingly smaller scales until viscous forces are comparatively strong enough to dissipate the energy into heat [48]. When limited to two-dimensional (2D) turbulence the process by which this happens changes significantly and the cascade is in fact inverted [60]. For now we consider the case of statistically homogeneous 3D turbulence of sufficiently high *Re* in the absence

of body forces.

Turbulent flows consist of vortices (eddies) of a wide range of scales. We introduce ℓ and η to represent the characteristic values of the largest and smallest length scales that can be found in a turbulent flow and u and v to represent the characteristic velocity fluctuations of eddies at these scales. Here ℓ and u are known as the integral scales, which are set in part by the overall geometry of the flow (for example, the diameter of a pipe and the flow velocity through it) and η and v are known as the small scales, which are determined by the dynamical processes within the turbulence.

The zeroth law of turbulence states that far away from any boundaries and in the limit of $Re \to \infty$ the mean rate of dissipation of kinetic energy, ϵ, is finite and dependent only on the integral scales. Dimensional analysis shows:

$$\epsilon \sim u^3/\ell \,. \tag{1.13}$$

In most turbulent flows energy is transferred from the mean flow to turbulence at the integral scales. On the other hand, energy is dissipated through viscous dissipation which acts at the smallest scales, where the velocity gradients are highest. It follows that

$$\epsilon \sim u^3\ell \sim \nu(v/\eta)^2 \,. \tag{1.14}$$

This shows that there is a link between the integral scales and the small scales. Energy enters the turbulence at the largest scales, it then gets transferred to vortices of the smallest scale, where it is converted into heat through viscous dissipation. The question now is: How does this transfer of energy occur?

One highly influential hypothesis was put forward by Richardson (1922) and was later refined by Kolmogorov (1941) among others. Richardson proposed that this transfer of energy occurs in the form of a cascade of energy, where the cascade part implies that the energy transfer takes place over a long chain of separate inertial transfers. Vortices of size ℓ_0 transfer their kinetic energy to vortices of slightly smaller size ℓ_1 which then transfer energy to increasingly smaller vortices of size $\ell_{n+1} \lesssim \ell_n$ until the small scales are reached and the energy is converted to heat. It is not implied that there are a discreet number of sized vortices ℓ_n, but it is implied that this is a multi-step process.

If it were the case that this transfer was such a multi-step process Kolmogorov hypothesized that for an incompressible flow subject to homogeneous isotropic turbulence the energy transfer for a vortex of intermediate size r, where $\ell \gg r \gg \eta$, with characteristic velocity u_r was given by

the dissipation rate ϵ. This resulted in Kolmogorov's two-third law:

$$u_r^3/r \sim \epsilon \ , \ u_r^2 \sim (\epsilon r)^{2/3} \ . \tag{1.15}$$

The physical mechanism behind the cascade is believed to be fuelled by vortex stretching. Turbulence can be considered hierarchy of vortices of different scales. Suppose there is an eddy of size r, which sits in the shadow of a larger eddy. It will get strained by this larger eddy, which will lead to the stretching or compression of the smaller one. As explained at the start of section 1.2.1, stretching of a vortex will cause its kinetic energy to increase in accordance with (1.11), while compression will cause a decrease in kinetic energy. This inviscid process shows an energy-exchange between larger and smaller scales. If now we have a multitude of smaller eddies in the shadow of the larger ones, one may expect the net energy flux between the scales to be zero, but this is not the case. While energy is transferred in both direction the stretching of eddies causes their intensity to increase, which in turn enhances the transfer of energy. As a net result this means that the energy flux down to the smaller scales dominates. This process underpins the transfer of energy from large scales to small scales.

Furthermore, from (1.15) we can see that the strain induced by eddies of size r scales as, $S_{ij} \sim u_r/r \sim \epsilon^{1/3} r^{-2/3}$. This means that vortices of size r are predominantly strained by vortices marginally larger than r. Vortices of size $s \gg r$ only advect smaller vortices with little distortion as their velocity field is nearly uniform on the scale of these smaller vortices. Conversely, since u_r increases with scale, the vortices that benefit most from the strain supplied by the vortices marginally larger than r are likely to be slightly smaller than r. The localness of this energy flux in scale space underpins the multi-step nature of Richardson's hypothesis.

Though (1.15) has been largely verified experimentally, there exists little hard evidence for Richardson's energy cascade, but many consider it to be a plausible process by which energy is transferred in 3D turbulent flows.

1.2.3 Two-dimensional turbulence

Two-dimensional turbulence is an idealized concept. Due to the unavoidable presence of boundaries, which introduce 3D structures, it is almost impossible to achieve full two-dimensionality outside of numerical experiments, though many experimental, geophysical and industrial flows can exhibit a wide number of characteristics of 2D turbulence far from any boundaries. The two earliest theories on 2D turbulence were formulated independently from one another by Kraichnan (1967) [31] for the case of forced turbulence and Batchelor (1969) [5] for decaying turbulence. For this study we will mainly focus on Kraichnan's theories as we are interested in forced turbulent

flows.

On a superficial level one might expect 2D and 3D turbulence to be fairly similar as the random motions can in both cases be attributed to the chaotic mixing of the vorticity field, but in reality they are wholly different. This difference can readily be seen in (1.11). If we are limited a 2D flow, then $(\boldsymbol{\omega} \cdot \nabla)\mathbf{u} = 0$ and so the vortex stretching mechanism, supposedly responsible for the cascade of energy in 3D turbulence, cannot exist. In the inviscid limit of 2D systems the vorticity is conserved along fluid particle trajectories.

A quantity of interest in turbulence is the amount of kinetic energy per unit mass E. In 2D homogeneous systems the evolution of E reads as

$$\frac{dE}{dt} = 1/2\frac{d}{dt}\langle \mathbf{u}^2 \rangle = -\nu Z = \epsilon \ , \tag{1.16}$$

where $Z = \langle \omega^2 \rangle$ is the enstrophy and ϵ is the energy dissipation rate. The evolution of Z, in 2D homogeneous systems, is given by

$$\frac{dZ}{dt} = -\nu \langle (\nabla \omega)^2 \rangle = \beta \ . \tag{1.17}$$

Here β is the enstropy dissipation rate. Looking at (1.17) it can be seen that in 2D turbulence Z decreases monotonically and is bounded by its initial value Z_0. Consequently from (1.16) it becomes apparent that the rate of dissipation of kinetic energy $\epsilon \to 0$ in the limit of $\nu \to 0$. In this sense E is a conserved quantity as $Re \to \infty$. This is very different from 3D turbulence where energy dissipates at a rate independent of ν, as can be seen in (1.15). Due to the vortex stretching the enstrophy in 3D turbulence is in constant flux, increasing and decreasing at largely the same rate.

The conservation of vorticity along fluid particles and E being a conserved quantity in the inviscid limit led Kraichnan [31] to propose the existence of two inertial ranges of scales each with their own distinct cascade. One where there is a constant flux of energy from the injection scale to increasingly larger scales and another where there is a constant flux of enstrophy from the injection scale down to increasingly smaller scales. These are known as the inverse energy cascade and the enstrophy cascade. This differs from 3D turbulence where energy cascades down from the larger injection scales down to increasingly smaller scales. Kraichnan showed that for a triadic interaction between three modes with wavenumbers $\boldsymbol{k}$, $\boldsymbol{p}$ and $\boldsymbol{q}$, each with their own energy density E_i and enstrophy density Z_i, there is a preferential transfer of energy to modes with smaller wavenumbers while there is a preferential transfer of enstrophy to larger wavenumbers. Over many iterations this leads to the energy transferring to the larger scales and enstrophy transferring

to smaller scales.

As a consequence of this double cascade vortices develop in a very distinct manner for both inertial ranges. Broadly speaking vortices in 2D turbulence can be classified as either strong or weak. Their relative strength is determined by the local strain field of the flow, which is set by the initial conditions of the flow. If the vortex or a patch of vorticity is weak it gets strained by the flow. Because the vorticity is conserved, if a patch of vorticity gets stretched along one dimension it has to contract along the other, leading to the formation of fine vortex filaments. This in turn increases the vorticity gradients which, looking at (1.17), fuels the cascade of enstrophy down to smaller scales. This led Kraichnan to derive an energy spectrum for the enstrophy cascade that scales as $E(k)\ k^{-3}$, with the dissipative mechanism at the small scales being diffusion due to viscosity. Studies have found spectra that scale quite differently to the propesed k^{-3} scaling. When Kraichnan formulated his theories one aspect of 2D turbulence was still unknown at the time. This was the presence or emergence of long-lived coherent structures in these types of flows. These large scale structures have a direct influence on the smaller scales as they drive the strain of the flow field. This means that the enstrophy cascade is nonlocal, unlike 3D turbulence where vortices are only affected by vortices slightly larger (or smaller) than themselves.

If a patch of vorticity is relatively strong it remains largely immune from dissipation and tends to form long-lived nearly circular vortices as energy flows to increasingly larger scales. In Kraichnan's view this inverse cascade is in fact a transient state as , in purely 2D turbulence, there is no energy sink at the larger scales. And so energy would flow to ever increasingly larger scales. Experimentally this energy sink is generated through friction with boundaries, numerically this can be represented by adding a friction term to the Navier-Stokes equation. The process by which large scale structures form in 2D turbulence was found to be different for both forced and decaying turbulence. For decaying turbulence it was found that vortices could merge if they were separated by less than a certain critical distance and form a larger vortex in the process [60]. This gradual merger of like sign vortices drives the flow of energy to the larger scales and will eventually lead to a decaying 2D turbulent flow field to be inhibited by only two large counter rotating vortices.

For forced turbulence the formation of large eddies is more akin to an aggregation process. As described by Tabeling [60] it turns out that for forced turbulence the size of the vortices are confined around the injection scale. They are continuously nucleated due to forcing and have a limited lifetime which scales as $1/\beta$. Soon after they are formed they are distorted and moved around by the action of neighbouring vortices and tend to, on average, aggregate with other like sign vortices in order to conserve energy. These clusters generate larger eddies conveying energy towards the larger scales. These clusters have a finite size as the vortices feeding them only have a limited lifespan. This is not to say that the merger of like sign vortices does not happen, but these

events are considered rare. Kraichnan proposed that the energy spectra for the inverse cascade would scale as $E(k)\ k^{-5/3}$.

To summarize, the behaviour of 2D and 3D turbulence is very distinct. If forced at a some scale ℓ 3D turbulence will see energy cascade down to increasingly smaller scales until viscosity can dissipate the energy. The resultant flow field is thus often characterized by vortices of the injection scale down to smaller scales. In 2D turbulence enstrophy cascades down to smaller scales while energy cascades to increasingly larger scales. Enstrophy dissipates at the smallest scales while energy dissipates at the large scales due to external friction. The resultant flow field is characterized by strained vortex filaments and clusters of vortices forming large scale eddies.

1.3 Rotating turbulence

An inherently 3D turbulent flow field can approach a nearly 2D state, often referred to a quasi-two-dimensional (Q2D) state. This Q2D state can be achieved through a number of methods. One such method is by applying a Coriolis force to the flow field. In such a rotating turbulent flow field both direct and inverse energy cascades have been observed simultaneously [10, 12, 53, 66] and a consequence of this is that the flow's ability to dissipate energy decreases significantly when the strength of the Coriolis force is increased [43].

The earliest experiments on the subject of rotating turbulence were carried out by Ibbetson & Tritton (1975) [27] where they observed freely decaying turbulence in a rotating annulus. They observed a phenomenon that has been seen by many other studies since, in that rotation causes eddies to grow along the axis of rotation, forming columnar structures. Furthermore they suggested that inertial waves are important for transporting energy across the flow, though no direct evidence could be given at the time.

Two similar experiments carried out by Hopfinger *et al*. (1982) [26] and Dickenson & Long (1983) [17], focussed on the case of continuously forced turbulence. In both studies the flow was forced locally by rapidly oscillating a grid, generating an inhomogeneous flow field where Ro gradually drops away from the oscillating grid. Hopfinger *et al*. observed that as Ro dropped below $\mathcal{O}(1)$, long-lived columnar structures aligned with the axis of rotation occupied the flow, dramatically increasing the anisotropy. They also observed an apparent preference for these structures to be cyclonic (i.e. $\boldsymbol{\omega}$ aligned with $\boldsymbol{\Omega}$), which has been confirmed frequently since by other studies [10, 21, 42, 58]. The study by Dickenson & Long was focussed on the early stages of the flow build-up and how the 'turbulent cloud' that was generated would spread. They found that when $Ro > 1$ and rotation is weak, the cloud would spread at a rate of $\sqrt{\nu_t t}$, where $\nu_t t$ is turbulent diffusivity. But when $Ro \leq \mathcal{O}(1)$ the cloud would spread at a rate proportional to t. Which would

suggest dispersion of energy through a wave-like mechanism, consistent with Ibbetson & Tritton. Jacquin *et al*. (1990) [28] studied the case of near-homogeneous decaying rotational turbulence. By rotating a honeycomb in a windtunnel turbulence was generated. They observed that the rate of decay of energy is inhibited by rotation and that for $Ro \leq \mathcal{O}(1)$ the integral length scale parallel to the axis of rotation grows linearly with time, $\ell_{\parallel} \sim t$.

Numerous numerical studies followed, a review of which can be found in Cambon & Scott (1999) [9] and more recently in Godeferd & Moisy (2015) [22], which showed a disconnect with the experiments. Experiments are limited to cases where $Ro \lesssim \mathcal{O}(1)$, while numerics often impose $Ro \ll 1$. Furthermore, though the formation of columnar structures was observed these appeared at much longer time-scales than those observed in experiments. As this late onset of structure formation could not readily be explained by linear wave theory it was thought it may be the consequence of another mechanism [64], namely the weak non-linear triadic interactions of inertial waves. Due to its similarity to the mechanism behind energy transfer in 2D turbulence this theory also provides an explanation for the presence of an inverse energy cascade in rotating turbulence. Though not explicitly stating Waleffe's work as the theoretical foundation for inverse energy cascade observed in studies on the subject, it is thought that the presence of an inverse energy cascade is the result of non-linear inertial wave interactions.

Of key interest to our study is how inertial waves influence the formation of columnar structures and as a consequence the promotion of anisotropy in these rotating turbulent flows. Here, we now review the two leading theories behind structure formation and the promotion of anisotropy in rotating turbulence.

1.3.1 Structure formation through linear wave propagation in homogeneous turbulence

In section 1.1.2 it was seen that specific inertial wave packets could be generated through oscillating an object at a frequency σ. What happens now when the object is replaced with a blob of vorticity that not only emits waves through low-frequency oscillations, but any arbitrary set of wave-vectors?

Consider a blob of vorticity positioned somewhere in an infinite rotating fluid. The blob of vorticity generates oscillations across a wide spectrum of frequencies, which can excite inertial waves with wave vectors $\mathbf{k}$, which in turn propagate energy away from the blob. The direction of wave energy propagation can be determined from (1.9). For an initial condition with a wide frequency range of oscillations one might expect that energy disperses in every direction.

Davidson *et al*. (2006) [15] showed however these blobs of vorticity evolve into columnar ed-

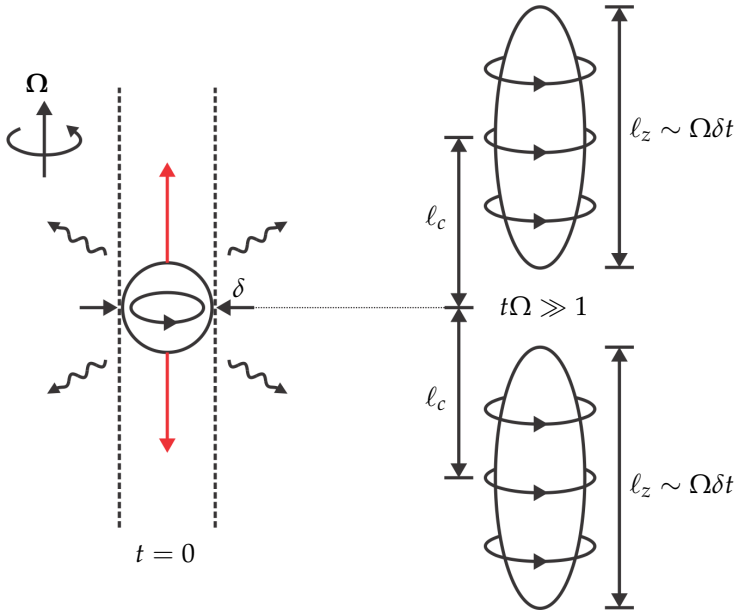

Figure 1.2: Energy from the initial vortex of characteristic size δ can disperse in every direction (wiggly lines) but the angular momentum in tangent cylinder (dashed lines) can only disperse along the axis of rotation (red arrow). As a result the energy density along the axis of rotation is the highest and after a time $t\Omega \gg 1$ a pair of columnar vortices are formed at a distance ℓ_c from the starting point and have a length ℓ_z.

dies aligned with the axis of rotation, where $(\mathbf{\Omega} \cdot \nabla)\mathbf{u}$ is small, similar to a Taylor column, where $(\mathbf{\Omega} \cdot \nabla)\mathbf{u} = 0$. Consider a blob of vorticity of size δ with a control volume around it in the shape of a cylinder which encapsulates the vorticity field and is aligned with the axis of rotation, see figure 1.2. Davidson *et al*. showed that the angular momentum within this control volume can only disperse along the axis of rotation. And while energy disperses in every direction away from the initial blob at a velocity $\mathbf{c}_g \sim \delta\Omega$, there exists a strong bias for dispersion of energy along the axis of rotation. Energy thus primarily propagates away from the initial blob along either direction of the axis of rotation, creating a pair of columnar vortices. These vortices have a length $\ell_z \sim \delta\Omega t$ and their centres are located at $\ell_c \sim \delta\Omega t$. These transient columns form spontaneously as a result of linear wave propagation. Furthermore Screenivasan & Davidson [58] showed that this behaviour is not limited to the case of $Ro \ll 1$, but can hold up to $Ro \sim 1.4$, where $Ro = |u_{max}|/2\Omega\delta$ with u_{max} being the maximum velocity measured at $t = 0$. Davidson *et al*. considered the specific case of inhomogeneous decaying turbulence, where a singular blob could develop freely without being affected by others. Staplehurst *et al*. (2008) [59] expanded on this work by considering the initial condition of homogeneous turbulence. Such a flow field could be seen as consisting of many blobs of vorticity randomly but uniformly distributed in space. The off-axis radiation of energy could affect the formation of structures in this particular case. Using two-point velocity correlations

the mean length of the columnar structures ($\ell_{\parallel}$) that formed were measured over time and it was found that $\ell_{\parallel} \sim \delta\Omega t$, which was then confirmed using a numerical model. This mimicked the behaviour of the individual blobs and lent evidence to the hypothesis that structure formation in rotating turbulence could be driven through linear wave propagation. This theory suggests that columnar structures, generated though linear wave propagation, will grow indefinitely in length until a boundary is reached. It is still an open question what happens to these structures for large time-scales.

1.3.2 Structure formation through weak non-linear interactions of inertial waves

Based on the findings from early numerical studies Waleffe (1993) [64] formed a theory triadic interactions in homogeneous turbulence, which was later expanded on by Smith & Waleffe (1999) [54] to incorporate rapid rotating turbulence. For a start we limit ourselves to conventional homogeneous turbulence, before expanding the theories to include rapidly rotating turbulence. Waleffe showed that an instantaneous incompressible velocity field $\mathbf{u}(\mathbf{x})$, measured in an inertial frame, can be decomposed into a sea of helical modes.

$$\mathbf{u} = \sum_{\mathbf{k}} \sum_{s=\pm 1} a_s(\mathbf{k}) \mathbf{h}_s(\mathbf{k}) \exp[j\mathbf{k} \cdot \mathbf{x}] \tag{1.18}$$

For any mode with wavenumber k, s indicates either positive (-1) or negative (+1) helicity, $a_s(\mathbf{k})$ are the amplitudes and $\mathbf{h}_s(\mathbf{k})$ defines its spatial structures.

When substituted into the Navier-Stokes equation this yields a solution where the non-linear interactions are restricted to modes that satisfy the so-called *triad relationship* $\mathbf{k} \pm \mathbf{q} \pm \mathbf{p} = 0$. If we consider the idealised situation where a single triad evolves independently on any other helical modes we have, as a consequence of energy and helicity conservation,

$$C_k + C_p + C_q = 0 \ , \ \ s_k k \, C_k + s_p p \, C_p + s_q q \, C_q = 0 \ .$$

Where C_i is an energy transfer coefficient and s_i is the mode's helicity which can be either positive (+1) or negative (-1). In order for these two statements to hold one of the three energy transfer coefficients has a sign opposite to the others. This single triad has three steady solutions, each of which corresponds to energy being held in a single mode, two of these modes turn out to be linearly stable and the third unstable. The unstable mode corresponds to the one with the sign of C_i opposite to the other two. Waleffe showed that when $k < p < q$, the unstable mode is k when the helicity of p and q have an opposite sign, or that the unstable mode is p when p and q have the same sign. Now there are two possibilties: either energy flows from the unstable mode

to the other two or it absorbs energy from the other two. For homogeneous turbulence we have many interacting triads. Waleffe proposed that, on average, one would expect energy to pass from the unstable mode to the two stable modes. This is referred to as the *instability assumption*, and it appears to be consistent with numerical simulations.

Smith & Waleffe (1999) proposed that these theories can be applied to rapidly rotating turbulence. For one, inertial waves are helical structures which, when you have a vast multitude of them can be expressed as follows

$$\mathbf{u} = \sum_{\mathbf{k}} \sum_{s=\pm 1} a_s(\mathbf{k}) \mathbf{h}_s(\mathbf{k}) \exp[j(\mathbf{k}\cdot\mathbf{x} - \sigma_s t)] \ , \tag{1.19}$$

which is similar to (1.18), with the addition of a time-dependent term $\exp[-j\sigma_s t]$, where σ_s is the wave frequency. When inserted into the Navier-Stokes equation this yields a solution where the non-linear interactions are restricted to modes that again satisfy the triad relationship. These modes each have a characteristic frequency σ_{s_i}. It is shown that the main contribution showed to the non-linear interaction comes from modes which satisfy the *resonant condition* $\sigma_{s_k} + \sigma_{s_p} + \sigma_{s_q} = 0$. Contributions from modes which satisfy $\sigma_{s_k} + \sigma_{s_p} + \sigma_{s_q} \neq 0$ average out to zero over periods of time far greater than those imposed by Ω. This is used as an explanation for the long time-periods over which structures form in numerical studies on rotational turbulence.

If again we consider the idealized situation of a single triad of modes evolving which satisfy both the triad relationship and the resonant condition we have the following,

$$k\cos\vartheta_k + p\cos\vartheta_p + q\cos\vartheta_q = 0 \ , \ \ s_k\cos\vartheta_k + s_p\cos\vartheta_p + s_q\cos\vartheta_q = 0 \ ,$$

where $\cos\vartheta_k = k_{\|}/k$, which can be rewritten to give

$$\frac{\cos\vartheta_k}{s_p q - s_q p} = \frac{\cos\vartheta_p}{s_q k - s_k q} = \frac{\cos\vartheta_q}{s_k p - s_p k} \ . \tag{1.20}$$

The addition of this resonant condition promotes the growth of anisotropy and as a consequence the emergence of columnar structures. To prove this we look again to the instability assumption, now with the additional restrictions of (1.20) taken into account. Again we have $k < p < q$. If $s_p = s_q$, then p transfers energy to the other two (on average), but due to (1.20) we also require $|\cos\vartheta_p| > |\cos\vartheta_k|, |\cos\vartheta_q|$. This means that energy is transferred from the wavevector most closely aligned with the rotation-axis to those closer to the transverse plane. Now if $s_p = s_q$ then k is the unstable mode, transferring its energy (on average) to the other two, but again due to (1.20) we have $|\cos\vartheta_k| > |\cos\vartheta_p|, |\cos\vartheta_q|$. Which again insinuates that energy trans-

fers to wavevector more closely aligned with the plane transverse to the axis of rotation. This means that if the instability assumption holds, then resonant triad interactions favour the formation of columnar structures, increasing anisotrophy. Though inverse energy cascades have been observed both experimentally the triadic interactions have not been experimentally observed in the context of rotating turbulence, however Bordes *et al*. (2012) [7] was able to observe such triadic interactions for marginally steady rotational flows.

1.3.3 Recent experimental studies

Table (1.1) shows a compilation of experimental studies conducted on rotating turbulence over the years. Apart from the earliest studies, the measurement technique used to capture the local velocity field amongst all studies is largely the same. The experiments are divided based on their method of forcing. In decaying experiments a flow field is brought to a state of (nearly) homogeneous turbulence through a single impulse, often a grid towed through the flow field, and left to decay in time. In forced experiments a flow field is continuously forced locally, generating an inhomogeneous turbulent flow field and left to decay spatially. Diffusive experiments can be considered a subcategory of forced experiments, where the forcing mechanism essentially introduces no mean flow. Though not all experiments will be discussed the studies mentioned in table (1.1) form the basis for knowledge on measurement and analytical techniques used through out this thesis.

Authors	Flow regime	Type of forcing	Ro
Ibbetson & Tritton (1975) [27]	Decay	Single grid stroke	0.3 - 1.9
Hopfinger *et al*. (1982) [26]	Diffusive	Oscillating grid	3 - 33
Dickenson & Long (1983) [17]	Diffusive	Oscillating grid	1.4 - 12
Jacquin *et al*. (1990) [28]	Spatial decay	Grid in windtunnel	4 - 95
Baroud *et al*. (2003) [4]	Forced	Jets & sinks	$Ro_\omega = 0.06$ - 1.1
Morize *et al*. (2005) [42]	Decay	Single grid stroke	2.4 - 120
Davidson *et al*. (2006) [15]	Diffusive	Single oscillation	$Ro_\omega = 1.5$ - 3.5
Staplehurst *et al*. (2008) [59]	Decay	Single grid stroke	$Ro_\omega = 1$ - 2.7
Kolvin *et al*. (2009) [29]	Forced	Jets & sinks	-[†]
van Bokhoven *et al*. (2009) [6]	Forced	Electromagnetic forcing	$Ro_\lambda = 0.01$ - 0.15
Moisy *et al*. (2011) [39]	Decay	Single grid stroke	5 - 20
Duran-Matute *et al*. (2013) [19]	Forced	Oscillating Torus	-
Yarom *et al*. (2014) [67]	Forced	Jets & sinks	$Ro_u = 0.006$ - 0.02
Campagne *et al*. (2014/15) [10, 11]	Forced	Axial flaps	$Ro_u = 0.07$ - 0.3

Table 1.1: Compilation of experimental studies on rotating turbulence over the past few decades (based on Godeferd & Moisy [22]). Rossby numbers are based on grid parameters where relevant, Ro_ω, Ro_u are the micro-Rossby number based on the *rms* of the vorticity and velocity field respectively and Ro_λ is the Rossby number based on Taylor micro-scale. [†] No mention of Ro is given in the paper, but the same setup was later used by Yarom *et al*. [67] for follow-up experiments.

Davidson *et al*. quantified the formation of columnar structures in rotational turbulence, which was largely an expansion on earlier studies conducted by Hopfinger and Dickenson & Long. In their experiment a turbulent flow was forced locally by a single grid oscillation, allowing columnar vortices to grow into the quiescent field. Davidson *et al*. showed that for the case of inhomogeneous rotational turbulence the early stages of structure formation appeared to be dominated by linear inertial wave interactions as described in section (1.3.1). Measurements were conducted using pearlescence [52], a technique where small plate-like particles, mixed into the fluid, align with the flow and selectively reflect incoming light. These platelets highlight regions of intense, persistent strain. As such, they are good for identifying large-scale structures while being largely unaffected by small-scale turbulent motions. This is done by illuminating the flow field with a lightsheet generated simple light source such as halogen lights. This allowed for a straightforward measurement of both the width and length of the columnar structures as a function of time, which provided proof for the formation of structures through linear wave propagation.

Staplehurst *et al* [59] expanded on this study by examining the same phenomena in an initially homogeneous turbulent flow field. The flow was forced by lowering a grid through the entire tank once it reached solid body rotation and then let it decay overtime. The flow was again recorded using pearlescence. Because the columnar structures are elongated along the axis of rotation, they could be identified and their growth could be tracked using two-point cross correlations along said axis. Another technique used was particle-image-velocimetry (PIV) [62], a technique used in almost all relevant experimental studies on this subject in recent memory. The principle of PIV is to seed a carrier fluid with small, neutrally bouyant, inertialess particles which are often coated in order to increase their reflective properties, these are referred to as tracer particles. These particles are illuminated using a lasersheet and the flowfield is recorded using a single or multiple CCD or CMOS cameras over a multitude of frames. The resulting velocity field is obtained by calculating local cross-correlations between two consecutive frames. Both pearlescence and PIV results showed that structures in homogeneous rotating turbulence form in a similar fashion to those observed by Davidson *et al*.. Recent studies largely follow the same experimental method. The major difference between studies arises in the way the flow is forced and how the recorded flow fields are analysed.

In a study by Kolvin *et al*. [29] a flow is continuously forced at the bottom of a tank through simultaneous fluid injection and withdrawal through a lattice of numerous sources and sinks spread out in a hexagonal pattern. Similar to Hopfinger *et al*. this generates a flow that decays spatially from a 3D turbulent flow to a 2D turbulent flow. This experimental setup was later used by Yarom *et al*. (2013/2014) [66],[67] for a number of studies expanding on this work. Of key interest in these studies was the role inertial waves play in rotating turbulence. Due to the fact that inertial

waves cannot exist beyond frequencies greater than 2Ω, high rotation rates are needed to ensure a large range of frequencies across which they can be observed and analysed. As such the setup was designed to allow for extremely high rotation rates (up to $4\pi rad/s$). By measuring the velocity field at a given height, well above the point of forcing, Kolvin *et al*. showed through spatial Fourier analysis that large scale motions (i.e. low wavenumber) propagate faster than small scale motions, exactly in line with (1.9) and (1.10b). Yarom *et al*. [66],[67] showed, through both spatial and temporal Fourier analysis, that for low *Ro* turbulent flows a majority of a flows energy is contained within inertial waves and that there exists an *inverse* energy cascade, with energy transferring into ever larger structures.

The relation between waves, turbulence and columnar structures was beautifully illustrated by a small experiment carried out by Duran-Matute *et al*. (2013). In their experiment inertial waves of a set frequency are focused into a single point using a oscillating torus. At this focal point a small patch of turbulence is generated and a coherent columnar structure forms as a result. Though distinct from other experiments discussed, in that turbulence is a consequence of interactions of inertial waves rather than the other way around, this experiment strongly suggests non-linear inertial wave interactions drive the mechanism behind columnar structure formation.

The presence of an inverse energy cascade and the transfer of energy in general was explored in great detail by Campagne *et al*. (2014/2015) [10, 11]. The forcing mechanism used in their experiments is unique compared to others used in this field of study. Their forcing mechanism consists of a set of plates/flaps spanning the entire height of their flow field. By flapping these plates back and forth (like clapping ones hands together) vortex dipoles are emitted into the region of interest. By placing a number of these generators in a circular pattern all aimed at the same central region, turbulence can be generated which is continuously forced, but nearly homogeneous along the axis of rotation. In their [10] work they explored the energy transfer of both horizontal and vertical kinetic energy on a scale-by-scale basis and how these are affected by the rotation rates. They found for the horizontal energy transfer there exists a double energy cascade, with a *direct* cascade at the smallest scales and an *inverse* cascade at the largest scales of the flow. As the rotation rate is increased this separation is pushed to increasingly smaller scales. The vertical energy transfer was observed to be direct across all cases studied. Campagne [11] showed that the growth of anisotropy at the larger scales of a rotating turbulent flow field is well described by wave turbulence where the waves follow the dispersion relation for inertial waves, in accordance with Yarom *et al*. [67]. At the smaller scales however this breaks down, due to small scales be swept away by motions at the larger scales.

In summary, two main theories exist to explain the mechanism that drives the formation of columnar structures in rotating turbulence. One theory states that linear inertial wave are the

main cause for energy propagation in rotating turbulence and have a strong bias for propagation along the axis of rotation, thus driving the formation of columnar structures, which is supported by experimental [15, 29, 59] and numerical [58] evidence. The other theory invokes non-linear triadic interactions between inertial waves as the cause for columnar structure formation, which is supported by experimental [10, 19, 66] and numerical [12, 53] evidence. At the time of writing there is no consensus as to whether the formation of columnar structures is driven by the mechanisms explored in sections (1.3.1) and (1.3.2), but from all studies discussed so far it appears that the mechanics of rotating turbulent flows are intrinsically linked to the existence of inertial waves.

1.4 Magnetohydrodynamic flows & turbulence

The growth of anisotrophy and subsequent formation of columnar structures is a phenomena not unique to rotating turbulent flows as there exist numerous methods by which a (turbulent) flow field can tend towards two-dimensionality. In MHD flows a strong magnetic field $\mathbf{B}$ is applied across an electrically conducting fluid (i.e. a liquid metal) generating and electric current density $\mathbf{J}$. In turn, their mutual interaction creates a Lorentz force density $\mathbf{J} \times \mathbf{B}$ on the flow field, which can cause the field to become invariant along the magnetic field, similar to the Coriolis force in rotating flows. Both rotational flows and MHD flows are described by largely the same governing equations, but there are significant differences [49]. A major difference between the two types of flows is that in rotational flows energy gets transported through inertial waves, while the electromagnetic forces in MHD flows are strictly dissipative [55]. This difference has a profound effect on the mechanism responsible for the formation of columnar structures in turbulent MHD flows.

There exist a number of important dimensionless numbers that describe a MHD flow, namely:

$$Re = \frac{u\ell}{\nu} \ , \ N = \frac{\sigma B^2 \ell}{\rho u} \ , \ Ha = \sqrt{\frac{\sigma}{\rho u}} B\ell \ , \ Rm = \mu\sigma\ell u$$

Here σ,B,ρ and μ are the electrical conductivity, the magnetic field strength, fluid density and the magnetic permeability. Here Re is the standard Reynolds number, N is the interaction parameter which gives a coarse ratio between the Lorentz forces and inertial forces, Ha is the Hartmann number, which gives the ratio between viscous forces and Lorentz forces and Rm is the magnetic Reynolds number. When Rm is large (highly conducting fluids) there is a two-way interaction between $\mathbf{u}$ and $\mathbf{B}$, with $\mathbf{u}$ distorting the magnetic field lines and $\mathbf{B}$ reacting back on the velocity field through a resulting Lorentz force. When Rm is small any distortions to $\mathbf{B}$ by $\mathbf{u}$ are small compared to the imposed magnetic field and so $\mathbf{B}$ is more or less independent of $\mathbf{u}$, but $\mathbf{B}$ still influences the velocity field. For the rest of this section we consider only flows that adhere to the

so-called low Rm-approximation, $Rm \leq 10^{-2}$.

For a magnetic field $\mathbf{B} = B\hat{e}_z$ the governing equations are the Navier-Stokes equations, Ohm's law and the conservation of mass and charge.

$$\partial_t \mathbf{u} + \mathbf{u} \cdot \nabla \mathbf{u} + \frac{1}{\rho}\nabla p = \nu \nabla^2 \mathbf{u} + \frac{B}{\rho}\,\mathbf{J} \times \hat{e}_z \ , \tag{1.21}$$

$$\frac{1}{\sigma}\,\mathbf{J} = -\nabla\phi + B\boldsymbol{u} \times \mathbf{e}_z \ , \tag{1.22}$$

$$\nabla \cdot \boldsymbol{u} = 0 \ , \tag{1.23}$$

$$\nabla \cdot \mathbf{J} = 0 \ , \tag{1.24}$$

where ϕ is the electric potential. If we take the curl of (1.22) and take (1.23) into account, the effect of the Lorentz force becomes more clear [50]

$$\nabla \times \mathbf{J} = \sigma B \partial_z \mathbf{u} \ .$$

What this shows is that gradients of horizontal velocity along $\mathbf{B}$ induce electric eddy currents with a vertical component. The resultant Lorentz force, $\boldsymbol{F}_L = \mathbf{J} \times \mathbf{B}$, tends to dampen this velocity gradient. In the limit of low Rm Sommeria *et al*. [55] showed that momentum is diffused along the direction of the magnetic field.

The momentum for an initial blob of vorticity in an infinite fluid, of initial size δ subject to a magnetic field $\mathbf{B} = B\hat{e}_z$, would diffuse along a length ℓ_z in a characteristic time $t = \tau_J(\ell_z/\ell_\perp)^2$, where $\ell_\perp \approx \delta$ and τ_J is the Joule dissipation time. This can also be expressed as

$$\frac{\ell_z}{\ell_\perp} \sim N^{1/2} \tag{1.25}$$

What (1.25) shows is that in the limit of $B \to \infty$ the columnar structures would have an 'infinite' length implying $\partial_z u_z = -\nabla_\perp \cdot \mathbf{u}_\perp = 0$. When a flow is bounded by two insulating walls along the bottom and top and is driven by injecting a current I through point electrodes at the bottom wall, a Hartmann boundary layer forms along the boundaries as a consequence of viscous friction opposing $\boldsymbol{F}_L$. Sommeria *et al*. [56] showed that in the Q2D limit where $N \to \infty$, $Ha \to \infty$, the azimuthal velocity in the core of each vortex in the flow was linearly dependent on the current.

When B is finite, implying both N and Ha are finite, a horizontally divergent flow exists and the resultant $\boldsymbol{F}_L$ ought to be opposed by viscous or inertial forces in the core of the flow field. Potherat & Klein [50] explored exactly this configuration in the three-dimensional limit. When inertia can be neglected ($N \to \infty$) and Ha is finite they showed that there is a finite distance ℓ_z

across which injected current is exhausted away from the electrodes. The structures that form over the electrode induce a velocity field in the bulk of the flow which results in a characteristic azimuthal velocity U_b, where both ℓ_z and U_b are shown to scale as

$$\frac{\ell_z}{\ell_\perp} \sim \frac{\ell_\perp}{h} Ha \,, \tag{1.26}$$

$$U_b \sim I \,. \tag{1.27}$$

Here h is the distance between the two insulating walls. In turbulent regimes, N is finite and viscous effect can be neglected. Fluid is set in motion up to a distance ℓ_z corresponding to (1.25) and assuming $Ha \to \infty$ the resultant U_b was shown to scale as

$$U_b \sim I^{2/3} \,. \tag{1.28}$$

Both (1.27) and (1.28) where shown to hold experimentally in the same study, showing that the mechanism that drives structure formation in MHD turbulence is driven by a Lorentz force diffusing momentum along the magnetic field whilst opposed by inertial forces.

1.5 Summary

The purpose of this thesis is to study the transition from 3D to 2D turbulence in the presence of background rotation and the particular influence that inertial waves have on the physical processes driving these flows.

In an incompressible fluid flow where $Ro \ll 1$ and $Re \gg 1$ the Navier-Stokes equation simplifies to a linear equation which, if the flow can be considered steady, results in the flow field being invariant along the axis of rotation. This is referred to as the Taylor-Proudman theorem.
Under steady conditions anisotropic columnar structures, known as Taylor columns [61], form under the combined influence of both viscous forces and the Coriolis force [41]. When a turbulent flow field is subject to a Coriolis force the flow field can manifest itself in either three or two dimensions, depending on the relative strength of the Coriolis force, resulting in either a direct or inverse energy cascade where energy travels from large to small scale structures or its inverse respectively. When the Coriolis force is substantially strong ($Ro < 1$) columnar structures, elongated along the axis of rotation, can form in the turbulent flow fields.
Inertial waves, a form of internal waves unique to rotating flows [24], are thought to be at the heart of the mechanism driving the formation of these columns in rotating turbulence, due to their ability to efficiently transport energy and them having been shown to carry a significant amount of

the overall turbulent kinetic energy [33, 67].

There are two main theories which explain this mechanism. The first [15] invokes that linear inertial waves have a preferential direction for energy propagation along the axis of rotation. The second theory [54] states that the formation of these structures is the result of weak non-linear resonant triadic inertial wave interactions. Both theories are supported by strong numerical and experimental evidence.

However, anisotropy and the resultant columnar structures also manifest themselves in the absence of turbulence and inertial waves. Furthermore inertial waves can only exist in a limited flow regime, suggesting there may be other mechanisms at play in rotating turbulence that are wave-free.

Similar columnar structures are found in MHD turbulent flows. In the low Rm limit the mechanism responsible for the formation of these columnar structures has been shown to be diffusive in nature [55],[50]. Similarities between MHD and rotating flows allow us to apply the methodology of said MHD flows to the rotating case, the consequences of which are explored in the following chapter.

Chapter 2

Anisotropy and structure formation in rotating turbulent flows

Anisotropy in rotating flows is often studied in the context of turbulence in fast rotating systems. Most commonly manifesting itself in the form of elongated columnar structures, anisotropy in these types of flows is thought to be the consequence of the interactions of inertial waves, either through non-linear triadic interactions [9, 54] or by linear inertial waves transporting energy throughout the flow field [15, 59]. These theories however do not adequately account for flow structures observed in rotating flows such as Taylor columns. Analytical solutions of these columns [40, 41] are entirely steady and neglect non-rotating inertia, excluding the effects of inertial waves.

Inspired by this and studies on anisotropy in magnetohydrodynamic turbulence we explore the potential for an alternative mechanism promoting anisotropy in rotating flows not involving inertial waves.

In the first section of this chapter we apply a similar methodology to Sommeria *et al*. (1982) [55] and Potherat & Klein (2014) [50] to the case of rotating flows where $Ro \ll 1$ showing the Coriolis force is greater than the inertial forces acting on the flow field. We discuss how, as a consequence of a horizontally divergent flow, a Coriolis force is opposed by either viscous or inertial forces and how this leads to the formation of columnar structures in the absence of any boundaries. This is expanded on by introducing boundaries and a method by which momentum is injected into the flow. We then consider our theory in the context of continuously forced rotating turbulent flows with a non-zero average flow in time. This is achieved by rewriting the governing equations in terms of the average flow quantities. The reason for doing so is that the average of such a type of

flow is both steady in nature and subject to the influence of inertial waves. As such, these flows are the ideal battleground for mechanisms both with and without waves to compete in promoting anisotropy.

In the second section we consider how the flow field develops when $Ro \geq 1$ locally. This is relevant as the experimental methods by which we seek to test the theories derived in this chapter will locally cause inertial forces to be large compared to the applied Coriolis force.

2.1 Rotating turbulent flows in the limit of $Ro \ll 1$

Before continuing, it has to be stated that the theories derived in section 2.1 were not derived by the author himself, but rather by Prof. Alban Pothérat. These theories formed the original motivation for the entirety of this study. Here the author's own version of the derivation of these theories is presented.

Consider a blob of vorticity in an incompressible fluid far from any boundaries subject to background rotation $\mathbf{\Omega} = \Omega \mathbf{e}_z$. This blob of vorticity, under action of the Coriolis force, is elongated to a columnar structure aligned with the axis of rotation. In the limit of $\Omega \to \infty$ both effects of inertia and viscosity are negligible and the Taylor-Proudman theorem states $\partial_z u_z = 0$ which, according to $\nabla \cdot \mathbf{u} = 0$ implies that $\nabla_\perp \cdot \mathbf{u}_\perp = 0$, where $\perp$ refers to the axis perpendicular to the axis of rotation. The flow is columnar and the structure that forms has an 'infinite' length [49]. However, if Ω is finite $\partial_z u_z \neq 0$ and there must exist divergent flow perpendicular to the axis of rotation. The resulting Coriolis force has to be opposed by either viscosity or inertia, exhausting the momentum of the blob of vorticity and limiting its length to a finite length ℓ_z.

This is the end-state of our system and we are interested in defining scaling laws on the characteristic length (ell_z) and width ($\ell_\perp$) of these structures and the characteristic velocities (U) they induce.

2.1.1 Columnar structure length ℓ_z

We begin by seeking a scaling for ℓ_z. To start we assume to be operating in a flow regime where $Ro \ll 1$. We define the equations of motion using the Navier-Stokes equation in a rotating frame. Furthermore the fluid is incompressible and we are far away from any boundaries.

$$\frac{D\mathbf{u}}{Dt} + \nabla(p/\rho) = \nu \Delta \mathbf{u} + 2\mathbf{u} \times \mathbf{\Omega} \ , \tag{2.1}$$

$$\nabla \cdot \mathbf{u} = 0 \ . \tag{2.2}$$

Here $\frac{D}{Dt} = \partial_t + \mathbf{u} \cdot \nabla$ is the material derivative, Δ is the Laplacian operator, $\mathbf{\Omega} = \Omega \mathbf{e}_z$ and p is the pressure force reduced by the centrifugal force acting on the fluid. From (2.1) we derive three governing equations for our flow system, by taking the z-component of (2.1), the curl of the z-component and the divergence of (2.2)

$$\left[\frac{D}{Dt} - \nu\Delta\right] \omega_z = \boldsymbol{\omega} \cdot \nabla u_z + 2\Omega \partial_z u_z \, . \tag{2.3}$$

$$\left[\frac{D}{Dt} - \nu\Delta\right] u_z = \frac{1}{\rho}\partial_z P \ , \tag{2.4}$$

$$\nabla \cdot (\mathbf{u} \cdot \nabla)\mathbf{u} = 2\Omega\omega_z - \frac{1}{\rho}\Delta P \ . \tag{2.5}$$

These three equations allow us to estimate the horizontally divergent flow that exists for columnar structures when Ω is finite. This is done using scaling arguments. Consider a structure of length ℓ_z, width $\ell_\perp$ and velocity U. From this we assume $\omega_z \sim U/\ell_\perp$. Furthermore $\ell_z \gg \ell_\perp$, which implies $\nabla \sim \ell_\perp^{-1} + \ell_z^{-1} \approx \ell_\perp^{-1}$. Using these scaling arguments it can be shown that

$$\frac{|\nabla \cdot (\mathbf{u} \cdot \nabla)\mathbf{u}|}{|2\Omega\omega_z|} \sim \frac{U^2/\ell_\perp^2}{2\Omega \, U/\ell_\perp} = \frac{U}{2\Omega\ell_\perp} = Ro \, ,$$

which shows that in the limit of $Ro \ll 1$ the LHS of (2.5) can be neglected. Given (2.5) the above implies that:

$$\frac{1}{\rho}P \cong 2\Omega\Delta^{-1}\omega_z \, , \tag{2.6}$$

where Δ^{-1} is the inverse Laplacian operator. It can be solved numerically by defining the right boundary conditions based on the geometry of the flow.

We now consider two flow regimes. In the viscous regime the viscous forces outweigh the inertial forces ($Re = U\ell_\perp/\nu \ll 1$) and thus oppose the horizontally divergent flow. In the inertial regime the inertial forces outweigh the viscous forces ($Re \gg 1$) and oppose the divergent flow.

For the viscous regime the inertial term $\boldsymbol{\omega} \cdot \nabla u_z$ in (2.3) can be dropped. The other inertial term (D/DT) in (2.3) and (2.4) scales as the inverse of the viscous time-scale $\nu/\ell_\perp^2$. This is of the same order of magnitude as the viscous term ($\nu\Delta$). While this inertial term can be kept its contributions to the governing equations, based on scaling arguments, drop out when scaling laws for ℓ_z are derived. For clarity, we chose to take these inertial term into the viscous term to give:

$$-\nu\Delta\omega_z = 2\Omega\partial_z u_z \, , \tag{2.7}$$

$$-\nu\Delta u_z = \tfrac{1}{\rho}\partial_z P \, . \tag{2.8}$$

Combining (2.6) and (2.8) gives:

$$\begin{aligned} -\nu\Delta u_z &= 2\Omega\partial_z\Delta^{-1}\omega_z \,, \\ 2\Omega\partial_z u_z &= \tfrac{4\Omega^2}{\nu}\partial_{zz}\Delta^{-2}\omega_z \,. \end{aligned}$$

Which when inserted in (2.7) gives:

$$-\nu\Delta\omega_z = \frac{4\Omega^2}{\nu}\partial_{zz}\Delta^{-2}\omega_z \,. \tag{2.9}$$

We now apply scaling arguments to (2.9)

$$\begin{aligned} \frac{\nu}{\ell_\perp^2} &\sim \tfrac{4\Omega^2}{\nu}\tfrac{1}{\ell_z^2}\ell_\perp^4 \,, \\ \ell_z^2 &\sim (\tfrac{2\Omega\ell_\perp^2}{\nu})^2\ell_\perp^2 \,, \\ \ell_z^V &\sim \ell_\perp Ek^{-1} \,. \end{aligned} \tag{2.10}$$

Where $Ek = \nu/2\Omega\ell_\perp^2$ is the Ekman number, which gives the ratio between the viscous forces and the Coriolis force acting on the flow field. This length scale ℓ_z^V can be interpreted as the distance needed for viscous effects to exhaust the horizontally divergent flow that drives the column. It is based on a balance between the viscous forces and the Coriolis force. It is similar to the analytical solution for Taylor columns implied by Moorse & Saffman [40, 41].

Following the above we drop the viscous terms in (2.3) and (2.4) for the inertial regime, to give:

$$\frac{D}{Dt}\omega_z \cong 2\Omega\partial_z u_z \,, \tag{2.11}$$

$$\frac{D}{Dt}u_z = \frac{1}{\rho}\partial_z P \,. \tag{2.12}$$

The terms $|D\omega_z/Dt|$ and $|\boldsymbol{\omega}\cdot\nabla u_z|$ in (2.3) are of the same order of magnitude. As such, when making scaling arguments we can take the $\boldsymbol{\omega}\cdot\nabla u_z$ term into the material derivative, as is done in (2.11). Combining (2.6), (2.12) and applying scaling arguments gives:

$$\begin{aligned} \frac{1}{\rho}P &\sim 2\Omega\omega_z\ell_\perp^2 \,, \\ \frac{U}{\ell_\perp}u_z \sim \frac{1}{\rho}P\frac{1}{\ell_z} &\sim 2\Omega\omega_z\frac{\ell_\perp^2}{\ell_z} \,. \end{aligned}$$

Applying the same scaling arguments to (2.11) then gives:

$$\begin{aligned} \frac{U}{\ell_\perp}\omega_z &\sim \frac{2\Omega}{\ell_z}u_z \sim \left(\frac{2\Omega\ell_\perp}{\ell_z}\right)^2 \frac{\ell_\perp}{U}\omega_z \,, \\ \ell_z^2 &\sim \left(\frac{2\Omega\ell_\perp}{U}\right)^2 \ell_\perp^2 \,, \\ \ell_z^I &\sim \ell_\perp Ro^{-1} \,. \end{aligned} \tag{2.13}$$

Where ℓ_z^I can be interpreted as the distance needed for inertial effects to exhaust the horizontally divergent flow that drives the column. Knowing the characteristic dimensions of the columnar structures, we can approximate the velocity fields they induce.

2.1.2 Characteristic velocity U

In our experiments a fluid flow is forced through simultaneous injection and withdrawal of fluid through a number of forcing points between two no-slip walls whilst subject background rotation, reminiscent of the experiments carried out by Potherat & Klein [50] where a liquid metal fluid flow is forced by injecting an electric current through electrodes placed in a checkerboard pattern between two insulating no-slip walls, whilst it is subject to a high magnetic field. Their particular method of forcing creates columnar structures of opposite vorticity over each electrode, whose characteristic velocity was derived [55] and later experimentally shown to scale with the current.

In this section we use a similar approach for the characteristic velocity our columnar structures ought to induce. Consider a flow field that is forced by injecting (or withdrawing) fluid at a constant flow rate Q through a source (sink) at a bottom wall with a fluid of infinite height above it. The flows is subject to a constant rotation speed $\mathbf{\Omega} = \Omega\mathbf{e}_z$ that is strong enough to ensure $Ro < 1$ across the entirety of the flow field. Columnar structures are thought to form according to (2.10) and (2.13) over the injection point with width $\ell_\perp$ and height ℓ_z. These structures induce a characteristic velocity U along the plane perpendicular to the axis of rotation. Here we derive scaling laws for U based on (2.10) and (2.13). This is done as U can more readily be obtained experimentally. Figure 2.1 shows a sketch of the steady structures assumed to form over the injection points and provides a general overview of all relevant quantities.

As a result of Coriolis force a boundary layer forms along the bottom wall where fluid is injected. This boundary layer is called the Ekman layer. It's thickness is given by $\delta_E = \sqrt{\frac{\nu}{\Omega}}$. The fluid that is injected spreads between the core of the flow and the Ekman layer, which gives

$$Q = Q_b + Q_c \,, \tag{2.14}$$

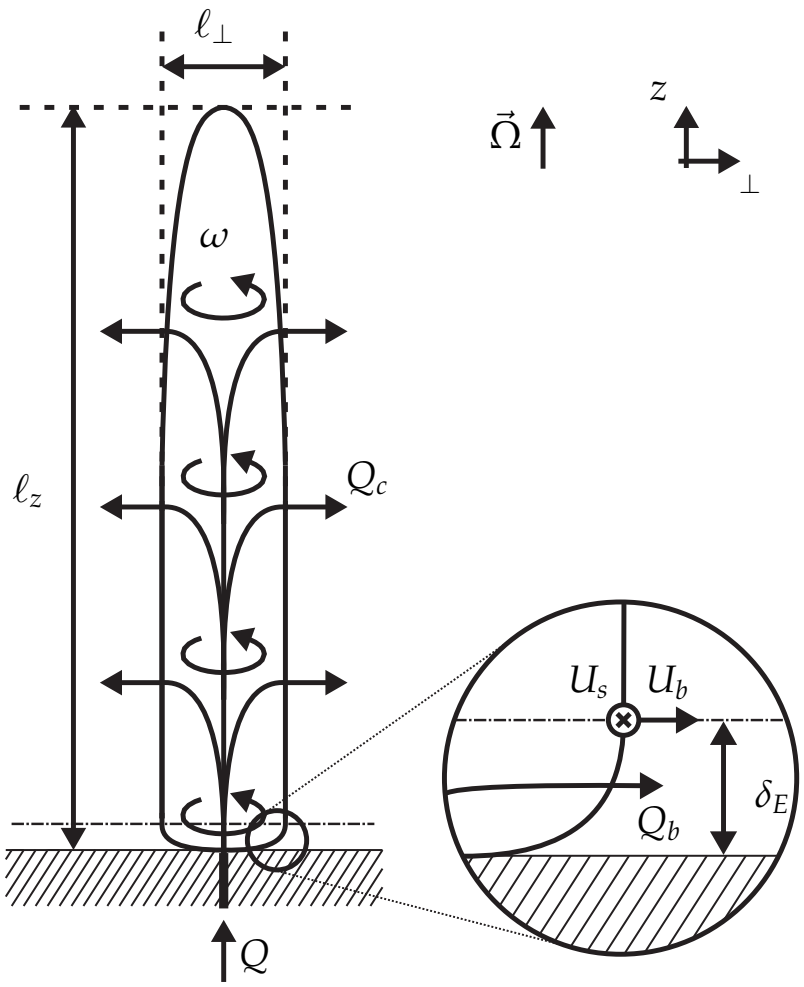

Figure 2.1: Sketch of the columnar structures that are assumed to form through fluid injection at a flow rate Q subject to a strong Coriolis force. Injected fluid is spread between the core of the flow and the Ekman boundary layer.

where Q_b is the flow rate through the Ekman layer and Q_c is the flow rate through the core of the flow.

The velocity just above the Ekman boundary layer has both a radial and azimuthal component. The radial velocity we refer to as the bulk flow velocity U_b and the azimuthal we refer to as the swirl velocity U_s. From the Ekman boundary layer theory [47] the local radial flow rate Q_r across δ_E can be approximated as:

$$Q_r \sim \frac{1}{2}\delta_E U_s \,. \tag{2.15}$$

When integrated across the surface of the columnar structure we get

$$Q_b = \int_0^{2\pi} Q_r \ell_\perp d\theta = \pi \ell_\perp \delta_E U_s \,. \tag{2.16}$$

We assume that $\delta_E \ll \ell_z$ and we assume that the columnar structures can be approximated as having cylindrical shape, giving

$$Q_c \sim 2\pi U_b \ell_\perp \ell_z \ . \tag{2.17}$$

Assuming $U_b \sim U_s$, giving $Q_b \sim \pi \ell_\perp \delta_E U_b$, equations (2.16) and (2.17) can be combined to give:

$$Q \sim 2\pi \ell_\perp^2 U_b \left(\sqrt{\frac{1}{2}Ek} + \frac{\ell_z}{\ell_\perp} \right) \,. \tag{2.18}$$

Equations (2.10) and (2.13) provide an estimate on ℓ_z. We estimate U_b by assuming $U_b \sim u_\perp$. Then using (2.2) we rewrite (2.3) to give:

$$-\nabla_\perp \cdot u_\perp = \partial_z u_z = \frac{1}{2\Omega}\left[\frac{D}{Dt} - \nu\Delta\right]\omega_z - \boldsymbol{\omega}\cdot\nabla u_z \ . \tag{2.19}$$

Again we consider the separation between the viscous and inertial regime. For the viscous regime we have from (2.19):

$$\begin{aligned} -\nabla_\perp \cdot u_\perp &= \frac{\nu}{2\Omega}\Delta\omega_z \,, \\ \frac{U_b}{\ell_\perp} &\sim \frac{\nu}{2\Omega}\frac{1}{\ell_\perp^2}\frac{U}{\ell_\perp} \,. \end{aligned}$$

Which can be rearranged to give,

$$U_b \sim Ek\, U \,. \tag{2.20}$$

Combining (2.10),(2.18) and (2.20) gives

$$U^V \sim \frac{Q}{2\pi\ell_\perp^2(1+(\sqrt{1/2})Ek^{3/2})}\,. \tag{2.21}$$

Similarly for the inertial regime we have, following the above, from (2.19):

$$\begin{aligned} -\nabla_\perp \cdot u_\perp &\cong \frac{1}{2\Omega}\frac{D}{Dt}\omega_z\,, \\ \frac{U_b}{\ell_\perp} &\sim \frac{U^2}{2\Omega\ell_\perp^2}\,, \\ U_b &\sim Ro\,U\,. \end{aligned} \tag{2.22}$$

Combining (2.13),(2.18) and (2.22) gives

$$U^I \sim \frac{Q}{2\pi\ell_\perp^2(1+(\sqrt{1/2})Ro\;Ek^{1/2})}\,. \tag{2.23}$$

Unsurprisingly both (2.21) and (2.23) show that U is strongly influenced by the flow rate Q. The effect of the rotation speed Ω on U manifests itself due to the presence of the Ekman boundary layer. In (2.21) and (2.23) this is represented by the term containing Ek in the denominator. For most physical and experimental flows studied $Ek \ll 1$ and $Ro < 1$ so the effect of Ω on U ought to be minor. Moreover what this tells us is that if the fluid was somehow injected through a theoretical point source or far away from any boundaries this contribution to (2.21) and (2.23) ought to drop entirely.

In the derivation of (2.21) and (2.23) we assume that the structure is driven by injecting fluid through a source at flow rate Q. The same reasoning however, can be applied to a structure that is driven by withdrawing fluid through a sink at flow rate Q.

2.1.3 Average flow equations

We now consider the governing equations (2.3)-(2.5) in the context of a rotating turbulent flow field with a non-zero average. As the flow is turbulent the fluctuating flow component becomes relevant and simultaneously, due to the Coriolis force, the influence of inertial waves has to be considered. The average flow quantities of these types of flows is steady yet influenced by fluctuations, providing the ideal battleground for mechanisms both with and without waves competing to promote anisotropy. Rewriting (2.3)-(2.5) in terms of the average flow quantities will provide the framework by which we identify flow regimes where either mechanism is dominant.

In this thesis we use several averages in our calculations and representations of our results.

A temporal average is represented by $\langle\cdot\rangle_t$, while a spatial average is represented by $\langle\cdot\rangle_{\mathbf{x}}$ and the ensemble average across both temporal and spatial dimensions is given by $\langle\cdot\rangle$.

We start by decomposing all quantities in (2.3)-(2.5) into their average and fluctuating component, i.e. $\mathbf{u}(t) = \langle\mathbf{u}\rangle_t + \mathbf{u}'(t)$. Where $\langle\mathbf{u}\rangle_t$ is the average flow component, $\mathbf{u}'(t)$ is the fluctuating flow component and $\langle\mathbf{u}'(t)\rangle_t = 0$. Applying this decomposition to (2.3)-(2.5) gives:

$$\left[\partial_t + (\langle\mathbf{u}\rangle_t + \mathbf{u}')\cdot\nabla - \nu\Delta\right](\langle\omega_z\rangle_t + \omega_z') = 2\Omega\partial_z(\langle u_z\rangle_t + u_z') + (\langle\boldsymbol{\omega}\rangle_t + \boldsymbol{\omega}')\cdot\nabla(\langle u_z\rangle_t + u_z') \ , \tag{2.24}$$

$$\left[\partial_t + (\langle\mathbf{u}\rangle_t + \mathbf{u}')\cdot\nabla - \nu\Delta\right](\langle u_z\rangle_t + u_z') = \frac{1}{\rho}\partial_z(\langle P\rangle_t + P') \ , \tag{2.25}$$

$$\nabla\cdot((\langle\mathbf{u}\rangle_t + \mathbf{u}')\cdot\nabla)(\langle\mathbf{u}\rangle_t + \mathbf{u}') = 2\Omega(\langle\omega_z\rangle_t + \omega_z') - \frac{1}{\rho}\Delta(\langle P\rangle_t + P') \ . \tag{2.26}$$

Equations (2.24)-(2.26) allow for a detailed study on the effects of the fluctuating flow component on the flow as a whole, but in this study we limit ourselves to studying the average flow quantities. These are obtained by taking the average of (2.24)-(2.26), which gives:

$$\langle\mathbf{u}\rangle_t\cdot\nabla\langle\omega_z\rangle_t - \nu\Delta\langle\omega_z\rangle_t = \langle\boldsymbol{\omega}\rangle_t\cdot\nabla\langle u_z\rangle_t + 2\Omega\partial_z\langle u_z\rangle_t - \langle\mathbf{u}'\cdot\nabla\omega_z'\rangle_t + \langle\boldsymbol{\omega}'\cdot\nabla u_z'\rangle_t \ , \tag{2.27}$$

$$\langle\mathbf{u}\rangle_t\cdot\nabla\langle u_z\rangle_t - \nu\Delta\langle u_z\rangle_t = \frac{1}{\rho}\partial_z\langle P\rangle_t - \langle\mathbf{u}'\cdot\nabla u_z'\rangle_t \ , \tag{2.28}$$

$$2\Omega\langle\omega_z\rangle_t = \frac{1}{\rho}\Delta\langle P\rangle_t + \nabla\cdot\langle\mathbf{u}'\cdot\nabla\mathbf{u}'\rangle_t \ . \tag{2.29}$$

The last term on the RHS of (2.29) can be neglected as $|\nabla\cdot\langle\mathbf{u}'\cdot\nabla\mathbf{u}'\rangle_t|/|2\Omega\langle\omega_z\rangle_t| \sim Ro$. Thus the mean pressure is governed by a geostrophic balance

$$2\Omega\langle\omega_z\rangle_t \approx \frac{1}{\rho}\Delta\langle P\rangle_t \ . \tag{2.30}$$

Further simplification of (2.27) and (2.28) through scaling arguments is not possible as it can be shown that all terms, excluding those containing a fluctuating component, in (2.27) are of $\mathcal{O}(U^2/\ell_\perp)$ and all terms in (2.28) are of $\mathcal{O}(U^2/\ell_\perp^2)$.

The fluctuating flow component and as a consequence inertial waves can influence the anisotropy of the average flow through the last two terms on the RHS of (2.27) and the last term of (2.28). By experimentally evaluating the magnitude of these terms to the other non-pressure terms in (2.27) and (2.28) we can identify flow regimes where the mechanism which promotes the anisotropy of the average flow is governed by a balance between static forces, fluctuating forces or both.

2.2 Structure formation in high Rossby number flows

So far we have considered the limit where $Ro \ll 1$ throughout the entire flow field. Under these circumstances we believe that a flow generated by a source or sink will be largely similar. The flow generated by a source, i.e. a jet, has a strong axial velocity close to the point of fluid injection. As the Coriolis force can only act on velocities perpendicular to the axis of rotation it is likely that close to the points of fluid injection structures may not develop as expected, due to characteristic velocities being too great or length scales too small. As a result ther may locally exist regions where the Coriolis force cannot influence the flow field and $Ro \geq 1$. This region we call the turbulent patch.

In the absence of rotation fluid forced into a quiescent field will lead to the formation of a jet. This jet, even if driven by a low flow rate, quickly becomes unstable [51] due to the shear between the moving fluid layer and the static fluid layer surrounding it, causing entrainment and a widening of the jet. This causes the axial velocity aligned with the centreline of the jet U to gradually decrease away from the point of fluid injection. In addition, it has been shown [48] that the radial velocity perpendicular to the axis of rotation $u \sim U$ and that the radius of the jet R increases linearly with distance to the point of injection z. Figure2.2 shows a sketch of how such a jet develops.

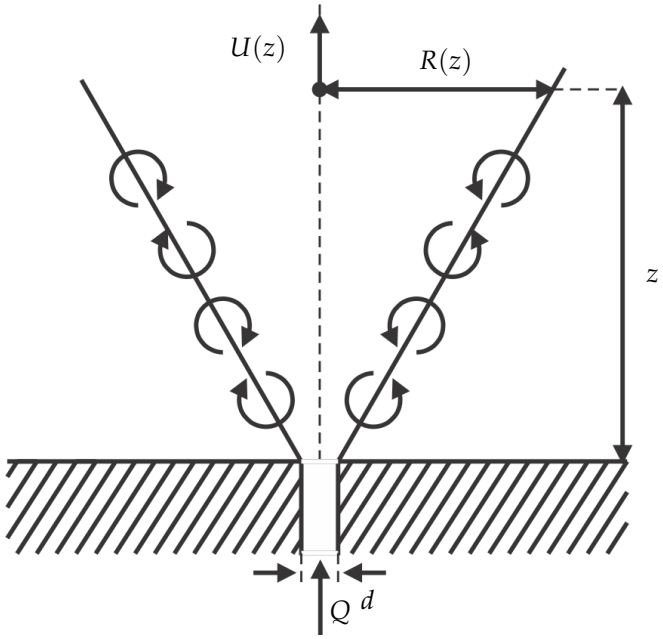

Figure 2.2: Two-dimensional sketch of the jet formed by injecting fluid into a quiescent field through a hole of diameter d at a flow rate Q. As the jet moves further away from its point of origin the axial velocity U_0 drops as the radius of the jet L increases due to fluid entrainment.

If this jet is now subjected to a background rotation aligned with the z-axis, $\mathbf{\Omega} = \Omega \mathbf{e}_z$, we can introduce a local Rossby number based on u and R, $Ro = u/2\Omega R$. Close to the point of fluid injection Ro is large, likely greater than unity, as u is relatively large while R is small. Away from the point of injection u decreases while R increases, resulting in a gradual decrease of Ro. As long as $Ro > 1$ the jet does not 'see' the Coriolis force and remains unaffected. Flow regions where this is the case are within the turbulent patch. When $Ro = 1$ the Coriolis force is strong enough to overcome the local inertial forces and this marks the end of the turbulent patch and is characterized as its height H. A similar turbulent patch was found by Maxworthy & Narimousa [37] in rotating turbulent convective flows. Following [37] we derive a scaling for H as follows.

Consider a jet aligned with the z-axis, being driven at a flow rate Q. The entire flow is subject to a Coriolis force of magnitude $\vec{\Omega} = \Omega \mathbf{e}_z$. At $z = H$ the local $Ro = 1$, the radius of the jet is R . Assuming an axisymmetric jet the axial velocity at H is approximated by

$$U(H) \approx \frac{Q}{\pi R^2} \, , \tag{2.31}$$

The Ro at $z = H$ is given by,

$$Ro = \frac{u}{2\Omega L} = 1 \ . \tag{2.32}$$

Knowing that $u \sim U$ [48], combing (2.31) and (2.32) gives,

$$\frac{Q}{8\pi\Omega L^3} \sim 1 \ .$$

Additionally we know [48] that $R \sim z = H$,

$$H \sim \left(\frac{Q}{8\pi\Omega} \right)^{1/3} \, , \tag{2.33}$$

thus giving us a scaling on the height H as function of Ω and Q.

Above the turbulent patch $Ro \leq 1$. At this point we assume columnar structures to form according to either (2.10) or (2.13). Interestingly, as these columnar structures form away from any bottom wall the effect of the Ekman boundary layer seen in (2.21) and (2.23) would disappear.

In this section we have only considered the height of the turbulent patch, but radially speaking the jet could still trigger large-scale (anti-)cyclonic motions. Far away from the point of injection the net flow in the jet moves radially outward. The velocity at which this occurs diminishes as one moves further away from the centreline of the jet. THe Coriolis force will act on this outward flow and in turn will generate an anti-cyclonic motion around the jet. However close to the point on injection entrainment causes an inward fluid motion, which could reach within the Ekman

layer. This inward motion has to draw fluid from the surrounding area and similar to the outward motion at the top of the jet its strength will diminish away from the centreline of the jet. The Coriolis force would then generate a large-scale cyclonic motion close to the lower boundary. As it is difficult to predict what shape such a transition from a cyclonic to an anti-cyclonic motion will take along the height of jet, we will focus exclusively on its height H.

2.3 Summary

In this chapter a theory was presented on the structures that form in a rotating turbulent flow forced through fluid injection at a constant flow rate Q subject to rotation speed Ω. When $\Omega \to \infty$ ($Ro \to 0$) Taylor-Proudman states that the flow is columnar and structures that form have an infinite length. When Ω is large but finite ($Ro < 1$) a horizontally divergent flow must exist and the associated Coriolis force is opposed by either viscous or inertial forces, which leads to structures of a finite length ℓ_z. In the viscous regime where $Re \ll 1$ viscous forces oppose the Coriolis force and as a consequence the length of the columnar structures ought to scale as $\ell_z^V \sim \ell_\perp Ek^{-1}$. In the inertial regime where $Re \gg 1$ inertial forces oppose the Coriolis force and $\ell_z^I \sim \ell_\perp Ro^{-1}$. The characteristic velocity these structures induce scales as $U \sim Q/\ell_\perp^2$. The velocity U has a dependency on Ω which enters the through the presence of the Ekman boundary layer but its impact is only observable when $Ek \approx 1$ or greater. The equations governing (2.10),(2.13),(2.20) and (2.22) were rewritten to represent the average flow quantities. These average flow equations (2.27)-(2.29) were shown to provide a framework by which we can identify flow regimes in rotating turbulent flows where different mechanisms promote anisotropy of the average flow, be they propagative or wave-free. When rotation is weak or inertial forces are relatively strong it was shown that locally we may have flow regions where $Ro > 1$ and as such these regions are unaffected by the Coriolis force. Such regions are expected to form close to the point of fluid injection, resulting in what is referred to as a turbulent patch whose height was shown to scale as $H \sim (Q/\Omega)^{1/3}$. This turbulent patch could itself trigger large-scale (anti-)cyclonic motion as well.

We are now in a position where our theories need to be tested. This requires an experiment where a rotating turbulent flow field is generated with a non-zero average. In the following chapter the experimental methods used in this study are discussed.

Chapter 3

Experimental method

In this chapter the experiment designed and used to test the theories outlined in Chapter 2 is discussed. The goal is to force a turbulent flow with a non-zero average subject to a Coriolis force and be able to visualize velocity fields in order to analyse the characteristic flow structures that form. Our experimental setup is similar to that of Yarom *et al*. and others [29, 66, 67] where an inhomogeneous turbulent flow is forced at a bottom wall through fluid injection/withdrawal. The relative strength of the Coriolis force increases away from the bottom wall as the inertial forces diminish.

This chapter is divided into three sections. In the first section the experimental setup that was designed and operated over the course of this study is discussed. In the second section techniques used for data acquisition and data processing are discussed and in the final section a number of important post-processing analysis techniques are explained in detail.

3.1 Experimental setup

The experiment consists of a large tank where a flow is forced through fluid injection and withdrawal whilst subject to a Coriolis force. Broadly speaking the setup used to perform the experiments can be divided into three major components: the turntable, which applies a steady background rotation speed, the tank in which a flow is forced and the measurements system used to record our experiments. Figure 3.1 shows a photo of the experimental setup with a detailed sketch highlighting all the important components.

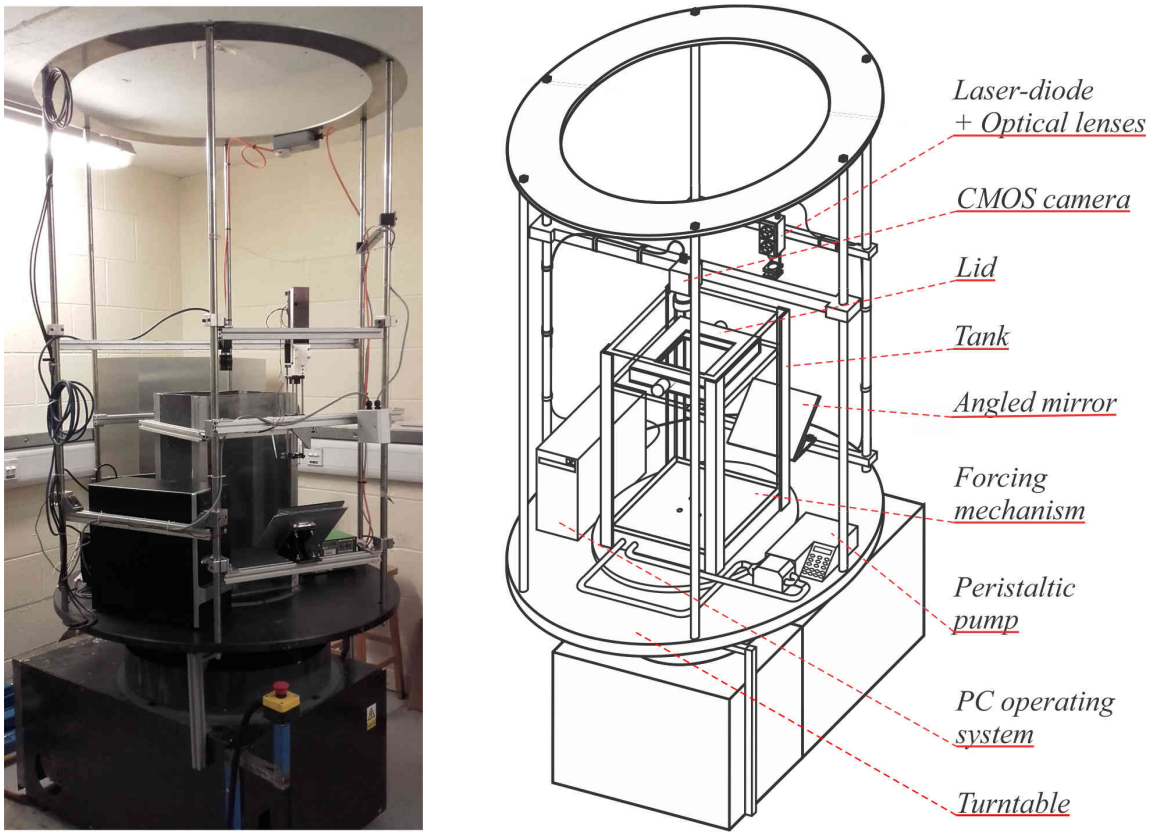

Figure 3.1: Photo of the experimental setup and a sketch highlighting the important components.

3.1.1 The rotating turntable

In order to apply a Coriolis force to the flow field the entire setup rests atop a turntable which rotates at a set rotation speed Ω. It is driven by small DC-powered motor connected to the table by a belt-drive, as can be seen in figure 3.2a. The belt is toothed in order to prevent it from slipping over time. The rotation rate of the motor is regulated by a controller terminal. A built-in feedback loop between the motor-controller setup measures the set rotation rate to the actual rotation rate of the table and adjust the motors performance accordingly. A second custom speed sensor is mounted at the bottom of the turntable. It is used to measure the fluctuations in the applied rotation rate. The sensor consists of a toothed wheel and a photo-electric diode which sends out a tick to a PC every time a tooth passes over the diode. By measuring the time between ticks, we can get a good approximation of the mechanical fluctuations.

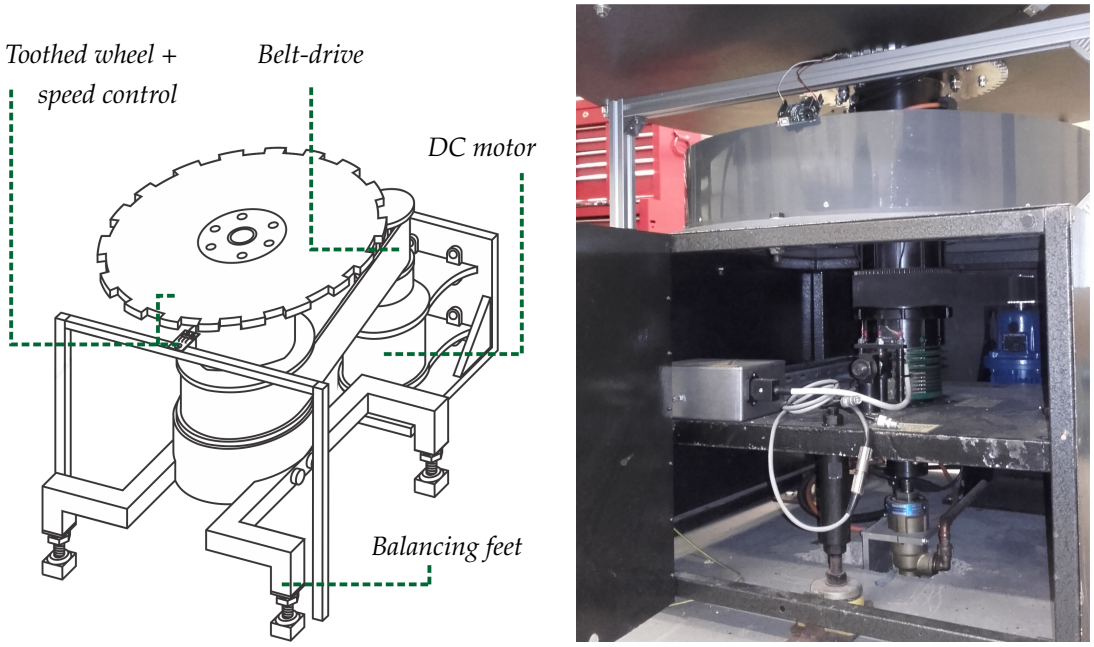

(a) (b)

Figure 3.2: a) A sketch high lighting the important components of the lower halve of the rotating turntable and upon which the rest of the experimental setup rests and b) a photo of the actual components.

Figure 3.3*a* shows relative error measured in Ω for various rotation rates. The error starts of relatively high as the motor is operating near its lowest possible rotation rate of 0.41 rad/s. The fluctuations measured in Ω can be attributed to mechanical losses. Across all Ω the error measured is of the order of 1%. The mechanical noise results in fluctuations in the velocity measured (Δu) which increase further away from the table's centre. At the highest rotation rate (4.19 rad/s) at the

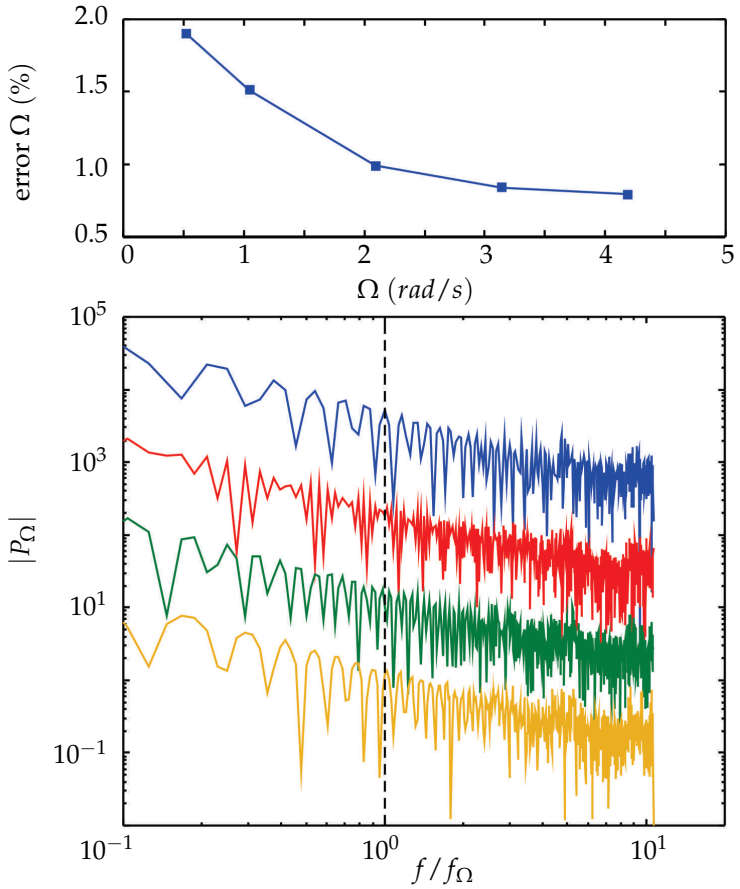

Figure 3.3: a) Relative error measured in the rotation rate Ω over a period of 5 minutes. Lowest rotation rate is 0.41 rad/s. b) Frequency spectra of $\Omega(t)$ for $\Omega = 0.52\ rad/s$ (blue), $\Omega = 1.05\ rad/s$ (red), $\Omega = 2.09\ rad/s$ (green) and $\Omega = 4.19\ rad/s$ (yellow). Frequency normalized by rotation frequency $f_\Omega = 2\pi/\Omega$. Note: spectra are shifted down two orders between rotation rates for visualization purposes.

edge of the tank $\Delta u \leq 0.5$ mm/s, which is negligible to the velocities forced across experiments. While error in Ω may be relatively small any periodic fluctuations in Ω, referred to as libration, can prevent a system from achieving solid body rotation or even lead to secondary flows forming [34, 44]. A temporal Fourier transform is applied to the signals measured in figure 3.3*a* to give us their respective frequency spectra $P_\Omega(f')$, where f' is the frequency normalized by the rotation frequency ($2\pi/\Omega$.) These spectra show no peaks, which implies there are no periodic fluctuations. This means libration should not be an issue in the experiments conducted.

3.1.2 Tank & forcing mechanism

A flow is forced inside a tank centred atop the rotating turntable, see figure 3.4. The tank has a rectangular shape with dimensions of 600x320x320mm. It consists of a number of perspex plates

glued together and has an open top which allows or ease of access. The tank is bolted to the turntable and reinforced with several braces along its height in order to increase its rigidity and as a consequence minimize influences due to mechanical vibrations. Four small brackets are placed glued to the bottom of the tank, these brackets support the forcing mechanism that drives the fluid flow (figure 3.4*c*). It is placed atop the brackets and bolted down onto them. This is done to allow narrow gap between the bottom of the tank and the forcing mechanism through which the necessary tubing can be connected to the mechanism without without disturbing the fluid above it.

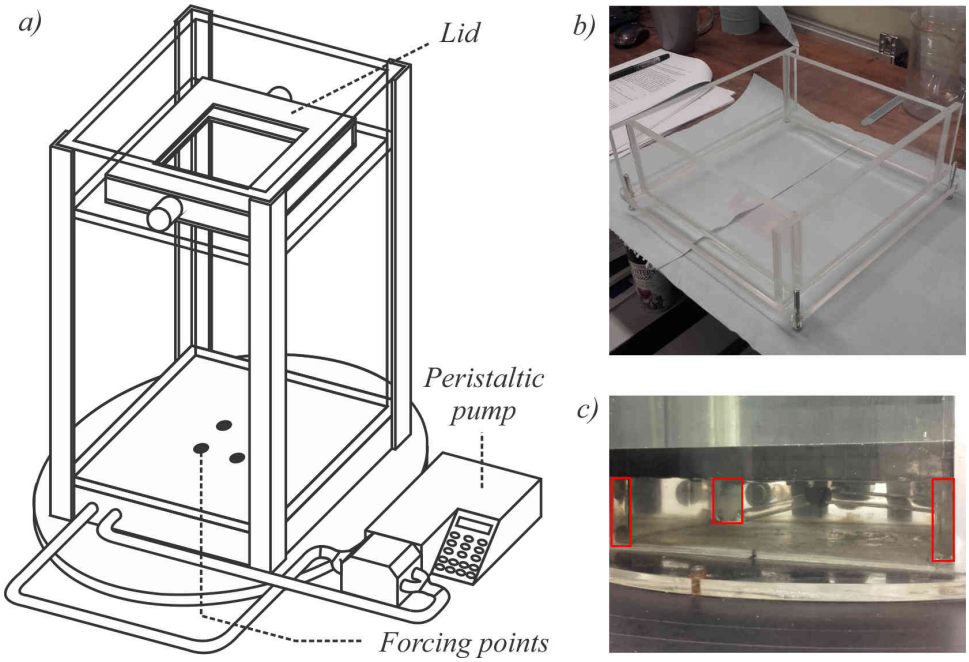

Figure 3.4: a) A sketch of the tank and forcing mechanism, highlighting all important components. b) Photo of the lid placed at the top of the flow to provide a clear viewing window and prevent deformation of the surface. c) Photo of the gap between the bottom of the tank and the forcing mechanism with tubing leading from forcing mechanism out to the pump, brackets on which the forcing mechanism rests are highlighted in red.

A circular cylinder, which is not represented in 3.4*a*, is placed atop the forcing device. This cylinder has a height of 400mm and an inner diameter of 300mm. It is placed inside the tank to provide a support structure for a lid, shown in figure 3.4*b*, that is placed atop in order to avoid free surface deformation and provide a clear viewing window for the measurement system. This configuration creates a flow domain that has a cylindrical shape with diameter D=300mm and height H =400mm.

The flow is forced through simultaneous fluid injection/withdrawal and is driven by a single pump. The pump is a Watson & Marlow 505DI peristaltic pump. Rather than provide a continuous

flow a peristaltic pump forces a flow at a flow rate Q at a set frequency. The range of frequencies for this model are 0.1-30Hz. As inertial waves can be generated by any periodic forcing [14] up to a frequencies of twice the rotation speed, there may exist a narrow range of operating parameters (specifically at low Q and high Ω) where specific inertial waves are generated.

The flow rate through each single forcing point plays a significant role in the scaling laws that were derived and as such it is important that it is set accurately. Because the entire forcing device is driven by a single pump, only the total flow rate through the system can be controlled. Steps have to be taken to ensure that the hydraulic resistance across each individual forcing point in either group of sources or sinks is equal, as any offset in resistance across these points will lead to a proportional offset in their respective flow rate. The hydraulic resistance is largely determined by two factors, first is the length of the tubing/channel from the pump to any forcing point; with a greater length leading to a greater resistance. Secondly, due to the background rotation, a parabolic pressure profile exists which increases the further you move away from the axis of rotation. This in turn increases the hydraulic resistance. It also changes with different rates of background rotation. In order to ensure a nearly equal hydraulic resistance across all forcing points the device is limited to a simple configuration on only four points (two sources and two sinks) in a square pattern centred on the axis of rotation.

The forcing mechanism consists of two aluminium plates bolted together. One plate contains four narrow holes with a diameter d =1mm which serve as our forcing points, figure 3.5 shows a prototype of the plates used. The distance between forcing points L =53mm. Wide channels are carved into the plate connecting two groups of two forcing points to outlets drilled into the second plate. These outlets are placed in a location such that the distance from pump to each source/sink is the same. This in combination with the equal distance to the axis of rotation ensures the same hydraulic resistance across each individual forcing point. This was tested prior to the experiments by forcing a set amount of fluid through either group of forcing points of the device, collecting the amount of fluid passed through both points and comparing the amounts. This was done for various flow rates and for various set amounts. An offset of less than 0.5% was found between forcing points of either group.

Far away from the point of forcing a source (or jet) can be characterized as having a radially outward flow, while a sink has a radially inward flow. When subject to background rotation the Coriolis force generates a counter- and co-rotating flow respectively, leading to counter- and co-rotating structures. By placing the sources and sinks in a cross-pattern four individual structures ought to form, each separated from the other structure with the same rotation by two with opposing rotation. The forcing mechanism was designed to generate such a quadrupole of co- and counter-rotating structures. However, close to the point of forcing an inward flow caused by en-

trainment of the jets can cause all four forcing points to generate a co-rotating flow. Leading to unanticipated dynamics.

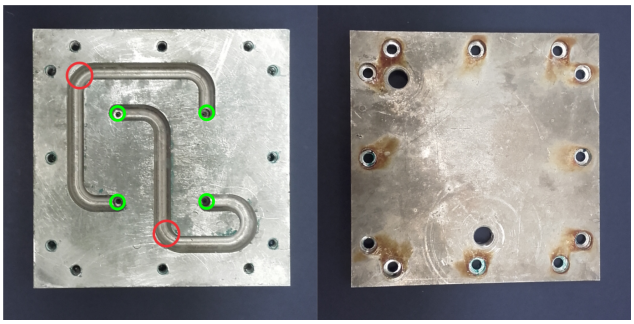

Figure 3.5: Plates that make up the forcing mechanism. Left plate contains both forcing points (green circles) and channels, right plate contains entry points which connect to the peristaltic pump, red circles highlight their approximate location on the left plate.

3.1.3 Measurement system

The dynamics of the flow are recorded through Particle Image Velocimetry (PIV) measurements, where small tracer particles that follow the flow field are illuminated allowing for the calculation of velocity fields from consecutive images [1]. The system used in these experiments is a single camera 2D-PIV system. In the experiments the carrier fluid is water and the tracer particles are silver-coated 10 μm hollow glass-spheres. A high-powered (1W) continuous diode-laser (532nm) is used to generate a lasersheet. The lasersheet is generated by passing the laser through a set of optical elements consisting of a concave lens, then a convex lens and finally a cylindrical lens. By varying the focal lengths and positions of the lenses a lasersheet is generated with an approximate thickness of 3mm that is consistent along the entire experimental plane.

The PIV system is set up is such a way that we can record the flow field along either horizontal or vertical planes of the tank. Experiments were carried out with a horizontal laser sheet at a height of both 150mm and 300mm from the bottom plate and with a vertical laser sheet aimed across a pair of forcing points, one source and one sink.

In order to conserve space the laser is aimed in a downwards direction onto a mirror (as can be seen in figure 3.1), creating a sheet along the horizontal plane of the tank at a prescribed height. The flowfield is recorded at a framerate of 30fps using a single Pointgrey Flea3 CMOS camera, operated using commercial software FlyCapture. The camera is suspended above the tank and is focused on an area of approximately 150x150mm centred on the axis of rotation. The camera's total resolution is 1048x1328 pixels, we use a grid of only 1040x1040 pixels in order to accurately centre the camera. This coupled with the area of focus leads to a spatial resolution of approximately 7

pixels per millimeter.

In the case of the experiments along the vertical plane the positions of the laser and camera are switched around. The laser generates a laser sheet in a downward direction directly across a source-sink pair. In these experiments two cameras are used to record the flow field along the entire height of the tank simultaneously. Both cameras are focused on an area of approximately 210x150mm at either the top of the tank or the bottom of the tank using their full resolution leading to a spatial resolution of approximately 7 pixels per millimeter. The areas of focus have a small overlapping region in the middle of the tank. Depending on the forcing parameters the cameras record at a framerate of 30 or 60 fps. This is done due to the fact that the vertical velocity component is substantially greater than the horizontal velocity component and limiting ourselves to 30fps would not allow us to accurately resolve it for all forcing parameters.

This high framerate is not applied across all experiments. For one, the limited buffer of camera/PC setup allows us to only capture a set number of images. By increasing the framerate there is a possibility that slow large scale phenomena are not captured adequately. Another potential risk is that with an increased framerate we do not record consecutively independent velocity fields, leading to oversampling of our data. We limit our the lower framerate wherever possible in order to accurately resolve velocities measured, capture slow dynamics and prevent egregious oversampling of data.

3.1.4 Dimensional analysis and experimental parameter range

Experiments are carried out by altering one of two control parameters; the flow rate (Q) through each of the forcing points of the forcing mechanism and the rotation speed (Ω) of the turntable. With these two control parameters we control the strength of the inertial forces and the Coriolis force, respectively, acting on the flow field. The third group of forces acting in the flow field are the viscous forces, which are set by the fluid used in the experiments (i.e. water) and these do not change between experiments.

Close to the forcing points there is a characteristic fluid velocity U_j which aligned with the axis of rotation and which is set by Q and the diameter (d =1mm) of the forcing points, which also acts as the characteristic length scale in this region. The forced inertial forces, represented as $U_j d = 4Q/\pi d^2$, can be balanced against the viscous forces, represented by ν, as the jet Reynolds number Re_Q, given by

$$Re_Q = \frac{4Q}{\pi \nu d} \ .$$

By increasing Q we increase Re_Q and in doing so the relative strength of the inertial forces in the flow are increased. The rotation speed Ω is measure of the strength of the Coriolis force, which

is represented as $2\Omega L^2$, where L is the characteristic length of the experiment and the 2 is there as it is a representation of the so-called Coriolis parameter. In previous experimental studies the characteristic length is often based on either a characteristic size of the experimental domain, such as the height of width of the tank containing the fluid flow, as this would be a measure of the greatest Coriolis force possible, or as a length scale based on the forcing mechanism used, such as the grid-size [42] or the distance between forcing points, as this would be a measure of the greatest Coriolis force applied initially. We opt to use the latter approach and use, similar to Kolvin *et. l.* [29], the distance between forcing points ($L = 53$mm) as the characteristic length scale. The balance between the applied Coriolis force and the viscous forces is represented by the Ekman number Ek which is given by

$$Ek = \frac{\nu}{2\Omega L^2} \ .$$

By increasing Ω, Ek is decreased and as a consequence the relative strength of the Coriolis force is increased.

One could form a third dimensionless group based on the balance between the applied inertial forces and the Coriolis force. The applied inertial forces are however largely aligned with the axis of rotation, while the Coriolis force only acts on forces perpendicular to the axis of rotation. As such this would not give an accurate representation of the balance between these forces acting against one another. Though as a consequence of applying a Q and Ω a velocity field will be induced, with a characteristic velocity U. This can give a balance between the resultant inertial forces and the applied Coriolis force, given by

$$Ro = \frac{U}{2\Omega L} \ . \tag{3.1}$$

The Rossby number Ro is an *a posterori* determined variable of the experiment. By increasing Q, Ro is likely to rise and by increasing Ω, Ro is likely to decrease. The effect of changing the control parameters is not exactly known as the relation between Q, Ω and U may not be entirely linear.

In experiments conducted along the horizontal planes there is another experimental variable, namely the height (h) of the laser sheet. In order to fully characterize our experiments in terms of dimensionless groups this h is normalized by the height of the tank (H =400mm), giving

$$h^* = h/H \ .$$

Figure 3.6 shows the range of control parameters covered by both experiments along the horizontal/vertical planes and static/transient experiments over the course of this study. As men-

tioned in section 1.1.2 there exists a narrow range of experimental parameters where specific inertial waves may be excited by the peristaltic pump driving the forcing mechanism, these parameters are highlighted in figure 3.6.

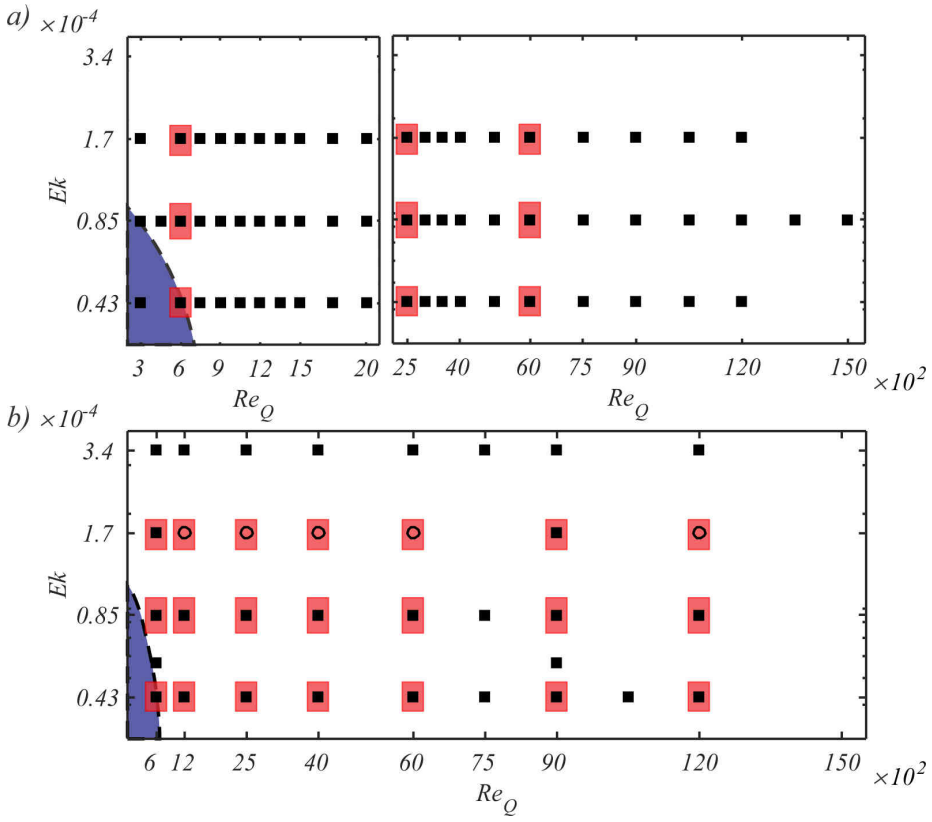

Figure 3.6: Range of experimental parameters for both the experiments conducted along the (a) horizontal planes and the (b) vertical plane. Static experiments (squares) carried out along a horizontal plane are conducted at $h^* = 0.38$ and $h^* = 0.75$. Points covered by red areas showcase the experimental parameters for the transient experiments; (circles) indicate experimental parameters for which only transient experiments were carried out. Blue areas highlight experimental parameters at which specific inertial waves may be excited by the peristaltic pump.

3.2 Data acquisition and validation

In this section the method by which data is acquired and processed is discussed. Experiments are carried out by applying inertial forces and a Coriolis force to a flow field. The fluid is brought to a state of solid-body rotation after which the forcing mechanism is initiated to 'force' a fluid flow and the resultant flow field is measured. Measurements are performed while the flow field is in a statistically steady state, called the *static* experiments, and while it transition from a still state to this statistically steady state, called the *transient* experiments.

3.2.1 Acquisition protocol

Prior to the recording any set of experiments steps have to be taken in order to ensure all elements are properly prepared and to ensure satisfactory results. The first step is filling the tank with fluid. Filling the tank is a step that only has to be taken every two to three weeks, when health and safety regulations require the fluid to be refreshed. Upon filling the tank with fluid the cylinder is placed inside the tank and the forcing device is turned on for a few hours in order to remove any trapped air bubbles inside the device and/or pump. Small imperfections or dirt on the walls of the tank or the sides of the cylinder cause a formation of micro bubbles. These bubbles will grow and accumulate and over time become large enough to obstruct both the light of the lasersheet and the area of focus of the camera(s). After filling the tank the setup is left to rest for a period of 24 hours after which the overwhelming majority of bubbles will have formed. These are then removed by stirring the fluid.

The second step is ensuring clear field of vision for the PIV system. The tank and our forcing mechanism are filled with water mixed with silver-coated tracer particles. Key to ensuring satisfactory PIV results is that the fluid-particle mixture is homogeneous. By vigorously stirring the mixture prior to any set of experiments problems originating from inhomogeneities are prevented. After stirring the fluid a calibration object is placed in the region of interested of the particular experiments. Both lasersheet and camera(s) are focused on this object and a calibration image is taken. The object is then removed and a lid is placed atop the cylinder inside the tank. Effort is taken to ensure no bubbles are trapped beneath the lid as these will interfere with our ability to perform measurements, either by obstructing the field of view of the camera or by deflecting the incoming lasersheet.

Once the fluid is properly mixed and cleared from bubbles it is left to settle for 5-10 minutes. Our experiments require that our flow field is in solid-body rotation. Tests have shown it takes around 30-45 minutes (depending on the rotation speed) for the flow field to achieve solid-body rotation. For the third step the table is slowly brought up to the required rotation speed over the course of 10 minutes. It is then left for 60 minutes prior to any experiments in order to ensure solid-body rotation is achieved.

The final step is dependent upon the nature of the experiment; whether it is a static or transient experiment being conducted. For the static experiments the forcing device is initiated and the flow is left to develop for a period of 60 minutes. This period is far greater than any imposed time-scale of the flow and this ought to ensure we are operating under a statistically steady state. The flow field is then recorded for a period of approximately 25 minutes. When forcing parameters are changed another waiting period of 60 minutes is applied before making any new measurements.

The goal of the transient experiments is to capture the early stages of the build-up of the fluid flow. Due to technical limitations the peristaltic pump driving the forcing mechanism and the measurement system that records the fluid flow are operated separately from one another. In order to capture the earliest stages of the fluid flow, the recordings are started prior to the initiation of the forcing mechanism and are left to record for a period of 5 minutes afterwards. The setup is then brought to rest and the third and fourth (final) step are repeated a total of 5 times for each setting of forcing parameters.

Due to the time-dependence of the transient experiments there is a significant difference between the statistical convergence of both the static and transient experiments. For example, in order to calculate an average velocity at a given location from the static experiments one simply needs to take an timed average of all velocity fields measured at that location, while for the transient experiments an average can only be attained by averaging out velocity fields measured at the given location at exactly the same time between separate experiments, severely limiting the amount of experimental samples. The total recording time for the static experiments is chosen such that the statistical error for the mean velocity fields is of the order of 10^{-2}. For the transient experiments a similar statistical error could be achieved by performing several dozens of experiments for each set of parameters, but that would severely limit the scope of the parameter regime that could be studied due to the high cost in time. Priority was given to study a wide range of parameters, hence the choice of only 5 separate experiment for each set of parameters for the transient experiments. This would allow us to explore the general dynamics at play, but would limit the ability to accurately determine higher order statistics.

3.2.2 PIV analysis

Recordings are processed using the PIVlab software developed for Matlab by Thielicke & Stamhuis [62]. Besides the tools to perform PIV analysis and calculate the velocity fields this software has tools for two other post-processing steps, namely the image pre-processing and data-validation. Here we will briefly highlight the individual steps for the entire PIV analysis.

Every experiment is subject to noise, this can take the for of mechanical vibrations, but it can also take the form of noise in the images recorded. These are caused by inconsistencies in lighting, be it by the source (laser), the emitter (tracer particle), receiver (camera) or the due to background lighting. In order to improve the measurement quality these inconsistencies need to be reduced through image pre-processing. In our experiments this happens in two steps with a third step being added for a limited number of experiments. Applying these image pre-processing steps significantly reduces the experimental noise in each experiment. First a contrast limited adaptive

histogram equalization (CLAHE) filter is applied to the image to smooth out differences between areas of high and low light intensity. This filter works by taking a histogram of all the light intensities in a local area of an image filtering out all intensities that fall far outside the mean. The second filter uses the relatively high intensity of the light emitted by tracer particles as a benchmark to filter out light that is much weaker, such as that caused by background lighting or static noise, by applying a high-pass filter. These two steps are often enough to produce suitable results. In the experiments along the vertical plane however, there are regions of extremely high light intensity near the top and bottom boundaries, caused by the reflection of light at these boundaries. In these experiments an intensity capping filter is applied to the images near these boundaries in order to more accurately determine the fluid flow. These exact workings of these filters are explained in more detail in the work by Thielicke & Stamhuis [62].

After image pre-processing recordings are processed through standard PIV calculations, where two consecutive images separated by a time dt are cross-correlated to give velocity fields [1]. This is done by taking the first image and dividing it into a grid of interrogation windows of $N \times N$ pixels. Each window on this grid is cross-correlated to the second image and the point where the correlation is the highest is the point where the window has translated over time dt, which in turn provides the local velocity at the centre of the interrogation window. To improve the accuracy of the analysis and to save processing time the region of the second image that is analysed is only the initial interrogation window plus a certain overlap region of size $M \times M$. These steps can be repeated several times with increasingly finer grids by using the initially calculated velocity fields as a guideline. In our experiments every set of images runs through two of these cycles. The first is on a grid with interrogation windows of 64×64 pixels with 50% overlap region (i.e. 32 pixels from any edge of the initial interrogation window.) For the second cycle the grid is reduced to interrogation windows of 32×32 pixels with a 50% overlap region. This results in velocity fields calculated on a 16×16 grid across the entire flow field. This, with the resolution of 7 pixels per milimeter, means the smallest length scales recorded are approximately 2.2mm.

3.2.3 Data validation and smoothing

Every experiment processed through the PIV analysis produces two velocity fields $u_x(x, y, t)$ and $u_y(x, y, t)$ that are still subject to experimental noise. Erroneous data is removed through two steps, the first is data-validation through statistical filtering and the second is by smoothing out the data.

The data-validation step is performed by using statistical filters implemented in the PIVlab software. Two filters are applied, the first is based on the velocity distribution of the entire flow

field. based on this distribution a mean and standard deviation are derived. Any point that deviates more than an N number times the standard deviation from the mean is eliminated. Care has to be taken that N is not set too low as that may eliminate the turbulent characteristics of the flow field. For our experiments we took a value of $N = 7$. This is a very high upper bound and so it is likely it will only affect erroneous data. Any data-point eliminated in this step is linearly interpolated with regards to the surrounding region. The second filter that is applied is a normalized median test [65]. The filter evaluates the data point with respect to a median calculated from a local area centred on said data point. Should the data deviates too much from this median, it is normalized by this median. As the filters not only eliminate erroneous data but also interpolate and and normalize the data where necessary this data-validation step generally produces spatially smoothed velocity fields.

As we are interested in both spatial and temporal derivatives of our flow fields the resultant velocity fields need to be smoothed out temporally as well as spatially. The smoothing algorithm applied is a custom low-pass frequency filter which uses a Fourier transform to alter the data sets into Fourier modes of a specific frequency. All modes with a frequency higher than a given threshold are eliminated and then a inverse Fourier transform is performed to give a filtered flow field. This is done using the *fft.m* and *ifft.m* functions in Matlab. When smoothing out data care has to be taken not to oversmooth said data and eliminate important physical fluctuations or characteristics from our results. Oversmoothing data has a minor impact on quantities such as the mean, standard deviation or the *rms*-value of the original flow field, but will have major impact on any derivatives taken as can be seen in figure 3.7.

Here we see the ratio between the ensemble *rms* of filtered (F^*) and unfiltered (F_0) data on both the absolute velocity and its time-derivative as function of the filtering frequency, characterized as timestep dt. For high frequencies (small dt) there is little difference between the filtered and unfiltered data, which rapidly drops as the filtering frequency is lowered ($dt \rightarrow 0.2$). In this regime the frequency filter largely effects experimental noise, but high frequency, often turbulent, fluctuations are also affected. As the filtering frequency is increased F^*/F_0 gradually levels out until lowering the filtering frequency has little effect ($dt > 0.3$), at this point the data is oversmoothed and physical characteristics of the flow field are severely affected. Based on these graphs a threshold frequency is computed. This is done by taking a value of dt that falls slightly above the bend seen in figure 3.7, indicated by the dashed line. This will likely eliminate most experimental noise, whilst leaving the majority of turbulent fluctuations and other flow characteristics of the flow field untouched.

Spatial derivatives are calculated using a second-order central difference scheme. This done using the *gradient.m* function of Matlab. Temporal derivatives are computed using a fourth order

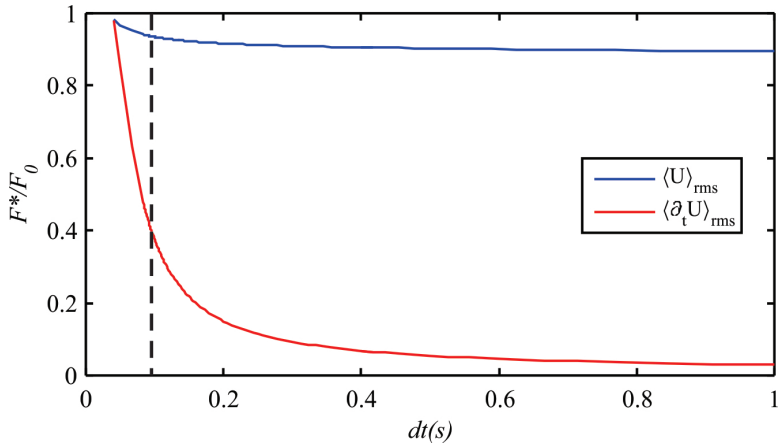

Figure 3.7: Ratio between filtered data (F^*) and unfiltered data (F_0) as function of the filtering timestep dt for the ensemble rms of the absolute velocity $\langle U \rangle_{rms}$ (blue) and the of its time derivative $\langle \partial_t U \rangle_{rms}$ (red). Dashed line indicates the location of the timestep chosen as the filtering timestep, equivalent to approximately $8Hz$.

central difference scheme. The methods highlighted in this section may not be sufficient for any derivatives beyond the first order. Computationally they are extremely efficient, which is of great benefit considering the large amounts of data that require processing.

3.2.4 Error-analysis

Due to the unsteady nature of turbulent flows, be they 2D or 3D, their dynamics are often studied by analysing their statistical properties, such as the mean flow velocity or its second and third order moments. While data validation and smoothing are able to eliminate most erroneous data, some errors inevitably slip through. This combined with the unsteady nature of the flow adversely affects the convergence of these statistical properties. To accurately represent the results a method is required to quantify the validity or convergence of these results.

A procedure introduced by Podesta *et al*. [46] is capable of quantifying the accuracy of statistical properties based on a N number of data samples. Furthermore it provides an estimate on how the accuracy will improve by increasing N. This procedure was developed for third-order moments in turbulent flows, but works similarly well for lower order statistics. Here the main points of their paper are highlighted.

Suppose there is a random variable X with a mean μ, a standard deviation σ and which has a number of moments M_n (here n refers to the n^{th} order moment.) Experimentally, these moments can be found by averaging out over a finite number of realizations N_s. As such, any moment M_n is itself a random variable, with a mean μ_n and standard deviation σ_n. It can be shown that the ratio between these two is given by the following.

$$|\frac{\sigma_n}{\mu_n}| = aN_s^{-1/2} \ , \tag{3.2}$$

where a is a positive constant which can be determined empirically by fitting a $N^{-1/2}$ curve to a plot where the ratio $|\sigma_n \setminus \mu_n|$ is given as function of different sample sizes N_s. Once a is known one can extrapolate the graph to get an estimate on the number of data points required to achieve a certain level of accuracy. Eq.(3.2) shows that the rate of convergence goes as $N_s^{-1/2}$ and the relative error ϵ associated with the convergence goes as

$$\epsilon = |\frac{M_n(N_s) - M_n(N_{max})}{M_n(N_{max})}| \ . \tag{3.3}$$

Here, $M_n(N)$ refers to the n^{th} order moment computed based on a N number of data points, with N_{max} being the maximum number of data points available. Eq.(3.3) scales as N_s^{-n}, where n is a constant. If the data points N are consecutively independent samples then $\epsilon \sim N_s^{1/2}$, similar to (3.2). This means that in order to improve the convergence of the data by a factor 10, the amount of samples provided needs to increase by a factor 100.

When the acquisition rate of data points far exceeds the relevant time scales of the signal that is being analysed the samples may not be statistically independent from one another and the data is oversampled. In these cases $n \to 0$ and the convergence improves less rapidly.

This behaviour can be seen in figure 3.8. Here we have a heavily oversampled data set from one of the experiments conducted. It consists of N_{max} velocity fields U_i, where i denotes the timestamp of the velocity field. For the original data set $i = 1, 2, 3, ...N_{max}$. The error ϵ_u that is calculated is error for the mean flow velocity. For this oversampled data set ϵ_u drops at a rate of approximately $N_s^{-1/4}$ (blue line). The error is then recalculated with a reduced data set. This reduced set is generated by dropping a number P velocity fields between consecutive fields from the original set. So when P =10 $i = 1, 11, 21, 31, ...N_{max}$ (red line.) This is then done again P =100 (green line) and P =800 (yellow line.) As P is increased ϵ_u drops more rapidly until the limit of $N_s^{-1/2}$ is reached. Increasing P beyond that point only increases ϵ_u.

In our experiments the error ϵ for any statistical quantity is calculated using (3.3) unless noted otherwise, with $N_s \approx 0.9N_{max}$. Effort is taken to get ϵ to the order of 10^{-2} or 1%.

3.3 Post-processing techniques

Once the recordings of the experiments have been processed and data on the velocity fields has been obtained they analysed further. In this section we discuss a number of techniques used in

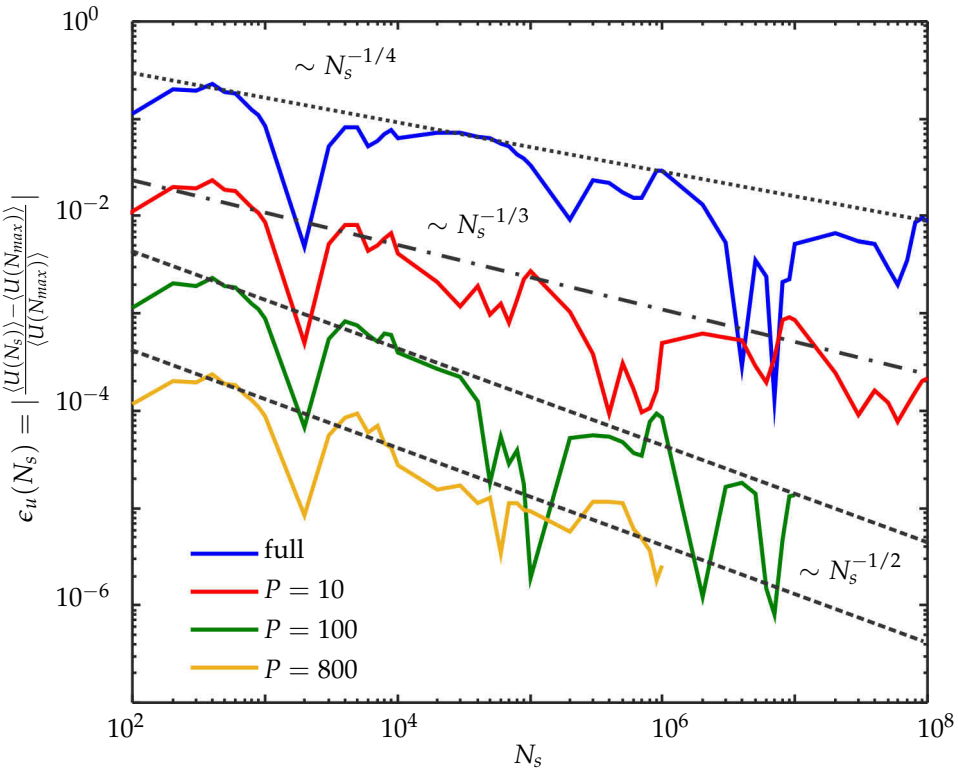

Figure 3.8: Relative error ϵ_u measured in $\langle|(u)|\rangle$ for an oversampled experimental data set. Data set is reduced by dropping P points between consecutive data points. Graphs for ϵ_u have been shifted down by a single order for visualisation purposes. Black dashed lines represent approximate scaling for ϵ_u as function of N_s. As P is increased the limit of $\epsilon_u \sim N_s^{-1/2}$ is reached (yellow) and further increases in P only increase ϵ_u.

the subsequent analysis of data.

3.3.1 Advanced Phase-Averaging

Part of our data analysis is concerned with the isolation and visualization of certain periodic structures. To visualize these periodic structures we extend upon a technique used by Cortet *et al*. [14] to visualize inertial waves of specific frequency called phase-averaging. This technique works by taking a data-signal and it cut into pieces of a given phase (or period). These pieces are then averaged out to reduce any noise on the signal. A drawback of this technique is that at the end you are only left with a single phase for further analysis, but for the strict purpose of visualization of periodic structures it is sufficient.

As Cortet *et al*. showed this technique works well when a flow field is being forced at a single known frequency and is only subject to experimental noise. The technique breaks down when the flow field is subject to a wide range of frequencies. It is then incapable of filtering out the influence of signals with marginally higher frequencies. This is illustrated in figure 3.9.

A test signal $x(t)$ consisting of frequencies of (0.5, 0.9, 1, 1.1, 2, 3)Hz and white noise is filtered using the phase averaging technique, a band-pass filter and the advanced phase averaging (APA) technique. The goal is to isolate a $1Hz$ signal. Figure3.9a shows the filtered signals and fig.3.9b shows their respective frequency spectra. The phase averaging technique and band-pass filter are unable to isolate the required signal. The phase averaging technique cannot eliminate frequencies significantly higher than the $1Hz$ signal, while the band-pass filter struggles to elimate signals close to the $1Hz$ signal. The APA technique combines the phase averaging technique and the band-pass filter to isolate the required signal. It's band-pass filter eliminates frequencies fall well outside the required range, while the phase averaging filter eliminates frequencies close to the target frequency.

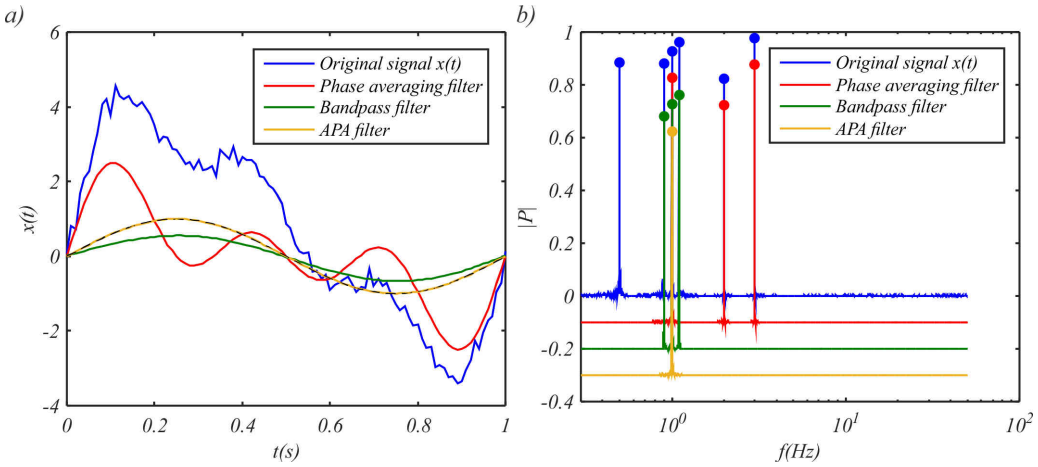

Figure 3.9: a) Test signal (blue) being filtered for a $1Hz$ signal using a phase-averaging filter (red), a bandpass frequency filter at 1 ± 0.2 Hz (green) and the advanced phase averaging filter (yellow), dashed line is an ideal $1Hz$ signal. b) Frequency spectra with maxima highlighted for various signals. Spectra are shifted to provide a clearer picture.

For this same test signal a similar result could be achieved using a narrow band-pass filter. The data analysed in this study are not as clearly defined as the test signal used in the above example. Another problem with a strict band-pass filter is that its quality, especially in the low-frequency regimes, is heavily dependent on the sampling frequency and length of the signal provided. There is significant possibility that such a filter can be made too strict, eliminating necessary information.

3.3.2 Deriving an upper-bound for the average flow equations

In order to evaluate (2.27) and (2.28) we require all three velocity components and their respective derivatives along each axis. The data obtained from experiments is strictly two-dimensional with experiments conducted along the horizontal planes giving velocity components (u_x, u_y) and

derivatives (∂_x, ∂_y), while vertical plane experiments give velocity components (u_x, u_z) and derivatives (∂_x, ∂_z). Because of this we cannot evaluate (2.27) and (2.28) directly. As such approximations have to be made.

For (2.28) we assume identical statistical properties along the axis perpendicular to the axis of rotation (i.e. x- and y-axis) due to the symmetry of the forcing and the geometry of the setup. Strictly speaking this allows us to assume $\partial_x \cong \partial_y$ which in turn allows us to evaluate the terms $\langle \mathbf{u} \rangle_t \cdot \nabla \langle u_z \rangle_t$ and $\langle \mathbf{u}' \cdot \nabla u_z' \rangle_t$ by taking

$$\langle u_x \rangle_t \partial_x \langle u_z \rangle_t \approx \langle u_y \rangle_t \partial_y \langle u_z \rangle_t \, ,$$
$$\langle u_x' \partial_x u_z' \rangle_t \approx \langle u_y' \partial_y u_z' \rangle_t \, .$$

which gives us upper bounds

$$\langle \mathbf{u} \rangle_t \cdot \nabla \langle u_z \rangle_t \leq |\langle u_z \rangle_t \partial_z \langle u_z \rangle_t| + 2|\langle u_x \rangle_t \partial_x \langle u_z \rangle_t| = |\langle \mathbf{u} \rangle_t \cdot \nabla \langle u_z \rangle_t|^e \tag{3.5a}$$
$$\langle \mathbf{u}' \cdot \nabla u_z' \rangle_t \leq |\langle u_z' \partial_z u_z' \rangle_t| + 2|\langle u_x' \partial_x u_z' \rangle_t| = |\langle \mathbf{u}' \cdot \nabla u_z' \rangle_t|^e \, . \tag{3.5b}$$

All the terms in (3.5) can be evaluated from experiments conducted along a vertical plane.

Approximation of (2.27) requires data from experiments along both horizontal and vertical planes. There are three terms in (2.27) which require additional steps in order for us to evaluate them, $\langle \mathbf{u} \rangle_t \cdot \nabla \langle \omega_z \rangle_t$, $\langle \mathbf{u}' \cdot \nabla \omega_z' \rangle_t$ and $\langle \boldsymbol{\omega}' \cdot \nabla u_z' \rangle_t$. The analysis for $\langle \mathbf{u} \rangle_t \cdot \nabla \langle \omega_z \rangle_t$ and $\langle \mathbf{u}' \cdot \nabla \omega_z' \rangle_t$ requires a similar approach that we will explain first. We decompose $\langle \mathbf{u} \rangle_t \cdot \nabla \langle \omega_z \rangle_t$ and $\langle \mathbf{u}' \cdot \nabla \omega_z' \rangle_t$ into their three separate components.

$$\langle \mathbf{u} \rangle_t \cdot \nabla \langle \omega_z \rangle_t = \langle u_x \rangle_t \partial_x \langle \omega_z \rangle_t + \langle u_y \rangle_t \partial_y \langle \omega_z \rangle_t + \langle u_z \rangle_t \partial_z \langle \omega_z \rangle_t \, , \tag{3.6a}$$
$$\langle \mathbf{u}' \cdot \nabla \omega_z' \rangle_t = \langle u_x' \partial_x \omega_z' \rangle_t + \langle u_y' \partial_y \omega_z' \rangle_t + \langle u_z' \partial_z \omega_z' \rangle_t \, . \tag{3.6b}$$

The first two of the RHS of either equations of (3.6) can be evaluated directly from any experiment along a horizontal plane, as we measure both velocity components and their respective derivatives, from which we can also evaluate $\omega_z = \langle \omega_z \rangle_t + \omega_z'$. The third term on the RHS has to be approximated. As u_z / u_z' and ω_z / ω_z' are obtained from different experimental planes these two

quantities need to be separated. We rewrite (3.6) as follows,

$$\langle u_i\rangle_t \partial_i \langle \omega_z\rangle_t = \partial_i(\langle u_i\rangle_t \langle \omega_z\rangle_t) - \langle \omega_z\rangle_t \partial_i \langle u_i\rangle_t \ , \tag{3.7a}$$

$$\langle u_i' \partial_i \omega_z'\rangle_t = \langle \partial_i(u_i'\omega_z')\rangle_t - \langle \omega_z' \partial_i u_i'\rangle_t \ . \tag{3.7b}$$

Here we briefly use Einstein notation. Notice that the second term on the RHS of either of the equations in (3.7) can be dropped as $\partial_i \langle u_i\rangle_t = \partial_i u_i' = 0$, due to $\nabla \cdot \mathbf{u} = 0$. So (3.6) can be written as

$$\langle \mathbf{u}\rangle_t \cdot \nabla \langle \omega_z\rangle_t = \partial_x(\langle u_x\rangle_t \langle \omega_z\rangle_t) + \partial_y(\langle u_y\rangle_t \langle \omega_z\rangle_t) + \partial_z(\langle u_z\rangle_t \langle \omega_z\rangle_t) \ , \tag{3.8a}$$

$$\langle \mathbf{u}' \cdot \nabla \omega_z'\rangle_t = \partial_x \langle u_x' \omega_z'\rangle_t + \partial_y \langle u_y' \omega_z'\rangle_t + \partial_z \langle u_z' \omega_z'\rangle_t \ . \tag{3.8b}$$

This rewritten equation does not change the fundamental problem we face, but an upper bound can be more easily evaluated for the last terms on the RHS of (3.8) from experimental data. We start with the last term in (3.8*a*). The difficulty is in applying the z-derivative along $\langle \omega_z\rangle_t$.

Consider for a moment a variable $f(z,t)$. Then,

$$\partial_z f \approxeq \frac{f(z+dz) - f(z)}{dz} \ . \tag{3.9}$$

This is a crude approximation of the z-derivative, but it could be applied to the $\langle \omega_z\rangle_t$ term across two horizontal planes a distance dz apart, while a z-derivative of $\langle u_z\rangle_t$ term can be extracted from experiments along the vertical plane in a similar fashion. Using (3.9) we are able to compute an upper bound for $\langle \mathbf{u}\rangle_t \cdot \nabla \langle \omega_z\rangle_t$ give by:

$$\langle \mathbf{u}\rangle_t \cdot \nabla \langle \omega_z\rangle_t \leq |\partial_x(\langle u_x\rangle_t \langle \omega_z\rangle_t)| + |\partial_y(\langle u_y\rangle_t \langle \omega_z\rangle_t)| + |\partial_z(\langle u_z\rangle_t \langle \omega_z\rangle_t)| = |\langle \mathbf{u}\rangle_t \cdot \nabla \langle \omega_z\rangle_t|^e \tag{3.10}$$

The last term on the RHS of (3.8)*b* can be further approximated using the Schwarz inequality to give,

$$\langle u_z' \omega_z'\rangle_t \leq \langle |u_z' \omega_z'|\rangle_t \leq (\langle u_z'^2\rangle_t \langle \omega_z'^2\rangle_t)^{1/2} \ , \tag{3.11}$$

The two terms on the RHS of (3.11) can each be evaluated from experiments along the vertical

plane or horizontal plane respectively. Again the only difficulty that remains is in applying the z-derivative to these two terms.

The problem with applying (3.9) is that it could miss intense small scale variations along the z-axis, this effect ought to be negligible for the average quantities used to approximate $\langle \mathbf{u} \rangle_t \cdot \nabla \langle \omega_z \rangle_t$, but can be severe when fluctuating quantities are concerned.

For $\partial_z \langle u_z' \omega_z' \rangle_t$ we consider another method where any variations in $f(z,t)$ are strictly due to plane wave motions with a wave number k and wave frequency σ.

$$f(z,t) \approx f_0 e^{i(kz-\sigma t)} \ ,$$

where f_0 is an arbitrary constant. Then,

$$\partial_z f \sim V^{-1} \partial_t f \ , \tag{3.12}$$

where $V = \sigma/k$ is the velocity of the wave. If we now consider these plane waves to specifically be inertial waves then (1.10b) shows $V \leq 2\Omega/k$, which is scale dependent. An upper bound for (3.12) is given by,

$$|\partial_z f| \leq V_M^{-1} |\partial_t f| \ , \ \ V_M = 2\Omega H \ , \tag{3.13}$$

where V_M is the maximum velocity possible for inertial waves in our system based on the largest length scale in our system H, which is the height of fluid tank. A more accurate approximation for $V^{-1}\partial_t f$ could be derived by performing a scale-by-scale analysis where $f(z,t)$ gets broken into a number of modes with wavenumber k using Fourier transforms. The $V^{-1}\partial_t f$ term is evaluated for each mode with a unique V at each scale and we then integrate across all modes k. This is however a computationally costly analysis. For this reason we did not perform a full scale-by-scale analysis. Combining (3.11) and (3.13) gives,

$$\langle \partial_z (u_z' \omega_z') \rangle_t \leq V_M^{-1} \left[(\langle |\partial_t u_z'^2| \rangle_t \langle |\omega_z'^2| \rangle_t)^{1/2} + (\langle |u_z'^2| \rangle_t \langle |\partial_t \omega_z'^2| \rangle_t)^{1/2} \right] \ . \tag{3.14}$$

Equation (3.14) gives an upper bound for the $\langle \partial_z (u_z' \omega_z') \rangle_t$ term that we can evaluate from the data at hand. The two terms on the RHS of (3.14) containing u_z' can be evaluated from experiments carried out along the vertical plane while the terms containing ω_z' can be evaluated from experiments conducted along the horizontal plane.

Combining (3.8b) and (3.14) gives an overall upper bound for $\langle \mathbf{u}' \cdot \nabla \omega_z' \rangle_t$.

$$\begin{aligned} \langle \mathbf{u}' \cdot \nabla \omega_z' \rangle_t \quad \leq \quad & |\partial_x \langle u_x' \omega_z' \rangle_t| + |\partial_y \langle u_y' \omega_z' \rangle_t| \\ & + V_M^{-1} \left[(\langle |\partial_t u_z'^2| \rangle_t \langle |\omega_z'^2| \rangle_t)^{1/2} + (\langle |u_z'^2| \rangle_t \langle |\partial_t \omega_z'^2| \rangle_t)^{1/2} \right] = |\langle \mathbf{u}' \cdot \nabla \omega_z' \rangle_t|^e \end{aligned} \tag{3.15}$$

The final term $\langle \boldsymbol{\omega}' \cdot \nabla u_z' \rangle_t$ in (2.27) is approximated using the Schwarz inequality to state,

$$\langle \omega_i' \partial_i u_z' \rangle_t \leq \langle |\omega_i' \partial_i u_z'| \rangle_t \leq (\langle \omega_i'^2 \rangle_t \langle (\partial_i u_z')^2 \rangle_t)^{1/2} . \tag{3.16}$$

Furthermore we assume, as before, that the flow is statistically similar along the axis perpendicular to the axis of rotation. Which allows us to state,

$$\langle \omega_x' \partial_x u_z' \rangle_t \approx \langle \omega_y' \partial_y u_z' \rangle_t \tag{3.17}$$

Using (3.16) and (3.17) allows us to evaluate $\langle \boldsymbol{\omega}' \cdot \nabla u_z' \rangle_t$. The components $\langle \omega_x' \rangle_t$, $\langle \partial_x u_z' \rangle_t$ and $\langle \partial_z u_z' \rangle_t$ can be evaluated experiments along the vertical plane, while $\langle \omega_z' \rangle_t$ can be determined from experiments along the horizontal planes.

$$\langle \boldsymbol{\omega}' \cdot \nabla u_z' \rangle_t \leq 2|(\langle \omega_x'^2 \rangle_t \langle (\partial_x u_z')^2 \rangle_t)^{1/2}| + |(\langle \omega_z'^2 \rangle_t \langle (\partial_z u_z')^2 \rangle_t)^{1/2}| = |\langle \boldsymbol{\omega}' \cdot \nabla u_z' \rangle_t|^e . \tag{3.18}$$

For all the upper bounds we derived care has to be taken that data analysed from the various experimental planes cover the same volume. This means terms containing ω_z are evaluated along a full horizontal plane at height h, while the terms associated to u_z and the derivatives are evaluated along a narrow band of the vertical plane at $z = h$.

3.4 Summary

The experimental setup consists of a rectangular tank filled with fluid placed atop a rotating turntable (fig.3.1). At the bottom of the tank a forcing mechanism is placed that allows for the simultaneous injection and withdrawal of fluid using a peristaltic pump. A flow is forced by applying a steady rotation rate Ω and flow rate Q. These control parameters are represented by the two non-dimensional numbers Ek and Re_Q, respectively (fig.3.6). Experiments are conducted while the system is operating under statistically steady conditions called the *static* experiments, though a number of experiments were conducted where the flow transitions from an initially still state (under solid body rotation) to the statistically steady state, called the *transient* experiments.

Experiments are recorded using 2D-PIV techniques focused on either a vertical plane aligned with the axis of rotation centred on a source/sink pair, or a horizontal plane perpendicular to the axis of rotation focused on a area capturing all sources/sinks. The velocity fields that are extracted from these recordings through standard PIV-analysis, using the PIVlab software, are smoothed out using high-pass frequency filters. Care has been taken that this smoothing of data only affects the experimental noise and not the turbulent characteristics of the flow.

At this point we are in a position to start testing our proposed theories. This is done over the course of the next three chapters. In the first chapter we seek to describe the flow field's topology under statistically steady conditions. This is done through the static experiments described in section 3.2.1. We want to know what flow structures develop, be they columnar structures or inertial waves, and how these flow structures react to changing control parameters. In the second chapter we test the theories outlined in Chapter 2 and discuss the impact of the results we find. In the third chapter we seek to understand how an initially still flow field transitions to the statistically steady state discussed in the previous two chapters. What mechanisms drive the propagation of the flow and how do these scale with the control parameters Ek and Re_Q. This is done through the transient experiments described in section 3.2.1.

Chapter 4

Jet-induced rotating turbulence

In the current chapter, we present the results obtained from our experiment whilst it is operating under statistically steady conditions. The purpose is to characterize the effect of both inertial forces and the Coriolis force have on the development of a rotating turbulent flow field that is generated through continuous fluid injection and withdrawal. We call this jet-induced rotating turbulence. The first question we seek to answer in this chapter is:

1. What flow structures develop in a jet-induced rotating turbulent system? And how do these structures develop with changes to the strength of inertial forces and the Coriolis force acting on the flow field?

Fluctuations in rotating turbulent flows can manifest themselves as inertial waves. These waves are known carry a significant amount of kinetic energy of the flow [66, 67] and could potentially play a major role in the development of the flow's anisotropy. The second question we seek to answer is:

2. How do inertial waves develop under the flow conditions of jet-induced rotating turbulence?

This chapter is divided into two sections aimed at answering these two questions. In the first section we describe the flow's topology across the experimental parameter range. In the second section we focus our attention on the generation and propagation of inertial waves in our system.

Over the course of this chapter results can be presented as averages. These are represented

by $\langle\cdot\rangle_{\mathbf{x}}$ for a spatial average, $\langle\cdot\rangle_t$ for a temporal average and $\langle\cdot\rangle$ for an ensemble average across both spatial and temporal dimensions. Our experiments are conducted by altering the control parameters flow rate Q and rotation speed Ω. As shown in section 3.1.4 these two quantities are represented by the following two dimensionless numbers respectively,

$$Re_Q = \frac{4Q}{\pi\nu d} \ , \quad Ek = \frac{\nu}{2\Omega L^2} \ ,$$

where d is the diameter of the forcing points, ν is the kinematic viscosity and L is the distance between forcing points. When experiments along a horizontal plane are concerned there is another key experimental variable, namely the height h of the plane. In the results this height in non-dimensionalized by the height H of the tank to give a $h^* = h/H$. Please refer to figure 3.6 for the full range of experimental parameters. Finally, the flow can be represented by its flow intensity, which is a consequence of the applied Re_Q and Ek. The flow intensity is measured *a posteriori* by means of a Rossby number Ro given by

$$Ro = U/2\Omega L \ ,$$

where $U = \langle|\mathbf{u}|\rangle$.

In order to show that the results we will be discussing were acquired under largely statistically steady conditions figure 4.1 shows the statistical error ϵ for the absolute velocity fields $U = \langle|\mathbf{u}|\rangle$. Where ϵ is determined using (3.3) derived in section 3.2.4, with $N_s = 0.9N_{max}$. Apart from a few outliers the bulk of ϵ found for the experimental data are of the order of 10^{-2} (1% error).

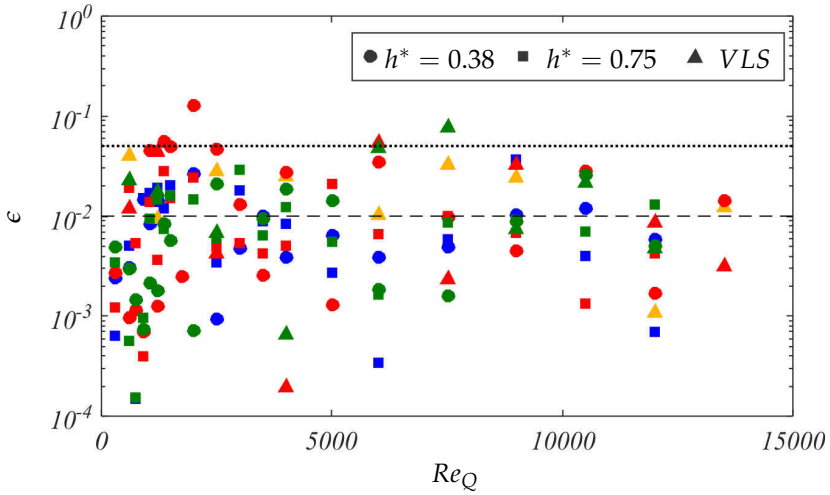

Figure 4.1: Statistical error ϵ found for the absolute flow velocity $U = \langle|\mathbf{u}|\rangle$ for experiments conducted at $Ek = 34.0 \times 10^{-5}$ (yellow), $Ek = 17.0 \times 10^{-5}$ (blue), $Ek = 8.50 \times 10^{-5}$ (red) and $Ek = 4.25 \times 10^{-5}$ (green). Dotted line corresponds to $\epsilon = 0.05$ or a statistical error of 5%

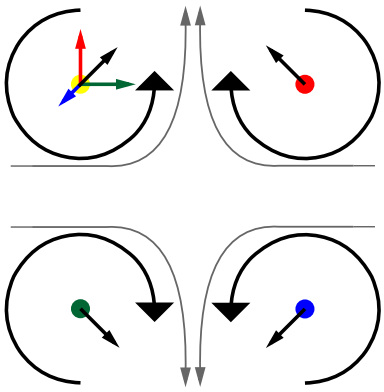

Figure 4.2: Sketch of a flow field induced by a quadrupole of four vortices. Coloured arrows show velocity induced by the vortex of the respective colour. Black arrows show the resultant induced velocity of three vortices acting on the fourth. Grey arrows show streamlines of the velocity field, which widen along one axis and compress along another.

4.1 General flow structure

In this section we seek to answer the first question set out at the beginning of this chapter. In addition, the flow's topology is compared to the topology that the experiment was designed for and upon which our theories are based.

4.1.1 Flow topology

As described in the previous chapter the forcing mechanism consists of two points of fluid injection (sources) and two point of fluid withdrawal (sinks) placed in a cross pattern at the centre of the bottom the tank. In the limit of low $Ek \ll 1$ and $Re_Q \ll 1$ we would expect a columnar vortex to form over each of the forcing points. Far away from the point of forcing a radially inward flow generated by a sink would generate a co-rotating vortex, while for a source, with its radially outward flow, would generate a counter-rotating vortex under the influence of the Coriolis force. This would create a quadrupole. A sketch of a flow induced by such a quadrupole is shown in figure 4.2. The four vortices induce a velocity on one another and the surrounding flow. If the four structures would be free to move the flow field would be stretched, widening along one axis while compressing along another, as shown by the grey streamlines in figure 4.2.

We begin by describing the flow topology in a marginally steady state at fixed control parameters of $Ek = 4.25 \times 10^{-5}$ and $Re_Q = 1200$. Figure 4.3 show the mean vorticity ($\langle \boldsymbol{\omega} \rangle_t$) and velocity ($\langle \mathbf{u} \rangle_t$) fields along horizontal planes at $h^* = 0.38, 0.75$ and along the vertical plane. From the two horizontal planes (fig.4.3a, b) we see that a vortex forms over each of the forcing points. Over the sinks a co-rotating vortex forms and over the sources a counter-rotating vortex forms. We indeed

have a quadrupole as predicted. We also see the stretching of the velocity field. In figure 4.3*a* the velocity field is compressed along the y-axis and widens along the x-axis. In figure 4.3*b*, where the sources and sinks are inverted, we see the opposite occur. If you look closely you see that the centre of the vortices is displaced with regards to the point of forcing. This is likely a consequence of the vortices being displaced by the velocity fields induced by the other vortices of the quadrupole.

Along the vertical plane (fig.4.3*c*) we see that the upper part of the flow is nearly uniform. This suggests that the vortices we saw along the horizontal plane reach across almost the entire height of the flow field and that four columnar structures form, one over each forcing point. Near the bottom of the flow field however we have two patches of high vorticity, which, in case for the source, resembles a structure of a jet in the absence of a background rotation [23], [48]. The patch over the source is unsteady and is considered turbulent. As was pointed out in section 2.2 such a structure could form due to inertia locally being too large for the dynamics to be influenced by the Coriolis force, leading to a local $Ro > 1$.

The top edge of this patch coincides with a point of high upwards velocity. We measure this height for each experiment conducted along the vertical plane. Due to the unsteady nature of the patch its height is determined over subsequent intervals, where the vertical velocity field is averaged out over a period of 30 seconds, exceeding any time-scale imposed by the experimental parameters as to ensure any fluctuations observed are due to the turbulent nature of the patch. For each interval t_i a height h_i is determined and the resultant structure height H_p is determined by $H_p = \langle h \rangle_t$. Equation (2.33) shows that the height H_p of a jet unaffected by the Coriolis force scales as $(Q/\Omega)^{1/3}$.

Figure 4.4 shows $H_p^3\Omega$ for various experimental settings. We see that the results largely scale with Re_Q, as predicted by (2.33). This shows that the region forms as a consequence of the inertial forces being too great to be affected by the Coriolis force. For $Re_Q > 1200$ there is a sudden increase in the relative error. This is linked to the turbulent intensity of the flow field increasing, but this will be discussed later. It has to be noted that experiments were conducted at greater Ek than shown in figure 4.4, but due to the high variance in measurements of h_i these were excluded. Due to the relative weakness of the Coriolis force the structure above the patch is not well defined in these cases and so the distinction between patch and columnar structure becomes less clear. This can be seen for a number of experiments conducted at $Re_Q = 600$ (green dots), where the error suddenly increases significantly.

The patch seen over the sink is similarly identified by a region of high vorticity. This patch however is steady. This suggests that the structure that forms over the sink is significantly different from the structure over the source. The strength relative to that of the patch seen over the source is weak and as $Re_Q > 1200$, it can no longer be identified from experiments. The dynamics of these

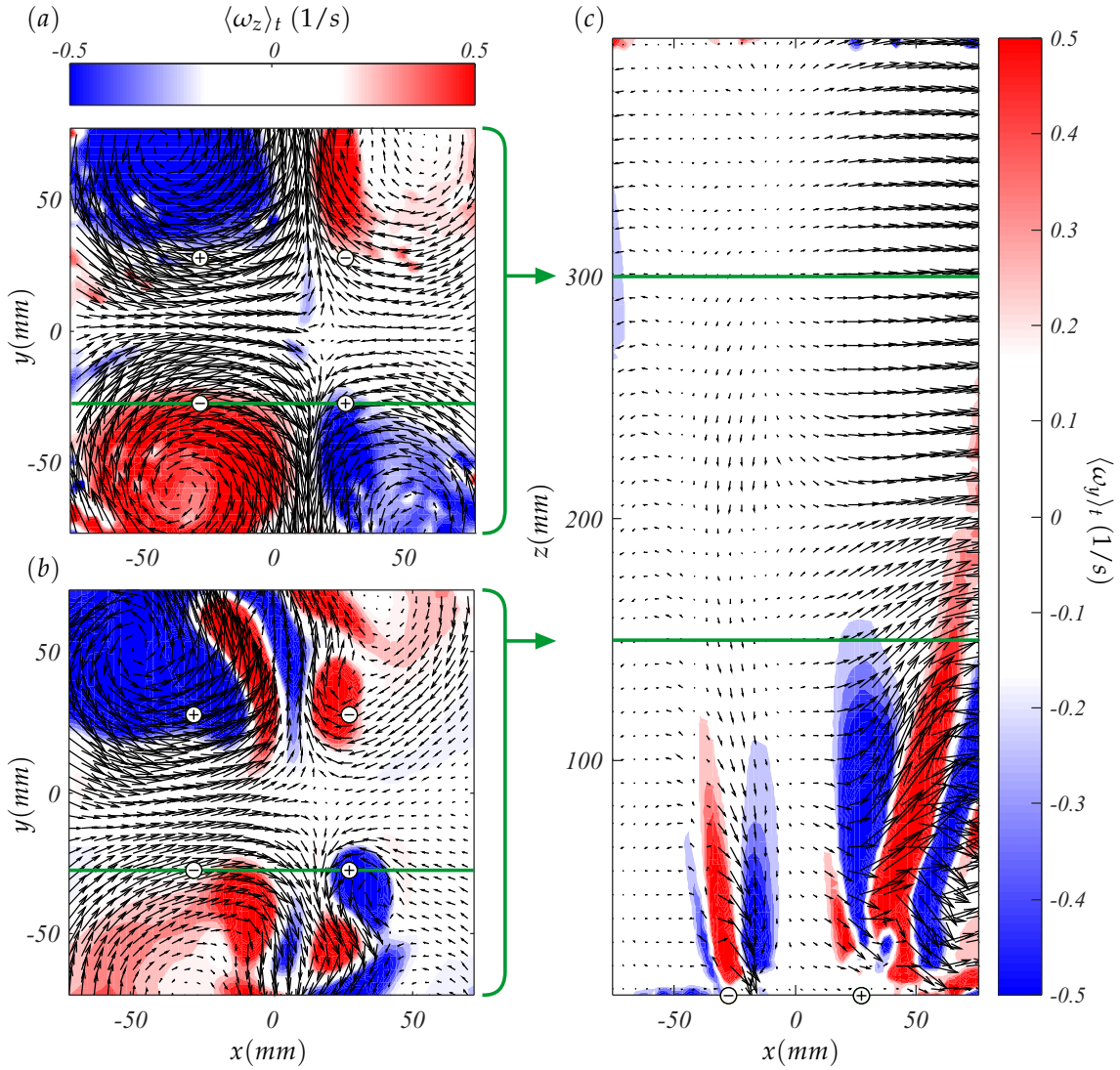

Figure 4.3: Contour plots of the mean vorticity $\langle\boldsymbol{\omega}\rangle_t$ field and vector plots of the mean velocity $\langle\mathbf{u}\rangle_t$ field along a horizontal plane at $h^* = 0.75$ (a), $h^* = 0.38$ (b) and along a vertical plane (c) for $Ek = 4.25 \times 10^{-5}$ and $Re_Q = 1200$. (+) and (-) show the position of sources and sinks, respectively.Green lines indicate the position of horizontal or vertical laser sheets in experiments carried out across different planes.

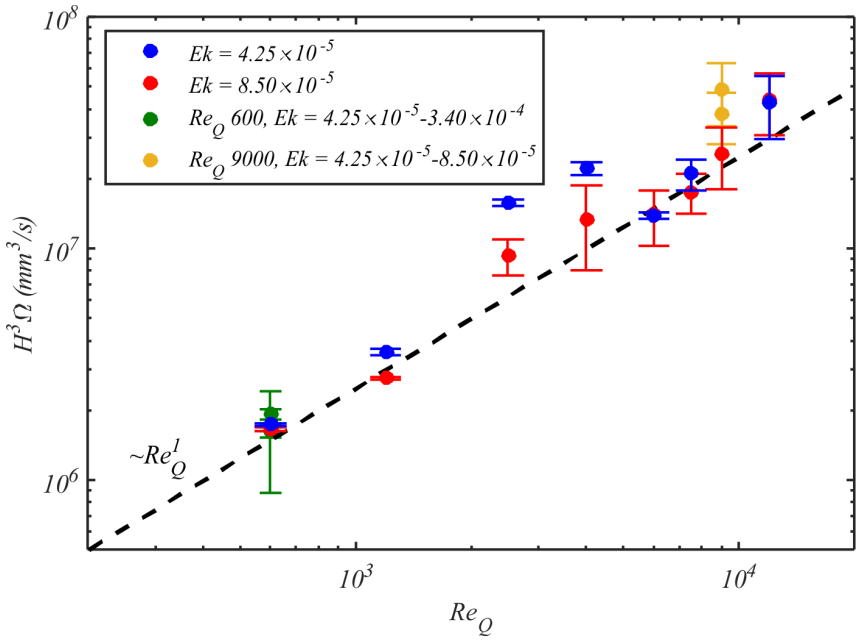

Figure 4.4: Patch height H_p cubed multiplied by the rotation speed Ω versus Re_Q for various experimental settings. Dashed line represents a scaling based on (2.33).

structures could not be fully investigated, due to the limited number of data-points for $Re_Q \leq 1200$. Investigation into the structures that form over sinks requires a higher resolution of the experimental parameter range for $Re_Q \lesssim 600$ and ideally in the absence of sources.

Due to the turbulent patch the flow field never operates under a strictly steady state. The velocity field is decomposed into its mean and fluctuating flow component as follows $\mathbf{u}(t) = \langle \mathbf{u} \rangle_t + \mathbf{u}'(t)$. The turbulent intensity, characterized by the ratio between kinetic energy carried by both the mean flow component ($E = \langle |\mathbf{u}| \rangle$) and fluctuating flow component ($E' = \langle |\mathbf{u}'^2| \rangle$) is shown in figure 4.5. We see from this that $E'/E \gtrsim 0.1$ across all parameter space. The flow field is unsteady under all experimental conditions. When plotted against the resulting Ro we see that as the relative strength of the inertial forces increases there is an increase in turbulent intensity until it plateaus at $E'/E = 1$ for $Ro \geq 0.03$. We now move on to examine the effect of changing Re_Q and Ek has on the flow field in more detail.

4.1.2 The effect of the jet Reynolds number Re_Q

In this section we fix Ek at 4.25×10^{-5} and examine the effect of altering Re_Q. Figures 4.6-4.8 show the mean vorticity fields $\langle \boldsymbol{\omega} \rangle_t$ and velocity fields $\langle \mathbf{u} \rangle_t$ along the various experimental planes.

Figure 4.6 shows the flow field along the vertical plane. We see that as $Re_Q \geq 1200$ the turbulent patch increases in width and in height, consistent with the results of figure 4.4. The patch is absent

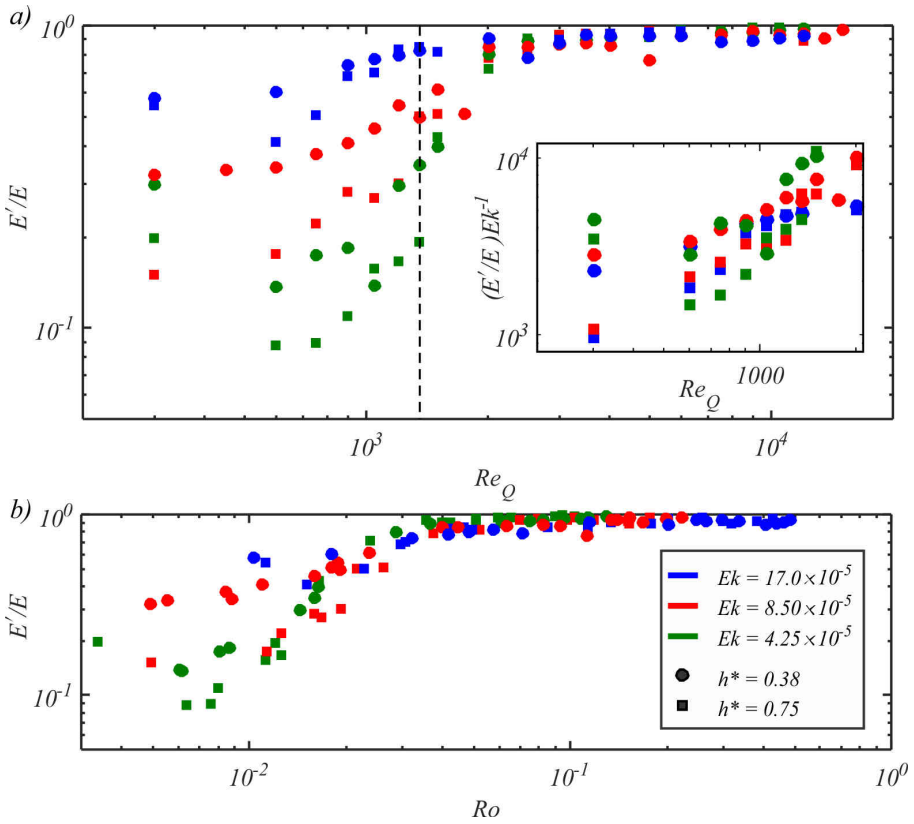

Figure 4.5: Turbulent intensity characterized by the ratio of kinetic energy carried by the fluctuating (E') velocity component and the average velocity component (E) as function of (a) Re_Q and (b) Ro across both horizontal planes and various Ek. Vertical dashed line in (a) indicates the point of $Re_Q = 1350$. (Inset) Turbulent intensity normalized by Ek up to $Re_Q = 2000$.

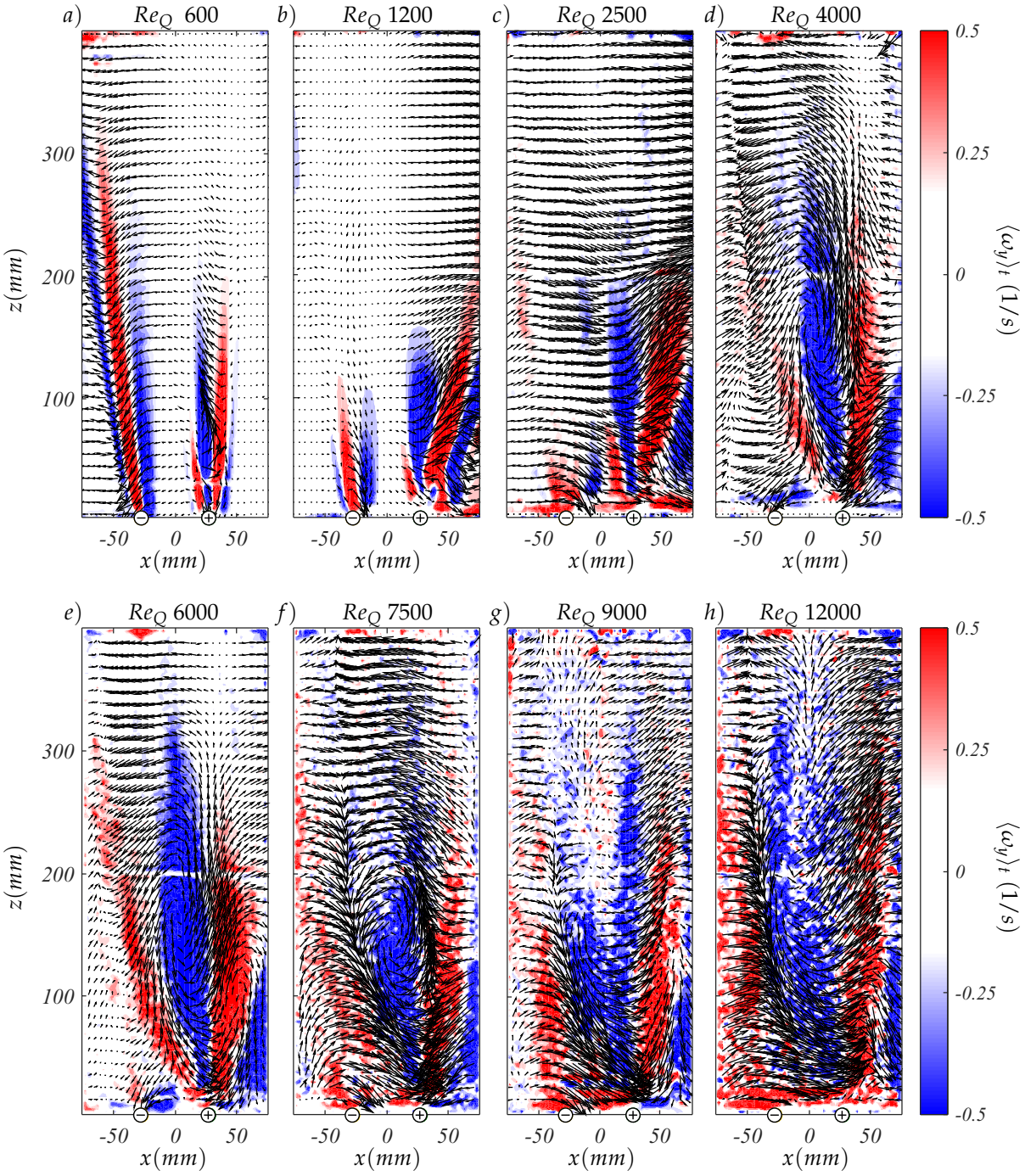

Figure 4.6: Contour plot of the $\langle\omega_y\rangle_t$ with vector plot of $\langle\mathbf{u}\rangle_t = (\langle u_x\rangle_t, \langle u_z\rangle_t)$ (arrows) for increasing Re_Q at $Ek = 4.25 \times 10^{-5}$. Averages are taken over a period of 300 seconds or 200 turntable rotations. (+) and (-) indicate the position of the source and sinks, respectively.

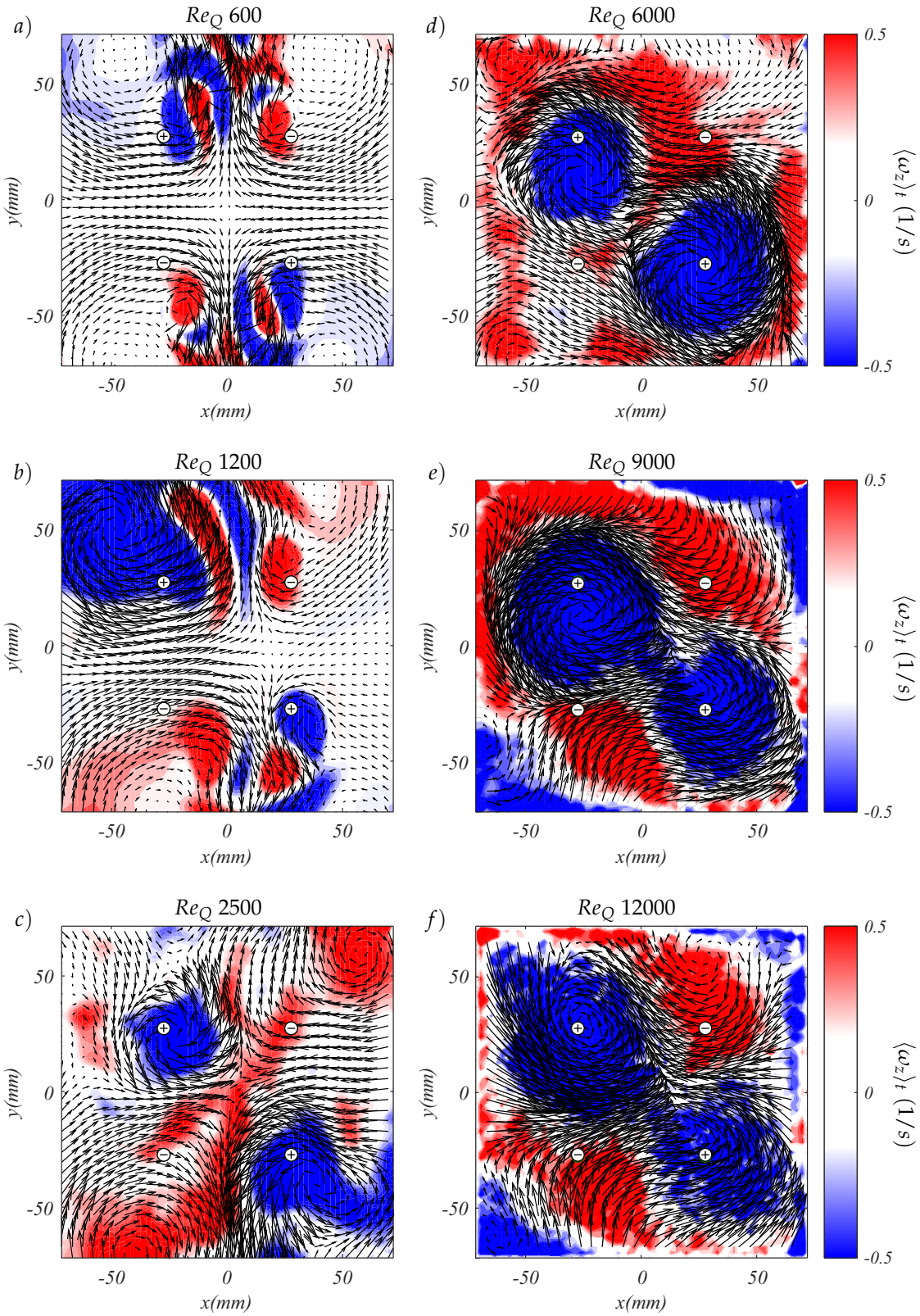

Figure 4.7: Contour plots of the $\langle\omega_z\rangle_t$ with vector plot of $\langle\mathbf{u}\rangle = (\langle u_x\rangle_t, \langle u_y\rangle_t)$ (arrows) for increasing Re_Q at $h^* = 0.38$ and $Ek = 4.25 \times 10^{-5}$. Averages are taken over a period of 300 seconds or 200 turntable rotations. (+) and (-) indicate the position of the source and sinks, respectively.

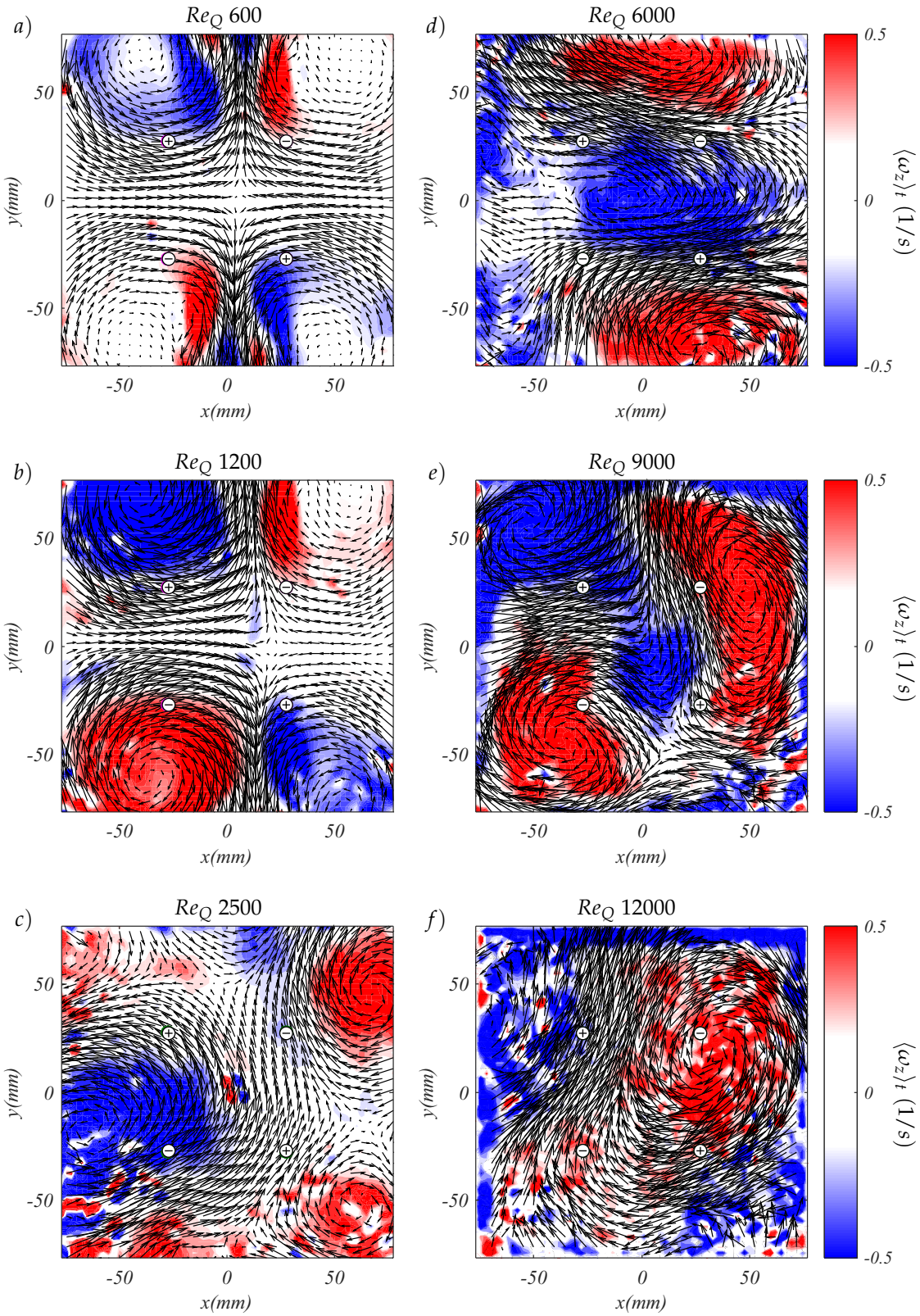

Figure 4.8: Contour plots of the $\langle\omega_z\rangle_t$ with vector plot of $\langle\mathbf{u}\rangle = (\langle u_x\rangle_t, \langle u_y\rangle_t)$ (arrows) for increasing Re_Q at $h^* = 0.75$ and $Ek = 4.25 \times 10^{-5}$. Averages are taken over a period of 300 seconds or 200 turntable rotations. (+) and (-) indicate the position of the source and sinks, respectively.

in the upper half of the flow where a gradual drop in inertial forces, due to injected momentum being exhausted, causes said forces to be outweighed by the Coriolis force. Along the z-axis of the flow field the horizontal velocity $\langle u_x \rangle_t$ component in figure 4.6 remains largely uniform for all Re_Q. This uniformity shows that the columnar structures in the flow field reach over a large height regardless of Re_Q.

From the horizontal flow profiles at $h^* = 0.38$ in figure 4.7 we observe that for $Re_Q = 600$ there is a quadrupole albeit its vorticity is slightly lower than that of the one observed for $Re_Q = 1200$. As Re_Q is increased the flow velocity around the vortices increases, resulting in the quadrupole being stretched further.

At $Re_Q = 2500$ we see a change in the mean flow profile. The columnar structures over the sources become more centred on the sources. Their vorticity appears to increase as their width slowly decreases. The columnar structures over the sinks widen and their centres move further away from the position of the sinks. As Re_Q is increased further the structures over the sources become wider until the point where they seem to almost form one large structure of same sign vorticity. The accumulation of like-sign vortices is a feature that has been seen other 2D turbulent flows [60]. The structures over the sinks no longer appear in the field of view, though patches of opposing vorticity do surround the larger structure, which suggests that the structures over the sink are still present in the flow field.

In figure 4.8 we examine the same profiles but at $h^* = 0.75$. For $Re_Q = 600$ and 1200 we see the quadrupole develop as before. At $Re_Q = 2500$, 4.8*c*, we see little resemblance with fig.4.7*c*. There is absolutely no symmetry left in fig.4.8*c*. This lack of symmetry can be seen at all $Re_Q \geq 2500$. This point coincides with the point at which the turbulent intensity, in figure 4.5, reaches a value of 1.0. Furthermore, mean flow profiles extracted over a different period of similar time show significant changes at $h^* = 0.75$, suggesting there is a change in overall flow topology.

Figures 4.9 and 4.10 show the instantaneous vorticity field $\boldsymbol{\omega}(t)$ and velocity field $\mathbf{u}(t)$ for $Re_Q = 1200$ and 2500 along both horizontal planes and the vertical plane at $Ek = 4.25 \times 10^{-5}$. Additional figures showcasing higher and lower Re_Q flow fields can be found in Appendix A.

Figure 4.9 shows that across all experimental planes at $Re_Q = 1200$ there is little shift in both the instantaneous vorticity field and velocity field over a long period of time. When compared against the mean flow fields seen in figures 4.6*b* 4.7*b* and 4.8*b* the instantaneous flow fields show almost no difference. This behaviour is observed along the horizontal plane experiments until $Re_Q \approx 1350$ for $Ek = 4.25 \times 10^{-5}$.

From the horizontal flow profiles in figure 4.10 we can observe that the instantaneous flow field is not necessarily formed of a small number of large structures. At $h^* = 0.38$ 4.10*b* the flow field shows a multitude of small vortices. These structures are not stationary. The movement of these

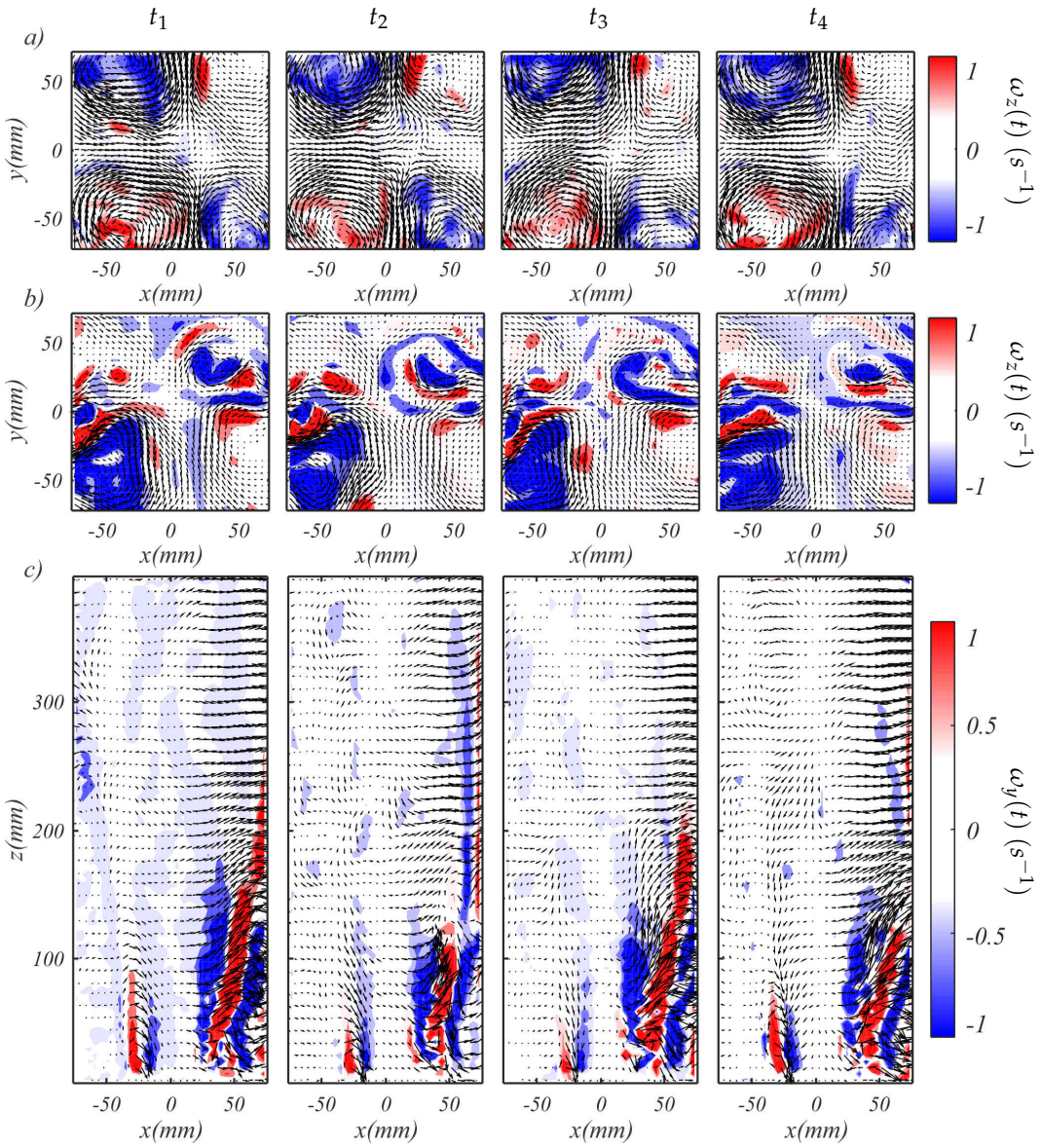

Figure 4.9: Contour plots of the instantaneous vorticity field $\boldsymbol{\omega}(t)$ and velocity field $\mathbf{u}(t)$ (arrows) across intervals t_1-t_4, each 15 seconds apart for $Re_Q = 1200$ and $Ek = 4.25 \times 10^{-5}$. Flow fields shown along a horizontal plane at (a) $h^* = 0.75$, (b) $h^* = 0.38$ and (c) along the vertical plane. Note: Flow fields shown are in fact averaged over a short time period of 5 frames for visualization purposes.

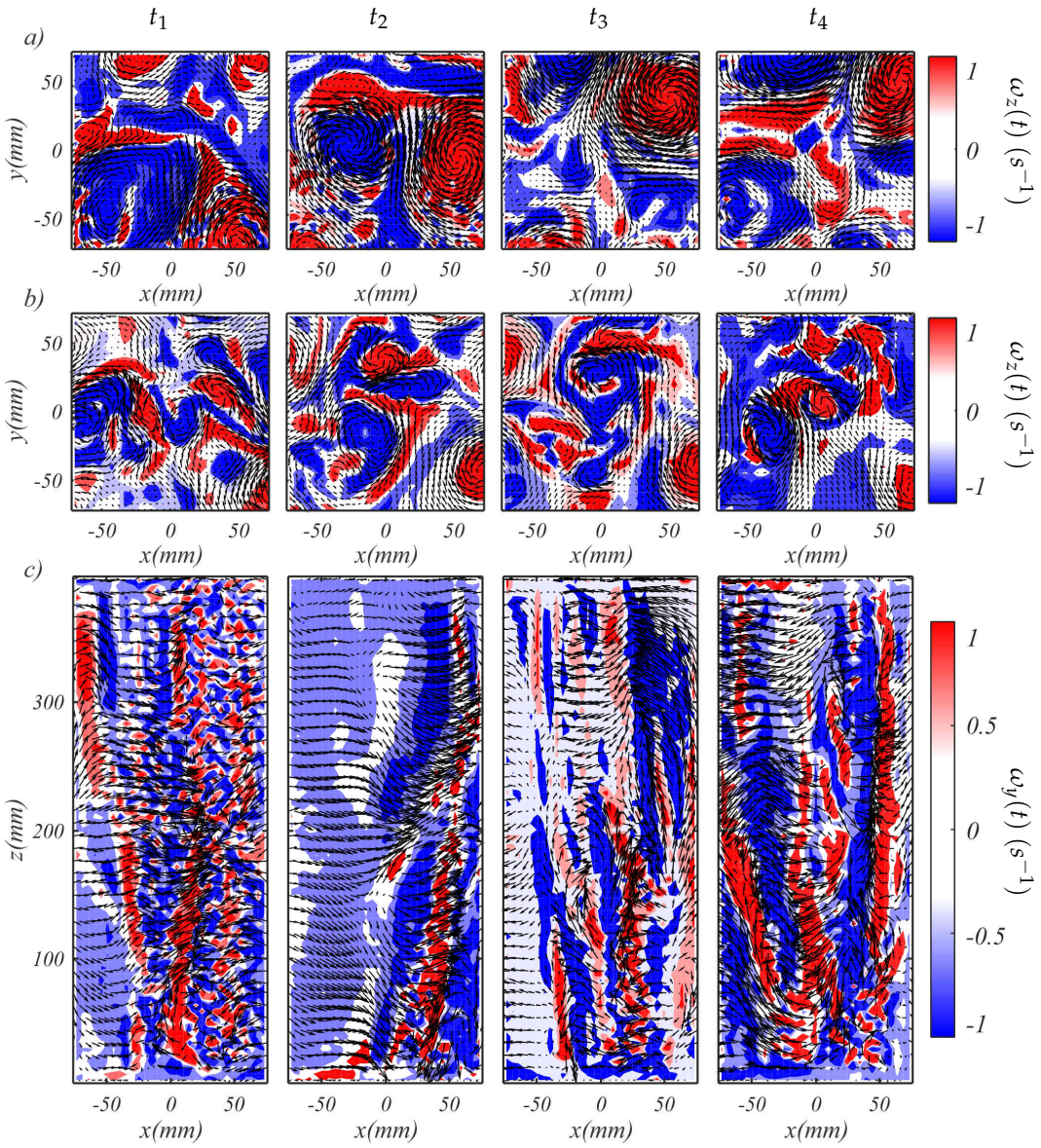

Figure 4.10: Contour plots of the instantaneous vorticity field $\boldsymbol{\omega}(t)$ and velocity field $\mathbf{u}(t)$ (arrows) across intervals t_1-t_4, each 15 seconds apart for $Re_Q = 2500$ and $Ek = 4.25 \times 10^{-5}$. Flow fields shown along a horizontal plane at (a) $h^* = 0.75$, (b) $h^* = 0.38$ and (c) along the vertical plane. Note: Flow fields shown are in fact averaged over a short time period of 5 frames for visualization purposes.

structures is best examplified in the flow profiles at $h^* = 0.75$ in figure 4.10*a*. At t_1 we see two large structures of opposite sign at the bottom of the graph. They move across the flow field at t_2,t_3 and t_4. We observe the displacement and stretching of vortex filaments around these larger structures. These phenomena are a common feature of 2D turbulent flows [16],[60] and have been shown to play a key part in energy transfer mechanism in 2D turbulence [12]. As Re_Q is increased further the horizontal profiles show increasingly larger structures with the flow field often consisting of two large structures of opposite sign moving around one another, with occasionally a smaller structure moving into view and being deformed, strained and ultimately consumed by the larger ones.

The vertical plane profiles show that at $Re_Q = 2500$ the flow field becomes littered with filaments of opposite vorticity. These filaments move across the flow field and likely represent the smaller columnar structures seen in horizontal profiles at $h^* = 0.38$. The turbulent patch that could be clearly identified from the mean flow profiles in figure 4.6 becomes obscured by the unsteady flow at $Re_Q = 2500$. This is the reason for sudden increase in error H_p observed earlier in figure 4.4.

In the vertical plane profiles at t_1 a long region of small vorticity patches can be seen on the right hand side of the flow field. Outside of this region there is a strong flow into this region. The interaction of these flows likely lead to these small patches of vorticity. Considering this region reaches almost across the entire height of the tank it is likely that here we observe a large columnar structure, with the lasersheet cutting right across its centre. This would also explain why along the centreline of this structure $u_x(t) \approx 0$. The greatest velocity component of a columnar structure is the azimuthal velocity. In a vertical slice along its centre the azimuthal velocity would be perpendicular to the vertical plane and almost unobservable using 2D-PIV techniques. As Re_Q is increased further the strands of vorticity become increasingly thinner and we see more occurrences of long regions of vorticity patches stretching across the tank height. These regions may be large columnar structures or simply a consequence of the flow field becoming more turbulent.

If we now relate the flow fields observed in figures 4.7*c*, 4.8*c* and 4.10 we can explain what happens as Re_Q is increased. At $Re_Q \leq 1200$ the flow field consists of a quadrupole set atop turbulent patch. As Re_Q is increased the quadrupole gets stretched and the turbulent patch grows in height. At $Re_Q \geq 2500$ these quadrupole becomes stretched too far and the columnar structures become detached from the points of forcing. Not only does this allow new structures to be formed, but these structures would continuously advect one another in that scenario, which is in line with the instantaneous behaviour of the flow field seen in figure 4.10. The detachment of columnar structures has been observed down to $Re_Q = 2000$ at $Ek = 4.25 \times 10^{-5}$. The symmetrical topology seen at $h^* = 0.38$ in figure 4.7 is likely the result of the turbulent patch penetrating into the horizontal plane. As the flow within the turbulent patch is unaffected by the Coriolis force its position

remains almost fixed, resulting in two structures suddenly centred over the sources in the mean flow profiles. This would be consistent with H_p measured at $Re_Q = 2500$ and $Ek = 4.25 \times 10^{-5}$.

4.1.3 The effect of the Ekman number Ek

In figure 4.5 we see that the turbulent intensity at $Re_Q < 2000$ is heavily dependent on Ek, with decreasing Ek resulting in a decrease in turbulent intensity. In the inset of figure 4.5 the turbulent intensity is normalized by Ek, showing an almost linear dependence. The figures do not collapse as there is likely to be a dependence on h^* that plays a role as well. This shows that the fluctuating velocity component is heavily influenced by the Coriolis force. This suggest that the fluctuations seen in the regime of $Re_Q < 2000$ are likely to be driven in large part by inertial waves, which are closely linked to the Coriolis force, rather than turbulent fluctuations.

In the remainder of this section we fix $Re_Q = 1350$ and examine the effect of altering Ek has on the flow topology. Figure 4.11 shows the average ($\langle\cdot\rangle_t$) and instantaneous vorticity and velocity field along the horizontal planes for $Re_Q = 1350$. At $Ek = 1.70 \times 10^{-4}$ (4.11a, b) we see similar behaviour to that observed in 4.7c and 4.8c. The mean flow profiles show little symmetry and the instantaneous flow field shows little correlation to the mean flow profile. There are two counter-rotating structures that appear to remain in a largely stable position over time in fig.4.11a. These are likely caused by the turbulent patch over the sources penetrating into the flow field at the height of $h^* = 0.38$. We however do not have measurements along the vertical plane at this $Re_Q = 1350$ nor were we able to accurately determine a value for H_p for cases where $Ek > 8.50 \times 10^{-5}$, so this cannot be asserted with certainty. If Ek is now decreased to $Ek = 4.25 \times 10^{-5}$ we see at $h^* = 0.75$ (fig.4.11f) that the mean flow field consists of a quadrupole and the instantaneous flow field deviates little from the mean behaviour, similar to behaviour seen in 4.9a and b. The cases in figures 4.11c, d and e fall in between the two scenarios previously described. Across all three cases the mean flow profiles show an almost symmetrical configuration that is close to a quadrupole. Their instantaneous flow field deviates only slightly from that of the mean flow field. Close examination of the velocity fields shows the large structures of the quadrupole remain in roughly the same location, but the surrounding flow sees a constant injection of smaller vortices, especially in the central region close to the points of forcing. These small vortices are advected and strained by the larger ones.

By increasing Ek we see a similar effect to increasing Re_Q, with the flow field becoming more unsteady with increasing Ek. When we combine the results for changing Re_Q and Ek we see a transition from one flow regime to another. In the first regime (Regime I) the flow configuration consists of a quadrupole of columnar structures set atop a turbulent patch, this regime corresponds

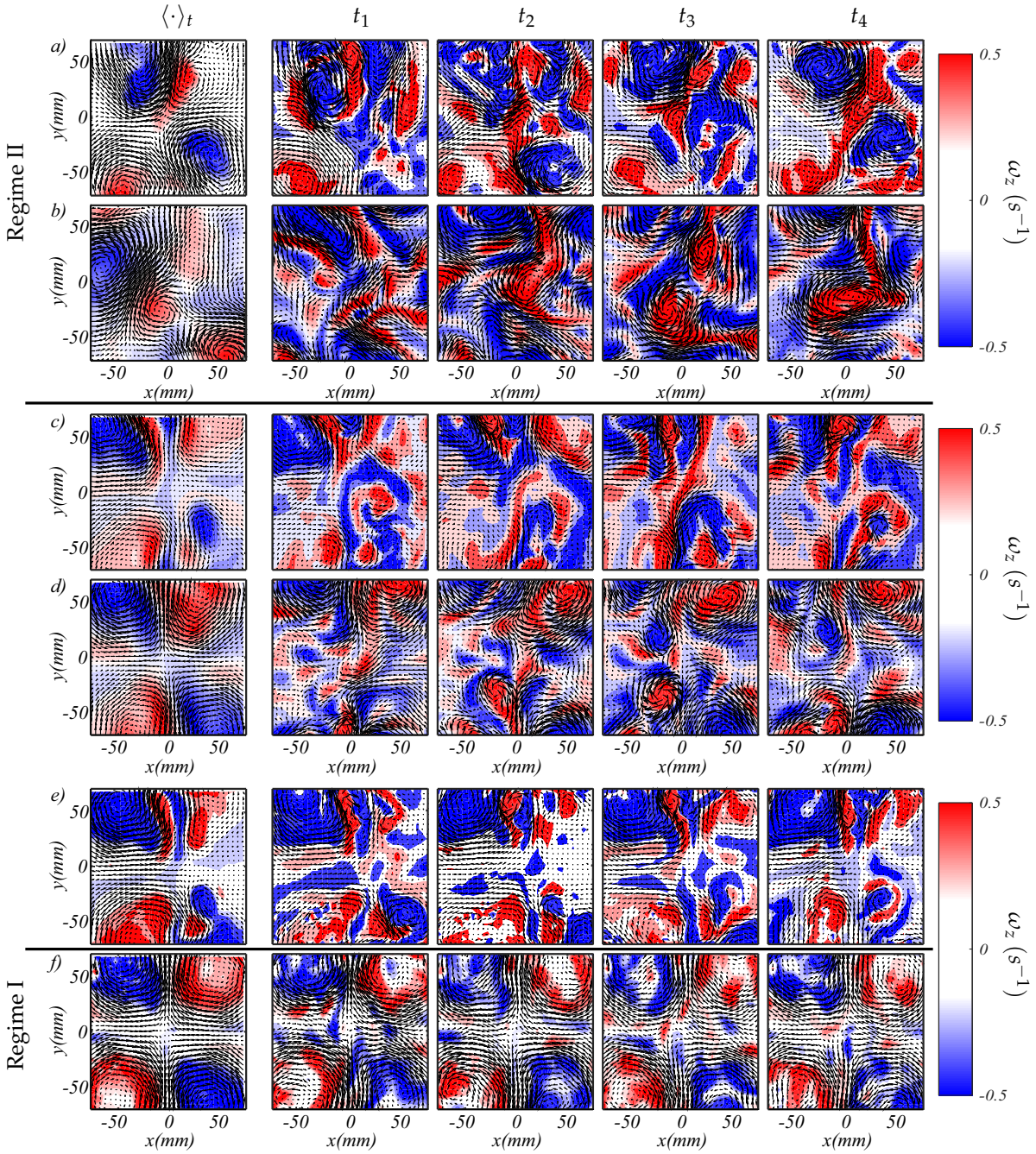

Figure 4.11: Contour and vector plot of the average ($\langle\cdot\rangle_t$) and instantaneous ($t_1 - t_4$) vorticity ($\omega_z(t)$) and velocity ($\mathbf{u}(t)$) field at $Re_Q = 1350$. Fields shown at (a,b) $Ek = 1.70 \times 10^{-4}$, (c,d) 8.50×10^{-5} and (e,f) 4.25×10^{-5} and at (a,c,e) $h^* = 0.38$ and (b,d,f) $h^* = 0.75$. Instantaneous flow fields are taken 15 seconds apart. Black lines separate experiments based on the dynamical regimes observed in figure 4.12. Note: Instantaneous flow fields shown are in fact averaged over a short time period of 5 frames for visualization purposes.

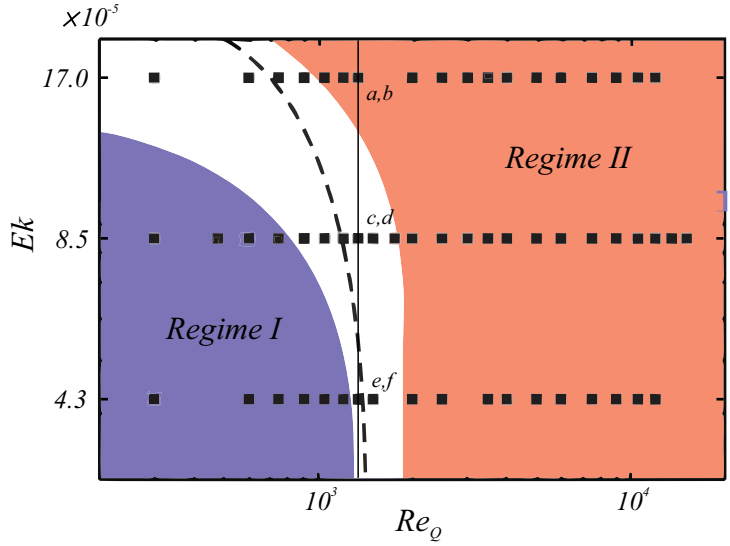

Figure 4.12: Outline of Regime I (blue) and Regime II (red), based on examination of the instantaneous vorticity and velocity field along the horizontal plane at $h^* = 0.38$ and the magnitude of turbulent intensity. Dashed line shows the extent of regime I for $h^* = 0.75$. Solid black line represents the experimental case studied in figure 4.11.

to figures 4.9 and 4.11f. In the other regime (Regime II) the quadrupole is stretched apart and new columnar structures are continuously formed and advected throughout the flow field, corresponding to figures 4.10 and 4.11a, b. Between these two regimes there exists a narrow transition regime where the quadrupole still exists but smaller structures are continuously injected from the forcing points and are advected by the quadrupole, as can be seen figures 4.11c, d and e. Regime I has been observed up to $E'/E \approx 0.3$ and regime II has been observed down to $E'/E \approx 0.8$. Figure 4.12 shows a rough outline of the two regimes based on our results.

4.1.4 Time-scale analysis

To further illustrate the change in dynamics we examine the characteristic time-scale of the flow. We approximate this characteristic time-scale using autocorrelations. The autocorrelation function $R(dt)$ for any given signal $y(t)$ of length T is given by

$$R(dt) = \frac{c(dt)}{c_0} \ , \ c(dt) = \frac{1}{T-1} \sum_{t=1}^{T-dt} (y(t) - \langle y \rangle_t)(y(t+dt) - \langle y \rangle_t) \ , \tag{4.1}$$

where dt is the delay/lag in the signal and $c_0 = c(0)$. This calculation is performed using the *autocorr.m* algortihm in Matlab for each point in the flow field. These autocorrelations are then averaged out spatially. The characteristic time-scale of the flow is taken as the first zero found in this autocorrelation function, which is commonly referred to as the decorrelation time (τ_{dc}).

For rotational flows a characteristic time-scale of the system τ is approximately equivalent to the rotation period, which for the current experiment is $\tau = 2\pi/\Omega$. Figure 4.13 shows the ratio of τ_{dc}/τ as function of both Re_Q and Ro.

Figure 4.13*a* shows when inertial forces are relatively weak ($Re_Q < 1200$, $Ro \lesssim 0.01$) the $\tau_{dc}/\tau \approx 1$, showing a strong dependence on the Coriolis force. Beyond this regime we see a sudden increase to $\tau_{dc}/\tau \sim$ 10-40. This increase appears to be largely inertia driven as any changes to Ek in either figure 4.13*a* or *b* do not result in a collapse of data. Regardless, this time-scale far exceeds any imposed time-scale by the forcing parameters of the experiments. It is also exceeds any time scale imposed due to mechanical noise, which generally are of the order of $10^{-1}\tau$ or smaller. This increase coincides with the transition from Regime I to II. At the time of writing no reason has been found for the sudden increase. We do assume it is phenomena based on the dynamics of the flow, likely linked to the transition from regime I to II. The result is counter-intuitive as an increase in turbulent intensity often corresponds to a decrease in characteristic time-scales of the flow.

After the sudden increase we see a steady decline in τ_{dc}/τ. This decrease scales as both $\sim Re_Q^{-1}$ and $\sim Ro^{-1}$, showing a clear linear dependence on strength of inertial forces. A decrease would be consistent with the flow field becoming more 3D turbulent, which would be the case with an increase in inertial forces.

For the case of $Ek = 17.0 \times 10^{-5}$ (blue) we see a rapid decrease with $\tau_{dc}/\tau \sim Re_Q^{-4}$ or $\sim Ro^{-4}$. This clearly shows a strong dependence on inertial forces.

If we look at figure 4.13*b* we see that decrease coincides with a range of $Ro \approx$ 0.3-0.4. Stapelhurst *et al*. [59] showed that for the case of decaying rotational turbulence inertial waves could exist up to $Ro \approx 0.4$. This tells us that in the range of $Ro \approx$ 0.01-0.4 the characteristic time scale is likely linked to the existence of inertial waves. Based on this we can speculate as to the cause of the sudden increase in τ_{dc}/τ as well. If we consider the time-scale observed to represent the formation of a columnar structure and if this formation were to be driven by near-resonant non-linear triadic inertial wave interactions [54], then this would require $\tau_{dc} \gg \tau$ as formation of structures under these conditions occurs over large time scales, far exceeding τ. Regardless of the origin of the sudden increase in τ_{dc}/τ what these results show is that we have to develop an understanding on how inertial waves manifest themselves and how they propagate in jet-induced rotating turbulence.

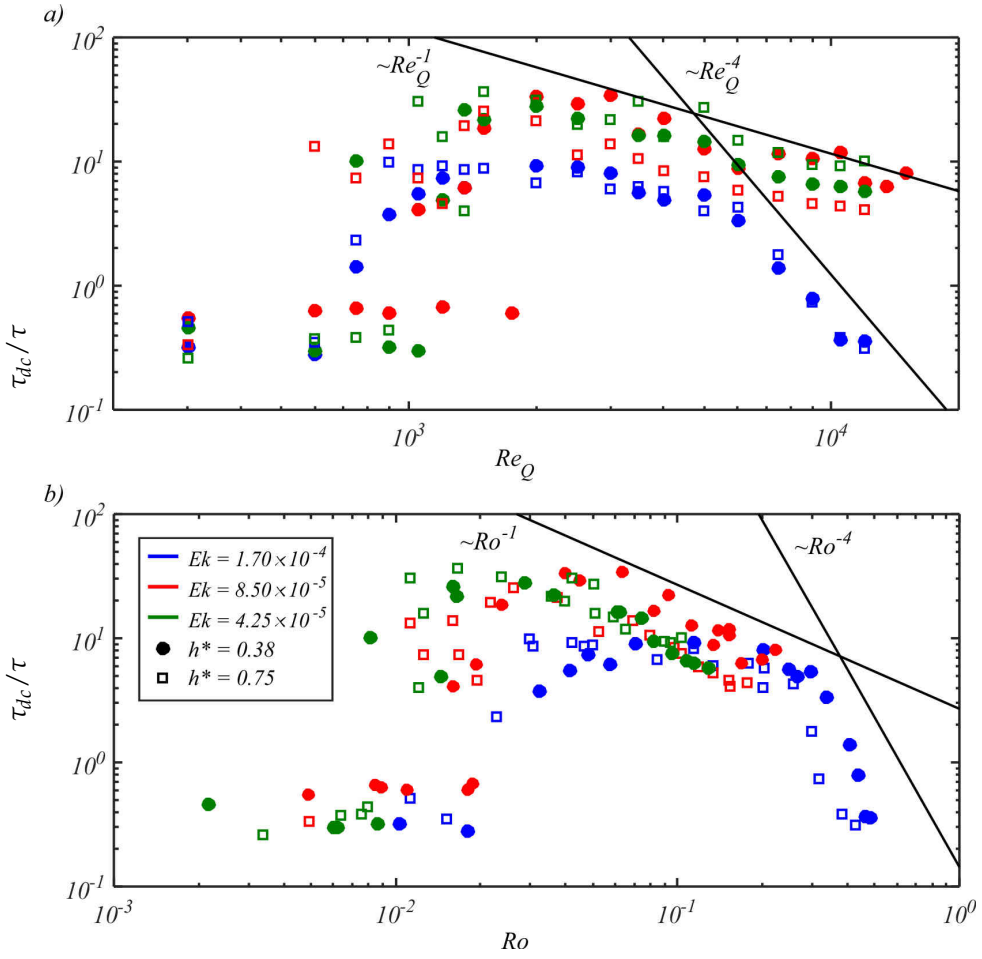

Figure 4.13: Decorrelation time τ_{dc} normalized by the rotation period $\tau = 2\pi/\Omega$ as function of (a) Re_Q and (b) Ro.

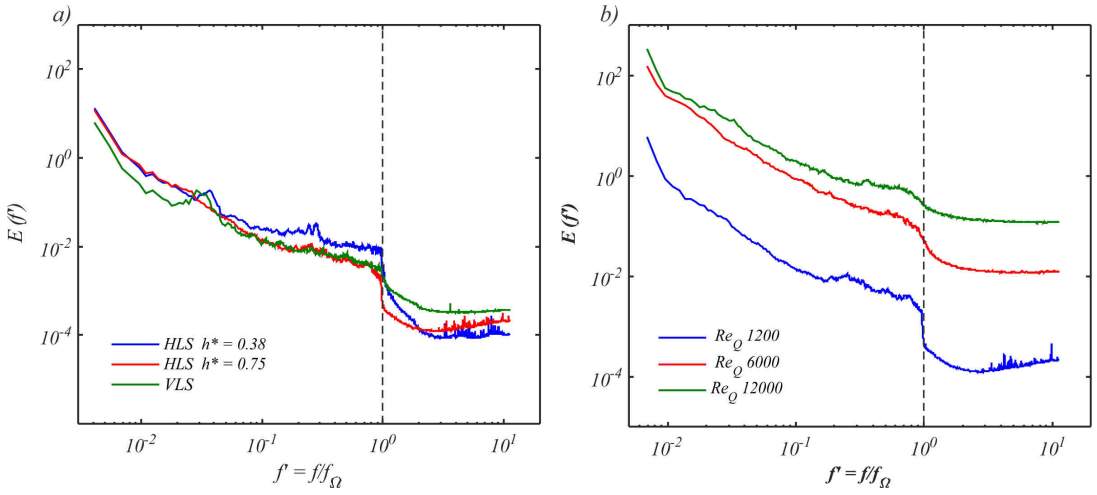

Figure 4.14: a) Energy spectra $E(f')$ against normalized frequency f' for $Re_Q = 1200$, $Ek = 4.25 \times 10^{-5}$ along the horizontal plane at $h^* = 0.38$ (blue), $h^* = 0.75$ (red) and along the vertical plane (green). b) Energy spectra for $Ek = 4.25 \times 10^{-5}$, $h^* = 0.75$ for $Re_Q = 1200$ (blue), $Re_Q = 6000$ (red) and $Re_Q = 12000$ (green).

4.2 The role of inertial waves in jet-induced rotating turbulence

The flow field that develops in the experiments is unsteady. As such, the fluctuating flow component of the flow field plays an important role in the overall dynamics of the flow. In flows subject to background rotation fluctuations can be due to inertial waves. In this section we seek to answer the second question set out at the beginning of this chapter: "How do inertial waves develop under the flow conditions of a flow excited by a jet-induced rotating turbulence?"

4.2.1 Frequency spectra

Inertial waves can exist up to a frequency equal to twice the rotation frequency of the background rotation, $f_\Omega = 2\Omega/2\pi$. When turbulence is introduced into a rotating fluid frequencies both above and below f_Ω are excited. A common method to show the presence of inertial waves in a turbulent flow field is to show the kinetic energy or enstrophy as function the frequency spectra [66]. If inertial waves are present in a flow field a drop in the energy spectra should be visible at $f = f_\Omega$ as inertial waves are known to carry a significant amount of the total kinetic energy for rotating flows [67].

For each point in any experiment the frequency dependent velocity field $\mathbf{u}(f)$ is derived from $\mathbf{u}(t)$ by applying a discrete Fourier transform over time. For any signal $y(t)$ of length T, $y(f)$ is given by

$$y(f) = \sum_{t=1}^{T} y(t) W_T^{(t-1)(f-1)} \quad , \quad W_T = e^{(-2\pi i/T)} \, . \tag{4.2}$$

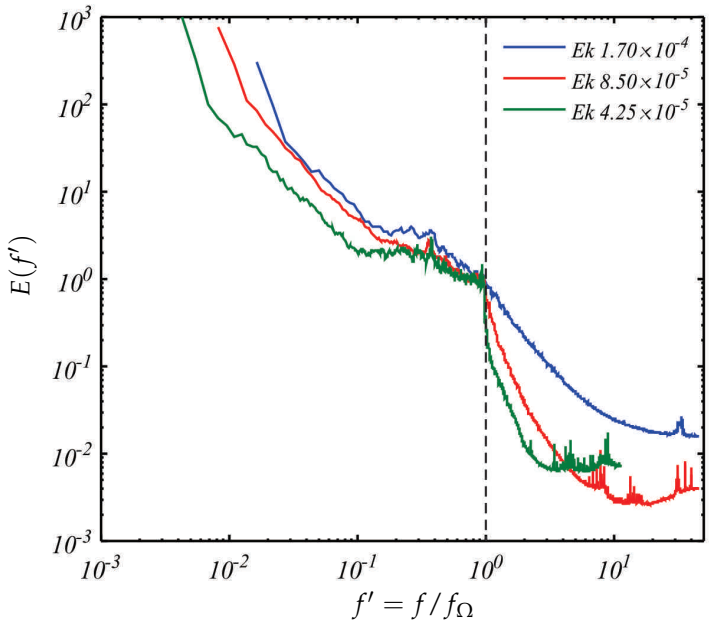

Figure 4.15: Energy spectra $E(f')$ against normalized frequency f' at $Re_Q = 2000$ along a horizontal plane at $h^* = 0.38$ for $Ek = 1.70 \times 10^{-4}$ (blue), $Ek = 8.50 \times 10^{-5}$ (red) and $Ek = 4.25 \times 10^{-5}$ (green).

This Fourier transform is applied using the fast Fourier transform function (*fft.m*) in Matlab. The energy spectrum is calculated by $E(f) = \langle |\mathbf{u}(f)^2| \rangle_{\mathbf{x}}$. We then normalize the frequency f by f_Ω to give $E(f')$, where $f' = f/f_\Omega$.

We fix $Re_Q = 1200$ and $Ek = 4.25 \times 10^5$ and see how $E(f')$ changes across the various experimental planes in figure 4.14*a*. As expected there is a sharp drop in $E(f')$ at $f' = 1$. We also see that the energy at $h^* = 0.38$ is slightly higher than at $h^* = 0.75$, which shows that regions further away from the bottom of the tank carry less energy than those closer to the forcing points. The drop along the vertical plane is less pronounced when compared to the horizontal planes. This is caused by the turbulent patch being taken into the overall calculation, which causes on average more energy to be carried by modes outside the inertial waves regime. Overall the results obtained across the various experimental planes present a coherent picture with differences between them reflecting the inhomogeneity of the flow.

In figure 4.14*b* Ek is fixed at $Ek = 4.25 \times 10^{-5}$ while Re_Q is steadily increased. We can see that the overall energy in the flow increases, which is consistent with the increase of energy injected into the system as Re_Q is increased. The sharp drop at $f' = 1$ gradually smooths out. This is caused by the flow becoming increasingly turbulent and as a result more energy is carried by modes outside the inertial wave range. Finally we fix Re_Q and alter Ek. Figure 4.15 shows $E(f')$ at $Re_Q = 2000$ and $h^* = 0.38$. As Ek is decreased the drop at $f' = 1$ becomes increasingly steep,

showing that more of the overall energy is carried by modes inside the inertial wave range. The behaviour seen in figures 4.14 and 4.15 are representative of all experiments carried out. All energy spectra $E(f')$ across both horizontal planes are shown additional figures in Appendix A.

4.2.2 Inertial wave generation and propagation

From the energy spectra it is clear that inertial waves are present in our flow field. Two interesting question now arise; first, where do they originate from? And second, how do they propagate throughout the flow? In order to isolate inertial waves we first compute the fluctuating components of the velocity field $\mathbf{u}'(t)$ from experiments carried out along the vertical plane. We then apply the Adcanced Phase Averaging (APA) filtering technique, explained in section 3.3.1, to these velocity fields at a filtering frequency F. Because the APA filter uses a frequency band-pass filter it is unable to isolate a single inertial wave mode, but rather it isolates a narrow range of modes centred on F. In order to isolate inertial waves would require $F \leq f_\Omega$. From the filtered velocity fields the vorticity field ω_y' is calculated.

We fix $Re_Q = 1200$ and $Ek = 4.25 \times 10^{-5}$. Figure 4.16*a* shows the contours of ω_y' as $F' = F/f_\Omega$ is increased steadily. For $F' < 1$ we see periodic structures that appear to originate from an area above the sources. This makes sense as the turbulent patch that forms above these sources excites modes with frequencies both above and below f_Ω, making it a natural 'source' for inertial wave generation.

From (1.9) we know that for inertial waves there exists a relation between the wave frequency σ and the angle of propagation θ. The dashed lines in fig.4.16 corresponds to θ predicted by (1.9), where $\sigma = F$. We know inertial waves cannot exist for $F' > 1$. For $F' = 1.5$ we no longer see any periodic structures and the modes are concentrated around the point of the turbulent patch. The periodic structures can be observed across a wide range of Ek as shown by figure 4.16*b* where Re_Q and f' are fixed at $Re_Q = 1200$ and $f' = 0.34$. The cross-patterns seen in the upper part of the flow fields in figure 4.16 can be explained by the structures reflecting off surfaces, a behaviour seen in the early experiments on rotational flows [24]. What this and the lack of patterns for $F' > 1$ shows is that fluctuations in the inertial wave range are propagated more effectively throughout the flow field than those outside the inertial wave range.

Figure 4.17 shows the filtering frequency F' against the propagation angle θ found for the periodic structures in the flow field across all experiments carried out. Only experiments where periodic structures could be clearly identified are represented in this graph. The angle θ is determined by fitting a straight line to several contours close to the forcing mechanism at the bottom of the flow field. The error here is based on a upper- and lower bound fit to these contours. It

can be seen that θ follows the behaviour predicted by the dispersion relation for inertial waves. Therefore we conclude that the periodic structures we see are inertial waves. The deviation of θ to the dispersion relation increases as F' approaches 1. This is only natural as the APA filtering technique operates using a narrow band-pass filter. And because $\sigma \sim \cos\theta$ the band-pass filter will capture a wider range of θ as F' approaches 1, increasing the scattering of the data.

For $Re_Q > 1200$ inertial waves could no longer be directly observed from the contours of ω'_y. This is caused by the more turbulent nature of the flow field for experiments carried out in Regime II (fig.4.12). In figure 4.9 we saw that in regime I a region of high vorticity remained in roughly the same location for all t, i.e. the location of the turbulent patch. For regime II regions of high vorticity are present through out the entire flow field and are continuously advected (fig.4.10). Staplehurst *et al*. [59] proposed that regions of high vorticity function as emitters of inertial wave packets. In order to isolate individual inertial waves using the APA filtering technique would thus become increasingly difficult.

In any case, these results show that the range of $f < f_\Omega$ is dominated by inertial waves and that simply separating the fluctuations based on f_Ω is an effective way of disentangling the inertial wave fluctuations from the random turbulent fluctuations, especially for $Re_Q \leq 1200$.

So far we have not commented on the effect of Re_Q and Ek have on the wavelength λ of the inertial waves. From figure 4.16 it is clear there are numerous waves propagating across the flow field. As they move, they are affected by other waves, reflect off surfaces and slowly attenuate. Because of these various effects no algorithm could be written to extract λ accurately. Across the narrow range of control parameters where individual waves could be observed, none of the changes seen in λ as a result of changing control parameters could be confirmed to represent a consistent trend.

4.2.3 The energy of inertial waves

The previous results show that part of the fluctuations are due to inertial waves. To quantify their contribution to the overall flow an upper bound on the amount of energy they carry is derived. This is done using the fact that inertial waves can only exist up to frequencies of f_Ω. By splitting the fluctuating velocity field $\vec{u'}$ into two ranges, one strictly due to turbulent motions free from inertial waves with frequencies $f > f_\Omega$ called the turbulent (subscript T) range. In the other range the fluctuations are in part due to inertial waves with frequencies $f < f_\Omega$, this range is called the Inertial Wave (subscript IW) range. Fluctuations in the IW-range may not be due to inertial waves, but it is difficult to directly distinguish between inertial waves and turbulent fluctuations within this range.

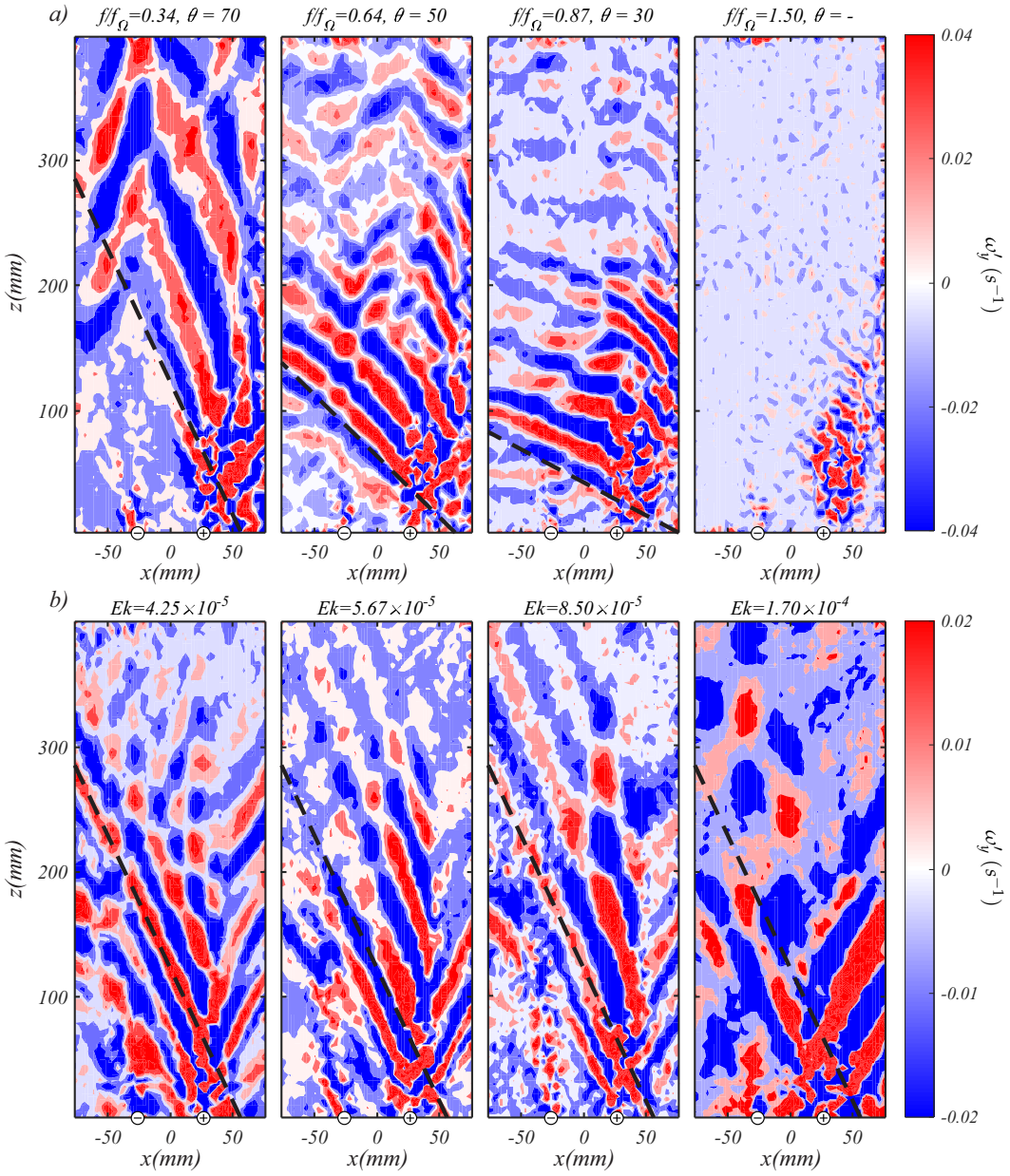

Figure 4.16: a) Contour plots of Advanced Phase Averaged vorticity field ω_y' for an experiment carried out at $Re_Q = 1200$ and $Ek = 4.25 \times 10^{-5}$. Fields are filtered at various normalized frequency f/f_Ω. b) Contour plots of advanced phase averaged vorticity field ω_y' for an experiment carried out at $Re_Q = 600$ and $f/f_\Omega = 0.34$, for various Ek. Dashed lines correspond to propagation angle θ predicted by (1.9) where $\sigma = f$. (+) and (-) indicate the approximate position of the source and sink, respectively.

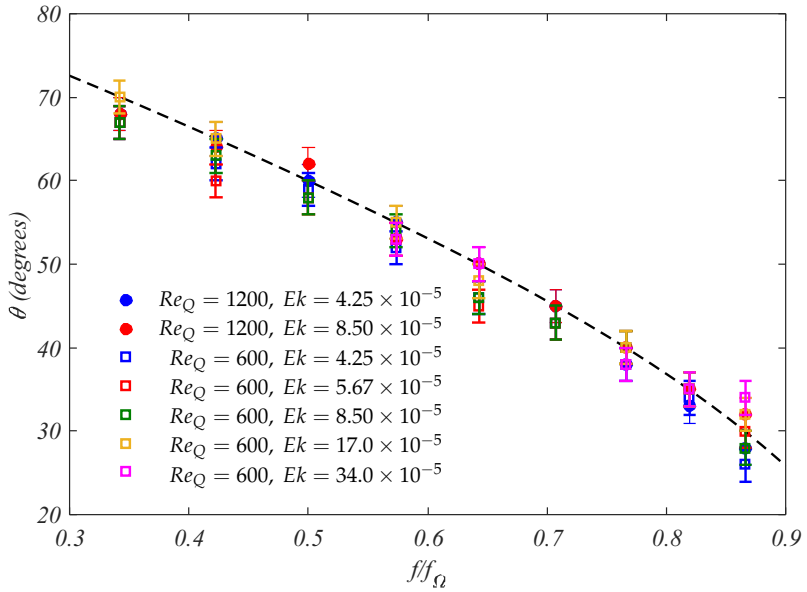

Figure 4.17: The observed angle of propagation θ of the periodic structures against the filtering frequency f/f_Ω. Dashed line represents the dispersion relation for inertial waves (1.9).

We perform a temporal Fourier transform on the fluctuating velocity field $\mathbf{u}'$. We then eliminate all the modes/frequencies above the f_Ω threshold and perform a discrete inverse Fourier transform, which for any Fourier series $y(f)$ of length T is given by

$$y(t) = \frac{1}{T}\sum_{f=1}^{T} y(f) W_T^{-(t-1)(f-1)} \quad , \quad W_T = e^{(-2\pi i/T)} \, . \tag{4.3}$$

This calculation is performed using the *ifft.m* function in Matlab. The result is a velocity field $\mathbf{u}'_{IW}$ where only modes within the IW-range are kept. The kinetic energy carried by IW-modes (E'_{IW}) and all fluctuating modes (E') are calculated from both $\mathbf{u}'$ and $\mathbf{u}'_{IW}$, using $E' = \langle |\mathbf{u}'^2| \rangle$.

Figure 4.18 shows the ratio E'_{IW}/E' as function of Ro, across both horizontal planes and various Ek. At both h^* we see a general trend that when $Ro \leq 0.05$, most of the kinetic energy is carried by IW-modes.

For $Ro \gtrsim 0.05$ the ratio E'_{IW}/E' decreases, but the trend shows an h^* dependency. Between 4.18*a* and *b* we see that IW-modes carry relatively more energy than T-modes at greater h^*. This is explained by Coriolis force being able to sustain the IW-modes as inertial waves, but not the T-modes. Resulting in the IW-modes being able to persist longer before losing energy. This was illustrated in figure 4.16*a* where inertial waves could be seen across the entire flow field while the turbulent fluctuations remained concentrated around the turbulent patch. Regardless, for $Ro \gtrsim 0.05$ the ratio E'_{IW}/E' decreases. The reason for the decrease is two-fold. First, an increase

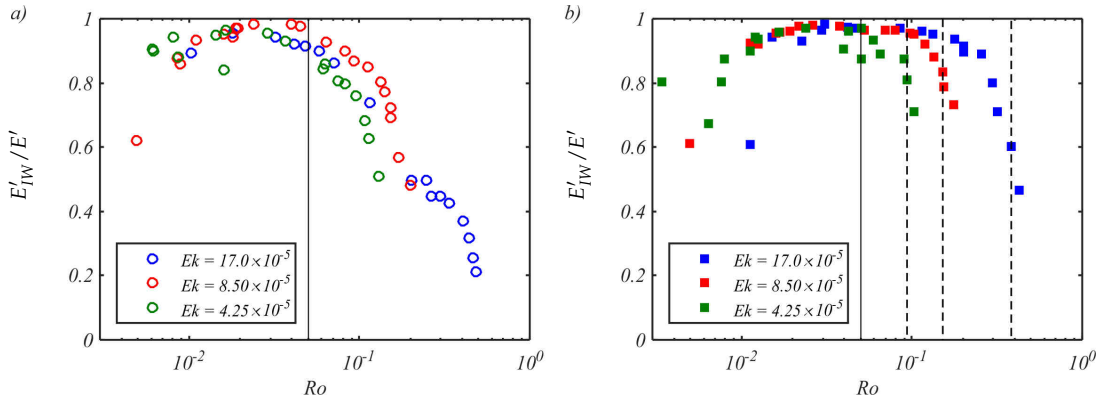

Figure 4.18: Ratio between kinetic energy carried by fluctuations in the IW-range (E'_{IW}) and energy carried by all fluctuations (E') as a function of Ro and Ek along the horizontal planes at (a) $h^* = 0.38$ and (b) $h^* = 0.75$. Solid black line shows the point of $Ro = 0.05$.

in applied inertial forces will inevitably lead to a more turbulent flow, which will see more energy being carried by T-modes, decreasing the ration E'_{IW}/E'. This effect is best exemplified in figure 4.18*a*, where we see a steady decrease with increasing Ro. Second, we know that inertial waves get disrupted by random turbulence and that for decaying rotational turbulence inertial waves can exist up to $Ro \approxeq 0.4$ [59]. In our experiments both inertial waves and the non-linearities that disrupts are excited by the turbulent patch whose relative size and strength is set by the applied inertial forces. The result of this can be seen in figure 4.18*b* where E'_{IW}/E' rapidly diminishes. These points where E'_{IW}/E' suddenly decreases (dashed lines) occurs at different values of Ro for different Ek, but occurs at the same $Re_Q = 10^4$.

Figure 4.19 shows the absolute values for E'_{IW} and E' as function of Re_Q and Ek. From figure 4.19*a* we see that the kinetic energy carried by IW-modes increases at a rate which scales as Re_Q^3 up to $Re_Q \approx 3000$.

We know from figure 4.18 that for low Ro, corresponding to low Re_Q, the majority of energy is carried by IW-modes, so it is expected that E' initially follows a similar trend to E'_{IW} for low Re_Q as is seen in figure 4.19*b*.

Based on both (2.21) and (2.23) we expect that the energy carried by the overall flow E to roughly scale as Re_Q^2. We also know from figure 4.5 that the turbulent intensity initially increases to a value of 1 as Re_Q approaches 2000 or Ro approaches 0.03. This requires the increase in E' to outpace the increase in E, hence $E' \sim Re_Q^3$ is unsurprising. No explanation however can be given for the power of 3.

For $Re_Q \geq 3000$ we see a different behaviour. In figure 4.19*a* E'_{IW} appears to plateau. Kolvin *et al*. [29] suggested an upper limit to the amount of energy carried by inertial waves may exist

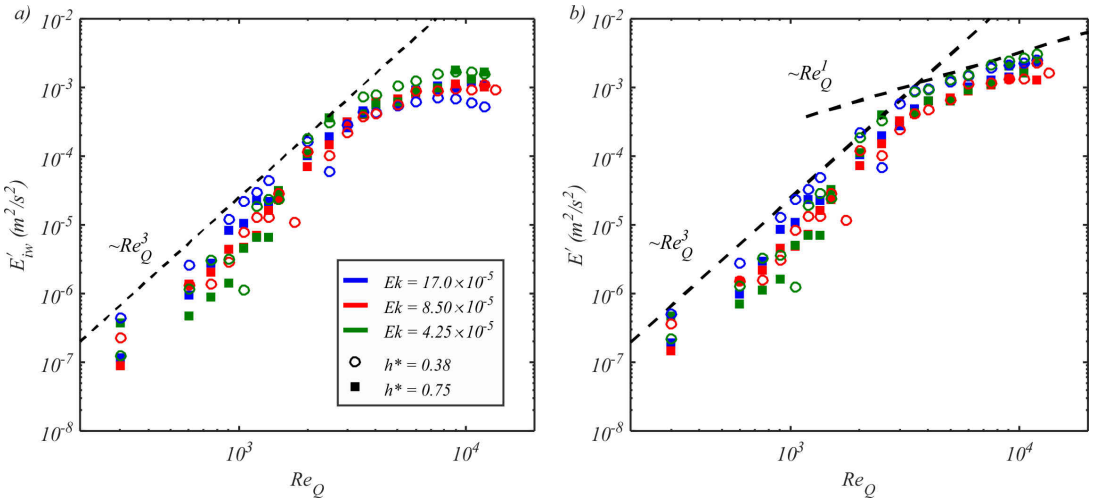

Figure 4.19: a) Kinetic energy carried by fluctuations in the *IW*-range (E'_{IW}) and b) kinetic energy carried all fluctuating modes (E') as a function of the Re_Q and Ek. Dashed lines show approximate scalings as function of Re_Q.

in forced rotating turbulence as other non-linearities excited by turbulence may disrupt inertial waves. The experimental range is however too narrow to confirm this trend as there is some discrepancy between the experiments conducted at the various Ek. Figure 4.19*b* shows that for $Re_Q \geq 3000$ E' continues to increase linearly with Re_Q and appears independent on Ek. This shows the fluctuations in this regime are increasingly due to turbulent motions.

4.3 Summary

Our flow is forced through fluid injection and withdrawal through a square pattern of two sources and two sinks, subject to a Coriolis force. At low Re_Q and Ek The flow topology consists of a quadrupole consisting of four columnar structures set atop an unsteady turbulent patch (regime I) that forms over the sources, due to local inertial forces being too great to be affected by the Coriolis force. While the presence of the patch was anticipated the marginally steady flow topology under these conditions is significantly different from the fully stable quadrupole upon which our theories in section 2.1 are based. The fluctuating velocity component and resultant turbulent intensity are heavily influenced by Ek in this regime, which suggests the fluctuations are likely to be driven in large part by inertial waves.

As Re_Q or Ek are increased the turbulent patch grows in height (fig.4.4), the turbulent intensity increases (fig.4.5) and the quadrupole becomes stretched under its own influence. At a certain point the structures of the quadrupole become detached from their forcing points and are advected by one another. New structures are continuously injected into the flow field which subsequently

advect others in turn (regime II.) Fluctuations in this regime are likely to be driven in part by the turbulent fluctuations of the patch as well as the unsteady motions of the various structures moving throughout the flow field. A rough outline of the parameter range of regimes I and II can be seen in figure 4.12. Between these two regimes we also see that the characteristic time-scale of the flow field, given by the decorrelation time τ_{dc}, increases significantly (fig.4.13). Not only is this result counter-intuitive as a transition to a regime with higher turbulent intensity would suggest a decrease in τ_{dc}, but this characteristic time is far greater than any time-scale imposed by the experiment. In regime II τ_{dc} is scales inversely with the inertial forces of the flow as a rate of Ro^{-1}, which increases to a rate of Ro^{-4} as the local $Ro \gtrsim 0.3$, likely linked to the flow no longer being able to support inertial waves.

Using the fact that inertial waves can exist up to frequencies f_Ω all modes of the fluctuating velocity field $\mathbf{u}'$ can divided into two ranges based on their frequency f. These are the IW-range, where $f \leq f_\Omega$ and the T-range, where $f > f_\Omega$. Inertial waves have been shown to be present in the flow field across all experimental parameters by observing a drop in $E(f')$ at $f' = 1$ (figures 4.14 and 4.15.)

Individual inertial waves were identified, using the APA filtering technique, to originate from the turbulent patch and propagate throughout the flow field (figure 4.16.) Waves could only be identified whilst the system was operating under conditions of regime I. In regime II waves are thought to be continuously emitted by various patches of vorticity, making it difficult to visualize inertial waves using the APA filtering technique.

Fluctuations within the IW-range were shown to carry the majority ot the kinetic energy of the overall fluctuating flow for $Ro \geq 0.05$. As Ro is increased more energy is carried by fluctuations in the T-range (fig.4.18*a*). As Ro increases there comes a point where the inertia of the fluctuating flow becomes too great to sustain inertial waves and these get disrupted by said inertia (fig.4.18*b*). This point occurs at $Re_Q = 10^4$.

Figure 4.5 showed that across the entire experimental parameter range the flow field can be considered turbulent. These turbulent flow fields were shown to have a non-zero average flow (fig.4.6-4.8) and we could see columnar structures develop, either remaining in a fixed location (fig.4.9) or translating across the flow field (fig.4.10). Similarly we have seen evidence of inertial waves propagating through out the flow field (fig.4.16). All these results show that a jet-induced rotating turbulent flow field is the ideal candidate to test whether the mechanism promoting anisotropy in rotating turbulent flow fields could be wave-free, as outlined in the theories of section 2.1. This is done in the following chapter.

Chapter 5

A waveless mechanism for anisotropy in rotating turbulence

From the previous chapter we know how the flow topology for jet-induced turbulence changes across the experimental parameter range. Columnar structures are found to form under the flow conditions considered and we see evidence of inertial waves being present across all experiments conducted. The existence of the columnar structures raises the question:

1. Do the columnar structures develop according to the scaling laws derived in chapter 2?

This is done by evaluating the flow field with respect to (2.10), (2.13), (2.21) and (2.23). This will allow us to identify whether the structures, and as a consequence anisotropy, develop under the combined influence of the Coriolis force and viscous or inertial forces. As implied by the analytical solution of Stewartson layers by Moore & Saffman [40, 41], the mechanism driving the formation of steady columnar structures in the limit were inertia can be neglected, such as Taylor columns, consists of a balance between the Coriolis force and viscous dissipation. Most importantly this mechanism is free from inertial waves. Similar steady structures have been seen in our experiments, but as the turbulent nature of our flow field suggests we cannot neglect inertia. Additionally we know inertial waves are present in our flow field and they can carry significant amount of the overall kinetic energy of the flow. Thus the possibility exists that the columnar structures form as a consequence of the inertial wave interactions as proposed by Davidson *et al*. [15] or Smith & Waleffe [54]. Considering the wave-free mechanism in the limit were inertia can be neglected, an interesting question becomes:

2. Can we identify a mechanism for anisotropy in rotating turbulence in which inertial waves play no part?

As our turbulent flow field has a non-zero average flow evaluating the magnitude of the terms in (2.27)-(2.29) for the average flow quantities will allow us to identify whether the anisotropy of the average flow develops a consequence of balance between static and/or fluctuating forces. By further dividing these fluctuations into random turbulent ones and inertial waves we could identify flow regimes where inertial waves play no part.

This chapter is divided into main two sections, each addressing one of the questions outlined. In a third section we summarize the results of this chapter. Experiments are presented using the same control parameters and variables as in chapter 4, additionally the same mathematical operators and subscripts are used as well. Where necessary these will be highlighted again.

5.1 Scaling laws for columnar structures in rotating turbulence

In the derivation of the scaling laws (2.10), (2.13),(2.21) and (2.23) we considered two flow regimes. The viscous regime, where $Re \ll 1$, and the inertial regime, where $Re \gg 1$. While there is a distinct difference to the applied inertial forces, characterized by Re_Q, and the local inertial forces, it is unlikely we will be able to observe the viscous regime with the current parameter regime where $Re_Q \geq 300$. We begin by evaluation of the characteristic velocity U as the velocity field induced by columnar structures ought to see very little change across these two regimes, according to (2.21) and (2.23).

5.1.1 Characteristic velocity U

Equations (2.21) and (2.23) show that the characteristic velocity induced by the columnar structures scales as $U \sim Q/\ell_\perp^2$. This can be non-dimensionalized in terms of the control parameter Re_Q as $Re_U \sim Re_Q$, where $Re_U = UL/\nu$. The U also showed a dependence on Ω, caused by the Ekman boundary layer forming along the bottom wall where the fluid is injected. It's effect ought to be observable when $Ek = \mathcal{O}(1)$, but considering $Ek \ll 1$ across the entire parameter range its effect on Re_U ought to be negligible. From experiments conducted along the horizontal planes we choose $U = \langle\sqrt{u_x^2 + u_y^2}\rangle$, where $\langle\cdot\rangle$ refers to an ensemble average across both spatial and temporal dimensions. We choose the distance between forcing points L as our characteristic length scale. Figure 5.1*a* shows Re_U across all experiments conducted along the horizontal planes at $h^* = 0.38$

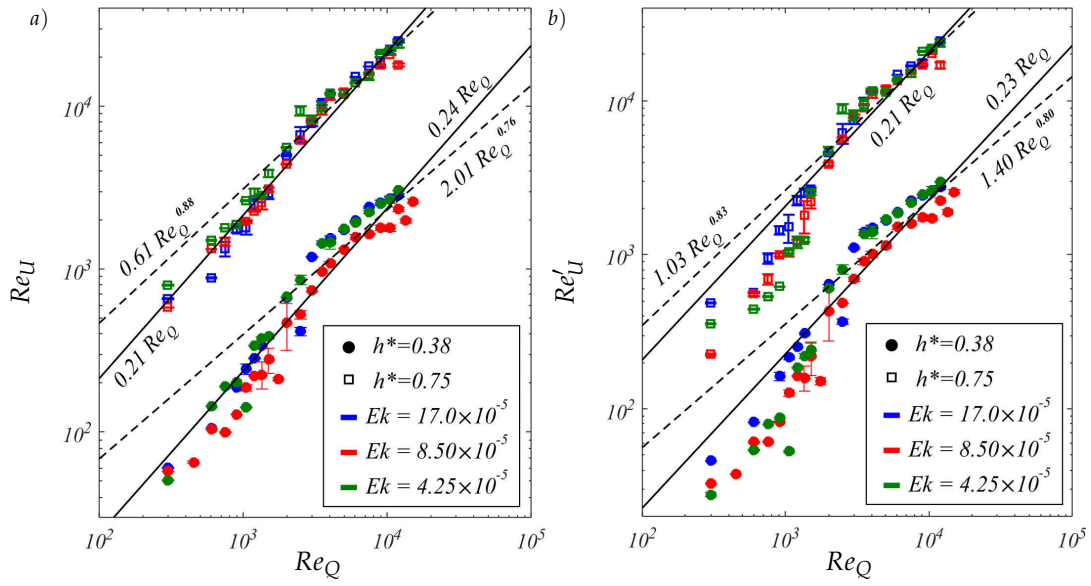

Figure 5.1: a) $Re_U = UL/\nu$, where $U = \langle\sqrt{u_x^2 + u_y^2}\rangle$ against Re_Q at various Ek. b) $Re'_U = U'L/\nu$, where $U' = \langle\sqrt{u_x'^2 + u_y'^2}\rangle$ against Re_Q at various Ek. Solid black lines shows a linear fit of the experimental data, dashed line shows a powerlaw fit of data where $Re_Q \geq 3000$. Data at $h^* = 0.75$ has been shifted up one order for visualization purposes.

and 0.75.

We see that along both planes Re_U scales a linearly with Re_Q and that there is no observable dependence on Ek. This linear dependence on Re_Q for Re_U tells us that the columnar structures that form develop under the combined influence of the Coriolis force and the viscous or inertial forces. As the linear dependence of Re_U on Re_Q applies to both the viscous and inertial regimes further investigation is required to establish whether viscous or inertial forces are opposing the Coriolis force induced by the horizontally divergent flow.

From figure 4.5 we know that $E \approx E'$ for $Re_Q \geq 1500$ which suggests that the fluctuating flow component closely follows the average flow. Figure 5.1*b* shows $Re'_U = U'L/\nu$, where $U' = \langle\sqrt{u_x'^2 + u_y'^2}\rangle$, against Re_Q. For $Re_Q \geq 1500$ we do observe a linear dependence of Re'_U on Re_Q. This implies that the forces that influence the development of the structures may not be static forces.

For all cases explored we see that around $Re_Q \approx 3000$ there is a bump in the Re_U profiles. This could indicate a transition to another dynamical regime where Re_U does not scale linearly with Re_Q. A fit of the experimental data for $Re_Q \geq 3000$ suggests both Re_U and Re'_U scale as $Re_Q^0.8$. $Re_Q = 3000$ roughly coincides with the transition to where the regime II dynamics are observed and the increase in turbulent intensity seen in fig.4.5, where $E'/E \approx 1$. Whether the observed

bump indicates a shift to a different dynamical regime or is a local phenomenon would require us to expand the Re_Q parameter range to see if the $Re_U \sim Re_Q^{0.8}$ constitutes a continuous trend.

5.1.2 Columnar structure length ℓ_z

From figures 4.9 and 4.10 we have seen that columnar structures develop over the turbulent patch and throughout the flow field. The structure length ℓ_z of these columnar structures is derived from experiments conducted along the vertical plane using two-point velocity correlation along the z-axis [59],[2].

The correlations function $C_u(\delta z)$ is calculated from velocity fields recorded along the vertical plane. Here δz is the separation between two points along the z-axis and C_u is given by,

$$C_u(\delta z) = \langle \int_A u_x(x, z+\delta z) u_x(x,z) dx dz \rangle_t \, . \tag{5.1}$$

Here A is the area of the flow field captured by the experiments along the vertical plane and $\langle \cdot \rangle_t$ is a temporal average. Correlations are calculated for the x-component of the velocity field as the z-component is strongly influenced by the presence of the upper boundary. These calculations are performed for full velocity field u_x and fluctuating flow component u_x'.

When a correlation function is derived, the characteristic length scale is determined by finding the first zero in $C_u(\delta z)$. However the $C_u(\delta z)$ found in our experiments remain well correlated until the upper wall is reached and no shift in ℓ_z could be seen from these results. A similar problem was encountered by Staplehurst *et al*. [59]. They circumvented this by first normalizing $C_u(\delta z)$ by $C_0 = C_u(0)$ and then using an artificial threshold β. When $C_u/C_0 = \beta$ at $\delta z = Z$ the lengthscale ℓ_z is determined by:

$$\ell_z = \int_0^Z \frac{C_u(\delta_z)}{C_0} dz \, . \tag{5.2}$$

Across all experiments we chose a constant value of $\beta = 0.5$. Figure 5.2 shows both ℓ_z and ℓ_z', based on u_x and u_x' respectively, as function Ro. With Ro based on U and U' measured along the horizontal plane at $h^* = 0.75$. Note that for $Ek = 34.0$ and 5.67×10^{-5}, no experiments along the horizontal plane were conducted. As such Ro was derived based on velocities measured at $Ek = 17.0 \times 10^{-5}$ and 8.50×10^{-5} respectively. This is justified as fig.5.1 shows a negligible influence of Ek on Re_U.

For $Re_Q < 2500$ neither ℓ_z or ℓ_z' follow any behaviour set by either (2.10) or (2.13), likely due to the local inertial forces resulting from Re_Q lying between the viscous and inertial regime. For $Re_Q \geq 2500$, which coincides with $Re_U, Re_U' \approx 600$, ℓ_z and ℓ_z' steadily decrease with increasing Ro.

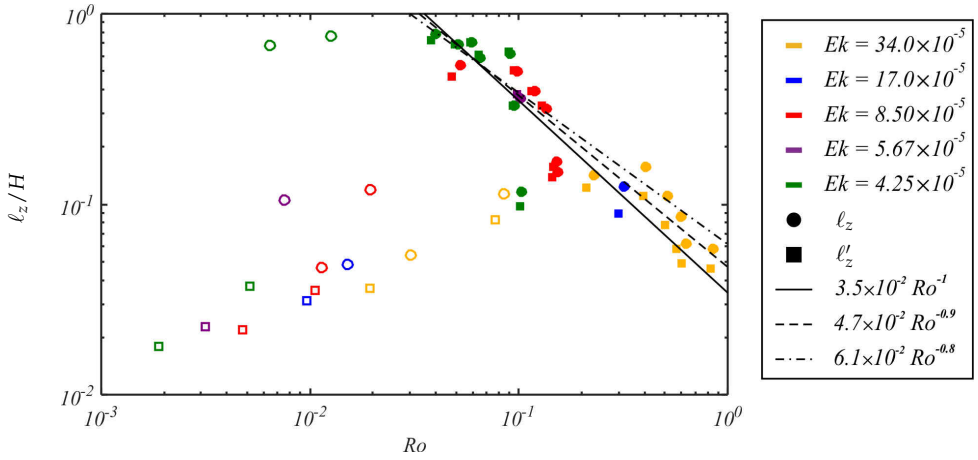

Figure 5.2: Columnar structure length ℓ_z measured across various Re_Q and Ek normalized by tank height H. Open symbols $Re_Q < 2500$, filled symbols $Re_Q \geq 2500$. Solid line shows a Ro^{-1} fit of data where $Re_Q \geq 2500$. Dashed line shows a $Ro^{-\alpha}$ fit ℓ_z and dashed-dotted line shows a similar fit for ℓ'_z where $Re_Q \geq 2500$.

Both a linear (solid black line) and power law (dashed lines) fit of the data shows good agreement with Ro^{-1} scaling proposed by (2.13) for both ℓ_z and ℓ'_z.

This, along with the results shown in fig.5.1, confirms that the columnar structures that are found form under the influence of both the Coriolis force and the inertia. However inertia can be associated to either the average flow or the fluctuating flow component and the results shown in figures 5.1 and 5.2 do not give a conclusive stance on either of these two types of inertia being the dominant force. To answer this question we move on to evaluate (2.27)-(2.29) and relative importance of each of their non-pressure terms. By doing this we can identify flow regimes where either the average flow, Coriolis force and/or fluctuations drives the anisotropy of the average flow.

5.2 The average flow equations

Exactly evaluating all the terms in (2.27) is not possible with the experimental data at hand. As was shown in section 3.3.2 an upperbound for these terms can be extracted from data across all three experimental planes. Similar methods are used to derive an upperbound for the non-pressure terms in (2.28). These upperbounds are highlighted by the superscript $|\cdot|^e$.

Figures 5.3*a*, *b* and *c* show the magnitude of theupperbound for the Coriolis term $|2\Omega\partial_z\langle u_z\rangle_t|^e$ and both fluctuating terms $|\langle \mathbf{u}'\cdot\nabla\omega'_z\rangle_t|^e$, $|\langle \boldsymbol{\omega}'\cdot\nabla u'_z\rangle_t|^e$ relative to the average inertial term $|\langle\mathbf{u}\rangle_t\cdot\nabla\langle\omega_z\rangle_t|^e$ of (2.27).

The viscous term $|\nu\Delta\langle\omega_z\rangle_t|^e$ is found to be significantly smaller than $|\langle\mathbf{u}\rangle_t\cdot\nabla\langle\omega_z\rangle_t|^e$ for all

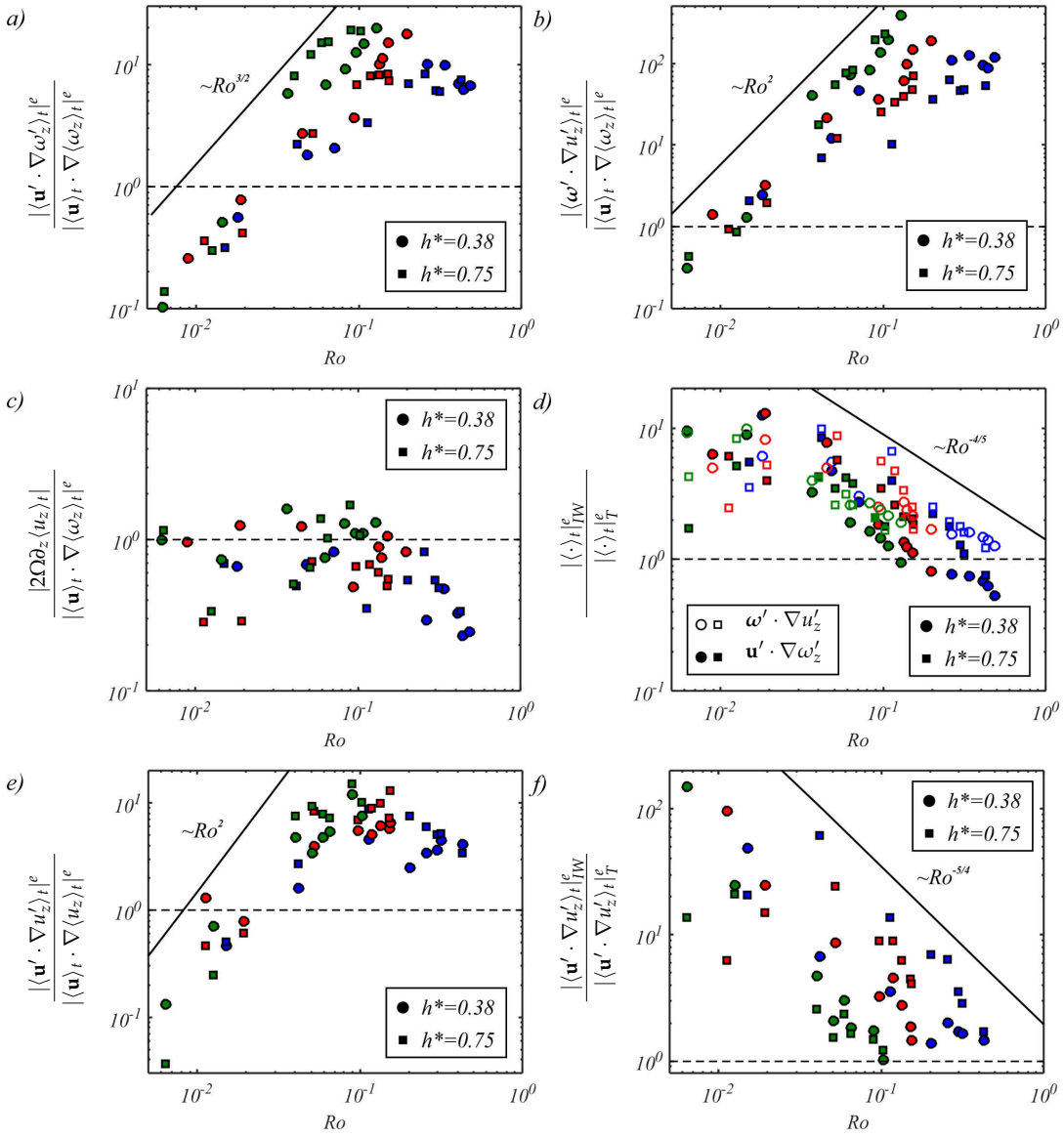

Figure 5.3: a,b,c) Ratio between the various terms of (2.27) and its average inertial term $|\langle \mathbf{u} \rangle \cdot \nabla \langle \omega_z \rangle|^e$. d) Ratio between the magnitude of inertial wave (IW) and turbulent (T) fluctuations to the overall fluctuating terms $|\langle \mathbf{u}' \cdot \nabla \omega_z' \rangle_t|^e$ and $|\langle \boldsymbol{\omega}' \cdot \nabla u_z' \rangle_t|^e$ in (2.27). e) Ratio between the fluctuating term $|\langle \mathbf{u} \cdot \nabla u_z \rangle_t|^e$ of (2.28) and its average inertial term $|\langle \mathbf{u} \rangle_t \cdot \nabla \langle u_z \rangle_t|^e$. f) Ratio between the magnitude of inertial wave (IW) and turbulent (T) fluctuations to the overall fluctuating term $|\langle \mathbf{u}' \cdot \nabla u_z' \rangle|^e$ in (2.28). For all graphs (blue) $Ek = 17.0 \times 10^{-5}$, (red) $Ek = 8.50 \times 10^{-5}$ and (green) $Ek = 4.25 \times 10^{-5}$. Note: Solid lines show an approximate scaling with Ro of the trends observed. No physical reason was found for any of these scalings.

experimental parameters. This is unsurprising as we are operating in flow regimes where $Re \sim Re_Q \gg 1$. The viscous term is neglected in the rest of the analysis.

As was shown in chapter 4, by separating the fluctuations based on their frequency, relative to the cut-off frequency for inertial waves into the IW-range and T-range, we can isolate the contributions made to $|\langle \mathbf{u}' \cdot \nabla \omega_z' \rangle_t|^e$ and $|\langle \boldsymbol{\omega}' \cdot \nabla u_z' \rangle_t|^e$ due to random turbulent fluctuations (subscript $|\cdot|_T$) and those ,in large part, due to inertial waves (subscript $|\cdot|_{IW}$). For clarity, for remainder of this chapter, we refer to fluctuations within the IW-range as inertial waves, with the caveat that within this range there also exist random turbulent fluctuations. Figure 5.3*d* shows that across almost all parameter space, and in particular for $Ro < 0.1$, contributions to the fluctuating terms due to inertial waves outweigh the contributions by random turbulent fluctuations. Which allows us to state:

$$|\langle \mathbf{u}' \cdot \nabla \omega_z' \rangle_t|^e_{IW} \approxeq |\langle \mathbf{u}' \cdot \nabla \omega_z' \rangle_t|^e ,$$
$$|\langle \boldsymbol{\omega}' \cdot \nabla u_z' \rangle_t|^e_{IW} \approxeq |\langle \boldsymbol{\omega}' \cdot \nabla u_z' \rangle_t|^e .$$

Figure 5.3*a*, *b* and *c* show that at $Ro \approx 0.02$ all terms in (2.27) are of comparable magnitude. Figure 5.3*a* and *b* show that both fluctuating terms scale as Ro^2 up until $Ro \approx 0.1$ where they saturate around value of 10 to 100. This regime roughly coincides with the point where the relative energy carried by inertial waves (figure 4.18) drops significantly. No physical reason has been found for this Ro^2 scaling.

In figure 5.3*c* we see that the Coriolis term $|2\Omega \partial_z \langle u_z \rangle_t|$ remains of equal magnitude to $|\langle \mathbf{u} \rangle_t \cdot \nabla \langle \omega_z \rangle_t|^e$ up to $Ro \approx 0.1$ where is appears to gradually decrease. This decrease is expected as Ro approaches 1, the effect of the Coriolis force ought to diminish.

Figures 5.3*e* and *f* show similar comparisons for the non-pressure terms in (2.28). The viscous term $|\nu \Delta \langle u_z \rangle_t|^e$ is again negligible compared to the average inertial term $|\langle \mathbf{u} \rangle_t \cdot \nabla \langle u_z \rangle_t|^e$ and the fluctuating term $|\langle \mathbf{u}' \cdot \nabla u_z' \rangle_t|^e$ throughout the entire parameter regime.

Figure 5.3*f* shows, similarly to fig.5.3*d*, that across all parameter contributions to $|\langle \mathbf{u}' \cdot \nabla u_z' \rangle_t|^e$ are largely due to inertial waves and we can state,

$$|\langle \mathbf{u}' \cdot \nabla u_z' \rangle_t|^e_{IW} \approxeq |\langle \mathbf{u}' \cdot \nabla u_z' \rangle_t|^e .$$

Both figures 5.3*d* and *f* show that the contribution of inertial waves to the overall fluctuating terms diminishes at a rate of approximately Ro^{-1}. This strong dependence on Ro again shows that the fluctuations within the IW-range are most likely due to inertial waves. No physical reason has been found for the Ro^{-1} scaling.

Figures 5.3*e* shows that $|\langle \mathbf{u}' \cdot \nabla u_z' \rangle_t|$ scales as Ro^2 up to $Ro \approx 0.1$ where it saturates at a value of around 10. Furthermore we see that at $Ro \approx 0.02$ all non-pressure terms in (2.28) are of equal magnitude. Overall this shows a very similar story to what was observed for the terms in (2.27).

From figure 5.3 we can asses the following. First, for $Ro \gtrsim 0.1$ the anisotropy of the average flow, governed by (2.27)-(2.29), is set in large part by the fluctuating flow component. As Ro approaches 1 the influence of the Coriolis force diminishes while the fluctuating component of the flow will be dominated by turbulent fluctuations. As such; we refer to the flow regime where $Ro \gtrsim 0.1$ as the *weakly rotating regime*.

For $0.02 \lesssim Ro < 0.1$ the anisotropy of the average flow is set by a balance between the average flow and fluctuating flow, where the fluctuations are almost entirely set by inertial waves. This allows us to rewrite (2.27) to give the following balance:

$$\langle \mathbf{u} \rangle_t \cdot \nabla \langle \omega_z \rangle_t \cong \langle \boldsymbol{\omega} \rangle_t \cdot \nabla \langle u_z \rangle_t + \langle \boldsymbol{\omega}' \cdot \nabla u_z' \rangle_{t,IW} - \langle \mathbf{u}' \cdot \nabla \omega_z' \rangle_{t,IW} \,. \tag{5.4}$$

The Coriolis force still plays an important role, but it manifests itself through the full fluctuation equations (2.24)-(2.26). We call this rotation dominated turbulent flow regime where, $0.02 \lesssim Ro < 0.1$, the *inertial wave regime*.

Interestingly for $Ro \lesssim 0.02$ and $Ro \to 0$ the magnitude of the fluctuation terms in (2.27) and (2.28) quickly diminishes and the anisotropy of the average flow is governed by a balance between the inertia of the average flow and the Coriolis force. This regime we call the *Coriolis regime*. Figure 5.4 gives a sketch of the three flow regimes identified based on the experimental parameter range. Across all experiments we see that these flow regimes have a minor dependency on h^*. The separation between the Coriolis and inertial wave regime is dependent on the relative magnitude of the inertial wave fluctuations. As inertial wave propagate energy efficiently across all h^*, as seen in figure (4.16), their magnitude remains almost constant and so the separation between the Coriolis and inertial wave regimes is expected to remain nearly uniform across h^*. The separation between the inertial wave regime and the weakly rotating turbulence regime depends on the relative magnitude of the turbulent fluctuations. As was seen in figure (4.18) turbulent fluctuations are less efficient at carrying energy away from the bottom wall and as such they decay significantly as h^* increases. This would mean that the separation between the inertial waves regime and the weak rotating turbulence regime gets pushed to greater Re_Q and Ek as h^* increases. This dependency of the flow regimes on h^* was recovered from experiments and can be seen in figure (5.4).

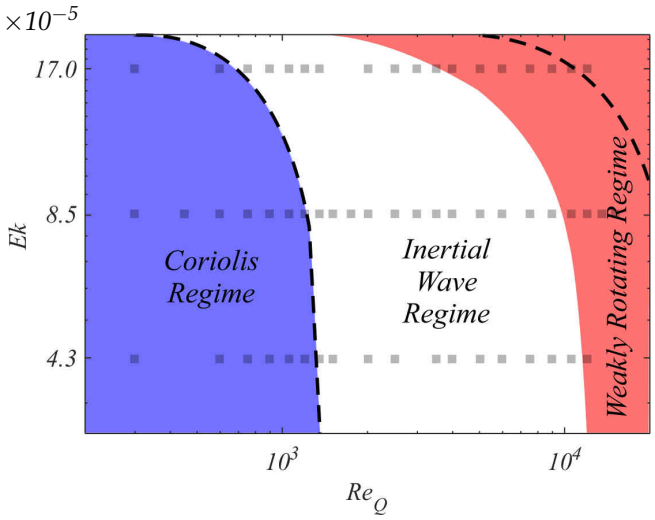

Figure 5.4: Sketch of the various flow regimes as function of Re_Q and Ek, where different mechanisms govern the anisotropy of the average flow. Coloured regions correspond to results at height of $h^* = 0.38$ while dashed lines correspond to a height of $h^* = 0.75$

In the Coriolis regime (2.28) and (2.30) can be combined an rewritten to give,

$$\langle \mathbf{u} \rangle_t \cdot \nabla \langle u_z \rangle_t = 2\Omega \Delta^{-1} \partial_z \langle \omega_z \rangle_t + TF \,. \tag{5.5}$$

Where TF is a term due to fluctuations that are not due to inertial waves. When combined with (2.27) this gives,

$$(\langle \mathbf{u} \rangle_t \cdot \nabla)^2 \langle \omega_z \rangle_t \langle \mathbf{u} \rangle_t \cdot (\langle \boldsymbol{\omega} \rangle_t \cdot \nabla \langle u_z \rangle_t) \approxeq 4\Omega^2 \Delta^{-1} \partial_{zz} \langle \omega_z \rangle_t + 2\Omega \partial_z (\langle \mathbf{u} \rangle_t \cdot \nabla \langle u_z \rangle_t) + TF \,. \tag{5.6}$$

The term $2\Omega \partial_z (\langle \mathbf{u} \rangle_t \cdot \nabla \langle u_z \rangle_t)$ on the RHS of (5.6) corresponds to the Coriolis force. It can be broken down into two separate components, $|\partial_z \langle \mathbf{u} \rangle_t \cdot \nabla \langle u_z \rangle_t|$ and $|\langle \mathbf{u} \rangle_t \cdot \nabla \partial_z \langle u_z \rangle_t|$. The latter of these two components could be diffusive in nature due to its second spatial derivative. The current experiments do not allow us to determine whether the 'diffusive' component of the Coriolis term is in fact diffusive or propagative in nature, but by comparing the magnitude of the two components we can establish their relative importance. For both terms we compute and upperbound in a similar fashion to what was done for the terms in (2.27) and (2.28). Figure (5.5) shows the relative magnitude of these two terms. Across all parameter space $|\langle \mathbf{u} \rangle_t \cdot \nabla \partial_z \langle u_z \rangle_t|^e > |\partial_z \langle \mathbf{u} \rangle_t \cdot \nabla \langle u_z \rangle_t|^e$ and the results do not suggest this will change as $Ro \to 0$. This at the very least establishes that the 'diffusive' component of the Coriolis term is of significant importance.

The anisotropy of the average flow in the Coriolis regime is given by (5.5) and (5.6). Our experimental results show evidence that in the limit of $Ro \to 0$ time-dependent inertial waves play

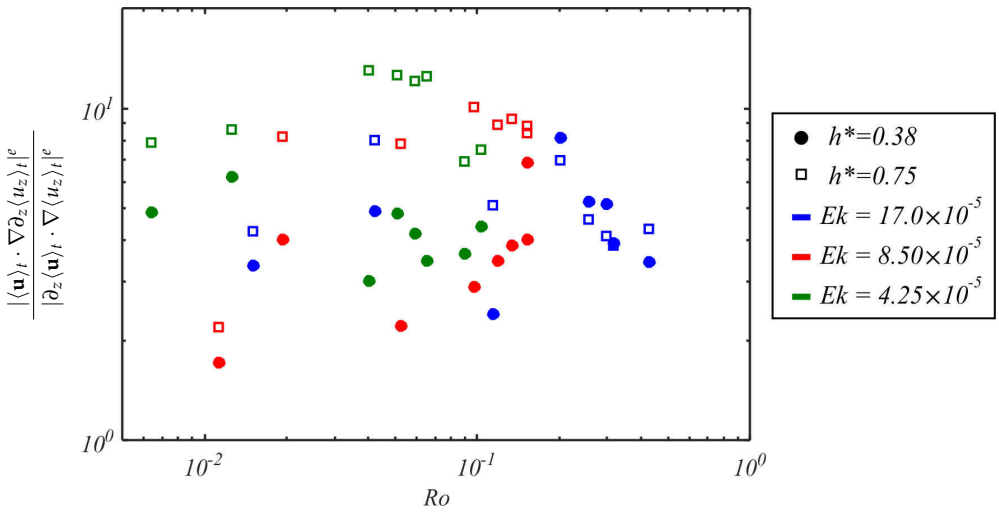

Figure 5.5: Ratio between the magnitude of the two components of the Coriolis term $2\Omega\partial_z(\langle \mathbf{u} \rangle_t \cdot \nabla \langle u_z \rangle_t)$ in (5.6).

no part in the mechanism driving the anisotropy of the average flow. The mechanism driving the anisotropy of the average flow for a rotating turbulent flow is similar to that of the one driving the formation of Taylor columns. In both cases anisotropy is materialised by a horizontally divergent flow, which is either driven by viscous friction (Taylor columns) or by inertia (turbulence).

If we consider (2.13) in the limit of $Ro \to 0$ then $\ell_z^I \to \infty$ across all scales $\ell_\perp$, implying the flow becomes quasi-two dimensional down to the smallest horizontal viscous scales. This would also imply that the inertial waves are not responsible for the two-dimensionalisation of the average flow either.

5.3 Summary

In this chapter it was shown that the length of the columnar structures found (figure 5.2) and the velocity fields these structures induce (figure 5.1) closely follow the scaling laws proposed for the inertial regime (2.13) and (2.23). This showed us that the columnar structures form as a result of a balance between inertial forces and the Coriolis force. As the local inertial forces result in $Re > 1$ across all experiments no evidence could be found for the scaling laws proposed for the viscous regime.

Closer examination of the terms in (2.27) and (2.28) revealed (fig.5.3) that the balance between inertia and Coriolis force, which governs the mechanism driving the average flow's anisotropy, gradually shift from one where the inertia is associated to the fluctuating flow to one where it is associated to the average flow, which resulted in three flow regimes being identified (fig.5.4).

In the inertial wave regime and the weakly rotating regime the anisotropy of the average flow constitutes a balance between the average flow inertia and that of the fluctuating flow. In the inertial wave regime ($0.02 \lesssim Ro < 0.1$) these fluctuations are largely due to inertial waves, while in the weakly rotating regime ($Ro \gtrsim 0.1$) these are increasingly due fluctuations that are not inertial waves. In the Coriolis regime ($Ro \lesssim 0.02$) the influence of the inertial waves rapidly diminishes and in the limit of $Ro \to 0$ we identified a mechanism for the average flow anisotropy, governed by (5.5) and (5.6), in which inertial waves play no part.

We now understand what mechanism drives a rotating turbulent flow field while it is operating under statistically steady conditions. But what mechanism drives the development of such a flow from an initially still state in solid body rotation, especially in the earliest stages? This question in addressed in the following chapter.

Chapter 6

Spatial development of a rotating transient turbulent flow field

In the current chapter, we present the results obtained from our experiments whilst it transitions from an initially still state, in which the system is operating under solid-body rotation, to the statistically steady state discussed in previous chapters.

In rotating turbulent flows the spatial development of the flow field is commonly studied by tracking the translation of the turbulent front, i.e. the part of the flow field that is gradually set in motion as the specific forcing mechanism is initiated. Both Davidson *et al*. [15] and Kolvin *et al*. [29] showed that when the Coriolis force is strong (i.e. $Ro < 1$) the translation of the turbulent front is driven by a propagative mechanism driven by Linear Inertial Waves (LIW). Where structures propagate at a velocity comparable to that of the group speed of inertial waves $U_{IW} = 2\Omega d$, where d is the characteristic size of the structure. This ensures large scale structures propagate faster than small scale structures. Dickenson & Long [17] observed a transient behaviour where the front would initially translate at a rate of $\sqrt{t}$ with time t when the Coriolis force was relatively weak ($Ro \geq 1$) to a propagation speed that would scale linearly with t when $Ro < 1$, suggesting propagation by inertial waves.

As LIW theory [24] is scale dependent the transient behaviour is likely to be scale dependent as well. Here we seek to explore this scale-dependency of the transient behaviour in greater detail. Our experimental setup is uniquely qualified for this as the presence of the turbulent patch under statistically steady flows conditions shows our flow field transitions from a region dominated by inertia to one dominated by the Coriolis force.

This chapter is divided into three sections. In the first the method by which the experimental

data is analysed is explained. In the second the development of the flow field in the absence of a Coriolis force is explored. As the spreading of the turbulent front transitions away from this behaviour as the Coriolis force is introduced an understanding of this advection driven mechanism is required. In the third section we explore the effect of the Coriolis force on the spreading of the turbulent front. We find that the mechanism transitions from one driven by advection (inertia) to propagation mechanism driven by LIW theory.

In this chapter we used the transient experiment, explained in section 3.2.1, to conduct our measurements. Here the experimental setup is brought to a state of solid body rotation and the flow field is recorded upon initiating the forcing mechanism. Experiments are presented using the same control parameters and variables as in chapter 4, additionally the same mathematical operators and subscripts are used as well. Where necessary these will be highlighted again. Experimental noise is reduced by running the experiment five times per set of control parameters and averaging the resultant velocity fields across each measurement.

6.1 Experimental detection of the turbulent front

When the spreading of the turbulent front is set by LIW theory there is a scale-dependency on the spreading speed. In order to highlight this dependence we apply a similar analysis method to that of Kolvin *et al*. [29] to the velocity fields found in experiments conducted along the vertical plane centred on a source/sink pair. The method will be briefly explained here.

We start from the velocity field $\mathbf{u}(x,z,t)$, where x and z correspond to the axes perpendicular and parallel to the axis of rotation, respectively. For any velocity field $\mathbf{u}(x,z)$ at any time t a Fourier transform is applied along the x-axis, generating a scale dependent field $\mathbf{u}(k,z)$, where k is the wavenumber associated to a particular scale. The Fourier transform is performed using the *fft.m* function in Matlab. From $\mathbf{u}(k,z)$ an energy spectra $E(k,z) = |\mathbf{u}(k,z)^2|$ is calculated. This operation is then performed for each timestep t, giving us $E(k,z,t)$. From $E(k,z,t)$ temporal energy profiles $E(t)$ can be obtained by fixing z and k. In the rest of the chapter z is non-dimensionalized by the height of flow field H, giving $z^* = z/H$.

Figure 6.1*a* and *b* show $E_i(t)$ for two modes k_i, where $k_{i+1} > k_i$. The energy profiles shown are for an experiment conducted in the absence of background rotation at $z^* = 0.38$ and subject to background rotation at $z^* = 0.63$. For each $E_i(t)$ profile we see that it transitions from an initially low energy state to high energy state. When $E_i(t)$ passes a threshold value between these two states we say that mode k_i has arrived at z^* at the arrival time τ_i.

This threshold value is set by taking the average between the low energy state, calculated from velocity field recorded prior to the initiation of the forcing mechanism, and the high energy state,

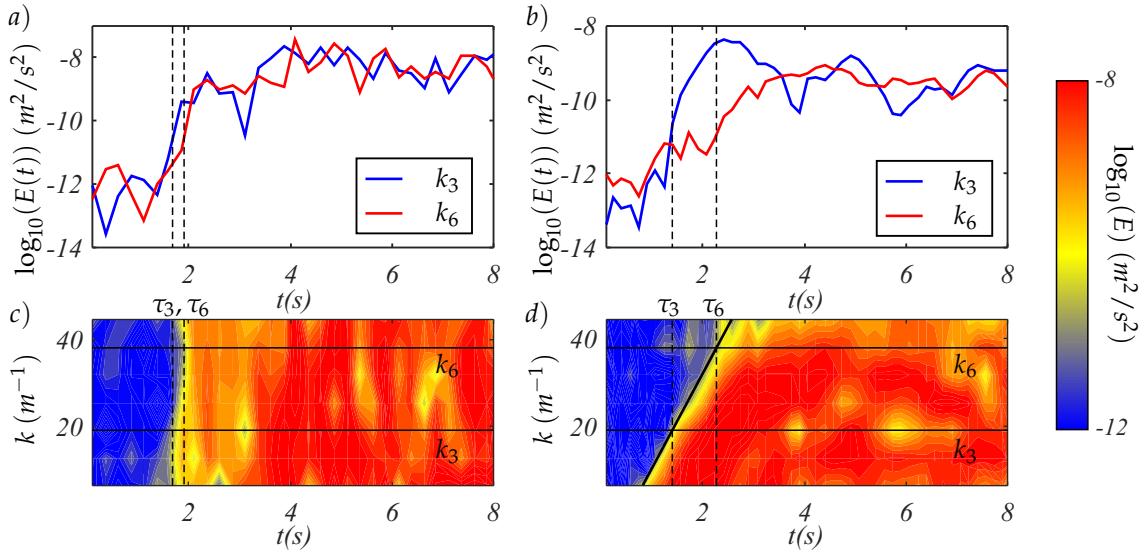

Figure 6.1: a,b) Temporal energy profiles $E(k_\perp, t)$ for modes $k_{\perp,3}$ and $k_{\perp,6}$. c,d) Contourplots of $E(k_\perp, t)$. Experiments conducted at a,c) $Ek = \infty$, $Re_Q = 2500$, $z^* = 0.38$ and b,d) $Ek = 4.25 \times 10^{-5}$, $Re_Q = 2500$, $z^* = 0.63$. Arrival times (τ_3, τ_6) are represented by dashed lines. d) Solid black line shows contour shape predicted by LIW theory.

calculated from velocity field recorded after the entire flow field is excited. The arrival times for modes k_i are indicated by the dashed lines in figure 6.1

From figure 6.1*a* we see that for the non-rotating experiment modes k_3 and k_6 arrive at $z^* = 0.38$ at roughly the same time $t \approx 2$ seconds. Figure 6.1*b* shows that for the rotating experiments there is a strong k-dependence on the arrival times τ_3 and τ_6. Mode k_3 arrives at $z^* = 0.63$ in $t \approx 1.5$ seconds while k_6 arrives in $t \approx 2.2$ seconds. By performing this analysis across all z^* the translation of each separate mode k_i can be tracked.

The experimental noise in the early stages of flow build-up close to the bottom wall remains relatively high across all experiments conducted. For experiments the τ acquired at $z^* < 0.2$ are likely overestimates from the actual arrival times. Finally, the translation can be visualized by plotting contours of $E(k, z^*, t)$ as is done in figure 6.1*c* and *d* for the same two experimental cases as before. If the translation is independent of k then the contours appear as almost vertical lines. When there is a k-dependence the contours appear slanted. Based on LIW theory we can predict the shape of the contours assuming the translation is fully driven by inertial waves. In the results presented in this chapter this is done by plotting a solid black line as is done in figure 6.1*d*.

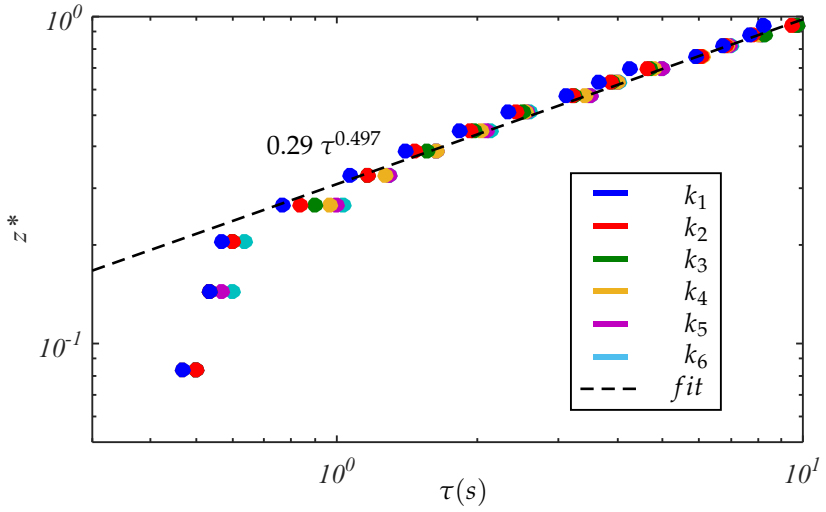

Figure 6.2: Arrival time τ at height z^* for the first six modes k_i at $Re_Q = 2500$ in the absence of rotation ($Ek = \infty$). Translation is independent of the wavenumber k when $Ek = \infty$. Dashed line is a power law fit of the experimental data for $z^* \geq 0.2$.

6.2 Translation in the absence of background rotation

Consider a jet entering into a quiescent field in the absence a Coriolis force. As the jet moves into the field its front propagates at a speed set by the initial jet velocity U_J and then gradually slows down as the front moves a distance z away from its point of origin. The gradual decrease of the translation velocity occurs because the jet spreads and momentum is lost. As our forcing mechanism consists in part of two jets, it likely behaves in a similar fashion to that of a single jet flow. Review of the literature did not reveal any studies suggesting a potential k-dependence on the translation of the turbulent front for a single jet. Nor was there any suggestion in the literature on steady jets [48] to suggest a k-dependence on its characteristics such as the translation of jets or the decay of the axial velocity.

Figure 6.2 shows $z^*(\tau)$ for $Re_Q = 2500$. The first six modes with wavenumber k_i are shown. This behaviour is representative for all Re_Q explored. The arrival time τ appears independent of k. For $z^* \geq 0.2$ the $z^*(\tau)$-profile roughly scales as $\sim \sqrt{\tau}$. Figure 6.3*a* shows $z^*(\tau)$ for all Re_Q explored in absence of background rotation. Here $z^*(\tau)$ is taken as an average over the first six modes $k_{\perp,i}$. The greater Re_Q the lower the value of τ for a given height z^*. This is expected as $Re_Q = 4Q/\pi\nu d = U_J d/\nu$. It has been shown [48] that a single steady turbulent jet is self-similar with regards to the jet Reynolds number Re_Q. By multiplying τ by Re_Q, as seen in figure6.3*b*, we see that all data collapses almost onto a single curve. This shows that, in our experimental range for Re_Q, the non-dimensional translation velocity of the turbulent front is exclusively dependent on Re_Q, which suggest the development of the turbulent flow in its earliest stages may be self-

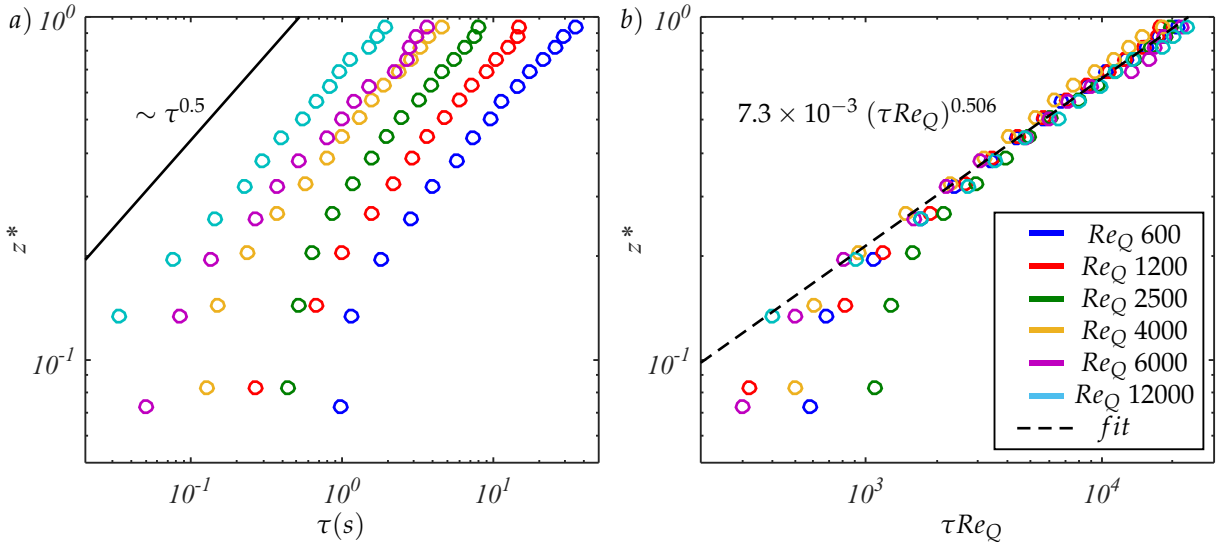

Figure 6.3: a) Arrival time τ at height z^* at $Ek = 4.25 \times 10^{-5}$ across all Re_Q, taken as the average across first six modes k_i. Black line shows a $\sqrt{\tau}$ scaling. b) Arrival time multiplied by Re_Q, where $Re_Q \sim U_J$, causing data to collapse onto single curve for $z^* \geq 0.2$, showing translation is similar to that of a single jet where $h(t) \sim \sqrt{U_J t}$. Dashed line is an fit of data where $z^* \geq 0.2$

similar as well. From figures (6.2) and (6.3) we can conclude that in our experiment the translation of the turbulent front in the absence of a Coriolis force is advection driven and scales as:

$$z^*(\tau) \sim \sqrt{Re_Q \tau}\,. \tag{6.1}$$

6.3 Translation subject to background rotation

Figure 6.4 shows the energy contours of $E(k,t)$ at various z^* at $Re_Q = 2500$ across all Ek explored. Additional contour plots at various control parameters Re_Q and Ek along the vertical plane are presented in Appendix A, showcasing behaviour consistent with the results presented here.

What we see across all three cases explored here is that the spreading of the jet initially is independent of k and thus advection driven. As z^* increases we see a gradual shift towards the propagative mechanism of LIW theory. This shift towards LIW theory occurs sooner for small k than for large k.

For $Ek = 17.0 \times 10^{-5}$ (figure 6.4a) the contour for all modes $k > 20$ remain vertical which shows that all modes translate at an equal velocity. For modes $k < 20$ we see the contour progressively become more slanted, which shows these modes are translating faster. These modes tend towards the mechanism predicted by LIW theory and at $z^* = 0.75$ they almost exactly follow the predicted behaviour. This transient behaviour can also be seen for the other two cases presented, with more

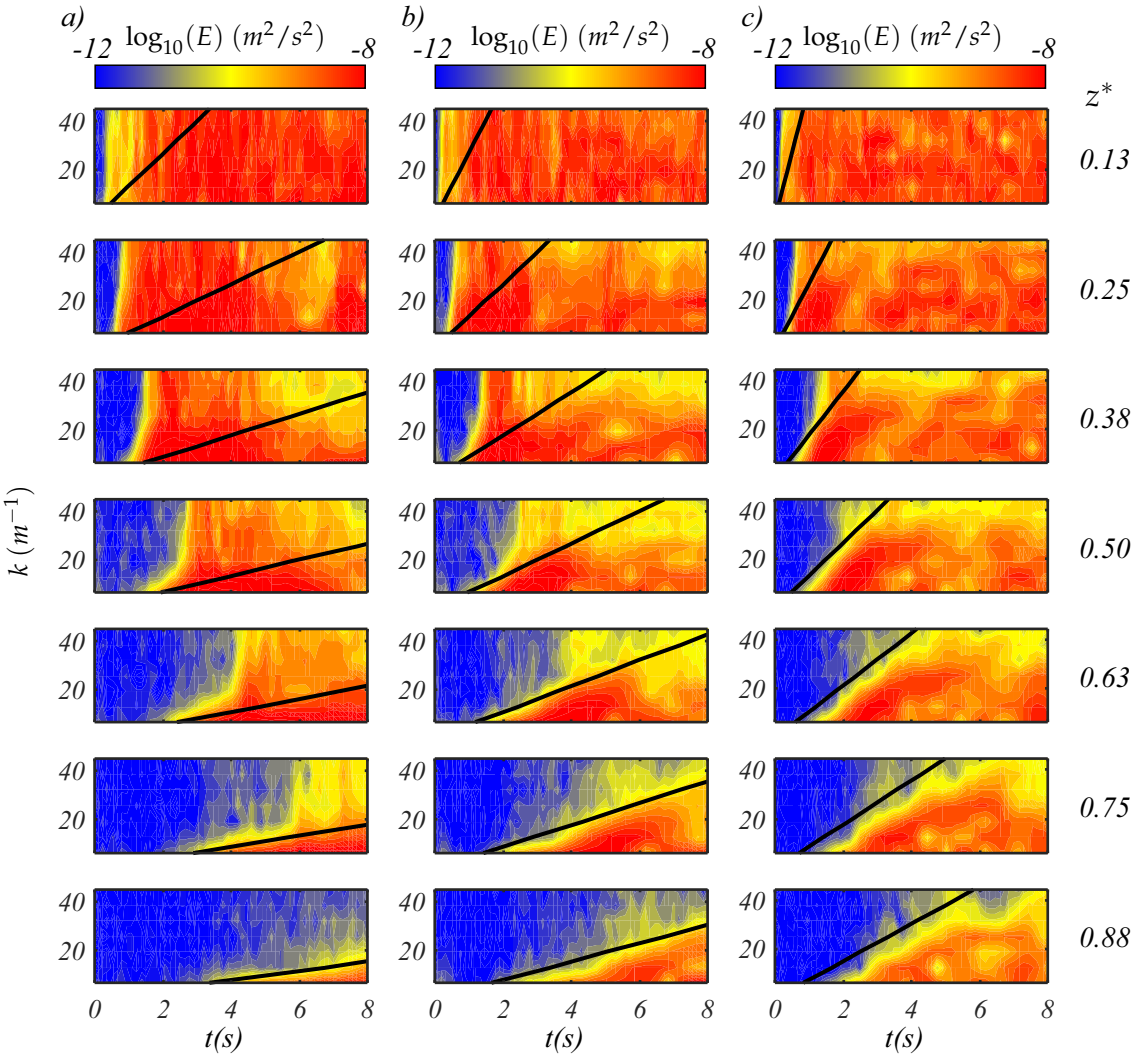

Figure 6.4: Contourplots of $E(k,t)$ across a number of heights z^* at a) $Ek = 17.0 \times 10^{-5}$, b) $Ek = 8.50 \times 10^{-5}$ and c) $Ek = 4.25 \times 10^{-5}$. Solid black lines represent the predicted shape of the contours assuming propagation is fully driven by LIW theory.

modes being affected and the transition to LIW theory occurring at lower z^* as Ek is reduced. The transient behaviour can always be seen to occur first for the smallest modes k.

In the absence of rotation the spreading velocity of the front would decay to zero as $z \rightarrow \infty$, with no k-dependence. But as figure 6.4 suggests, when a Coriolis force is introduced the translation velocity decays until it reaches a lower bound. At this point the translation velocity remains almost constant.

To explain the behaviour seen in figure 6.4 we propose that the Coriolis force introduces a lower bound for the translation velocity of the turbulent front, which is set by the group speed of inertial waves $U_{IW}(k) = 2\Omega/k$ [24]. We introduce a local Rossby number Ro^* based on the ratio between a characteristic translation velocity U representative of the inertial forces and the Coriolis force at scale k^{-1},

$$Ro^* = Uk/2\Omega = U/U_{IW} \, . \tag{6.2}$$

While $Ro^* > 1$ the inertial forces are too great to be affected by the Coriolis force and thus the front spreads through advection as if no Coriolis force were present. Due to the limited number of experimental runs, determining the exact translation velocity of the front $U(z)$ from our results has proven to be difficult. At the time of writing this problem has not yet been resolved. If however we assume that the spreading velocity decays inversely with z, similar to that of a single steady jet, given by $U(z) \sim U_J d/z$ then (6.2) gives:

$$Ro^* \sim \frac{U_J d}{z} \frac{k}{2\Omega} \, . \tag{6.3}$$

Eq.(6.3) does not provide the exact representation for Ro^* in our specific experiment, but it can be used to illustrate the behaviour seen in figure 6.4. Consider an arbitrary mode excited through a jet with wavenumber k, potential group speed $U_{IW}(k)$ and initial velocity $U_J > U_{IW}$. Initially $Ro^* > 1$, but gradually due to loss of momentum and spreading of the jet U decreases and so Ro^* tends to unity. When Ro^* reaches unity the Coriolis force is able to sustain mode k in the form of an inertial wave with group speed $U_{IW}(k)$ and so mode k propagates according to LIW theory. Suppose we fix k, U_J and Ω, then (6.3) shows that increasing z will reduce Ro^*. Equation (6.3) shows that the height z where $Ro^* = 1$ will decrease when Ω is increased or k is decreased. This is in line with the behaviours observed in figure 6.4.

Eq.(6.3) tells us that for a fixed Ω reducing U_J ought to ensure any mode k will propagate according to LIW theory at a lower z^*. We test this by fixing $Ek = 4.25 \times 10^{-5}$ and changing Re_Q.

Figure 6.5*a* shows $z^*(Re_Q\tau)$ profiles for the first mode k_1 for various Re_Q at $Ek = 4.25 \times 10^{-5}$. Only the first mode is shown as the associated Ro^* ought to be closer to unity, so the transition from an advective mechanism to a propagative mechanism ought to be more visible. The τ are

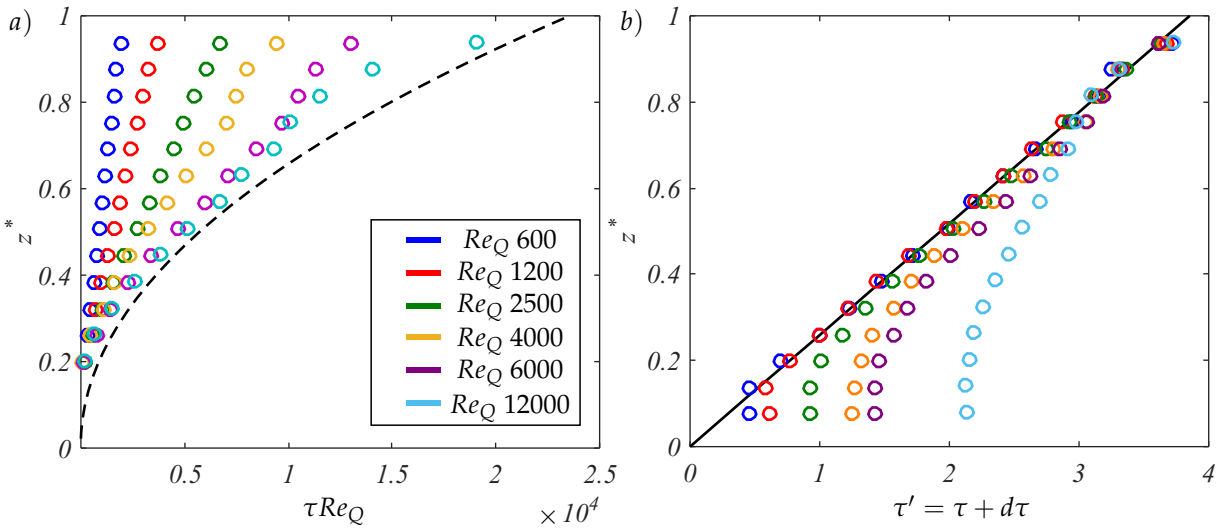

Figure 6.5: a) Arrival time τ at height z^* for first mode k_1 at $Ek = 4.25 \times 10^{-5}$. τ is multiplied by Re_Q to illustrate deviation from the non-rotating propagation. Dashed line is the experimental fit found in fig.6.3. b) Black line represent arrival time τ_{IW} at z^* for pure LIW propagation of mode k_1. τ for experiments compensated by timestep $d\tau$ such that at $z* = 0.93$, $\tau' = \tau_{IW}$.

multiplied by Re_Q to more clearly identify when the rotating experiment deviates from the non-rotating case explored earlier.

From figure 6.5*a* it can be seen that for low Re_Q the front translates significantly faster for the rotating experiments. At $Re_Q = 12000$ there is little difference between the rotating and non-rotating experiment with a deviation from the non-rotating profile occurring when $z^* > 0.6$. As expected the deviation occurs at lower z^* when Re_Q is reduced.

Finally it is assumed that the translation velocity of the turbulent front decays to a lower bound set by the group speed of inertial waves. This velocity would therefore scale linearly with τ. This is tested as follows, for mode k_1 we derive a group speed $U(k_1) = 2\Omega/k_1$ and compute the theoretical arrival time τ_{IW} at z^* assuming full LIW propagation across the entirety of z^*. For experiments τ is compensated by a timestep $d\tau$ such that at $z^* = 0.93$, $\tau' = \tau + d\tau = \tau_{IW}$.

The black line in figure 6.5*b* represent τ_{IW}. When experimental datapoints fall below this line the translation of mode k_1 is faster than that predicted by LIW theory. For $Re_Q = 600$ we see that k_1 initially translates faster but then almost immediately propagates according to LIW theory. This transition occurs at greater z^* as Re_Q is increased. For $z^* > 0.8$ mode k_1 propagates according to LIW theory across all Re_Q. This transient behaviour can be seen across all Ek and Re_Q as was seen in figure 6.4, lower Ek or Re_Q imply a more rapid transition to LIW propagation for any mode $k_\perp$.

6.4 Summary

The translation of the turbulent front is characterized by $z^*(\tau)$. In the absence of background rotation there is no observable dependence of $z^*(\tau)$ on the wavenumber k (fig.6.2) and $z^*(\tau)$ scales as $\sqrt{Re_Q \tau}$ (fig.6.3) similar to the behaviour of a single turbulent jet.

When subjected to background rotation the translation of the front becomes k-dependent (fig.6.4), with smaller k modes translating faster than larger modes.

Initially a mode k translates due to advection as the local inertial forces are too great to be affected by the Coriolis force, but gradually the translation velocity and the associate inertial forces diminish and the mechanism driving the translation of mode k transitions to a propagative mechanism set by LIW theory. To illustrate this we introduced Ro^* in (6.2) and (6.3).

It is assumed that while $Ro^* > 1$ the mechanism driving the translation of mode k is advection driven and when $Ro^* = 1$ the Coriolis force is able to sustain mode k as an inertial wave propagating according to LIW theory.

Though it is based on the vertical velocity profile of a steady jet (6.3) could be used to illustrate the behaviour seen across our experiments (fig.6.4). Where either an increase in Ω and/or z or a decrease in U_J and/or k would promote the transition to the propagative mechanism. The most important aspect of (6.2) and (6.3) is that the transient behaviour from a mechanism governed by advection to one governed by LIW theory is itself k-dependent.

This transient behaviour could not be seen by Kolvin *et al*. [29] as the flow regimes they explored had a far stronger Coriolis force and weaker applied inertial forces with $Ek \lesssim 1.1 \times 10^{-5}$ and $Re_Q \lesssim 1300$, ensuring an almost immediate transition to LIW theory for all modes k.

At the time of writing this thesis additional experiments and analysis was required to validate the behaviour set out by (6.2). This analysis has been performed during the review stage of my thesis and it was found that indeed there is a transition from an advective to propagative mechanism when the local Ro^* reaches unity. Furthermore it was found that rotation suppresses the strength of advection as well. These results and subsequent publication can be found in Appendix B.

Chapter 7

General conclusions and outlook

In the present thesis we added to the understanding on the interplay between inertial waves and 3D and 2D turbulent dynamics. In this thesis we explored the influence of the inertial waves in the context of the flow topology of jet-induced turbulence, the promotion of anisotropy in a rotating turbulent flow field and the spatial development of a transient turbulent flow field.

In the experiment an inhomogeneous turbulent flow field is continuously forced through a pair of jets and sinks at a bottom wall of a tank, hence the name, jet-induced turbulence. In Chapter 4 it is shown that under statistically steady conditions a 3D turbulent patch forms near the point of fluid injection. It forms due to characteristic velocities being large and length scales being small leading to a local $Ro > 1$. Atop this patch, where $Ro < 1$, a marginally steady quadrupole of Q2D columnar structures set atop of it (Regime I). This quadrupole can become unsteady leading to the continuous injection and advection of columnar structures (Regime II). Figure 7.1 shows the outline of the two dynamical regimes identified in across the experimental range as well as other flow regimes that were identified over the course of this study. Inertial waves are found to be present under all experimental conditions and under the marginally steady conditions of Regime I individual inertial waves, with frequencies up to $f = 2\Omega$, can be seen being emitted by the turbulent patch. This provides experimental verification of the assumption by Davidson *et al*. [15] that blobs of vorticity can act as local inertial wave emitters. In line with results presented by Yarom *et al*. [67] and di Leoni *et al*.[33], inertial waves are found to carry a significant portion of the total turbulent kinetic energy E'. However, at Reynolds number $Re_Q \approx 3000$ energy is shown to flow almost exclusively into fluctuations that are not inertial waves, which leads to a plateau for the turbulent kinetic energy carried by inertial waves E'_{IW}. At $Re_Q \approx 10000$ we see that E'_{IW}/E' rapidly diminishes across all experiments, which is thought to be caused by random turbulence,

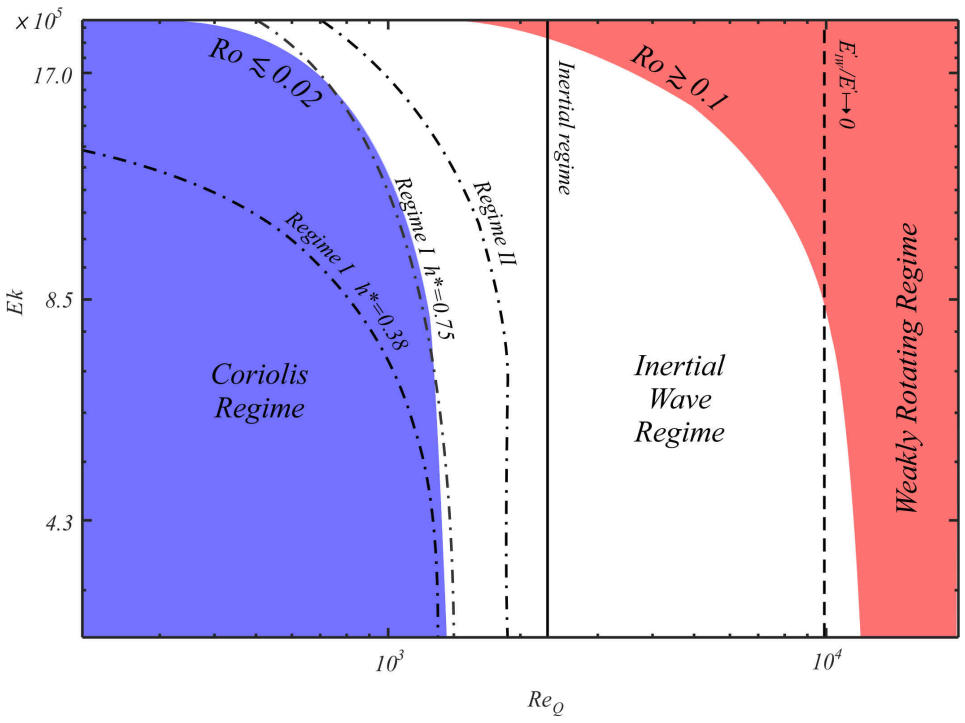

Figure 7.1: Outline of the various flow regimes observed across the experiments conducted in this study as function of the control parameters Ek and Re_Q. Dashed-dotted lines mark the the position of the dynamical regimes discussed in section 4.1, where a flow transitions from a marginally steady state (Regime I) of a quadrupole of set atop a turbulent patch to an unsteady state (Regime II) where columnar structures are continuously injected into the flow field and advected. Dashed line shows the point where E'_{IW}/E' rapidly diminishes as discussed in section 4.2, due to disruption of inertial waves by random turbulence. Solid line marks the start of the flow regime, where both columnar length scale ℓ_z and characteristic velocity U scale according to (2.13) and (2.23) for the inertial flow regime as discussed in section 5.1. Coloured regions mark the various regimes where different mechanisms govern the anisotropy of the average turbulent flow as discussed in section 5.2.

excited by the turbulent patch, disrupting inertial waves.

In Chapter 2 a new mechanism for the formation of columnar structures in rotating flows was introduced theoretically. For finite rotations $\partial_z u_z \neq 0$ and there exists a divergent flow that is perpendicular to the axis of rotation. This leads to columnar structures of distinct finite diffusion lengths ℓ_z^V and ℓ_z^I, depending on either viscous or inertial forces opposing the Coriolis force associated to the divergent flow. In Chapter 5 it is shown that the columnar structures that form in our rotating turbulent flow field and the velocity fields they induce scale according to the proposed theory for the inertial regime, where $\ell_z^I \sim \ell_\perp Ro^{-1}$ and $Re_U = UL/\nu \sim Re_Q$. This shows that the columnar structures form because of a balance between the Coriolis force and inertial forces, which can either be static or fluctuating.

By experimentally evaluating the relative magnitude of the various terms in the average flow equations we could quantify the influence of static forces and the fluctuating forces, which could be either due to random turbulence or inertial waves. This novel method allowed us to further develop the theory behind the force balance governing the anisotropy of the average turbulent flow. The mechanism that governs the anisotropy of the average turbulent flow is shown to span three flow regimes, which largely depend on the local Rossby number Ro.

For the inertial wave regime ($0.02 < Ro < 0.1$) and the weakly rotating regime ($Ro \gtrsim 0.1$), the mechanism involves a balance between the average flow inertia and the inertia of the fluctuating flow. For the weakly rotating regime these fluctuating forces are largely due random turbulence, while for the inertial wave regime they are almost entirely due to inertial waves. Surprisingly, however, in the Coriolis regime ($Ro \lesssim 0.02$) the influence of the inertial waves rapidly diminishes. In the limit of $Ro \to 0$ our results suggest that the mechanism promoting anisotropy of the average turbulent flow is governed by a balance, given by (5.6), between the average flow inertia (advection) and the Coriolis force. This mechanism is uninfluenced by time-dependent inertial waves and is similar to the mechanism which drives the formation of Taylor columns, except here inertia drives the horizontally divergent flow. In this regard, the columnar structures observed in Regime I, which roughly overlaps with the Coriolis regime, may be considered the inertial equivalent of Taylor columns.

In Chapter 6 it was shown that the turbulent front of a transient turbulent flow field, in the absence of a Coriolis force, spreads through an advection driven mechanism which is independent of wavenumber k. When a Coriolis force is applied it introduces a lower-bound for the spreading velocity which is equal to group speed for linear inertial waves. It was shown that modes with wavenumber k would initially be advected due to high local inertial forces. When the spreading velocity diminishes to the lower-bound the Coriolis force is able to sustain the mode as an inertial

wave with wavenumber k. As the lower-bound is inversely dependent on k the transition from an advection driven mechanism to a propagating mechanism is itself k-dependent, with large scale motions being more susceptible to the effects of the Coriolis force. This transient behaviour could be applicable to other forms of fluid forcing in rotating turbulence as well where initial inertial forces advect fluctuations at such great velocities that propagation by inertial waves is simply overridden. This would explain the deviation from linear inertial wave theory observed by both Dickenson & Long [17] and Davidson *et al*.[15] in grid-driven rotating turbulence.

The general conclusion that can be drawn from all areas of study is that in a narrow flow regime inertial waves play a key role in the physical processes governing rotating turbulence. In line with the established knowledge on rotating turbulence, this flow regime is bound by the relative strength of the inertial forces acting on the flow field. When these are too great Ro tends to unity or even exceeds it; resulting in inertial waves being disrupted and advection driven mechanisms beginning to govern the dynamics of the flow. Surprisingly, however, the flow regime is found to be bounded by the strength of the Coriolis force as well, at least with regard to the average flow anisotropy. In the limit of $Ro \rightarrow 0$ the influence of inertial waves rapidly diminishes and the mechanism promoting anisotropy involves a balance between static forces and thus is completely waveless. The implications of this discovery are significant, not only does it challenge the current paradigm that places inertial waves at the heart rotating turbulence, but it unveils an entirely new aspect of the problem at hand.

Outlook

The current experiment allowed us to explore a wide range of flow regimes, but improvements can be made. By moving to a 3D stereoscopic PIV system, the experiment could be greatly improved. This will eliminate the need to compute an upper-bound for each of the terms in the average flow equations. It will also allow us to explore if the new mechanism for anisotropy expands to large scale fluctuations and other parts of the turbulent spectrum by evaluating the full fluctuation equations (2.24-2.26). It may even provide insight as to why the influence of the inertial waves rapidly diminishes in the limit of $Ro \rightarrow 0$.

The transient experiments could be greatly improved by resolving a high number of measurements for each set of experimental parameters, which would allow accurate derivation of the spreading velocity of separate modes of different scales. Not only will this allow us to fully characterize the advection mechanism, but will allow us to understand under what exact conditions any mode will deviate from the advection mechanism and transition to the propagation mechanism.

A phenomenon that has remained unresolved in this thesis is the sudden increase in the characteristic time-scale of the flow. At the time of writing we can only speculate to its origin. The slope of the frequency spectra for large time-scales scales as $f^{-4/5}$ across the experiments. This suggested that our flow may be subject to flicker-noise, where our flow flickers between two states. By evaluating the probability density functions (pdf) of velocity and vorticity fields this noise could be identified if the pdf exhibited multiple maxima. However, the pdf's found were Gaussian, eliminating flicker-noise as the cause of the increase. The rapid decrease of τ_{dc} when $Ro \gtrsim 0.3$ does however suggest that the characteristic timescale is related to the dynamics of inertial waves. Finally, by applying the ideas from MHD turbulence to the case of rotating turbulence we were able to derive and identify a new mechanism for anisotropy in rotating turbulence. The existence of this mechanism shows that the similarities between rotating turbulence and MHD turbulence are far reaching. Considering the important role inertial waves play in promotion of anisotropy in rotating turbulence an argument could be made to explore the possibility of flow regimes in MHD turbulence where Alfven waves, the MHD counterpart to inertial waves, promote anisotropy in MHD turbulent flows.

Bibliography

[1] Adrian, R.J., J. Westerweel (2011) *Particle Image Velocimetry* - Cambridge University Press, ISBN 978-0-521-44008-0

[2] Aujogue, K., A. Potherat, B. Screenivasan, F. Debray (2018) *Experimental study of the convection in a rotating tangent cylinder* - Journal of Fluid Mech. **843**, pp.355-381

[3] Baker, N., A. Potherat, L. Davoust (2015) *Dimensionality, secondary flows and helicity in low-Rm MHD vortices* – **779**, pp.325-350

[4] Baroud, C.N., B.B. Plapp, H.L. Swinney, Z.-S. She (2003) *Scaling in three-dimensional and quai-two-dimensional rotating turbulent flows* – Phyiscs of Fluids **15**, 2091

[5] Batchelor, G.K. (1969) *Computation of the energy spectrum in two-dimensional turbulence* - Phys.Fluids Suppl. II, **12**, 233-239

[6] van Bokhoven, L.L.J, H.J.H. Clercx, G.J.F. van Heijst, R.R.Trieling (2009) *Experiments of rapidly rotating turbulent flows* - Physics of Fluids **21**, 096601

[7] Bordes, G., F. Moisy, T. Dauxios, P.-P. Cortet (2012) *Experimental evidence of a triadic resonance of plane inertial waves in a rotating fluid* - Physics of Fluids (**24**), 014105

[8] Busse, F.H. (2010) *Zonal flow induced by longitudinal librations of a rotating cylindrical cavity* – Physica D **240**, pp.208-211

[9] Cambon, C., J.F. Scott (1999) *Linear and Non-Linear models in Anisotropic Turbulence* - Ann. Rev. Fluid Mech. **31**, pp. 1–53.

[10] Campagne, A., B. Gallet, F. Moisy, P.-P. Cortet (2014) *Direct and inverse energy cascades in a forced rotating turbulence experiment* – Physics of Fluids **26**, 125112

[11] Campagne, A., B. Gallet, F. Moisy, P.-P. Cortet (2015) *Disentangling inertial waves from eddy turbulence in a forced rotating-turbulence experiment* – Phys. Rev. E **91**, 043016

[12] Chen, Q., S. Chen, G.L. Eyink, D.D. Holm (2005) *Resonant interactions in rotating homogeneous three-dimensional turbulence* - J. Fluid Mech. **542**, 139

[13] Cho, J. Y.-K., K. Menou, B.M.S. Hansen, S. Seager, (2008) *Atmospheric circulation of close-in extrasolar giant planets: I. Global, barotropic, adiabatic simulations* – Astrophys. J., **675**(1), pp. 817–845.

[14] Cortet, P.-P., C. Lamriben, F. Moisy (2010) *Viscous spreading of an inertial wave beam in a rotating fluid* – Phyiscs of Fluids **22**, 086603

[15] Davidson, P.A., P.J. Staplehurst, B. Dalziel (2006) *On the evolution of eddies in a rapidly rotating system* - Journal of Fluid Mech. **557**, pp.135-144

[16] Davidson, P.A. (2013) *Turbulence in Rotating, Stratified and Electrically Conducting Fluids* – Cambridge University Press, ISBN 978-1-107-02686-5

[17] Dickinson, S.C., R.R. Long (1983) *Oscillating-grid turbulence including effects of rotation* - Journal of Fluid Mech. **126**, pp.315-333

[18] Duran-Matute, M., L.P.J. Kamp, R.R. Trieling, G.J.F. van Heijst (2012) *Regimes of two-dimensionality of decaying shallow axisymmetric swirl flows with background rotation* – Journal of Fluid Mech. **691**, pp.214-244

[19] Duran-Matute, M., J.B. Flor, F.S. Godeferd, C. Jause-Labert (2013) *Turbulence and columnar vortex formation through inertial wave focusing* – Phys. Rev. E **87**, 041001

[20] Frisch, U. (1996) *Turbulence: The legacy of A.N. Kolmogorov* - Cambridge University Press - ISBN: 978-0-521-45713-2

[21] Gallet, B., A. Campagne, F. Moisy, P.-P. Cortet (2014) *Scale dependent cyclone-anticyclone asymmetry in a forced rotating turbulence experiment* – Phyiscs of Fluids **26**, 035108

[22] Godeferd, F.S., F. Moisy (2015) *Structure and Dynamics of Rotating Turbulence: A Review of Recent Experimental and Numerical Results* - Applied Mech. Rev. **67**, 030802

[23] Ghaem-Maghami, E., H. Johari (2010) *Velocity field of isolated turbulent puffs* - Physics of Fluids **22**, 115105

[24] Greenspan, H.P. (1968) *The Theory of Rotating Fluids* – Cambridge Univ. Press

[25] van Heijst, G.J.F., H.J.H. Clercx (2009) *studies on quasi-2D turbulence - effect of boundaries* – Fluid Dyn. Res. **41** (2009), 064002

[26] Hopfinger, E.J., F.K. Browand, Y. Gagne (1982) *Turbulence and waves in a rotating tank* - Journal of Fluid Mech. **125**, pp.505-534

[27] Ibbetson, A., D.J. Tritton (1975) *Experiments on Turbulence in a Rotating Fluid* - Journal of Fluid Mech. **68**(4), pp. 639–672.

[28] Jacquin, L., O. Leuchter, C. Cambon, J. Mathieu(1990) *Homogeneous Turbulence in the Presence of Rotation* - Journal of Fluid Mech. **220**, pp. 1–52.

[29] Kolvin, I., K. Cohen, Y. Vardi, E.Sharon (2009) *Energy transfer by inertial waves during the buildup of turbulence in a rotating system* - Phys.Rev.Let. **102**, 014503

[30] Klein, R., A. Potherat (2010) *Appearance of three dimensionality in wall-bounded MHD flows* – PRL **104**, 034502

[31] Kraichnan, R.H. (1967) *Inertial Ranges in Two-Dimensional Turbulence* - Physics of Fluids **10**(7), pp. 1417-1423.

[32] Kraichnan, R.H., D. Montgomery (1980) *Two-dimensional turbulence* – Rep. Prog. Physics, vol 43

[33] di Leoni, P.C., P.J. Cobelli, P.D. Mininni, P. Dmitruk, W.H. Matthaeus (2015) *Quantification of the strength of inertial waves in a rotating turbulent flow* – Physics of Fluids **26**, 035106

[34] Lopez, J.M., F. Marques (2011) *Instabilities and inertial waves generated in a librating cyclinder* – Journal of Fluid Mech. **687**, pp.171-193

[35] Lighthill, J. (1978) *Waves in Fluids* – Cambridge University Press

[36] Maassen, S.R., H.J.H. Clercx, G.J.F. van Heijst (1999) *Decaying two-dimensional turbulence in square containers with no-slip or stress-free boundaries* – Europhys. Lett., **46**(3), pp.339-345

[37] Maxworthy, T., S. Narimousa (1994) *Unsteady, Turbulent, Covection into a homogeneous, Rotating fluid with Oceanographic Applications* – Journal of Phys. Oceanography **24**

[38] Messio, L., C. Morize, M. Rabaud, F. Moisy (2008) *Experimental observation using particle image velocimetry of inertial waves in a rotating fluid* – Exp. Fluids **44**, pp.519-528

[39] Moisy, F., C. Morize, M. Rabaud, J. Sommeria (2011) *Decay laws anisotropy and cyclone-anticyclone asymmetry in decaying rotating turbulence* – Journal of Fluid Mech. **666**, pp.5-35

[40] Moore, D.B., P.G. Saffman (1968) *The rise of a body through a rotating fluid in a container of finite length* - Journal of Fluid Mech. **31**(4), pp.635-642

[41] Moore, D.B., P.G. Saffman (1969) *The flow induced by the transverse motion of a thin disk in its own plane through a contained rapidly rotating viscous liquid* - Journal of Fluid Mech. **39**(4), pp.831-847

[42] Morize, C., F. Moisy, M. Rabaud (2005) *Decaying grid-generated turbulence in a rotating tank* – Physics of Fluids **17**, 095105

[43] Morize, C., F. Moisy (2006) *Energy decay of rotating turbulence with confinement effects* – Physics of Fluids **18**, 065107

[44] Noir, J., M.A. Calkins, M. Lasbleis, J. Cantwell, J.M. Carnou (2010) *Experimental study of libration driven zonal flows in a straight cylinder* – Physics of Earth and Planetary Interiors **182**, pp.98-106

[45] Niino, H., (1978) *Turbulent jet in a rotating fluid*

[46] Podesta, J.J., M.A. Forman, C.W. Smith, D.C. Elton, Y. Malecot, Y. Gagne (2009) *Accurate estimation of third-order moments from turbulence* - Nonlin. Processes Geophys. **16**, pp. 99-110

[47] Pedlosky, J. (1987) *Geophysical Fluid Dynamics* - Springer, ISBN:0-387-90368-2

[48] Pope, S.B. (2000) *Turbulent Flows* - Cambridge University Press, ISBN: 978-0-521-59886-6

[49] Potherat, A. (2012) *Three-dimensionality in quasi–two-dimensional flows: Recirculations and Barrel effects* – EPL **98**, 64003

[50] Potherat, A. R. Klein (2014) *Why how and when MHD turbulence at low Rm becomes three dimensional* – Journal of Fluid Mech. **761**, pp.168-205

[51] Reynolds, A.J. (1962) *Observations of a liquid-into-liquid jet* - Journal of Fluid Mechanics, **14**(4), pp.552-556

[52] Savas, O. (1985) *On flow visualization using reflective flakes* - Journal of Fluid Mech. **152**, pp.235-248

[53] Smith, L.M., J.R. Chasnov, F. Waleffe (1999) *Crossover from Two- to Three-Dimensional Turbulence* – Phys. Rev. Lett. **77** (12), pp.2467-2470

[54] Smith, L.M., F. Waleffe (1999) *Transfer of energy to two-dimensional large scales in forced, rotating three-dimensional turbulence* – Physics of Fluids **11**, 1608

[55] Sommeria, J., R. Moreau (1982) *Why, how, and when, MHD turbulence becomes two-dimensional* – Journal of Fluid Mech., **118**, pp.507-518

[56] Sommeria, J. (1986) *Experimental study of the two-dimensional inverse energy cascade in a square box* – Journal of Fluid Mech., **170**, pp.139-168

[57] Sous, D., N. Bonneton, J. Sommeria (2004) *Turbulent vortex dipoles in a shallow water layer* – Physics of Fluids **16** (8)

[58] Screenivasan, B., P.A. Davidson (2008) *On the formation of cyclones and anticyclones in a rotating fluid* - Physics of Fluids **20**, 085104

[59] Stapelhurst, P.J., P.A. Davidson, B. Dalziel (2008) *Structure formation in homogeneous freely decaying rotating turbulence* – Journal of Fluid Mech. **598**, pp.81-105

[60] Tabeling, P. (2002) *Two-dimensional turbulence – a physicist approach* - Physics Reports **362**, 1-62

[61] Taylor, G.I. (1922) *The motion of a sphere in a rotating liquid* - Royal Society of London A **102**, 180

[62] Thielicke, W, E.J. Stamhuis (2014) *PIVlab – Towards User-friendly, Affordable and Accurate Digital Particle Image Velocimetry in MATLAB* - Journal of Open Research Software, **2**

[63] Vanyo, J.P. (1993) *Rotating Fluids in Engineering and Science* - Butterworth-Heinemann, ISBN: 978-0-7506-9261-8

[64] Waleffe, F., (1993) *Inertial transfers in helical decomposition* – Phys. Fluids A **5** (3), 667-685

[65] Westerweel, J., F. Scarano (2005) *Universal outlier detection for PIV data* – Experiments in Fluids **39**, 1096-1100

[66] Yarom, E., Y. Vardi, E. Sharon (2013) *Experimental quantification of inverse energy cascade in deep rotating turbulence* – Physics of Fluids **25**, 085105

[67] Yarom, E., E. Sharon (2014) *Experimental observation of steady inertial wave turbulence in deep rotating flows* – Nature Physics **10**, pp.510-514

[68] Yeung, P. K., Y. Zhou (1998) *Numerical study of rotating turbulence with external forcing* – Physics of Fluids **10**(11), pp. 2895–2909.

Appendix A

Additional figures

In this appendix we provide additional figures of results presented across this thesis. Additional commentary is given where necessary.

instantaneous flow fields - section 4.1

Figures (A.1-A.6)

Here we see additional instantaneous velocity and vorticity fields across all Re_Q explored for $Ek = 4.25 \times 10^{-5}$. $Re_Q = 600$ is within the marginally steady state of Regime I and so we see four columnar structures remain in a steady position over the forcing points. $Re_Q \geq 4000$ fall within the unsteady Regime II and so we see columnar structures propagate across the flow field.

frequency spectra - section 4.2

Figures (A.7-A.12)

Frequency spectra $E(f')$ obtained from experiments along the horizontal plane are presented. Here f' is the frequency normalized by the cut-off frequency for inertial waves f_Ω. At $f' = 1$ there is a significant drop in $E(f')$. Though there are a few outliers we see that as Re_Q is increased the overall energy in the flow increases. At a critical value of $Re_Q \approx 3000$ the energy carried by fluctuations with $f' \leq 1$ sees almost no increase while significantly more energy flows into fluctuations with $f' > 1$.

A spike in the frequency spectra is visible at high Re_Q and all Ek across both planes at $f' \approx 0.4$.

Inspection of the instantaneous velocity/vorticity field and frequency filtered fields did not reveal anything particular. No component of the experimental setup produces noise at these frequencies, as such the spike is likely linked to some physical process that has yet to be identified as the spike is visible across all *Ek*.

energy density contours - section 6.3

Figures (A.13-A.17)

Here we present the energy contours for the other experiments studied. Due to the relatively high error some contours have been dropped from the figures presented here.

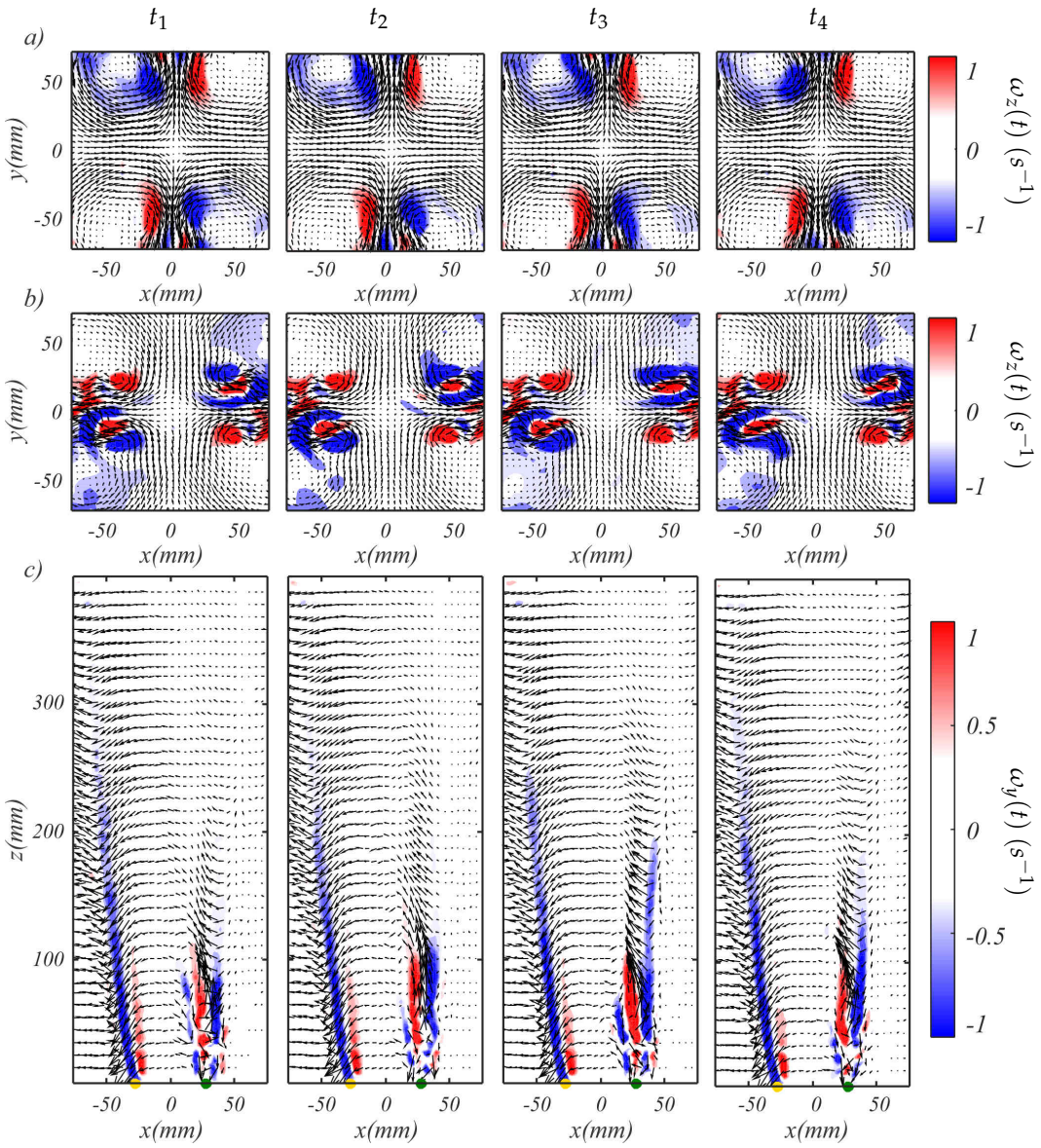

Figure A.1: Contour plots of the instantaneous vorticity field $\omega(t)$ and velocity field $\vec{u}(t)$ (arrows) across intervals t_1-t_4, each 15 seconds apart for $Re_Q = 600$ and $Ek = 4.25 \times 10^{-5}$. Flow fields shown along a horizontal plane at (a) $h^* = 0.75$, (b) $h^* = 0.38$ and along the vertical plane. Note: Flow fields shown are in fact averaged over a short time period of 5 frames for visualization purposes.

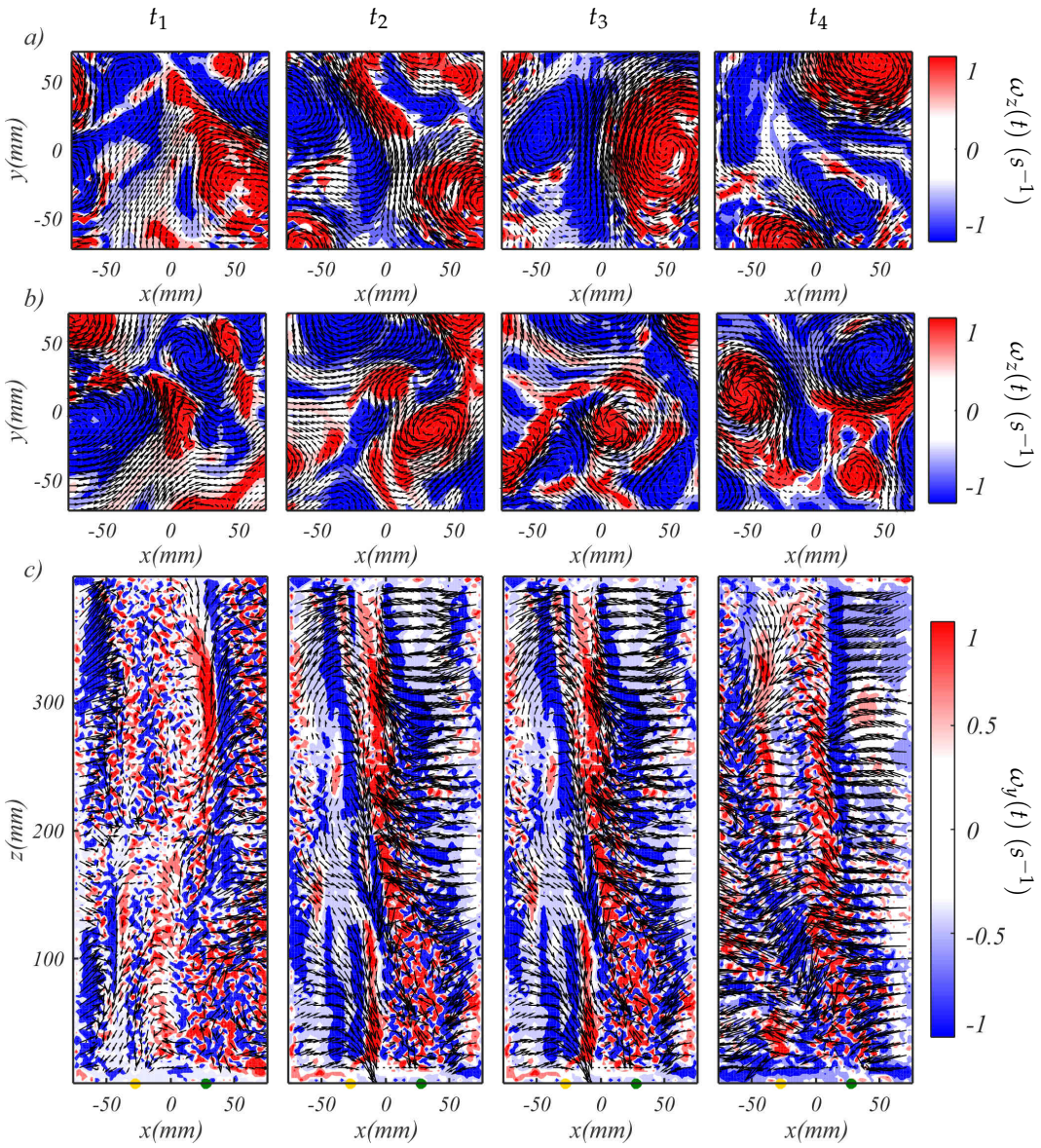

Figure A.2: Contour plots of the instantaneous vorticity field $\omega(t)$ and velocity field $\vec{u}(t)$ (arrows) across intervals t_1-t_4, each 15 seconds apart for $Re_Q = 4000$ and $Ek = 4.25 \times 10^{-5}$. Flow fields shown along a horizontal plane at (a) $h^* = 0.75$, (b) $h^* = 0.38$ and along the vertical plane. Note: Flow fields shown are in fact averaged over a short time period of 5 frames for visualization purposes.

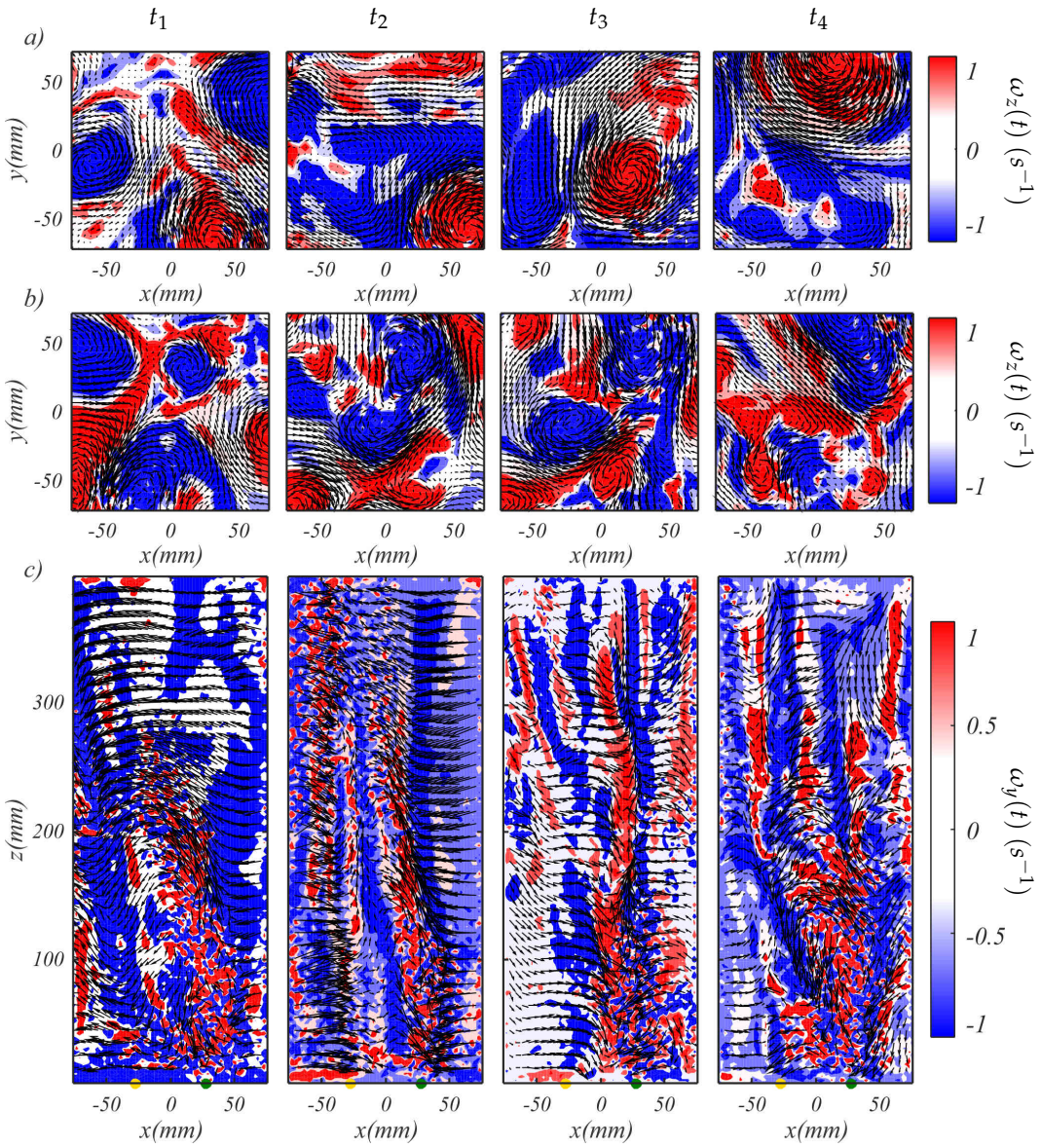

Figure A.3: Contour plots of the instantaneous vorticity field $\omega(t)$ and velocity field $\vec{u}(t)$ (arrows) across intervals t_1-t_4, each 15 seconds apart for $Re_Q = 6000$ and $Ek = 4.25 \times 10^{-5}$. Flow fields shown along a horizontal plane at (a) $h^* = 0.75$, (b) $h^* = 0.38$ and along the vertical plane. Note: Flow fields shown are in fact averaged over a short time period of 5 frames for visualization purposes.

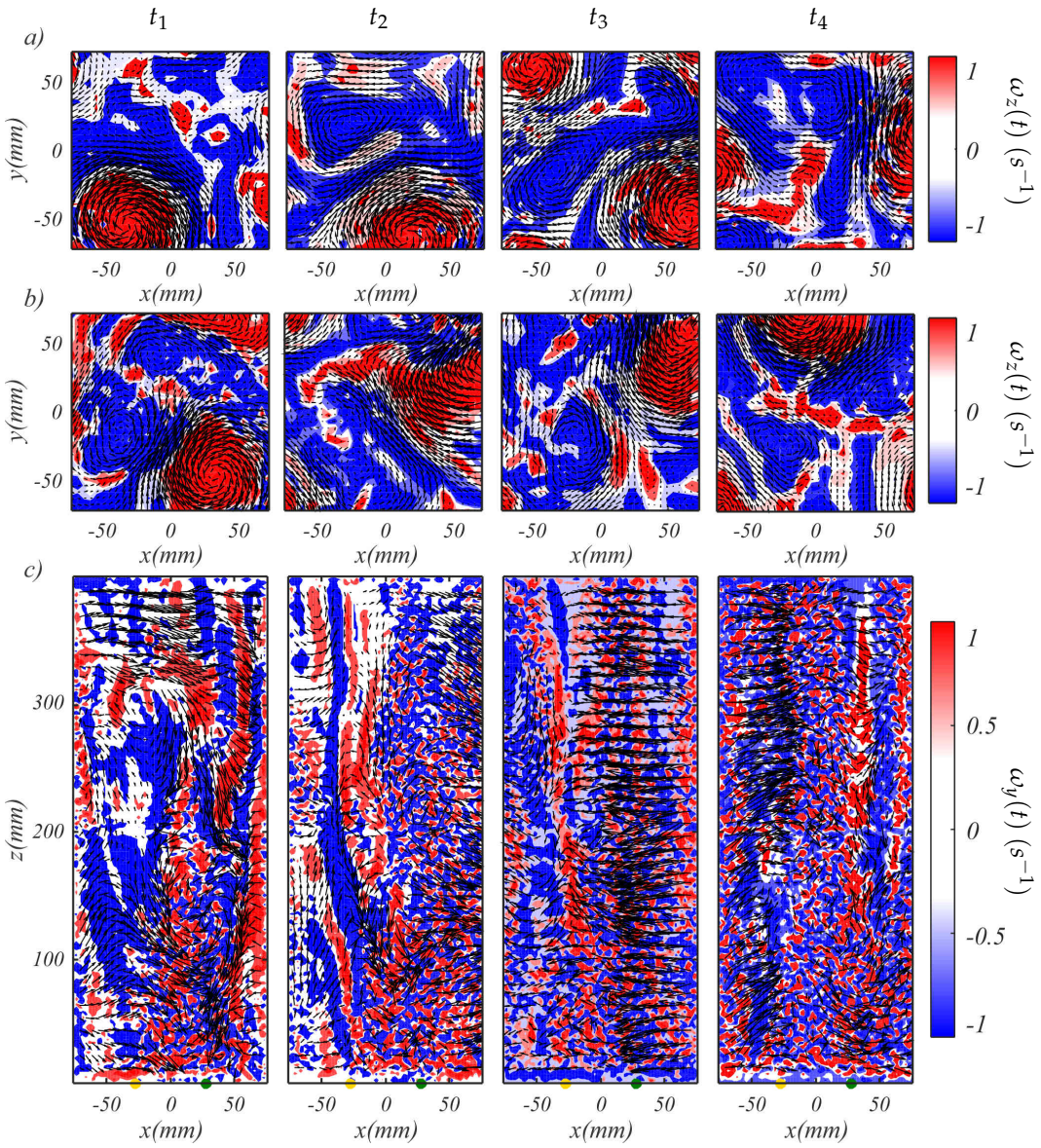

Figure A.4: Contour plots of the instantaneous vorticity field $\omega(t)$ and velocity field $\vec{u}(t)$ (arrows) across intervals t_1-t_4, each 15 seconds apart for $Re_Q = 7500$ and $Ek = 4.25 \times 10^{-5}$. Flow fields shown along a horizontal plane at (a) $h^* = 0.75$, (b) $h^* = 0.38$ and along the vertical plane. Note: Flow fields shown are in fact averaged over a short time period of 5 frames for visualization purposes.

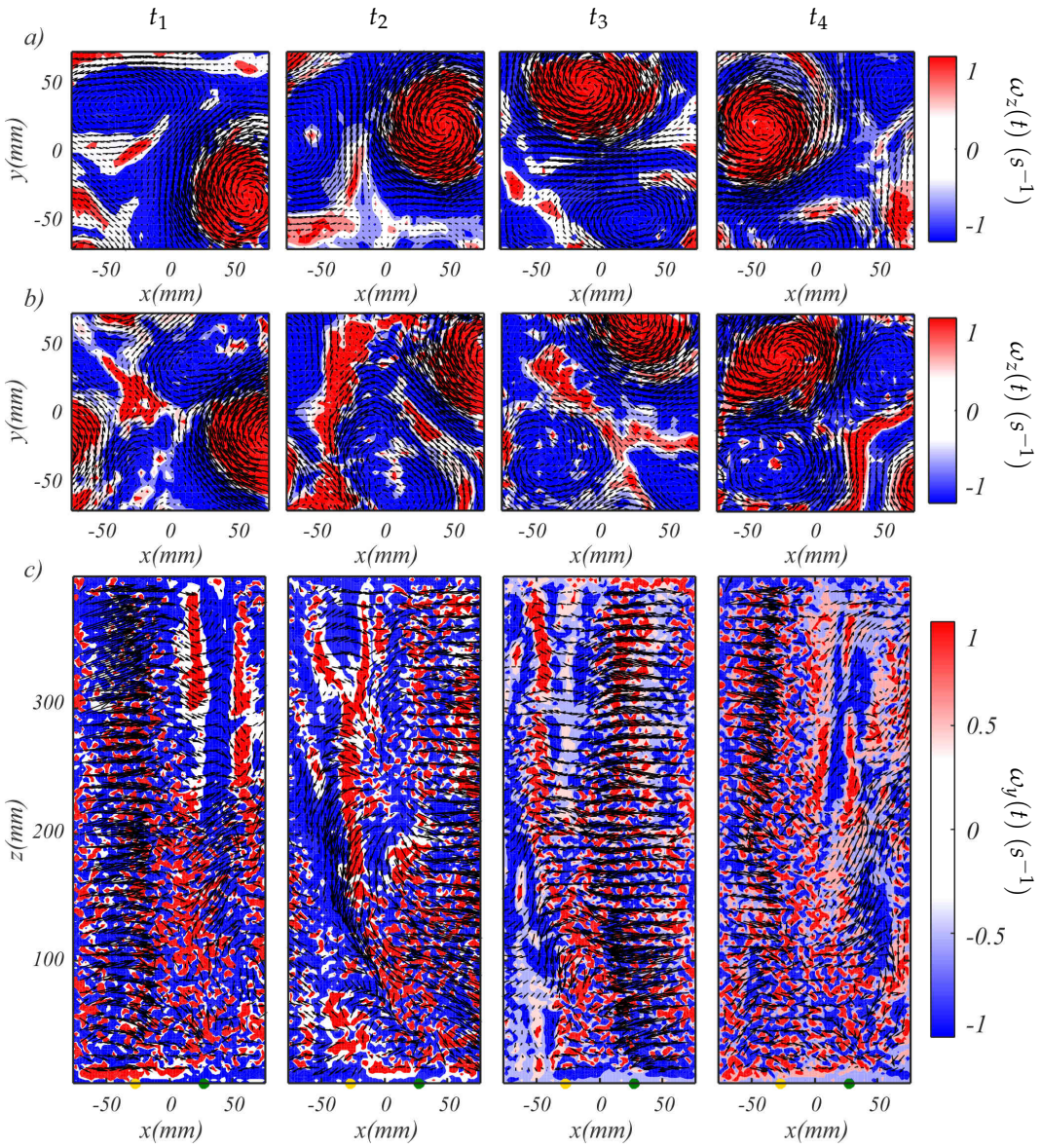

Figure A.5: Contour plots of the instantaneous vorticity field $\omega(t)$ and velocity field $\vec{u}(t)$ (arrows) across intervals t_1-t_4, each 15 seconds apart for $Re_Q = 9000$ and $Ek = 4.25 \times 10^{-5}$. Flow fields shown along a horizontal plane at (a) $h^* = 0.75$, (b) $h^* = 0.38$ and along the vertical plane. Note: Flow fields shown are in fact averaged over a short time period of 5 frames for visualization purposes.

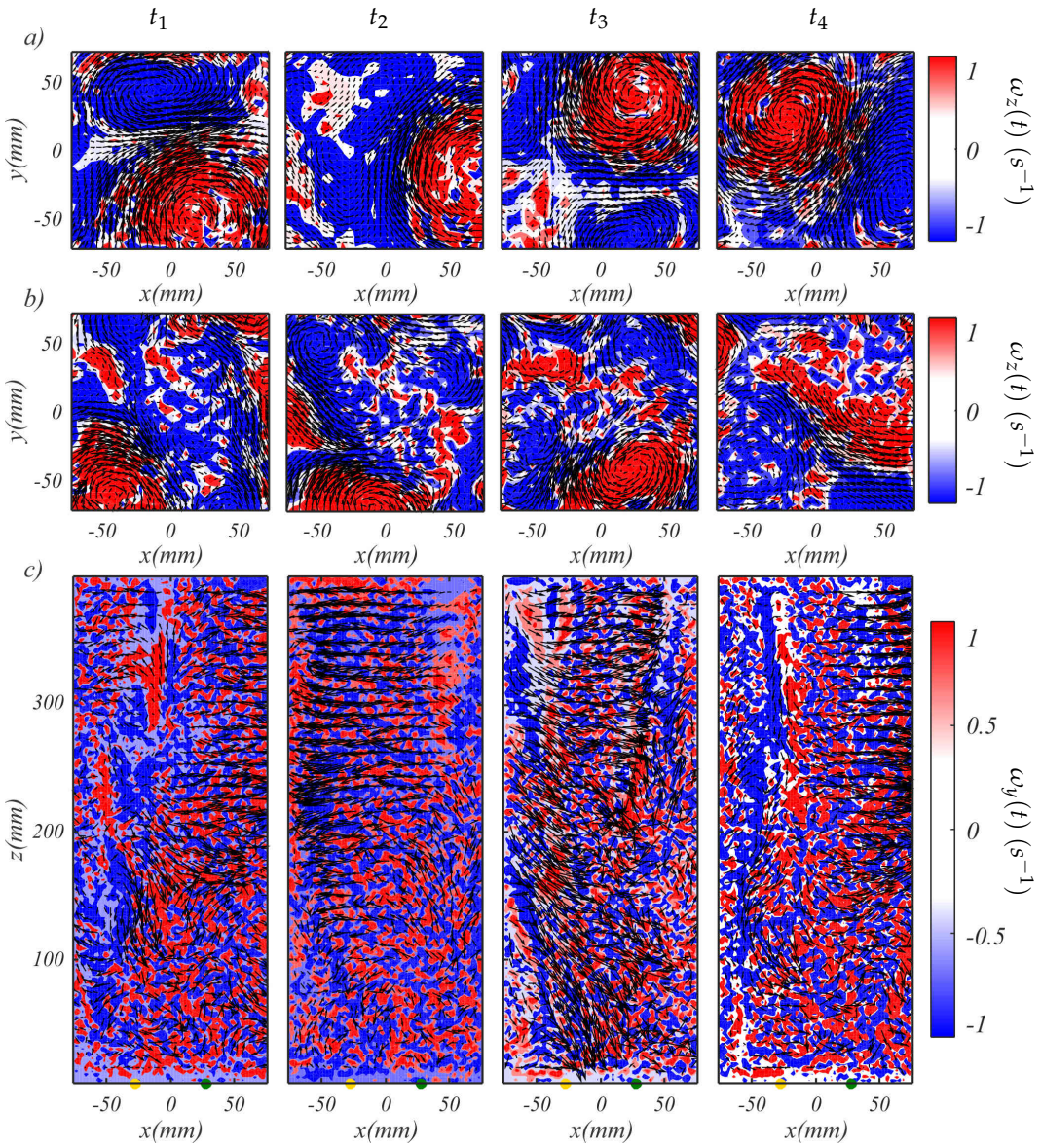

Figure A.6: Contour plots of the instantaneous vorticity field $\omega(t)$ and velocity field $\vec{u}(t)$ (arrows) across intervals t_1-t_4, each 15 seconds apart for $Re_Q = 12000$ and $Ek = 4.25 \times 10^{-5}$. Flow fields shown along a horizontal plane at (a) $h^* = 0.75$, (b) $h^* = 0.38$ and along the vertical plane. Note: Flow fields shown are in fact averaged over a short time period of 5 frames for visualization purposes.

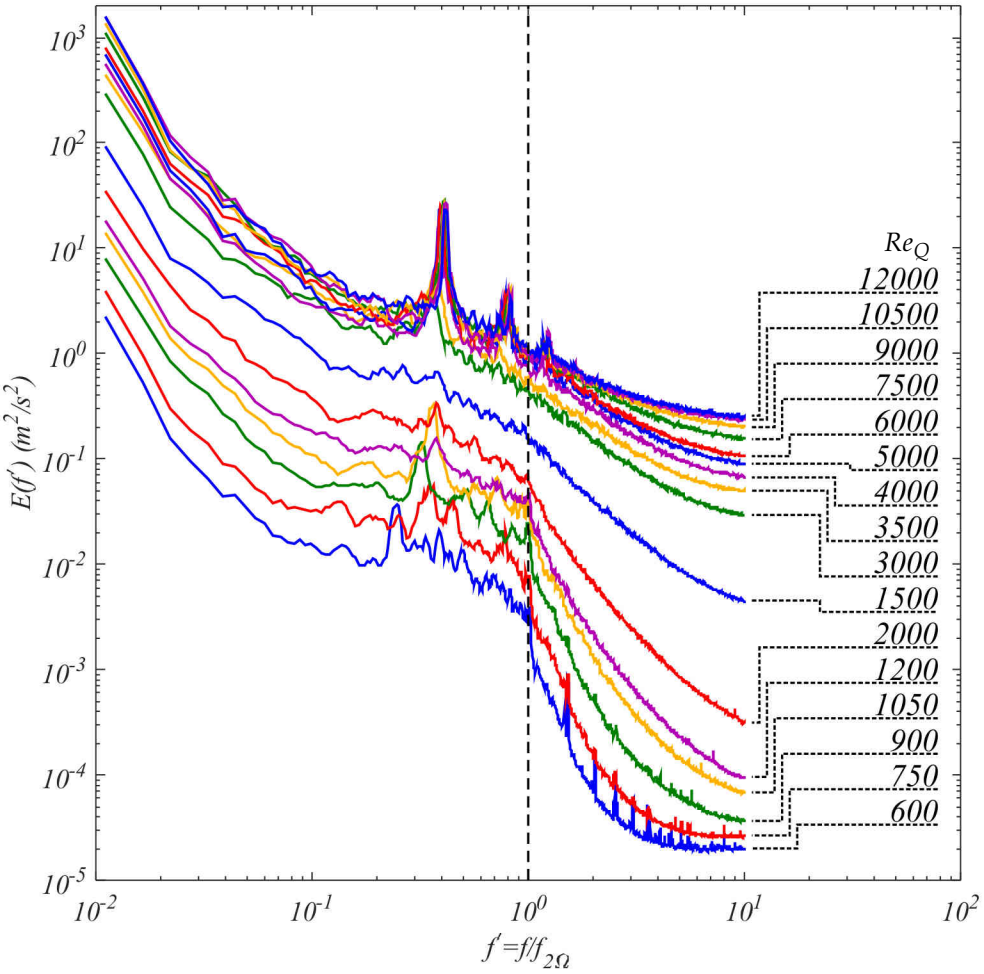

Figure A.7: Frequency spectra $E(f')$ with frequency normalized by the cut-off frequency for inertial waves f_Ω, at $Ek = 17.0 \times 10^{-5}$ and $h^* = 0.38$.

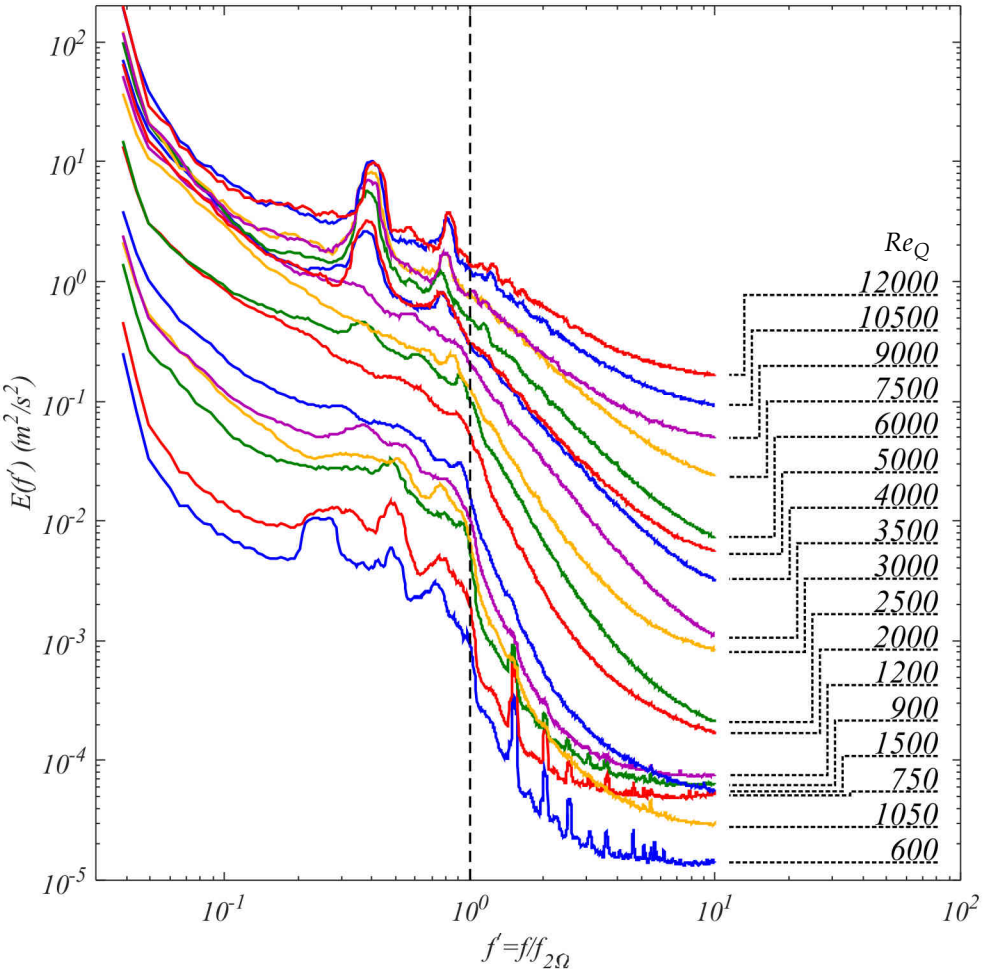

Figure A.8: Frequency spectra $E(f')$ with frequency normalized by the cut-off frequency for inertial waves f_Ω, at $Ek = 17.0 \times 10^{-5}$ and $h^* = 0.75$.

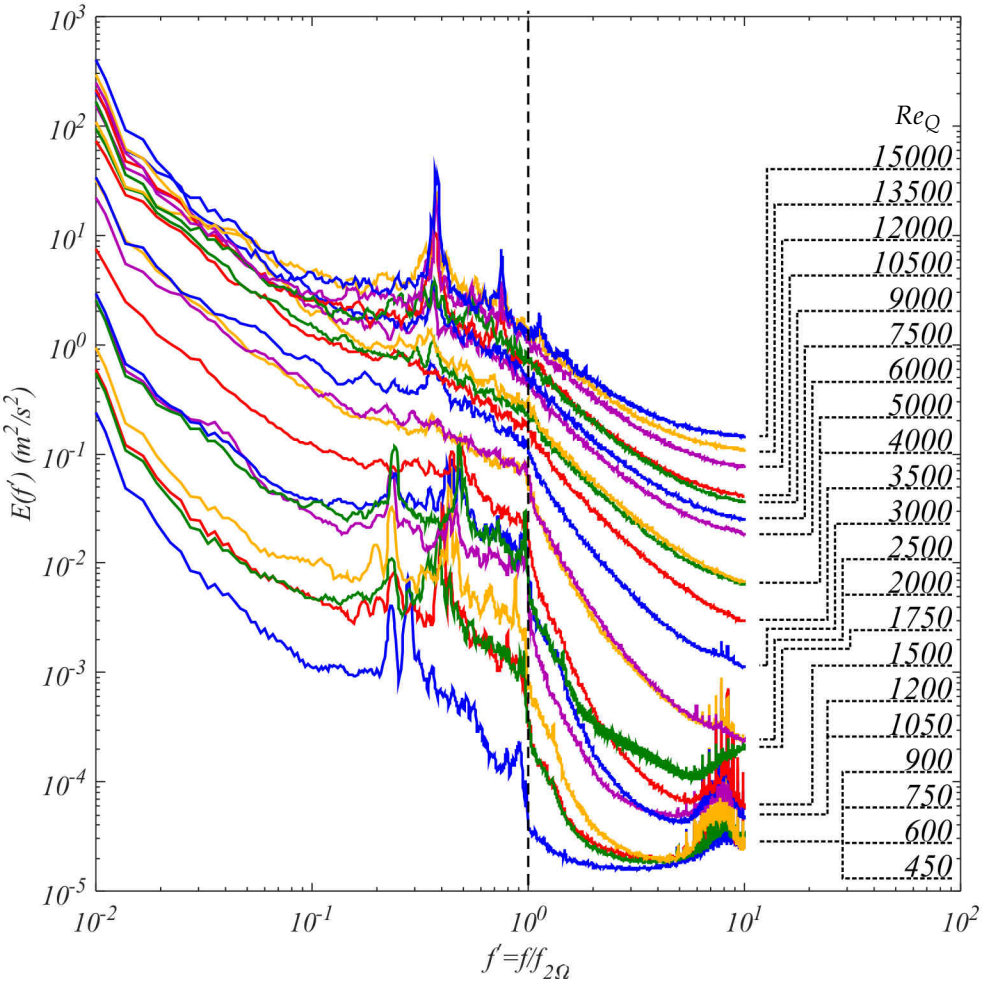

Figure A.9: Frequency spectra $E(f')$ with frequency normalized by the cut-off frequency for inertial waves f_Ω, at $Ek = 8.50 \times 10^{-5}$ and $h^* = 0.38$.

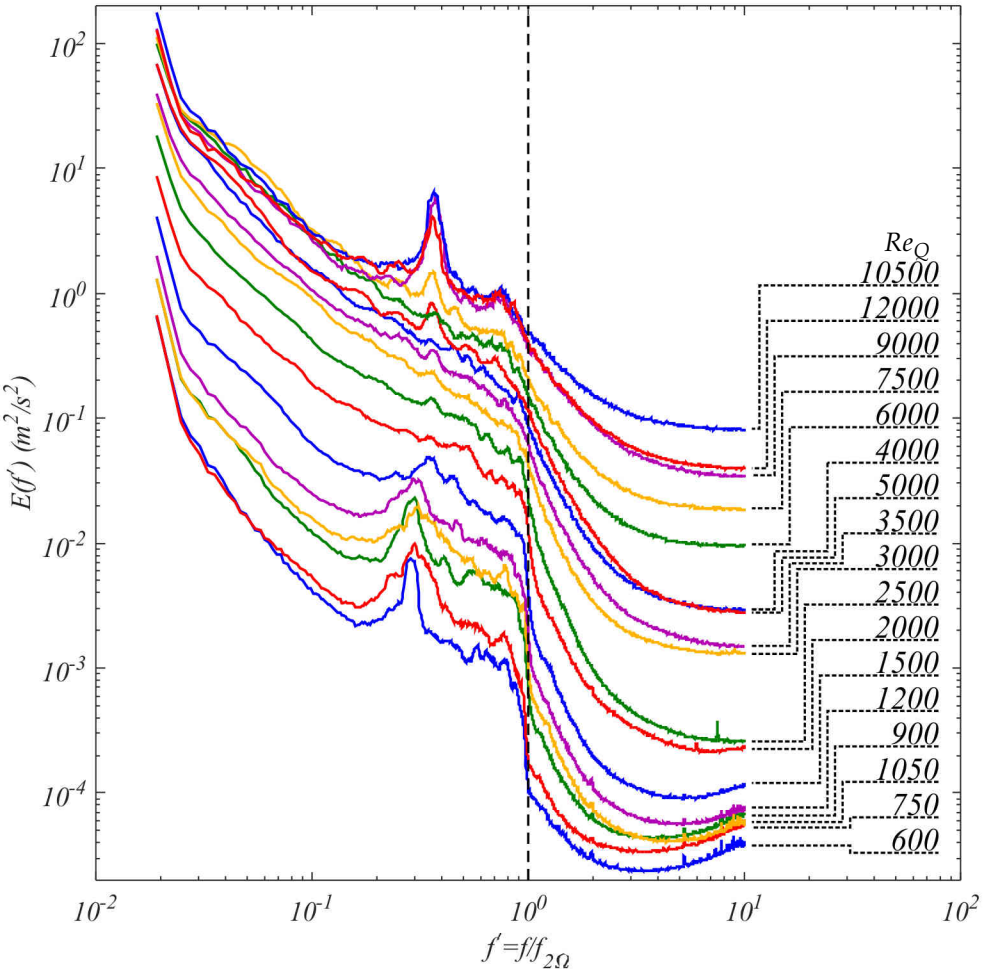

Figure A.10: Frequency spectra $E(f')$ with frequency normalized by the cut-off frequency for inertial waves f_Ω, at $Ek = 8.50 \times 10^{-5}$ and $h^* = 0.75$.

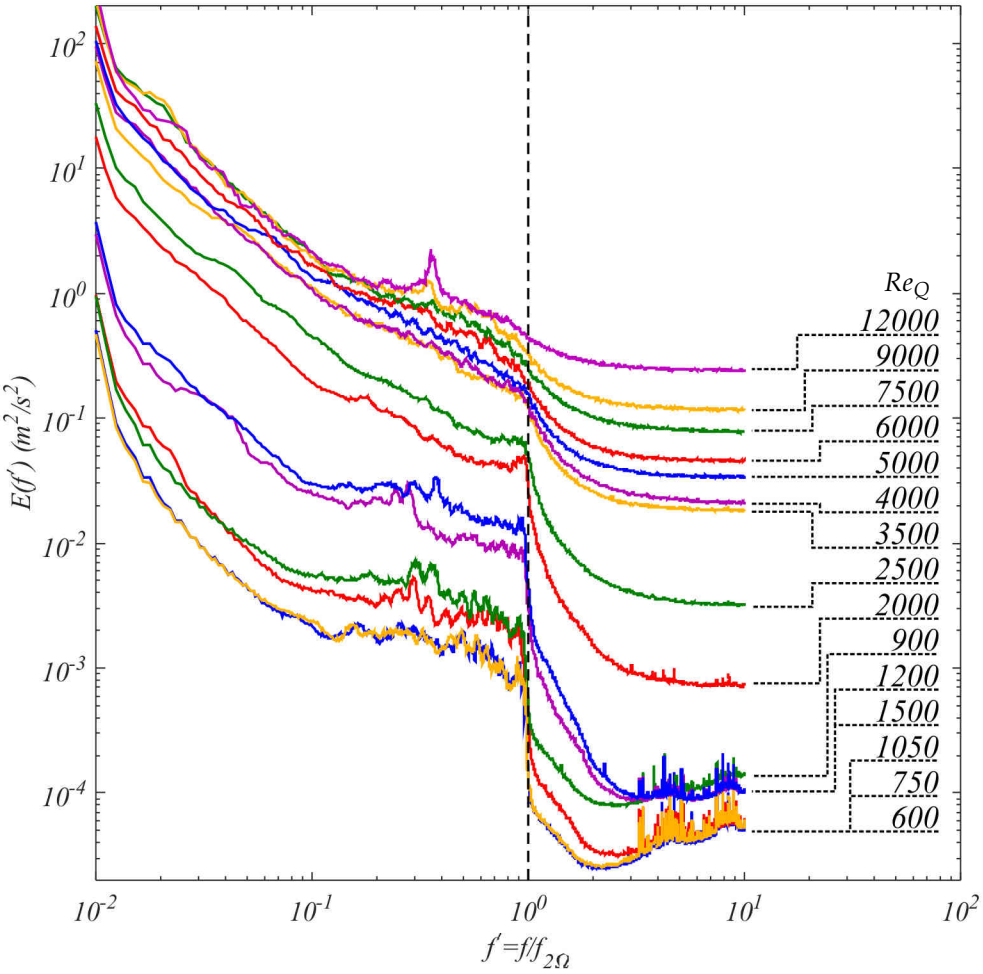

Figure A.11: Frequency spectra $E(f')$ with frequency normalized by the cut-off frequency for inertial waves f_Ω, at $Ek = 4.25 \times 10^{-5}$ and $h^* = 0.38$.

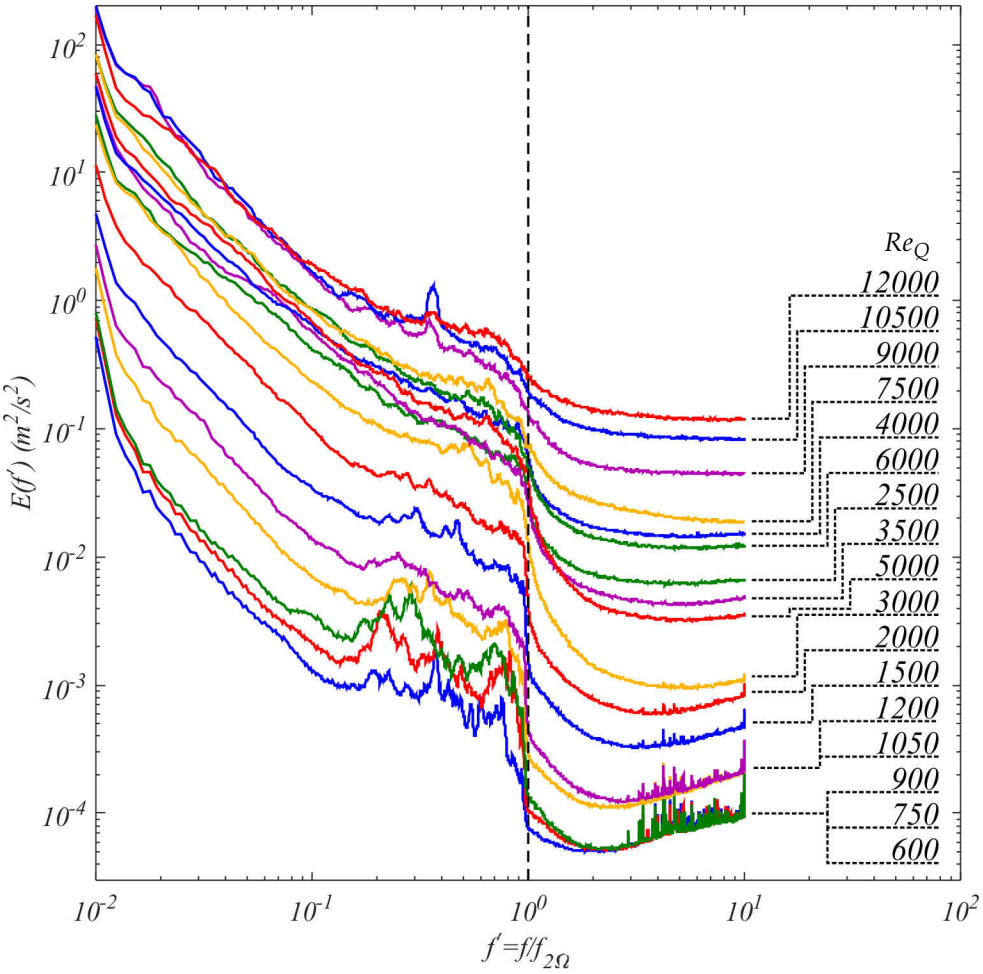

Figure A.12: Frequency spectra $E(f')$ with frequency normalized by the cut-off frequency for inertial waves f_Ω, at $Ek = 4.25 \times 10^{-5}$ and $h^* = 0.75$.

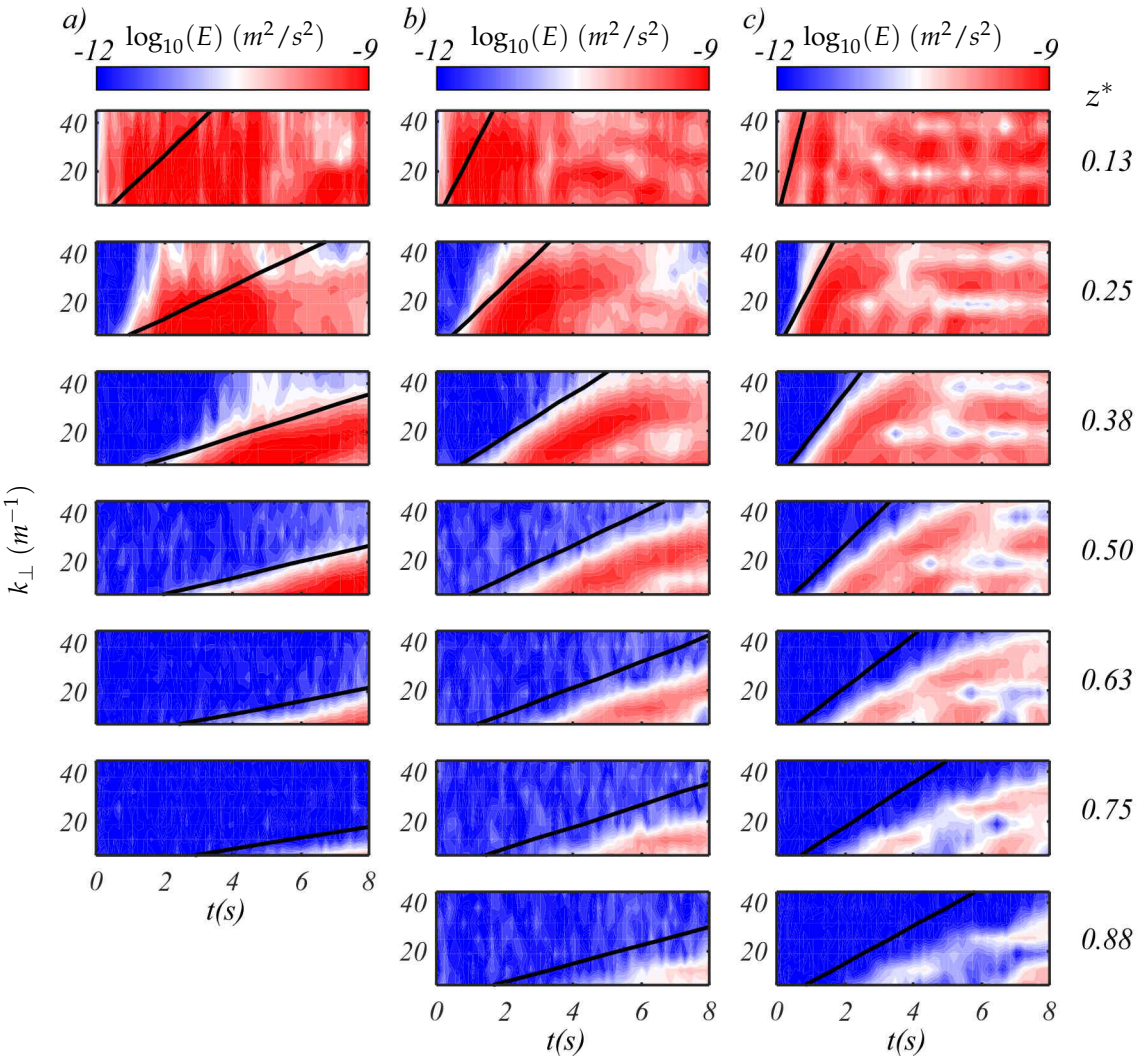

Figure A.13: Contourplots of $E(k_\perp, t)$ across a number of heights z^* at a) $Ek = 17.0 \times 10^{-5}$, b) $Ek = 8.50 \times 10^{-5}$ and c) $Ek = 4.25 \times 10^{-5}$ at $Re_Q = 600$. Solid black lines represent the predicted shape of the contours assuming propagation is fully driven by LIW theory. Certain contours were excluded due to high experimental errors

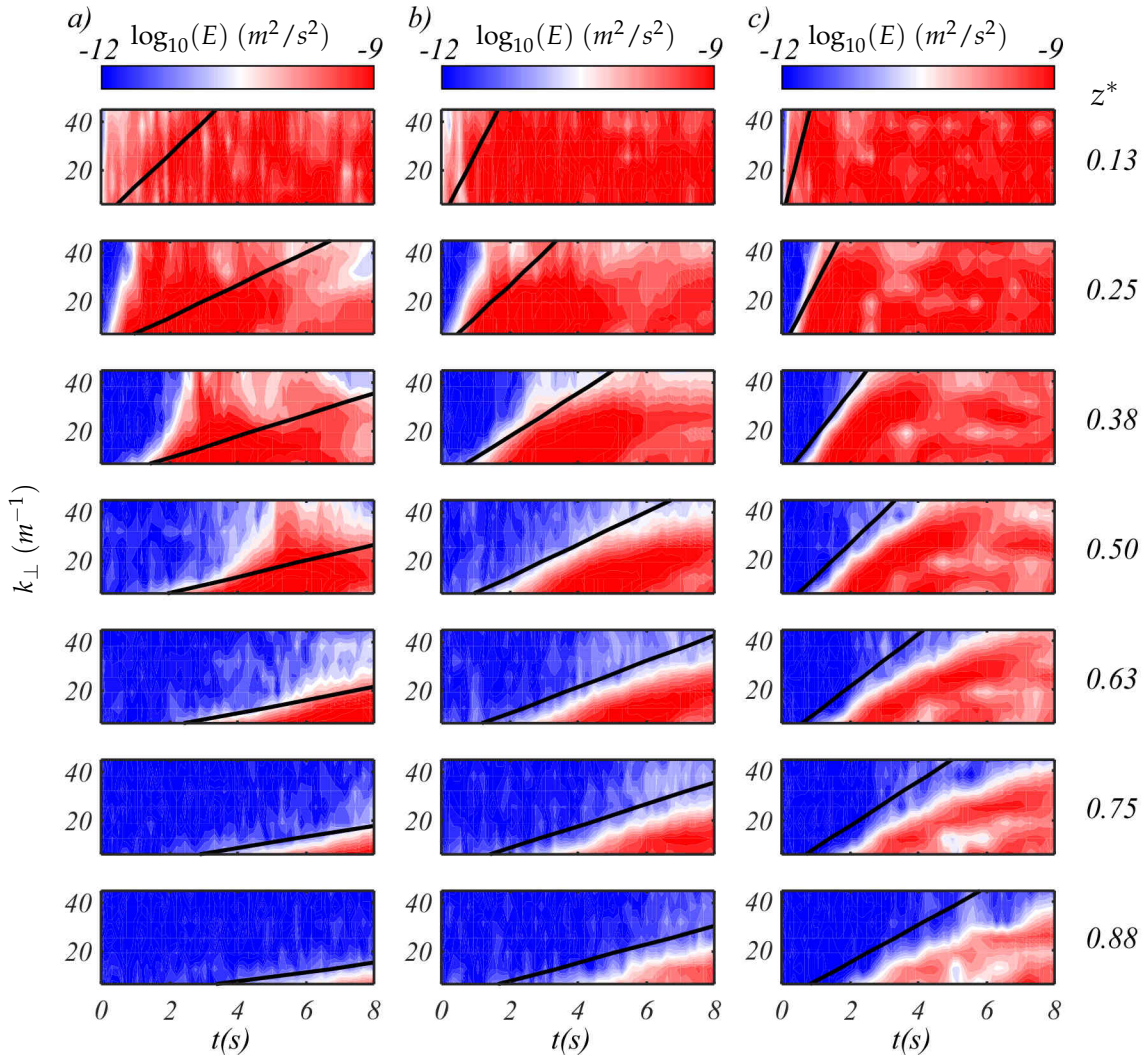

Figure A.14: Contourplots of $E(k_\perp, t)$ across a number of heights z^* at a) $Ek = 17.0 \times 10^{-5}$, b) $Ek = 8.50 \times 10^{-5}$ and c) $Ek = 4.25 \times 10^{-5}$ at $Re_Q = 1200$. Solid black lines represent the predicted shape of the contours assuming propagation is fully driven by LIW theory.

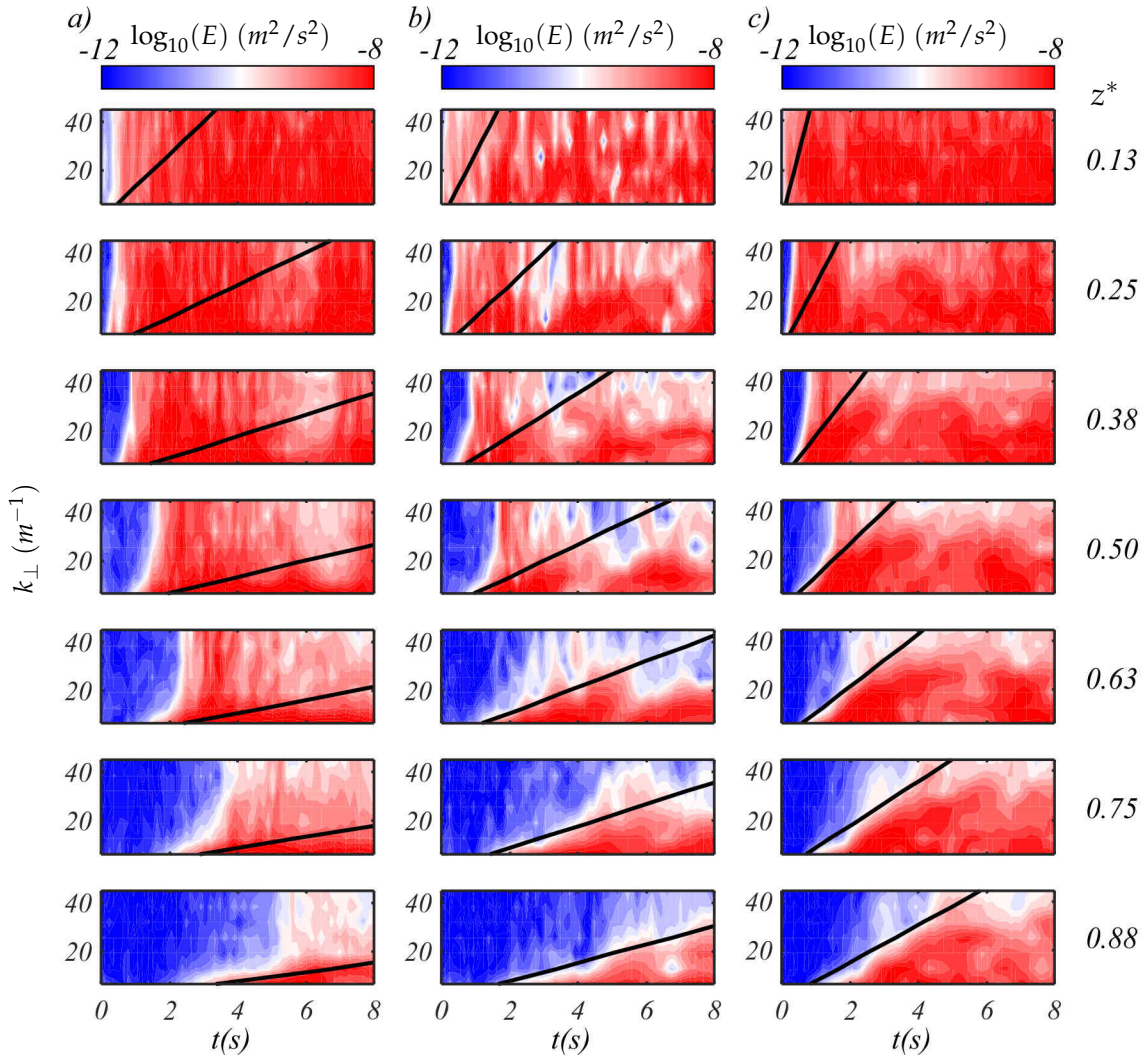

Figure A.15: Contourplots of $E(k_\perp, t)$ across a number of heights z^* at a) $Ek = 17.0 \times 10^{-5}$, b) $Ek = 8.50 \times 10^{-5}$ and c) $Ek = 4.25 \times 10^{-5}$ at $Re_Q = 4000$. Solid black lines represent the predicted shape of the contours assuming propagation is fully driven by LIW theory.

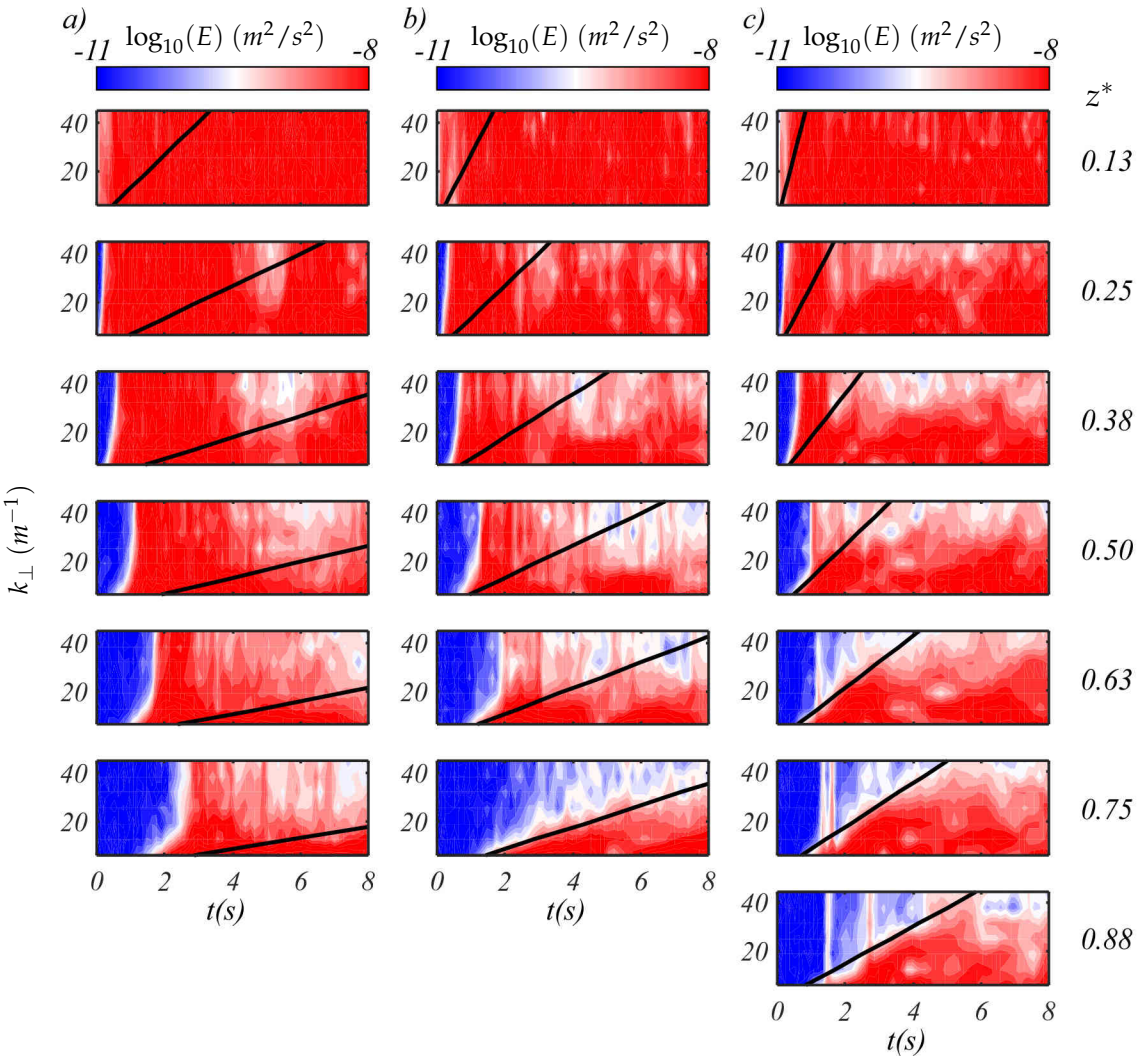

Figure A.16: Contourplots of $E(k_\perp, t)$ across a number of heights z^* at a) $Ek = 17.0 \times 10^{-5}$, b) $Ek = 8.50 \times 10^{-5}$ and c) $Ek = 4.25 \times 10^{-5}$ at $Re_Q = 6000$. Solid black lines represent the predicted shape of the contours assuming propagation is fully driven by LIW theory. Certain contours were excluded due to high experimental errors

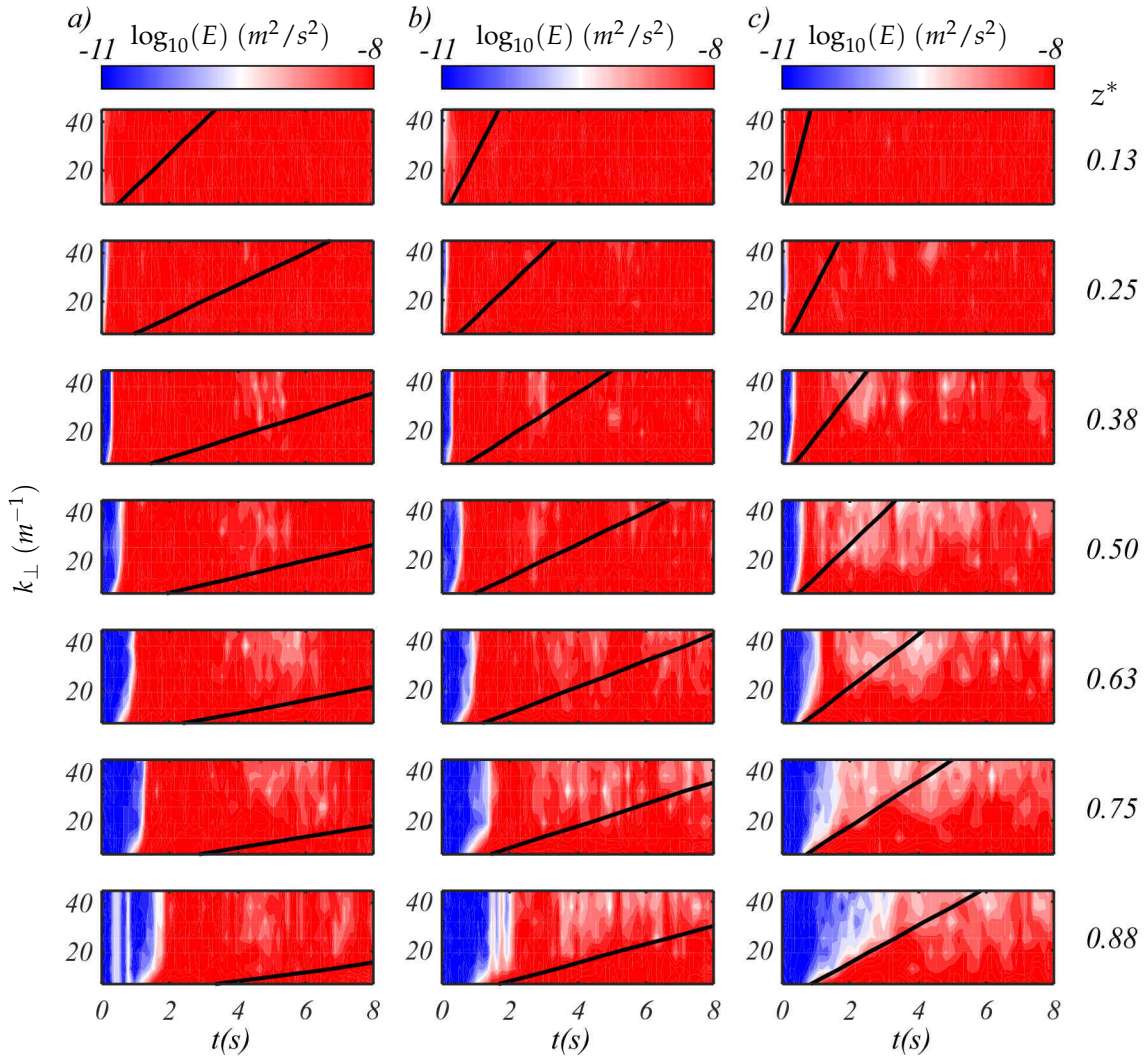

Figure A.17: Contourplots of $E(k_\perp, t)$ across a number of heights z^* at a) $Ek = 17.0 \times 10^{-5}$, b) $Ek = 8.50 \times 10^{-5}$ and c) $Ek = 4.25 \times 10^{-5}$ at $Re_Q = 12000$. Solid black lines represent the predicted shape of the contours assuming propagation is fully driven by LIW theory.

Appendix B

Conferences and Published work

B.1 Conference presentations

European Fluid Mechanics Conference 11 - Seville September 2016 - *On the formation mechanism of columnar structures in rotating turbulent flows* - J.A. Brons, P.J. Thomas and A. Pothérat

European Turbulence Conference 16 - Stockholm August 2017 - *On the formation of columnar structures in rotating turbulent flow fields* - J.A. Brons, P.J. Thomas and A. Pothérat

European Fluid Mechanics Conference 12 - Vienna August 2018 - *A mechanism for the growth of anisotropy in rotating turbulence* - J.A. Brons, P.J. Thomas and A. Pothérat

B.2 Published Work

J.A. Brons, P.J. Thomas and A. Pothérat (2019) *Mean flow anisotropy without waves in rotating turbulence* - arXiv: 1902.07984 - Under review for Phys. Rev. Lett.
J.A. Brons, P.J. Thomas and A. Pothérat (2019) *Transition between advection and inertial wave propagation in rotating turbulence* - arXiv: 1908.05462 - Under review for Journal of Fluid Mechanics

Mean flow anisotropy without waves in rotating turbulence

Jonathan A. Brons[1,2], Peter J.Thomas[1] and Alban Pothérat[2]
[1]*Fluid Dynamics Research Centre, School of Engineering, University of Warwick*
[2]*Centre for Fluid and Complex Systems, Coventry University*
(Dated: February 22nd, 2019)

We tackle the question of how anisotropy develops in flows subject to background rotation, especially turbulent ones. Inertial waves are generally accepted as the most efficient mechanism to transport energy anisotropically. They have been shown to transfer energy to large anisotropic, columnar structures. Nevertheless, they cannot account for the formation of simpler steady anisotropic phenomena such as Taylor columns. Here, we experimentally show that more than one mechanism involving the Coriolis force may promote anisotropy. In particular, in the limit of fast rotation, that is low Rossby number, the anisotropy of the average of a turbulent rotating flow develops neither as the result of inertial waves nor following the same mechanism as in Taylor columns, but from an interplay between the Coriolis force and average advection.

Subjecting a flow to background rotation tends to eliminate variations of velocity along the axis of rotation. The effect, first noticed by Lord Kelvin [1], was famously illustrated when Taylor observed that a fluid column exactly followed the motion of a coin placed at the bottom of a rotating tank [2]. The question of the anisotropic mechanism underlying the development of these columnar structures is, however, still open and is the focus of this work.

The anisotropy of rotating flows is most commonly studied in the context of turbulence in fast rotating systems such as planetary cores, atmospheres and astrophysical systems, where its origin is attributed to the propagation of inertial waves [3, 4]. Two main theories account for the spontaneous formation of large structures in these systems: one invokes nonlinear triadic interactions between inertial waves [5, 6]. The existence of such triads is supported by numerical simulations and by strong experimental [7–9] and numerical [10, 11] evidence of an inverse energy cascade, capable of transferring energy from small and medium scales to large quasi-two dimensional ones. The other theory argues that linear inertial waves account for most of the energy transport in rotating turbulence [12]. This was demonstrated numerically and experimentally in the context of the propagation of transient rotating turbulence [13–15].

None of these theories, however, satisfactorily account for the formation of the steady columns that Taylor observed. Indeed, the analytical solution for these columns [17] is entirely steady and neglects non-rotating inertia, thus excluding inertial waves. We therefore suggest that more than a single mechanism may exist to promote anisotropy of rotating flows and set out to determine conditions in which the best known mechanisms involving inertial waves may not be dominant. Beyond simple steady flows, we seek evidence of such alternative mechanism not involving inertial waves in the average components of turbulent flows, on the grounds these are both steady in nature and subject to the presence of inertial waves inherent to rotating turbulence. As such, they provide the ideal battleground for mechanisms with and without waves to compete.

We first derive scalings characterising anisotropy in steady and turbulent flows. Consider an incompressible flow of Newtonian fluid in a frame of reference rotating at constant angular velocity $\Omega\mathbf{e}_z$. The effect of the Coriolis force on a structure of size l_z along the axis of rotation, $l_\perp$ in the directions perpendicular to it and velocity U is readily seen from the $z-$component of the vorticity equation governing the velocity and vorticity fields $\mathbf{u}$ and ω:

$$\left(\frac{d}{dt}-\nu\Delta\right)\omega_z=\boldsymbol{\omega}\cdot\nabla u_z+2\Omega\partial_z u_z, \tag{1}$$

where, $d/dt=\partial_t+\mathbf{u}\cdot\nabla$. In the limit $\Omega\to\infty$ the flow is columnar, with $\partial_z u_z=0$, which implies $-\nabla_\perp\cdot\mathbf{u}_\perp=0$. For finite rotation, a horizontally divergent flow exists and the Coriolis force associated to it must be balanced either by inertial or viscous forces [18]. The divergent flow is estimated by means of the z-component and the divergence of the momentum equation.

$$\left(\frac{d}{dt}-\nu\Delta\right)u_z=-\partial_z\frac{p}{\rho}, \tag{2}$$

$$\nabla\cdot(\mathbf{u}\cdot\nabla\mathbf{u})=2\Omega\omega_z-\Delta\frac{p}{\rho}. \tag{3}$$

In both Taylor's experiment [2] and Moore & Saffman's analytical solution [17], inertia is neglected. In this limit (3) implies that the pressure is geostrophic $p=2\rho\Omega\Delta^{-1}\omega_z$, where the inverse of the Laplacian Δ^{-1} is defined with boundary conditions prescribed by the geometry. The rotational part of the Coriolis force can thus be expressed by virtue of (2) as [31]

$$2\Omega\partial_z u_z=4\frac{\Omega^2}{\nu}\partial_{zz}^2\Delta^{-2}\omega_z. \tag{4}$$

An almost identical mathematical form exists for the Lorentz force in electrically conducting fluids pervaded by an imposed magnetic field $B\mathbf{e}_z$, where it expresses that the Lorentz force diffuses momentum along $\mathbf{e}_z$ [19]. This finding was experimentally verified, establishing that the diffusive nature of the Lorentz force persists both in viscous and inertial regimes, albeit with different characteristic diffusion lengthscales [19–21]. In rotating flows explored here, the Coriolis force is of diffusive nature in

the inertialess limit. Its diffusion lengthscale along $\mathbf{e}_z$ follows from introducing (4) into (1) and applying scaling arguments [31]:

$$l_z^\nu(l_\perp) \sim l_\perp \frac{2\Omega l_\perp^2}{\nu} = l_\perp \frac{l_\perp^2}{H^2} E^{-1}, \tag{5}$$

where the Ekman number $E = \nu/2\Omega H^2$ represents the ratio of Coriolis to viscous forces, based on the domain height H (cf. fig.1). This lengthscale recovers the columnar lengthscale implied in Ref. [17]'s analytical solution. l_z^ν can be interpreted as the distance needed for viscous effects to exhaust the horizontally divergent flow that drives the column.

In contrast to Taylor's flow [2], inertia dominates in turbulent flows and balances the Coriolis force associated to the horizontally divergent flow in (1). Using this assumption and a similar derivation as for l_z^ν leads to an inertial scaling for l_z:

$$l_z^I(l_\perp) \sim \frac{2\Omega l_\perp^2}{U} = l_\perp Ro(l_\perp)^{-1}, \tag{6}$$

where the Rossby number $Ro(l_\perp) = U/2\Omega l_\perp$ represents the ratio of inertial to Coriolis forces at the scale of the structure considered.

To isolate the mechanisms controlling anisotropy, we consider a forced, anisotropic turbulent flow with non-zero average flow at large Reynolds number. A benefit of this choice of flow is that mechanisms controlling the anisotropy of the average flow that do not involve waves, as in Taylor columns, can be captured by simple event-averaging. At the same time, since turbulent fluctuations under strong rotation support inertial waves, these can potentially affect the anisotropy of the average flow. For these reasons, a turbulent flow with an average flow component offers a good testing ground to identify the conditions in which either propagative or wave-free mechanisms drive anisotropy. We start by deriving the equations for the average quantities: decomposing all quantities into their average and fluctuations, *e.g.* $\mathbf{u} = \langle \mathbf{u} \rangle + \mathbf{u}'$. Taking the average of (1)-(3), neglecting viscous friction yields:

$$\begin{aligned} \langle \mathbf{u} \rangle \cdot \nabla \langle \omega_z \rangle = \langle \boldsymbol{\omega} \rangle \cdot \nabla \langle u_z \rangle + 2\Omega \partial_z \langle u_z \rangle \\ + \langle \boldsymbol{\omega}' \cdot \nabla u_z' \rangle - \langle \mathbf{u}' . \nabla \omega_z' \rangle, \end{aligned} \tag{7}$$

$$\langle \mathbf{u} \rangle \cdot \nabla \langle u_z \rangle = \partial_z \frac{\langle p \rangle}{\rho} - \langle \mathbf{u}' . \nabla u_z' \rangle, \tag{8}$$

$$\Delta \frac{\langle p \rangle}{\rho} = 2\Omega \langle \omega_z \rangle - \nabla \cdot \langle \mathbf{u} \cdot \nabla \mathbf{u} \rangle. \tag{9}$$

In (9), $|\nabla \cdot \langle \mathbf{u} \cdot \nabla \mathbf{u} \rangle| / |\Omega \langle \omega_z \rangle| = \mathcal{O}(Ro)$, so for fast rotating turbulence ($Ro \ll 1$), the average pressure is mostly governed by a geostrophic balance

$$\frac{\langle p \rangle}{\rho} = 2\Omega \Delta^{-1} \langle \omega_z \rangle + \mathcal{O}(U^2 Ro). \tag{10}$$

Scaling arguments do not permit us to further simplify (8),(7). The reason is that since columnar structures are far longer than wide ($l_z^I \gg l_\perp$),$z-$derivatives can be approximated as $\partial_z \sim (l_z^I)^{-1}$, implying that all terms in (8) are $\mathcal{O}(U^2/l_\perp)$ and all terms in (7) are $\mathcal{O}(U^2/l_\perp^2)$. The potential influence of fluctuations on the anisotropy of the average flow can, however, be analysed by experimentally evaluating the magnitude of all the terms in (7) and (8). Of particular interest are the last two terms in (7) and the last term in (8) as fluctuations and thus inertial waves, can only affect the average flow through them.

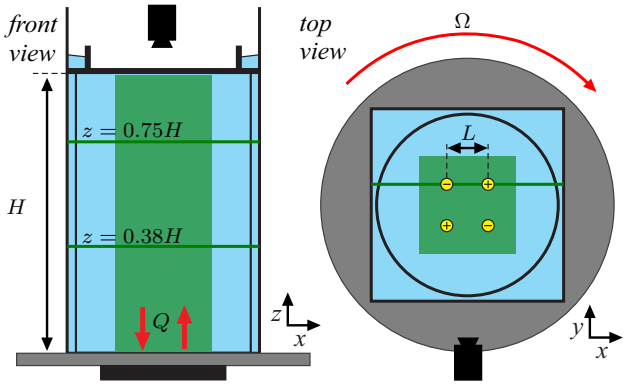

FIG. 1. Sketch of experimental setup. Green regions and lines show areas and positions of PIV planes used during measurements.

The experimental setup consists of a rectangular tank (600 mm×320 mm×320 mm) fitted at the centre of a rotating turntable. The flow is forced by injecting and subtracting fluid through four holes (diameter d = 1 mm) located at the corners of a L =53 mm square in the bottom wall of the tank (Fig. 1). All holes are connected to a peristaltic pump simultaneously injecting fluid through holes along one diagonal of the square and sucking fluid through the others, at the same constant flowrate Q through each hole. A cylinder (height 400 mm, ⌀ 300 mm) closed by a top transparent lid placed inside the tank prevents free surface deformation and provides a viewing window for the optical measurements. The setup is spun up into solid body rotation at a rotation speed Ω, before the pump is initiated. Prior to measurements, the flow is left to settle to ensure a statistically steady state. Statistical steadiness was ensured through convergence of statistical quantities around 1%.

The governing parameters are the Ekman number $E = \nu/2\Omega H^2$ and a forcing-based Reynolds number, $Re_Q = 4Q/\pi\nu d$. They are independently controlled by Ω and Q. The flow intensity is measured *a posteriori* by means an average-based and a fluctuations-based Rossby number $Ro = \langle |\mathbf{u}| \rangle_{\mathbf{x}t} / 2\Omega L$ and $Ro' = \langle |\mathbf{u}'^2| \rangle_{\mathbf{x}t}^{1/2} / 2\Omega L$, built on time and space averages $\langle \cdot \rangle_{\mathbf{x}t}$ over the horizontal visualisation plane at $z = 0.75H$. Experiments are performed over a range of parameters spanning $E = \{4.25, 5.67, 8.59, 17, 34\} \times 10^{-5}$ and $3 \times 10^2 \leq Re_Q \leq 1.5 \times 10^4$. In this range, the jets

penetrating the flow are always turbulent [22]. Velocity fields are measured with a 2D-PIV system: a laser sheet illuminates horizontal planes (HP) at $z = 0.38H$ or $z = 0.75H$, or a vertical plane (VP) aligned on a injection/subtraction pair. For visualisations in the HP, a 1.3MP CMOS camera records a 150 mm × 150 mm area centred on the tank at 30 fps. For the VP experiments, two cameras record an area of 400 mm ×150 mm at 60 fps along the tank. The smallest resolvable lengthscale is 2.1 mm in all planes.

Evaluating $\langle \boldsymbol{\omega}' \cdot \nabla u_z' \rangle$, $\langle \mathbf{u}' \cdot \nabla \omega_z' \rangle$ and $\langle \mathbf{u}' \cdot \nabla u_z' \rangle$, requires calculating expressions such as $\partial_z \omega_z$ that are not all directly accessible from 2D-PIV data. However, the symmetry of the forcing and the geometry allows us to assume identical statistical properties in the x and y directions, so that $|\langle \mathbf{u}' \cdot \nabla u_z' \rangle| \simeq 2|\langle u_x' \partial_x u_z' \rangle| = |\langle \mathbf{u}' \cdot \nabla u_z' \rangle|^e$ [31]. With the additional use of classical inequalities, an upper bound estimate is obtained for $|\langle \boldsymbol{\omega}' \cdot \nabla u_z' \rangle| \leq 2\langle |\omega_y'|^2 \rangle^{1/2} \langle |\partial_x u_z'| \rangle^{1/2} + \langle |\omega_z'|^2 \rangle^{1/2} \langle |\partial_z u_z'|^2 \rangle^{1/2} = |\langle \boldsymbol{\omega}' \cdot \nabla u_z' \rangle|^e$. All terms are evaluated from VP-PIV except $\langle |\omega_z'|^2| \rangle^{1/2}$, obtained from HP-PIV. Similarly, $|\langle \mathbf{u}' \cdot \nabla \omega_z' \rangle| \leq |\langle u_x' \partial_x \omega_z' \rangle + \langle u_y' \partial_y \omega_z' \rangle| + \langle |u_z'|^2 \rangle^{1/2} \langle |\partial_z \omega_z'|^2 \rangle^{1/2} = |\langle \mathbf{u}' \cdot \nabla \omega_z' \rangle|^e$.

Additionally, contributions from inertial waves to these terms are estimated by filtering out velocity and vorticity components whose frequency exceeds the maximum possible frequency of inertial waves, 2Ω [23]. An upper bound for the contribution of inertial waves is obtained by assuming that all remaining fluctuations in terms filtered in this way result from inertial waves (subscript IW). This assumption makes it possible to evaluate $\langle |\partial_z \omega_z'|^2 \rangle^{1/2}$, replacing ∂_z by an upper estimate $V_I(H)\partial_t$, where $V_I(H)$ is the fastest inertial wave group velocity, *i.e.* that associated to the largest possible scale in the vessel, H.

For the range of parameters we consider, turbulent jets form above the two injection/subtraction points and feed a small turbulent patch dominated by inertia rather than by the Coriolis force. This patch extends to a critical height h_p such that the local Rossby number at h_p reaches unity. A similar patch exists in turbulent convective plumes under the effect of rotation [24]. Columnar structures develop above the patch where $z > h_p$. Vertical lengthscales l_z and l_z', associated to their average and velocity fluctuations are obtained from VP experiments using two-point velocity correlations $C_{u_x}(\delta z)$ and $C_{u_x'}(\delta z)$ respectively calculated from the full velocity field u_x or its fluctuating part u_x' [25], where δz is the separation between two points along the $z-$axis. In practice, neither $C_{u_x}(\delta z)$ nor $C_{u_x'}(\delta z)$ fully decorrelate over $h_p \leq z \leq H$. Hence, following [14], l_z and l_z' are defined at an arbitrary value $\beta = 0.5$ of the correlations, rather than 0. From Figure 2, both l_z and l_z' follow the $l_z \sim LRo^{-1}$ scaling (6). This confirms that columns above the turbulent patch form under the combined influence of the Coriolis forces and inertia. Inertia may however be associated to the average flow or to fluctuations, which in turn may be either random or driven by inertial waves. Evaluating the relative importance of the terms in equations (7−9) shall therefore highlight the flow regimes where either inertial waves or static forces are active. For this, we first need to distinguish random turbulent fluctuations from inertial waves.

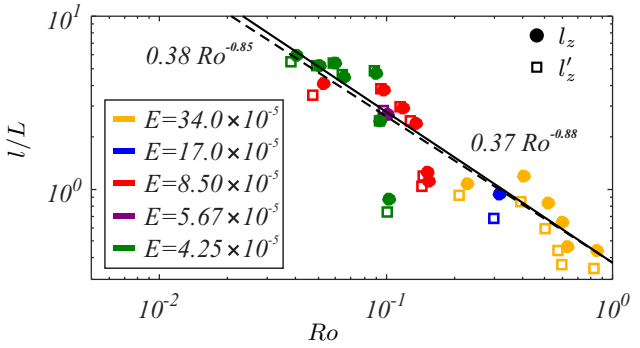

FIG. 2. Columnar structure length l_z based on u_x and l_z' based on u_z' normalised by L. Ro based on $|\mathbf{u}|$ and $|\mathbf{u}'|$ respectively. Solid and dashed black line show a fit of l_z and l_z' data respectively.

In the limit of fast rotation ($Ro \to 0$), inertial waves carry a significant share of the overall turbulent kinetic energy [26, 27]. To quantify this share, we split the turbulent energy spectrum into fluctuations of frequency f greater than the maximum frequency of inertial waves 2Ω [23], and fluctuations of frequency $f < 2\Omega$, which may result from inertial waves or from random turbulence. The ratio of the total energy contained in the lower part of the spectrum E'_{IW} to the total energy E' provides an upper bound for the fraction of the turbulent kinetic energy carried by inertial waves. Though global, this approach is similar to [28]'s scale-dependent disentanglement method.

Figure 3 shows that most of the fluctuations' kinetic energy lies within the spectral range of inertial waves provided $Ro \gtrsim 10^{-2}$ and $Re_Q < 4000$. The sharp drop of energy in the spectra precisely at $f = 2\Omega$ (Fig. 4a) suggests that the ratio E'_{IW}/E' indeed reflects the relative importance of inertial waves. The lower limit ($Ro < 10^{-2}$) coincides with a regime of weaker turbulence, dominated by 4 robust columnar structures sitting above the turbulent patch and aligned with the 4 injection/subtraction holes.

For $10^{-2} \leq Ro \leq 10^{-1}$, the angle of propagation θ of waves radiated from the turbulent patch is isolated by filtering $\mathbf{u}'$ at a specific frequency $f < 2\Omega$ (Fig.4b,c) following [29]. The relation between f and θ on Fig. 4c precisely follows the dispersion relation of inertial waves $f/2\Omega = \cos\theta$ [23], thus confirming that they account for most of the $f < 2\Omega$ part of the turbulent spectrum. The absence of inertial waves in the higher range of either Ro or Re_Q, reflects their disruption by random turbulence. In freely decaying turbulence, this phenomenon is controlled by the ratio between inertia and the Coriolis force, and takes place at $Ro' \gtrsim 0.4$ [14]. Here, inertial waves vanish for $Re_Q \gtrsim 10^4$, independently of the intensity of the Coriolis force, most likely on the

grounds that both the inertial waves and the inertia that disrupt them are driven by fluctuations in the turbulence patch whose intensity is entirely controlled by inertia.

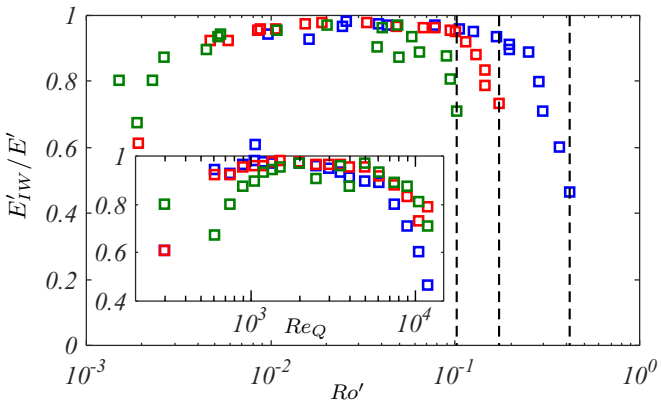

FIG. 3. Upper bound of energy carried by inertial wave fluctuations to energy carried by the fluctuations *vs.* Ro' at $z = 0.75H$ for various E. (inset) Same ratio *vs.* Re_Q. Same colour legend as Fig.2

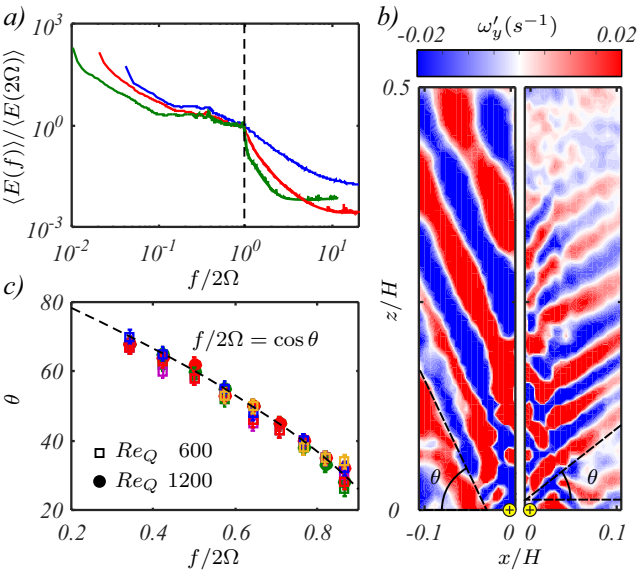

FIG. 4. a) Power spectra for $Re_Q = 2000$. b) Contours showing inertial waves radiated at angle θ from the turbulent patch at $f/2\Omega = 0.34$ (left), 0.76 (right) and $Re_Q = 1200$. c) Angle θ *vs.* f. Dashed line: dispersion relation for inertial waves [23]. Same colour legend as Fig.2

We are now in a position to estimate the nature and the magnitude of the contribution to anisotropy due to fluctuations arising from inertial waves in (7-9). From, figure 5a, the ratio $|\langle \mathbf{u}'\cdot\nabla u'_z\rangle|^e_{\rm IW}/|\langle \mathbf{u}\rangle\cdot\nabla\langle u_z\rangle|$ scales as Ro^2 both in the lower ($z = 0.38H$) and upper ($z = 0.75H$) parts of the flow for $Ro \lesssim 0.15$. For $Ro \gtrsim 2\times10^{-2}$, fluctuations due to inertial waves are greater than inertia due to the average flow and therefore balance the pressure gradient in (8). For $Ro \lesssim 2\times10^{-2}$, by contrast, this ratio becomes lower than unity and in the limit $Ro \to 0$, fluctuations due to inertial waves play no part in determining $\langle u_z\rangle$. It follows from (8) and (10) that in this limit,

$$\langle \mathbf{u}\rangle\cdot\nabla\langle u_z\rangle = 2\Omega\Delta^{-1}\partial_z\langle\omega_z\rangle + \mathrm{FT} + \mathcal{O}(Ro), \quad (11)$$

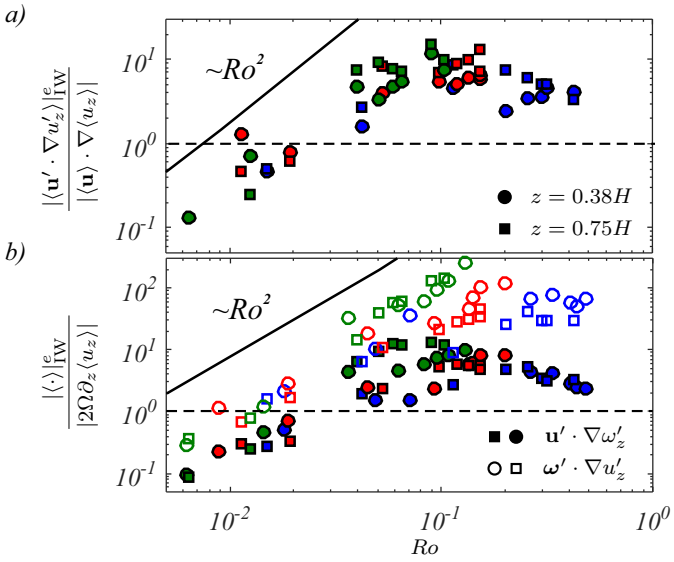

FIG. 5. a) Ratio $|\langle \mathbf{u}'\cdot\nabla u'_z\rangle|^e_{\rm IW}/|\langle \mathbf{u}\rangle\cdot\nabla\langle u_z\rangle|$ at $z = 0.38H$ (circles) and $z = 0.75H$ (squares). b) Ratio of $|\langle \mathbf{u}'\cdot\nabla\omega'_z\rangle|^e_{\rm IW}$ (closed symbols) and $|\langle \boldsymbol{\omega}'\cdot\nabla u'_z\rangle|^e_{\rm IW}$ (open symbols) to $|2\Omega\partial_z\langle u_z\rangle|$. Same colour legend as Fig.2.

where FT stands for any term involving fluctuations not due to inertial waves. Consequently, if inertial waves are to influence the anisotropy of the mean flow, they can only do so through the last two terms of (7).

Their part in this process is measured by the ratio of their contribution to inertial terms $|\langle \mathbf{u}'\cdot\nabla\omega'_z\rangle|$ and $|\langle \boldsymbol{\omega}'\cdot\nabla u'_z\rangle|$ (whose estimates are denoted $|\langle \mathbf{u}'\cdot\nabla\omega'_z\rangle|^e_{\rm IW}$ and $|\langle \boldsymbol{\omega}'\cdot\nabla u'_z\rangle|^e_{\rm IW}$) to the Coriolis term $|2\Omega\partial_z\langle u_z\rangle|$. From figure 5b, the variations of these ratios with Ro exhibit the same two regimes singled out in the analysis of (8). For $Ro \gtrsim 2\times10^{-2}$, they are greater than unity and grow until they saturate at values between 10 and 10^2. The saturation coincides with the regimes where inertial waves are superseded by random fluctuations (see figure 3), and marks the end of the rotation-dominated turbulent regime. For $Ro > 0.1$ and below the saturation, on the other hand, inertial waves dominate and (7) chiefly expresses a transfer of energy between them and the mean flow. For $Ro \lesssim 2\times10^{-2}$ and in the limit $Ro \to 0$, the mean Coriolis term dominates in (7) and from (11), it directly determines the flow anisotropy according to

$$\left(\langle \mathbf{u}\rangle\cdot\nabla\right)^2\langle\omega_z\rangle - \langle \mathbf{u}\rangle\cdot\nabla\left(\langle\boldsymbol{\omega}\rangle\cdot\nabla\langle u_z\rangle\right) \simeq 4\Omega^2\partial^2_{zz}\Delta^{-1}\langle\omega_z\rangle - 2\Omega\partial_z\langle \mathbf{u}\rangle\cdot\nabla\langle u_z\rangle + \mathrm{FT}. \quad (12)$$

Eq.(12) establishes our main result: in the limit $Ro \to 0$, time-dependent inertial waves are not part of the mechanism driving the anisotropy of the average turbulent flow in background rotation. The actual mechanism involves a balance between advection of the average flow and the

Coriolis force. From this point of view, it also differs from the diffusive process underpinning the formation of Taylor columns. In both cases, however, anisotropy is materialised by a horizontally divergent flow either driven by inertia (turbulent flows) or by viscous friction (Taylor columns). It is also noteworthy that in the limit $Ro \to 0$, $l_z^I(l_\perp)/h \to \infty$ for all scales $l_\perp$, and the flow becomes quasi-two dimensional. Hence, our main results also implies that inertial waves are not responsible for the two-dimensionalisation of the average flow either.

ACKNOWLEDGEMENTS

The authors would like to acknowledge support from the Engineering and Physical Sciences Research Council [grant number GR/N64519/01] for the manufacture of the rotating turntable facility and B. Teaca for computational resources used in processing experimental data. AP aknowledges support from the Royal Society under the Wolfson Merit Award Scheme

[1] J. Thomson, Letter to Lord Kelvin (W.Thomson), Glasgow University Library, MS Kelvin T120 (1868)
[2] G.I. Taylor, Royal Society of London A **102**, 180 (1922)
[3] P.A. Davidson, *Turbulence in Rotating, Stratified and Electrically Conducting Fluids* (Cambridge University Press, Cambridge, England, 2013)
[4] E. J. Hopfinger, F. K. Browand, and Y. Gagne, J. Fluid Mech. **125**, 505 (1982)
[5] L.M. Smith and F. Waleffe, Phys. Fluids **11**, 1608 (1999)
[6] C. Cambon and J.F. Scott, Annu. Rev. Fluid Mech. **31**, 1 (1999)
[7] C. Lamriben, P.P. Cortet, and F. Moisy, Phys. Rev. Lett. **107**, 024503 (2011)
[8] M. Duran-Matute, J.B. Flor, F.S. Godeferd and C. Jause-Lambert, Phys. Rev. E **87**, 041001 (2013)
[9] A. Campagne, B. Gallet, F. Moisy and P.P. Cortet, Phys. Fluids **26**, 125112 (2014)
[10] Q. Chen, S. Chen, G.L. Eyink and D.D. Holm, J. Fluid Mech. **542**, 139 (2005)
[11] L. M. Smith, J. R. Chasnov, and F.Waleffe, Phys. Rev. Lett. **77**, 2467 (1996)
[12] P.A. Davidson, P.J. Staplehurst and S.B. Dalziel, J. Fluid Mech. **557**, 135 (2006)
[13] I. Kolvin, K. Cohen, Y. Vardi and E. Sharon, Phys. Rev. Lett. **102**, 014503 (2009)
[14] P.J. Staplehurst, P.A. Davidson and S.B. Dalziel, J. Fluid Mech. **598**, 81 (2008)
[15] B. Screenivasan and P.A. Davidson, Phys. Fluids **20**, 085104 (2008)
[16] D.W. Moore and P.G. Saffman, J. Fluid Mech **31** (4), 635 (1968)
[17] D.W. Moore and P.G. Saffman, J. Fluid Mech **39** (4), 831 (1969)
[18] A. Pothérat, EPL **98**, 64003 (2012)
[19] J. Sommeria and R. Moreau, J. Fluid Mech. **118**, 507 (1982)
[20] A. Pothérat and R. Klein, J. Fluid Mech. **761**, 168 (2014)
[21] N.T. Baker, A. Pothérat, L. Davoust and F. Debray, Phys. Rev. Lett. **120**, 224502 (2018)
[22] S.B. Pope, *Turbulent Flows* (Cambridge University Press, Cambridge, England, 2000)
[23] H.P. Greenspan, *The Theory of Rotating Flows* (Cambridge University Press, Cambridge, England, 1986)
[24] T. Maxworthy and S. Narimousa, J. Phys. Ocean. **24** (1994)
[25] K. Aujogue, A. Pothérat B. Screenivasan and F. Debray, J. Fluid Mech. **843**, 355 (2018)
[26] E. Yarom and E. Sharon, Nature Physics **10**(7), 510 (2014)
[27] P.C. di Leoni, P.J. Cobelli, P.D. Mininni, P. Dmitruk and W.H. Matthaeus, Phys. Fluids **26** 035106 (2014)
[28] A. Campagne, B. Gallet, F. Moisy and P.P. Cortet, Phys. Rev. E **91**, 043016 (2015)
[29] P.P. Cortet, C. Lamribem and F. Moisy, Phys. Fluids **22**, 086603 (2010)
[30] J. Pedlosky, *Geophysical Fluid Dynamics* (Springer, New York, 1987)
[31] J.A. Brons, PhD, Coventry University, University of Warwick (2019)

Transition between advection and inertial wave propagation in rotating turbulence

Jonathan A. Brons[1,2]†, P. J. Thomas[1] and A. Pothérat[2]

[1]Fluid Dynamics Research Centre, University of Warwick, Coventry, UK

[2]Fluid and Complex Systems Research Centre, Coventry University, Coventry, UK

(Received xx; revised xx; accepted xx)

In turbulent flows subject to strong background rotation, the advective mechanisms of turbulence are superseded by the propagation of inertial waves, as the effects of rotation become dominant. While this mechanism has been identified experimentally (Dickinson & Long 1983; Davidson *et al.* 2006; Staplehurst *et al.* 2008; Kolvin *et al.* 2009), the conditions of the transition between the two mechanisms are less clear. We tackle this question by means of an experiment where we track the turbulent front away from a solid wall where fluid is injected in an otherwise quiescent fluid. Without background rotation, this apparatus generates a turbulent front whose displacement recovers the $z(t) \sim t^{1/2}$ law classically obtained with an oscillating grid (Dickinson & Long 1978) and we further establish the scale-independence of the associated transport mechanism. When the apparatus is rotating at a constant velocity perpendicular to the wall where fluid is injected, not only does the turbulent front become mainly transported by inertial waves, but advection itself is suppressed because of the local deficit of momentum incurred by the propagation of these waves. Scale-by-scale analysis of the displacement of the turbulent front reveals that the transition between advection and propagation is local both in space and spectrally, and takes place when the Rossby number based on the considered scale is of unity. The transition also took place during the evolution of the front: in almost all experiments, we observed that at certain scales, given fluctuations where first advected by the local velocity of fluid injection until the propagation of inertial waves exceeded the local velocity, at which point propagation by inertial waves of that scale took over.

Key words:

---

1. Introduction

The main transport mechanism in turbulent flow is advection. When turbulent flows are subject to background rotation, however, inertial waves offer an additional transport mechanism. The competition between them determines the anisotropy and transport properties of rotating turbulence. Here we determine the conditions in which either of them dominates, and especially the scale dependence of this competition.

Turbulence in rotation arises in a variety of industrial and natural contexts, such as centrifuges, precessing spacecraft or oceanographic and atmospheric flows (Vanyo 1993; Davidson 2013, 2015), where its specific transport and dissipative properties influence or even govern the dynamics of the processes involved. Its most distinctive feature is to form large, somewhat columnar structures aligned with the rotation that are perhaps

† Email address for correspondence: ac2002@coventry.ac.uk

most conspicuous in geophysical flows (Pedlosky 1987). The emergence of columnar structures in rotating flow was first reported in a letter by Kelvin (Thomson 1868) and subsequently illustrated in Taylor's famous experiment (Taylor 1922). Since then, a number of experiments and numerical simulations have reported the emergence of such columns in turbulent flows (Hopfinger *et al.* 1982; Bartello *et al.* 1994; Gallet 2015) and several scenarii have been proposed to explain their appearance. Underlying the question of how large columnar structures emerge, is the question of the processes by which rotating flows and rotating turbulence transport momentum and energy. This question itself hinges on the role played by two essential ingredients of rotating turbulence. The first one is the propagation mechanism associated to linear inertial waves (see Greenspan (1968) for the theory of these waves): for a wavevector $\mathbf{k}$, with frequency ω and background rotation Ω, inertial waves follow the dispersion relation, and associated group velocity

$$\omega = \pm 2\Omega \cdot \mathbf{e}_k, \qquad \mathbf{v}_g = \pm \frac{2}{k} \mathbf{e}_k \times (\Omega \times \mathbf{e}_k), \tag{1.1}$$

where $\mathbf{e}_k = \frac{1}{k}\mathbf{k}$. The preferential transport of momentum along the rotation by inertial waves indeed elongates an initially isotropic blob of vorticity along the axis of rotation at a speed of Ωt (Davidson *et al.* 2006). The second ingredient involves non-linear interactions (Cambon *et al.* 1997; Smith & Waleffe 1999; Cambon & Scott 1999). In this process, triadic interactions feed an inverse energy cascade towards large scales while non-resonant triads or quartets of waves transfer energy to modes aligned with the axis of rotation. This scenario is supported by numerical simulations and by strong experimental and numerical evidence of an inverse energy cascade (Campagne *et al.* 2014). However, Taylor's early experiments in a steady, laminar flow still exhibit anisotropic transport of momentum along the rotation in the absence of waves and non-linearities. This waveless and linear anisotropic transport was indeed recovered in the analytical work of Moore & Saffman (1968, 1969), and Pothérat (2012), and suggests that more than a single transport mechanism may exist in rotating flows. Along this line, our recent experiments showed that even in turbulent flows, the anisotropy of the mean flow may not necessarily result from the action of inertial waves or triadic interactions (Brons *et al.* 2019). Instead, average anisotropy may emerge from an interplay between rotation and nonlinear advection, somewhat similar to the interplay between viscous diffusion and rotation in Taylor's laminar flow experiment. Advection and propagation of inertial waves were even found to simultaneously act on fluctuations in nearly two-dimensional flows: while larger scale fluctuations satisfied the dispersion relation for inertial waves, smaller scales behaved as inertial inertial waves "swept" by the surrounding velocity field of the large quasi-two dimensional structures (Campagne *et al.* 2015).

With different mechanisms at play, the question arises of their precise domain of action, both in terms of the scales concerned and the main control parameter, the Rossby number $Ro = U/2\Omega l$, that controls the ratio of inertial to Coriolis forces (U and l are typical velocity and lengthscale.) One way to tackle the problem experimentally is to track the displacement of a turbulent front when the turbulence is produced by a localised forcing mechanism and progressively invades a domain of otherwise quiescent fluid. Most experiments of this type involve either jets along the rotation axis or oscillating grids, as respectively pioneered by McEwans (1976) and Dickinson & Long (1983). The latter showed that the position of the turbulent front evolved as $z_f \sim t^{1/2}$ as long as the local Rossby number based on z remained greater than unity. Past this point, Ro decreases, turbulence starts to exhibit wave patterns and the front travels as $z_f \sim \Omega t$, as consistent with the group velocity of inertial waves.

Grid experiments (Staplehurst *et al.* (2008)), on the formation of columnar structures in rotating turbulence, revealed that around a local critical Rossby number $Ro^{crit} \sim 0.4$ the flow transitions from a state where energy and momentum are mostly propagated by inertial waves (below Ro^{crit}) to one where they are mostly transported through advection. A recent numerical study on rotating turbulence ignited by a buoyancy anomaly showed that this transition could be spatially localised with regions dominate by inertial waves, while others where they are absent (McDermott & Davidson (2019)). This authors also confirmed a critical value of the Rossby number for this transition around 0.5, provided it is built on the correct large scale.

Recent scale-by-scale analysis of the turbulent front further showed that fluctuations were propagated at the group velocity of inertial waves corresponding to their length-scales, in the limit of strong rotation $Ro \ll 1$ (Kolvin *et al.* (2009), turbulence initiated by jets). In statistically steady turbulence, jet experiments (Yarom & Sharon (2014), $0.006 \leqslant Ro \leqslant 0.2$), and experiments with a 2D mechanical forcing (Campagne *et al.* 2015) confirmed that some of the fluctuations of frequency lower than 2Ω, the maximum frequency of inertial waves, satisfied the dispersion relation for inertial waves (but for the sweeping effect at high wavenumbers identified by Campagne *et al.* (2015)). The recent experiments of Burmann & Noir (2018) showed that inerial waves of a wide range of lengthscales emitted by a topography near an Ekman wall could speed up momentum transfer along the rotation axis and lead to an accelerated spin-up time following a step change in the rotation of a cylindrical vessel.
Although the role of inertial waves is clearly established in the limit $Ro \ll 1$ and in regions of the spectrum where $\omega \leqslant 2\Omega$, the limits of their regime of influence remains unclear, especially in terms of the lengthscales concerned. Both Dickinson & Long (1983) and Staplehurst *et al.* (2008) found that the momentum transport mechanism transitions from propagative regime to an advective one around Ro of the order of unity, however the scale-depenence of this transition remains unexplored. We set out to examine this specific question and, in particular, the scale dependence of the transport mechanisms in a transient turbulent flow under the effect of background rotation. We specifically target regimes where rotation may not dominate over the entire turbulent spectrum. The specific questions we seek to answer are:

(i) Is there a clear scale separation (in terms of the control parameter and the scales concerned) between advective or non-linear mechanisms on one side, and propagation on the other ?
(ii) if so, what is the quantitative threshold defining such a separation ?

Our approach relies on the tracking of the turbulent front in a flow forced by turbulent jets, with data processing techniques similar to those introduced by Kolvin *et al.* (2009) to analyse the scale dependence. The choice of a transient flow presents the advantage that momemtum transport can be easily characterised by tracking the progression of the turbulent front. The experimental setup is described in section 2. To first characterise the phenomenology of pure advection in our experimental setup, we first analyse non-rotating turbulence in the spirit of Dickinson & Long (1983) (section 3), before running experiments at several rotational velocities (section 4) and drawing conclusions (section 5).

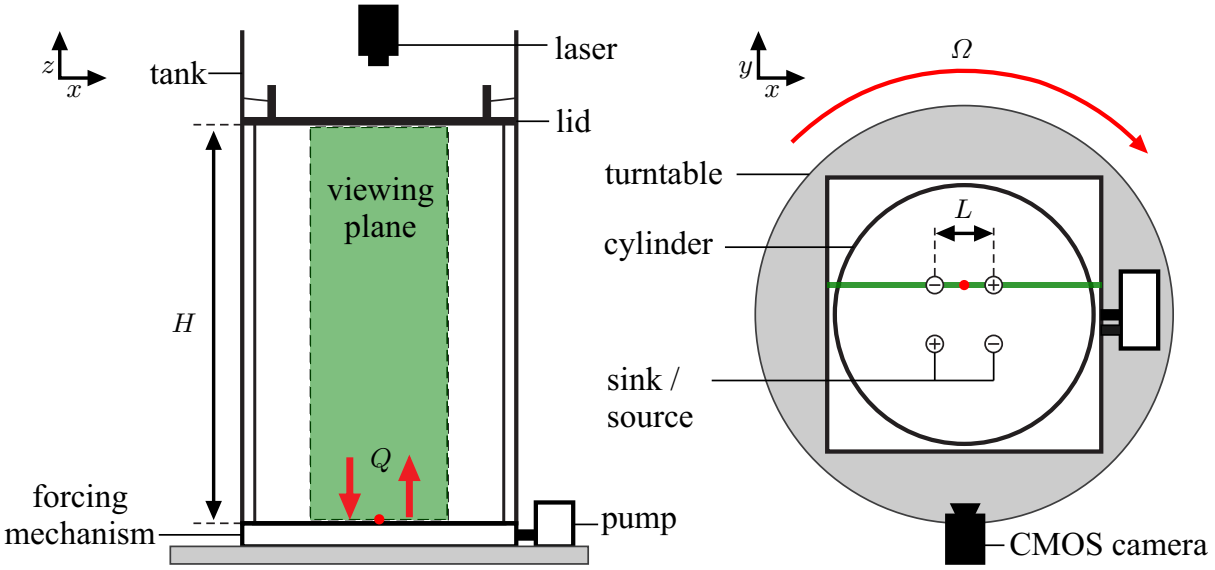

FIGURE 1. Sketch of the side- and top-view of the experimental setup, highlighting all important components. Green rectangle shows the approximate size of the flow field recorded and green line shows the position of the laser sheet across a source/sink pair. Red dot shows the position of the origin in our experiments. In top-view (+) refers to a source and (-) to a sink.

2. Experimental methods

2.1. *Experimental apparatus*

Figure 1 shows a sketch of the setup. The experiment consists of a rectangular tank (60 cm×32 cm×32 cm) centred on a rotating turntable, filled with water (viscosity $\nu = 1.0034 \times 10^{-6}$ m^2/s and density $\rho = 0.9982 \times 10^3$ kg/m^3). The temperature in the laboratory was kept at 20 °C.

A forcing mechanism, supported by four pillars at the corners of the mechanism, is placed underneath the bottom wall of the tank. This mechanism forces a flow by injecting and withdrawing fluid through four sources/sinks (diameter $d = 1$ mm) located at the corners of a square centred at the bottom wall of the tank. These sources and sinks are respectively identified by the (+) and (-) symbols in figure 1. The distance between the corners of the square is $L = 53$ mm. The choice of this square injection pattern provides a quadrupolar flow that remains near the centre of the vessel despite the wide range of Reynolds numbers we investigated. This ensures that measurements made in a fixed region of the flow but at different Reynolds numbers remain comparable to each other. The sources/sinks are connected to an external peristaltic pump via tubing housed underneath the forcing mechanism. The pump (Watson & Marlow 505-DI) is mounted on the turntable and allows for simultaneous fluid injection through one diagonal of the square (sources) and fluid withdrawal through the other diagonal (sinks), resulting in a zero net mass flux. The forcing mechanism is designed so that the difference in hydraulic resistance across each pair of sources/sinks is kept to a minimum, resulting in a difference in flow rates across these pairs of less than 0.1%. The flow rate Q through each of the sources and sinks is constant with values of $(0.5, 0.9, 2.0, 3.1, 4.7, 9.4) \times 10^{-6}$ m^3/s. A cylinder (height H=40 cm, ∅=30 cm) is placed inside the tank to provide support for a transparent lid placed atop, which prevents surface deformation and a gives clear viewing window for the measurement system.

During experiments a Coriolis force is applied by spinning the rotating turntable at a

constant rotation speed Ω. The turntable is driven by a DC-powered motor connected to the table via a belt-drive. Ω spanned $\{0, 0.52, 1.04, 2.09, 4.19\}$ rad/s with an error on Ω below 1%. The flow field is recorded using a 2D-PIV system. A laser sheet along the (x, z)-plane is aligned with a source sink pair and illuminates an area of approximately 40 cm$\times$ 15 cm, covering the entire height of the tank, as can be seen in figure 1. The laser sheet is generated using a 1 W/532 nm diode-laser and a custom lens system consisting of a concave, a convex and a cylindrical lens. The thickness of the laser sheet remains around 3 mm across the entire height of the flow field. The water is seeded with 10μm silver-coated hollow glass spheres, used as tracer particles. Two 1.3MP CMOS cameras are used to record respectively the top and bottom halves of the flow field and cover an area of 21 cm$\times$15 cm each. The recorded areas of these cameras have a small overlapping region of approximately 1 cm at the centre height of the flow field. The cameras record at a frame rate of 60 fps, that is sufficient to resolve the high velocities measured close to the point of fluid injection.

For each experimental run, the turntable is initially left to rotate until the fluid inside the tank has reached a state of solid body rotation with rotational velocity Ω. PIV data for a time interval with a length of approximately three seconds are then collected to establish the level of residual flow motion, that is noise, within the liquid nominally at rest within the rotating frame of reference. Finally the forcing mechanism is activated, at time $t_0 = 0$, generating a set of jets which penetrate into the flow field. The flow field is recorded for a period of 3 minutes from the time of activation of the forcing mechanism. We identify a time t_{end} for which turbulence occupies the entire vessel. We found $t_{\text{end}} < 100$ s for all experiments. The injection systems is then stopped and the flow is left to decay down to the level of noise recorded in solid body rotation, before the next activation of the injection system. Velocity fields are derived from recorded images by processing them using the PIVlab software (Thielicke & Stamhuis 2014) for Matlab. This is done on a 32$\times$32 pixel grid with a 50% overlap region. The combination of the camera resolution, its field of view and the resolution of the PIV grid result in the smallest resolvable length scale ℓ=2.1 mm. For each set of experimental parameters, a set of five separate measurements is recorded and the resultant velocity fields are averaged across these separate experiments in order to minimise uncertainties associated to the transient nature of the flow. This method is sufficient to capture the time-dependent event-average of the velocity with a standard deviation of about 5% across runs. Furthermore, although only the velocity component along the x and z direction are measured, the symmetry of the configuration implies that the flow is statistically invariant by rotation of $\pm\pi/2$. As such the 2D measurements provide a good representation of the 3D dynamics, in particular for estimating the group velocity of inertial waves of individual horizontal wavenumbers k.

2.2. *Control parameters*

We chose a rotating frame of reference with origin centred between two adjacent corners of the square, $\mathbf{e}_x$ and $\mathbf{e}_y$ in the horizontal plane and $\mathbf{e}_z$ pointing upwards, indicated by the red dot in figure 1.

Both Q and Ω provide control over two non-dimensional governing parameters, namely the Ekman number $Ek = \nu/2\Omega L^2 \in [17.0, 8.50, 4.25] \times 10^{-5}$ and a Reynolds number based on the flow rate, $Re_Q = U_0 d/\nu \in [600, 1200, 2500, 4000, 6000, 12000]$, where $U_0 = 4Q/\pi d^2$. Here L is chosen as the characteristic length scale to make comparison easier to experiments (Kolvin *et al.* 2009) as is done in table 1. Results are presented in non-

	Forcing	Re_Q	Ek	Ro_Q	z/L
Currrent	4 Jets	$(0.06-1.2)\times10^4$	$(4.25-17.0)\times10^{-5}$	$0.026-2.04$	$0.1-7.4$
Dickinson & Long (1983)*	Grid	n/a	$\geqslant 4.5\times10^{-6}$	n/a	$120-187$
Staplehurst *et al.* (2008)*	Grid	$83-130$	$(1.44-2.96)\times10^{-6}$	$0.5-1.4$	$120-187$
Kolvin *et al.* (2009)†	248 Jets	$\leqslant 1300$	$(6.4-10.8)\times10^{-6}$	$\leqslant 0.021$	$1.4-11.4$

TABLE 1. Comparision betwee the parameter range explored in the current experiments and experiments conducted by Kolvin *et al.*. *Ekman numbers are based on the containers heights. †Based on Ω and upperbound for Q given by Kolvin *et al.*.

dimensional form, using L and U_0 as reference length and velocity scales respectively. In comparison to the current experiment the experiments conducted by (Kolvin *et al.* 2009) applied a significantly stronger Coriolis force, while the applied inertial forces are almost always weaker than in the current experiment. This difference in parameters reflects a difference in purpose between both setups: while Kolvin *et al.* (2009)'s work targeted the limits of high rotation, and low inertia, we are targeting a transitional regime where inertia and the Coriolis force compete. Their ratio is measured by a Rossby number based on the injected velocity $Ro_Q = EkRe_Q$. For comparison with the experiments on rotating turbulent fronts, the attainable values of the non-dimensional parameters are reported in table 1.

2.3. *Data analysis*

To differentiate advective from propagative processes, we shall analyse the scale dependence of the processes governing the evolution of the turbulent front. For this, we follow a method similar to Kolvin *et al.* (2009): we first apply a discrete Fourier transform along x to the velocity field $\mathbf{u}(x,z,t)$ to obtain a space and time-dependent power density spectrum $E(k,z) = |\hat{\mathbf{u}}(k,z,t)^2|$, expressed in term of wavenumber k. This operation is performed for each acquisition timestep t. From this, variations of energy at one spatial location for a given wavelength are extracted by fixing z and k.

Figure 2 (a) and (b) shows example representations of $E(k,z,t)$ at $z/L = 2.83$ and $z/L = 4.72$ for one non-rotating and one rotating experiment, respectively. In each case, The time-variations of $E(k,z,t)$ exhibit a sharp transition from an initially low energy state at noise level to high energy, turbulent state. For any mode k we consider that the front has arrived at height z at arrival time τ for the lowest value of t such that $E(k,z,t)$ exceeds a threshold value between these two states. For each set of parameters (Re_Q, Ek) and each value of k, the threshold value $E_T(k)$ is defined as $E_T(k) = \frac{1}{2H}\int_0^H E(k,z,t_0)dz + \frac{1}{2H}\int_0^H E(k,z,t_{\mathrm{end}})dz$, *i.e.*, the average between the state of residual noise at $t < t_0$, and the state when turbulence has invaded the full domain at $t = t_{\mathrm{end}}$. The time of arrival at a prescribed height z of a given mode k is obtained as the time τ such that $E(k,z,\tau) = E_T(k)$. The position of the front at time τ of the physical domain containing energy in mode k is then simply tracked through the location $z(\tau)$ for which $E(k,z,\tau) = E_T(k)$. Additionally, the evolution of the spectral shape of the turbulent cloud is visualized by plotting contours of $E(k,z,t)$ as is done in figure 2

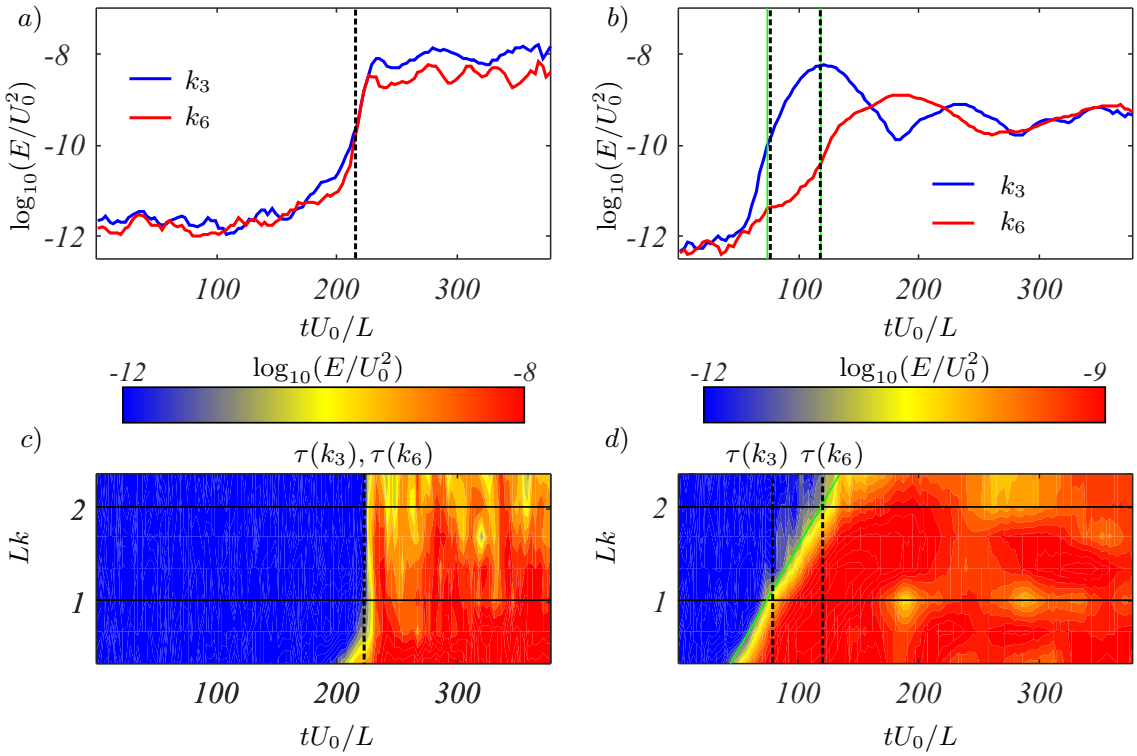

FIGURE 2. a,b) Temporal energy profiles $E(k,t)$ for modes $k_3L \approx 1.0$ and $k_6L \approx 2.0$ at $Re_Q = 2500$ and a height $z/L = 4.91$. c,d) Contour plots of $E(k,t)$, where solid black lines highlight $E(k,t)$ for modes k_3 and k_6. Experiments conducted at a,c) $Ek = \infty$ and b,d) $Ek = 4.25 \times 10^{-5}$. Arrival times $(\tau(k_3), \tau(k_6))$ are represented by dashed lines. Green lines in b) represent the theoretical arrival time for inertial waves with wavenumber k_3, k_6 respectively. Similarly, the green line in d) represent the theoretic contour of full linear inertial wave propagation.

(c) and (d) for the same two experimental cases.

Figure 2 (a) shows that mode k_3 and k_6 display the same variations in energy for all times, with both modes arriving at roughly the same time $\tau_3 U_0/L \approx \tau_6 U_0/L \approx 90$. This is reflected in the near vertical contour in figure 2 (c). Figure 2 (b) however shows that mode k_3 progresses substantially faster than mode k_6 arriving at time $\tau_3 U_0/L \approx 70$ and $\tau_6 U_0/L \approx 105$, respectively. This difference in displacement velocity observed in the rotating case translates into the slanted contour of figure 2 (d).

3. Advection of the turbulent cloud with and without background rotation

3.1. *Non-rotating jet experiments*

We first analyse the motion of the turbulent front in the absence of a Coriolis force (*i.e.* $Ek = \infty$), where no propagative behaviour is expected, to be able to quantify changes in behaviour when rotation is present. Under these circumstances the only available mechanism is advection. Figure 3 shows the motion of the front at $Re_Q = 6000$ for the first six modes of the Discrete Fourier Transform with wavenumber k_i, where $\{k_i\}_{i=1..6} = iN/W(N+2)$. Here W is the width of the recorded area ($W \approx$150 mm) and N the number of PIV grid-points along the horizontal plane (N=64.) For $Ek = \infty$ the motion of the turbulent front is independent of k. The position of the turbulent front follows a

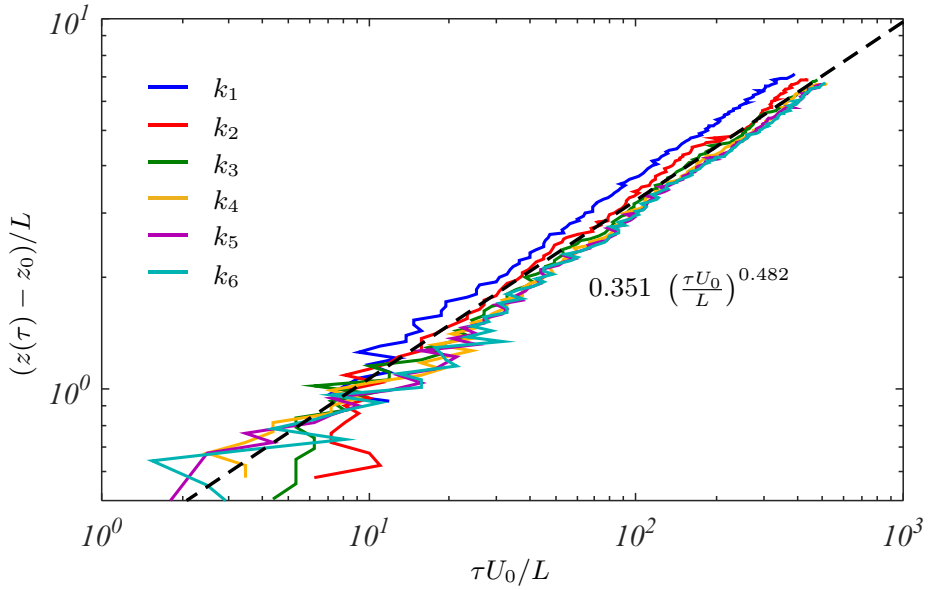

FIGURE 3. Arrival time τ at height z for the first six modes k_i at $Re_Q = 6000$ in the absence of rotation ($Ek = \infty$). Dashed line is a fit of the experimental data for $z \geqslant 0.8$.

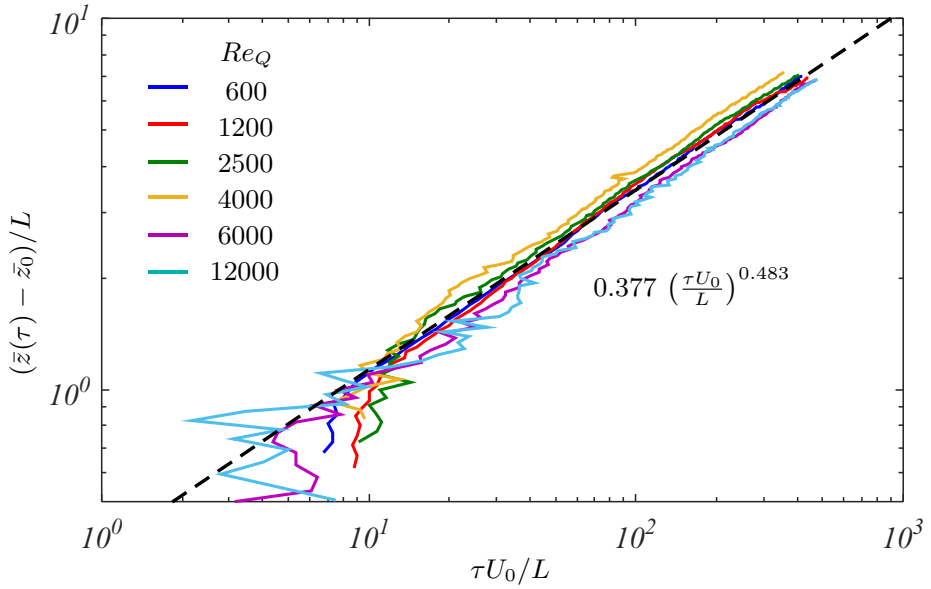

FIGURE 4. Arrival time τ at height z at $Ek = \infty$ across all Re_Q, where τ is taken as the average across first six modes k_i. Solid black line is a fit of data where $z/L \geqslant 0.8$

scaling of $(z-z_0)/L \approx (0.351 \pm 0.016)(\tau U_0/L)^{0.482\pm0.011}$ across all scales of the flow. This behaviour is observed for all Re_Q explored. Here, the offset z_0 is calculated so that the power law fit extends to $\tau = 0$. Since the jet is turbulent, all scales are displaced at the same velocity, the position of the turbulence front $\bar{z}(\tau)$ may be calculated as the average over the first six modes of the Discrete Fourier Transform used to calculate $E(k, z, t)$. Figure 4 shows the variations of $\bar{z}(\tau)$ with Re_Q in the absence of a Coriolis force. By non-dimensionalizing τ by the characteristic injection time L/U_0 the data for $\bar{z}$ collapses almost onto a single line for $\bar{z}/L \geqslant 0.8$. This shows that in the absence of rotation the

non-dimensional arrival time is determined solely by the injection velocity U_0 as

$$\frac{\bar{z}(\tau) - \bar{z}_0}{L} = (0.377 \pm 0.014) \times \left(\frac{\tau U_0}{L}\right)^{0.483 \pm 0.010}, \tag{3.1}$$

with corresponding velocity of the turbulent front as it progresses in the quiescent fluid,

$$\frac{U(z)}{U_0} = (6.41 \pm 0.11) \times 10^{-2} \left(\frac{z}{L}\right)^{-1.070 \pm 0.027}. \tag{3.2}$$

The z^{-1}-profile closely resembles the axial velocity profile of a single steady turbulent jet Pope (2000, p.100), most likely because of the nature of our forcing. Nevertheless, the fact that the transient jet exhibits the same profile as the statistically steady jet, indicates that the jet develops in such a way that the flow behind the front is in a statistically steady state even though the front continues to progress. In other words, the front "sweeps" through the quiescent fluid, leaving a statistically steady turbulent flow behind. This is confirmed by observing the shape of the turbulent region (see figure 7(a)) which only evolves by extending uwards, as the front progresses, but not radially. Momentum conservation implies that the turbulent region should grow linearly with the distance to the origin as a result. Again figure 7(a) seems to confirm that this is indeed the case.

Scaling (3.1) is near-identical to the front displacement law found experimentally by Dickinson & Long (1978) with an oscillating grid instead of jets. This law is itself in agreement with the theoretical prediction of Long (1978), expressed dimensionally as $z_{\mathrm{dim}}(t) \sim K t_{\mathrm{dim}}^{1/2}$, where constant K is expected to scale with the action generating the turbulence. While an exact determination of the parameters governing the variation of this quantity is not available in Dickinson & Long (1978)'s grid experiments, $K \simeq (0.43 \pm 0.02)(U_0 L)^{1/2}$ in the present case of jet-driven turbulence. The displacement offset $\bar{z}_{0\mathrm{dim}}$ lies in the range 0.5-2.0 cm, similar to the experiments of Dickinson & Long (1978) and Hopfinger & Toly (1976), most likely on the grounds that the small scale forcing from the grid and the jets lie in the same range of scales. Additionally, z_0 exhibits no variations of significance with either the wavelength considered or Re_Q (see figure 5, beyond fluctuations within the measurement error, which we estimate of approximately 0.5 cm). These results confirm that the 4-jet system generates a turbulent front with the same dynamics as the classic oscillating grid. Moreover they establish the scale-independence of the advective front motion.

Physically, z_0 corresponds the virtual point from where turbulent advection starts. A possible reason for which z_0 is not zero is that the jet is not turbulent at $\tau = 0$: the first stae of the development of the jet is laminar,followed by the development of instablities, which in turn lead to turbulence in a finite time. Hence the initial advection may not follow the turbulent advection law. It follows that if the advected position is extended back to $\tau = 0$ according to that law, the result may not coincide with the bottom of the tank but with an offset position z_0.

3.2. *Advection in the presence of background rotation*

As mentioned in introduction, one of the main reasons for the choice the transient jet configuration is that momentum transport can easily be tracked through the displacement of the turbulent front. In order to differentiate advection from other momentum transport mechanisms in the rotating jet, we first need to understand how rotation affects advection itself. This is done by calculating the Lagrangian flow Φ associated to the two-dimensional

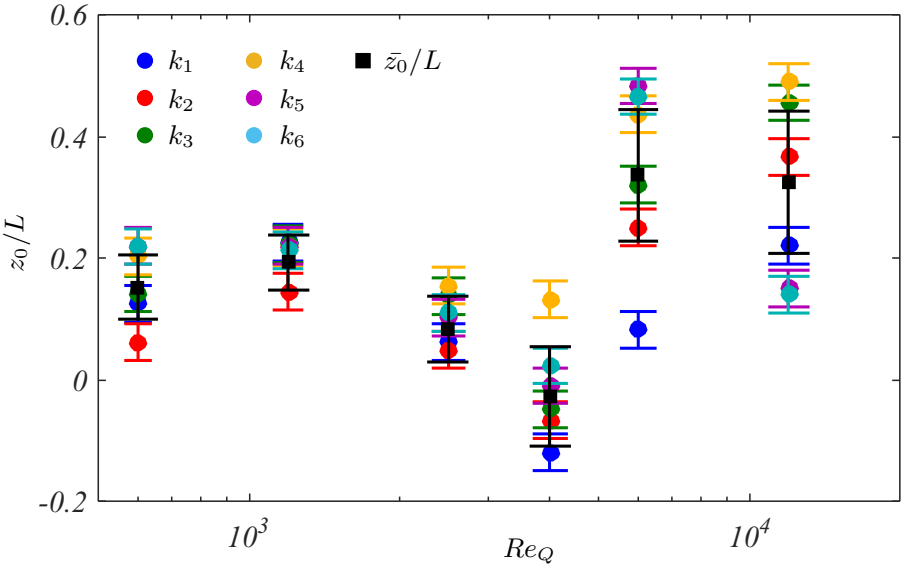

FIGURE 5. Offset z_0 measured across Re_Q and scales k_i at $Ek = \infty$.

flow field obtained from the PIV measurements for $\mathbf{u}(x, z, t)$. For a particle initially located at $\mathbf{r}_0 = (x(t = 0), z(t = 0)) = \mathbf{r}(t = 0)$,

$$\mathbf{r}(t) = \Phi(\mathbf{r}_0, t) = \int_0^t \mathbf{u}(\mathbf{r}(t'), t')dt'. \tag{3.3}$$

For the purpose of determining the motion of the turbulent front, we shall consider advection of a particle in the z direction only and calculate its virtual motion if it was purely advected by the jet. Additionally, since we are interested in the movement of the front and not of an actual particle, we shall consider the maximum advection velocity across the x direction rather than the local one and define the purely advective displacement as:

$$z^a(t) = \int_0^t \max_x \{u(x, z^a(t'), t') \cdot \mathbf{e}_z\}dt'. \tag{3.4}$$

It is noteworthy that the coordinate $z^a(t)$ does not track an actual fluid particle. Indeed, while fluid transport indeed occurs through advection, it doesnt occur through propagation of inertial waves. Momentum transport, on the other hand, does occur in both cases. More precisely, the turbulent front materialises the transport of the the fluctuating part of the momentum. The evolution of $z^a(t)$ is represented in two ways: figure 6 (a) shows $z^a(t)$ for $Re_Q = 1200$ and varying Ek, while 6 (b) shows $z^a(t)$ for $Ek = 4.25 \times 10^{-5}$ and varying Re_Q. Here $t = 0$ is set to the time when the particle is first displaced from its initial location at $z^a(0)/L \approx 2$. Figure 7 show snapshots of the jet velocity field with and without rotation, with the position z^a represented by a single particle. In the absence of rotation the position of the particle closely follows that of the turbulent front *i.e.* $z^a(t) \approx z(t)$. When rotation is present, the advected particles initially follow the turbulent front but falls well behind after this initial phase. The beginning of this second phase , which can be identified in figure 6 as the point where the curves deviate from the $Ek = \infty$ case, coincides with the appearance of chevron-patterns in the velocity field. These patterns are visible in figure 7 for $tU_0/L \geqslant 127.4$, and in the supplementary material: *movie1.avi*. These chevron patterns are a signature of inertial waves being emitted by the jets. A combination of frequency filtering and phase averaging (Cortet *et al.* 2010) revealed that the jets emit inertial wave packets of

all possible frequencies $\sigma < 2\Omega$ and propagation angles θ corresponding to the dispersion relation for inertial waves $\sigma = 2\Omega cos(\theta)$ (Greenspan 1968). The chevron pattern are a superposition of numerous waves, which allows us to briefly see the inertial waves. The details of this frequency analysis are reported in Brons *et al.* (2019). The slowdown of advection can be understood in terms of momentum conservation: since part of the momentum is conveyed by inertial waves ahead of the "purely advected" position, less momentum is locally available for purely advective momentum transport. The effect is all the more visible as rotation is important.

A third phase can be identified in figure 6 where the advection speeds up again. This phase may be to be caused by inertial waves reflected from the top wall travelling downward and practically cancelling the upward momentum transfer that impeded the momentum transfer in the second phase. From the onset of this third phase a reference velocity U_{ref}, based on time t and a length D can be determined. Here D is the distance from the bottom of the tank to the top and back down to the height of the onset i.e. $D = (0.8 - z)/H$. Figure 8 shows that U_{ref} normalized by linear inertial wave velocity $2\Omega L$ is independent of Ek, affirming the assumption that the onset of the third phase is caused by inertial waves reflected from the top of the vessel. It is noteworthy that while interactions between incident waves and waves reflected on the walls of the vessels can sometimes be seen in the patterns, these are indicative of linear waves interference, and not of nonlinear wave interaction. This suggests that the intensity of the waves generated in our experimental setup is too low for inertial waves to enter a nonlinear regime such as that observed when intentionally focusing inertial waves in a region of interaction (Duran-Matute *et al.* 2013). Following the suppression of momentum transport by inertial waves, the purely advected position resumes its progression at the non-rotating advective pace. Remarkably, not only is the velocity but also the position z^a independent of the rotation in this phase, as all positions follow a law:

$$\frac{z^a}{L} = (0.48 \pm 0.03) \left(\frac{tU_0}{L} \right)^{0.381 \pm 0.012} . \tag{3.5}$$

The value of the exponent, lower than the 0.5 value expected for pure advection may reflect that propagation by inertial waves isn't entirely cancelled, as the reflected wave are less intense than the incident ones. Importantly, the dynamics observed in the second phase establishes that not only does rotation introduce an additional transport mechanism with inertial waves, but advection is suppressed as a result. Furthermore, the dynamics of the third phase suggest that momentum transport by inertial waves may not be efficient in confined flows, in particular quasi-two dimensional ones.

4. Transition to inertial wave propagation

4.1. *Spectral profile of the turbulent front*

We now seek to characterise the motion of the actual turbulent front in cases where the experiment is rotating, having confirmed that it cannot be explained by advection alone. Figure 9 shows the spectral energy density contours of $E(k, z, t)$ at various heights z for $Re_Q = 1200$ across all values of Ek explored. This figure is representative of cases studied for all values of Re_Q. At $z/L = 0.94$ there is no discernible difference on the shape of contours between the cases with different values of Ek we investigated. Their near-vertical shape shows that all modes k arrive at the same time and thus all modes progress at approximately the same velocity.

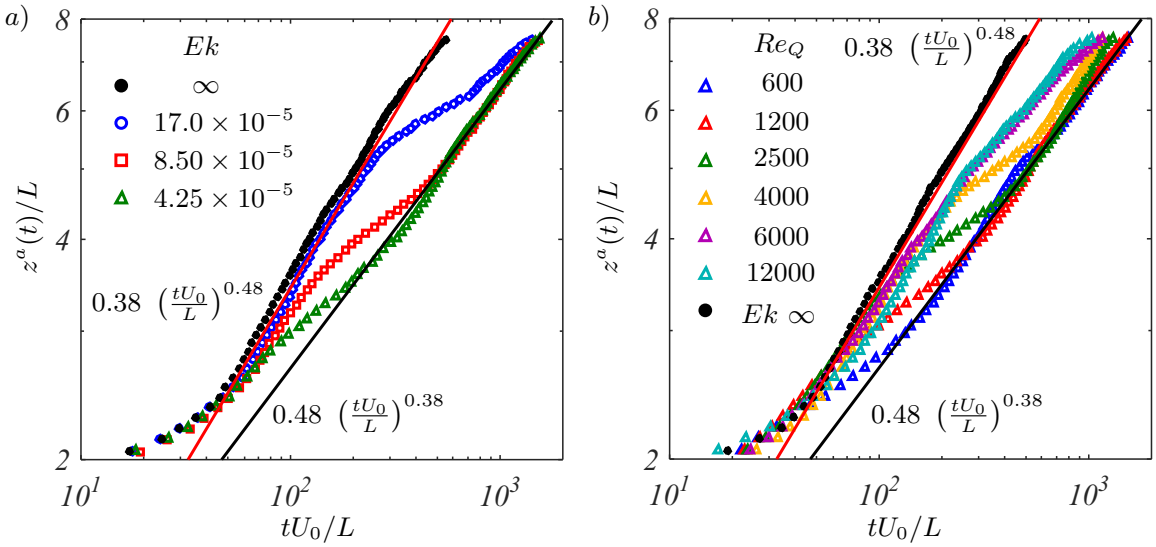

FIGURE 6. Position z^a of a particle placed at $z_0/L = 2$ as function of time. (a) $Re_Q = 1200$ with varying Ek. (b) $Ek = 4.25 \times 10^{-5}$ with varying Re_Q. Supplementary material: *movie2.avi* contains a video showing the evolution of the jet next to the evolution of $z^a(t)$ and $z(t)$. Time $t = 0$ corresponds to the time when the particle is first displaced

.

For a given value of Ek, the spectral contour of the turbulent front progressively changes shape at greater distance z from the bottom wall, exhibiting three regions: the lower wavenumbers arrive at a time indicating that they progress at the group velocity of an inertial wave of the same wavenumber (marked by solid lines). At the higher wavenumbers, by contrast, the front continues to exhibit the flat profile that characterises advection by the jet. These two regions of the front are linked up by a rather narrow transition region. As z increases, the low-wavelength region occupies an increasingly large part of the spectrum, while the high-k advective region shrinks and eventually disappears in all cases we investigated. This is consistent with the morphology of the jet which spreads and therefore slows down away from the source, implying that advection progressively weakens as z increases. For higher rotation (lower values of Ek) pictured on the different columns of figure 9, the transition between the propagative and the advective parts of the front becomes increasingly sharp and displaces towards increasingly higher wavenumbers. The overall picture is that structures of higher wavenumbers are advected by the jet whereas at low wavenumbers, larger structures propagate with inertial waves. As the Coriolis force that underpins inertial waves progressively overruns inertial forces associated to advection (either as z increases or as Ek decreases), low wavenumber propagation invades an increasingly wider waveband at the expense of high-wavenumber advection.

4.2. *Transport of individual modes*

A finer perspective on the mechanism at play can be gained by tracking individual modes as they are transported along the jet. Considering individual modes offers the opportunity to compare their propagation to the group velocity of inertial waves of the same wavevector along their trajectory. Figure 10 (a) shows such trajectories $z(t)$ for mode k_1, for several values of Re_Q at $Ek = 4.25 \times 10^{-5}$. The dashed line shows the trajectory of the turbulent front when $Ek = \infty$, *i.e.* driven by advection only. Trajectories at all Re_Q initially follow the advection trajectory and separate at a height

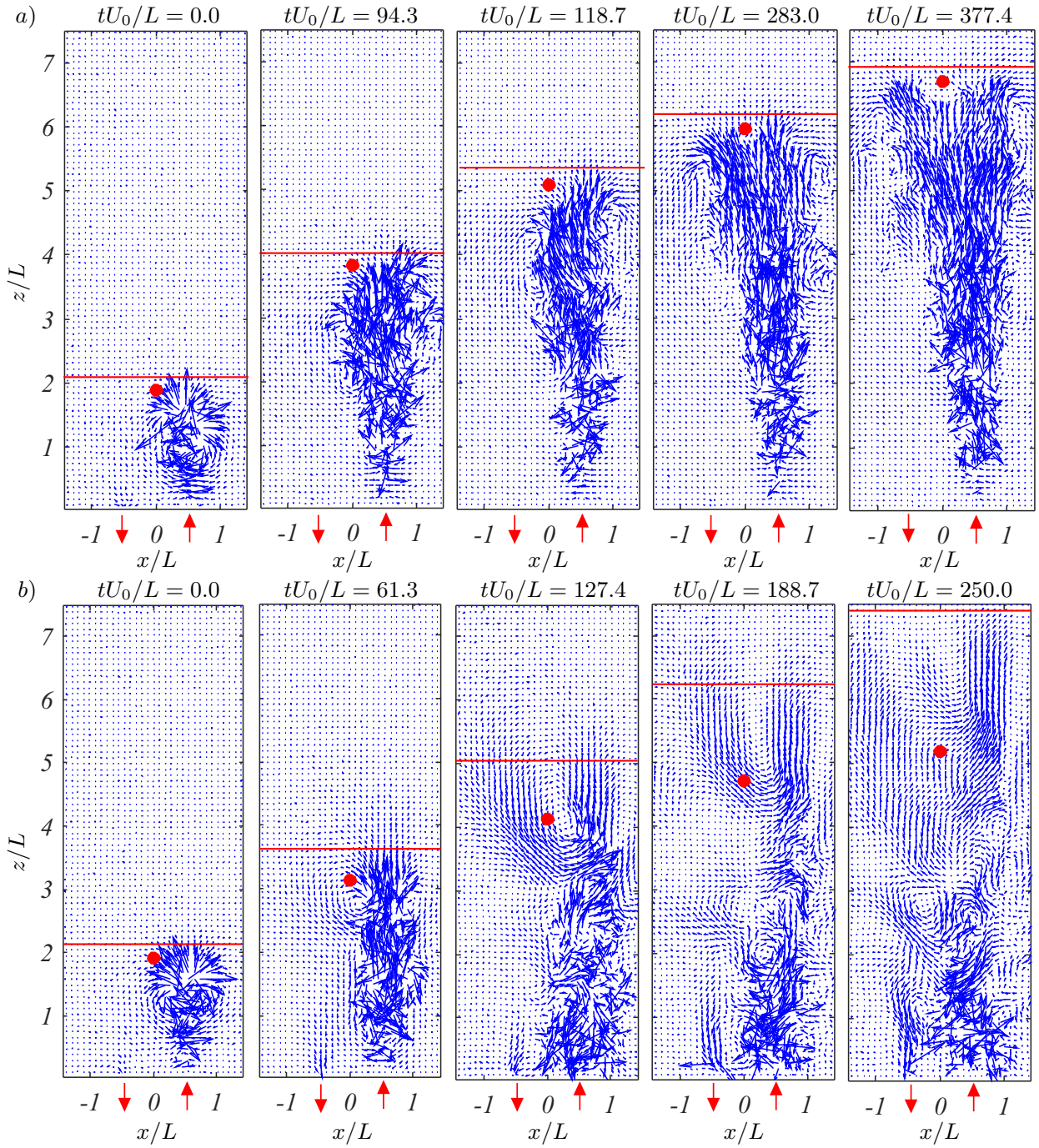

FIGURE 7. Snapshots of the jet velocity field for $Re_Q = 2500$ and a) $Ek = \infty$ and b) $Ek = 8.50 \times 10^{-5}$. Red dot shows the position $z^a(t)$ of a numerical particle initially positioned at $z_0/L = 2$, where $t = 0$ coincides $z/L = 2$. Red line shows the position of the front. The small difference in position between particle and front in (a) is artificial and caused by differences in sensitivity in methods used to measure their position. Red arrows indicates the point of fluid injection/withdrawal. Supplementary material: *movie1.avi* shows the simultaneous evolution of both jets represented here.

which increases with Re_Q. Past this point, mode k_1 progresses faster than if it was advected.

To highlight regions of the trajectory that are governed by inertial waves propagation, the trajectories of mode k_1 are plotted in figure 10 (b) for several values of Ek, using variables

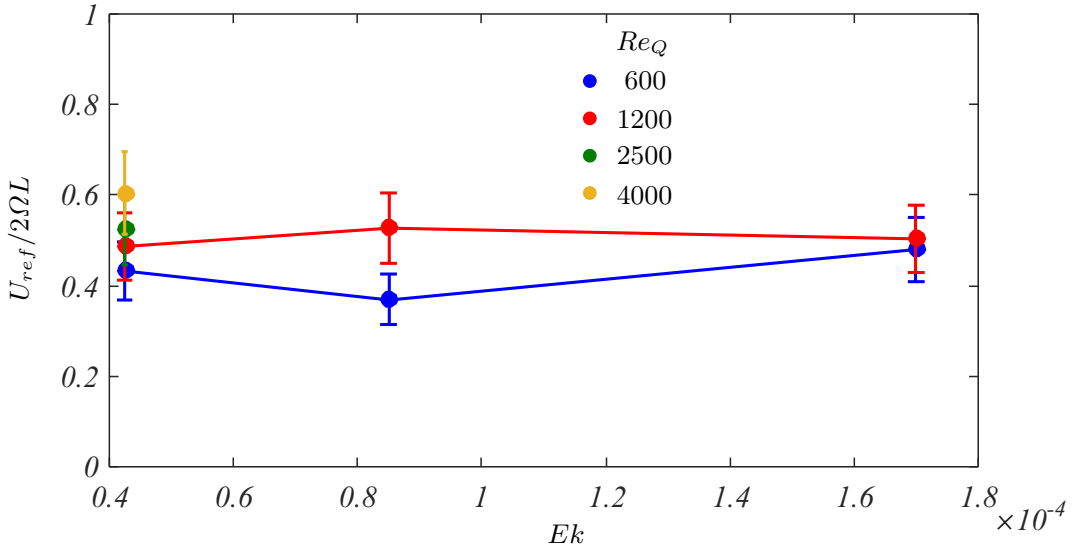

FIGURE 8. Reference velocity U_{ref} based on the point of onset of the third advection phase normalized by an inertial wave velocity $2\Omega L$ versus Ek. Only experiments where onset of third phase was observed were considered.

$(z - \Delta z)/z_{IW}$ and τ/τ_{IW}, where $z_{IW}(t) = 2\Omega t/k$, $z_{IW}(\tau_{IW}) = H$ and Δz is the offset between z and z_{IW} near the top of the tank. In these new variables, displacements at the group velocity of mode k_1 follow horizontal lines. As expected, trajectories start away from the horizontal propagation lines in the initial advective phase identified in figure 10(a), but gradually bend toward them until to end up following them closely. This shows that inertial wave propagation eventually takes over advection. For $Re_Q = 12000$ and $Ek = 17.0 \times 10^{-5}$ trajectories barely meet the theoretical propagation line, indicating that propagation never fully takes over within our experimentally accessible parameters. Overall convergence is all the faster as Re_Q and Ek are low, as inertial forces delay the transition from advection to propagation, while rotation accelerates it.

To quantify the transition from the advective to the propagative mechanism, we define the point of transition as $z_T = |z/(z_{IW} + \Delta z) - 1| \leqslant \beta$, where β is a chosen threshold value. The value of β has to be chosen as low as possible, however as β is lowered the results become increasingly susceptible to experimental noise. In order to keep this noise to a low level we chose $\beta = 0.2$. In addition, $|z/(z_{IW} + \Delta z) - 1|$ converges to 0 as z increases, regardless whether a full transition is achieved or not, so this method cannot be applied to all experiments conducted. Figure 11 shows z_T for k_1 across all Re_Q and Ek explored, with the exception of those where the transition was not fully achieved (such as for $Re_Q = 12000$ and $Ek = 17.0 \times 10^{-5}$). Values of mostly z_T obey a scaling dependent on the Rossby number only:

$$z_T/L \simeq (8.96 \pm 0.74) Ro_Q^{1/2}. \tag{4.1}$$

This scaling can be understood by considering that at the transition between the two phases, the length of the jet z_T has reached a point where Coriolis forces are sufficient to balance inertia. For $Ro_Q > 3 \times 10^{-1}$ a change of behaviour can be seen. This is an artefact of the method used to determine z_T. By lowering the value of β this change can be pushed to higher values of Ro_Q and z_T/L. Considering z_T as the largest lengthscale, in dimensional terms, it must satisfy $U(z_T)/z_T \sim 2\Omega$. In the absence of rotation effects, the jet develops as $U(z)/U_0 \sim d/z$ (Pope 2000, p.100), so z_T must scale as $z_T \sim (U_0 d/2\Omega)^{1/2}$, or equivalently, $z_T/L \sim Ro_Q^{1/2}$, as in (4.1). A similar criterion

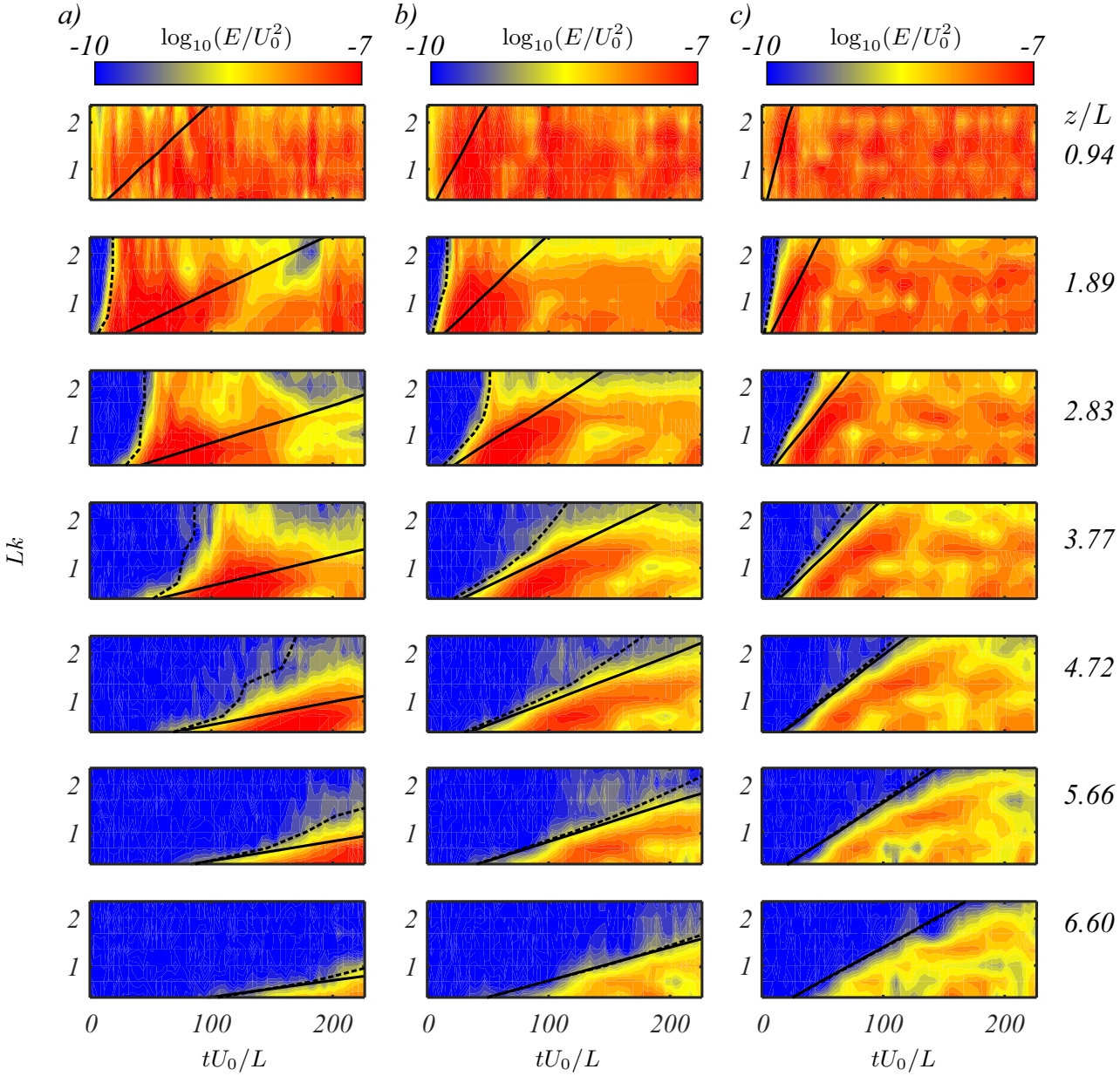

FIGURE 9. Contour plots of $E(k,t)$ across a number of heights z/L for $Re_Q = 1200$ at a) $Ek = 17.0 \times 10^{-5}$, b) $Ek = 8.50 \times 10^{-5}$ and c) $Ek = 4.25 \times 10^{-5}$. Solid black line represent the shape of the energy contours assuming propagation is fully driven by inertial waves, Dashed black line represent the the position of a numerical particle, based on (4.3).

was put forward by Burmann & Noir (2018) to explain the breakdown of inertial wave propagation in a spun up cylinder where the waves are emitted by a topography of the bottom wall. When turbulence is forced by an oscillating grid, Dickinson & Long (1983) similarly observe that the progression of the front is not affected by rotation in the early stages up to a critical distance, which these authors express (in our notations) as $z_T \simeq 0.36(fS^2/\Omega)^{1/2}$, in terms of the frequency f and stroke S of the grid. As such, fS is equivalent to forcing velocity U_0 and the scaling for z_T associated to the oscillating grid can be rewritten $z_T/S \simeq 0.36 Ro_Q^{1/2}$. It is similar to (4.1), even though reference lengthscales S and L are not necessarily directly comparable and the upward motion imprinted by the jet may contribute to stretch the patch upwards. It is noteworthy

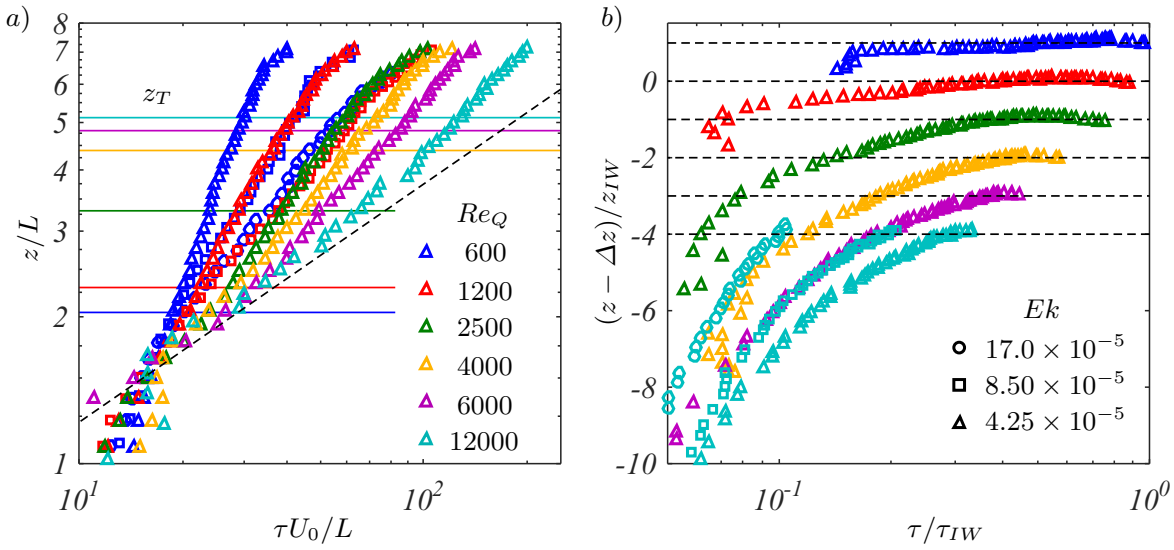

FIGURE 10. a) Arrival time τ at height z for first mode k_1 at $Ek = 4.25 \times 10^{-5}$ (triangles), $Ek = 8.50 \times 10^{-5}$ (squares) and $Ek = 1.70 \times 10^{-4}$ (circles). The dashed line represents (3.1). Coloured lines represents z_T where the motion of the turbulent front has transitioned to the propagative mechanism at $Ek = 4.25 \times 10^{-5}$. b) z and τ normalized by propagation of inertial wave with wavenumber k_1, represented by the dashed lines. Position z is displaced by a height Δz where transport mechanism shifts to a propagative mechanism. Experimental sets have been shifted down by a constant of 1 for clarity.

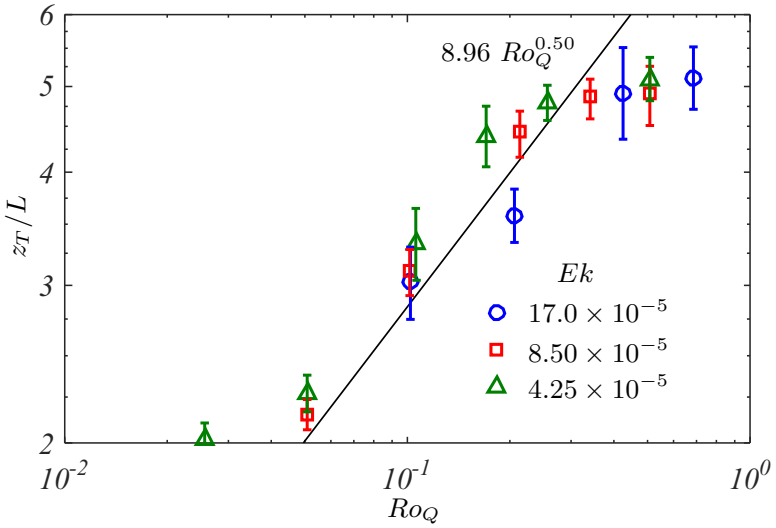

FIGURE 11. Height z_T beyond which the translation of scales of wavenumber k_1 are driven by the propagative mechanism.

that the transition point for mode k_1 coincides with the transition point for the whole front because because k_1 indeed represents the largest wavelength of the front, and is associated to the fastest inertial wave. For the same reason, this point also corresponds to the point of transition where advection itself starts being suppressed by the effects of rotation (see section 3).

4.3. *Scaling for the transition between advection and propagation*

The example of k_1 illustrates that fluctuations are first advected in the low part of the jet, as advection dominates near the injection point. As they progress through

the fluid domain, advection subsides as the jet spreads. At the same time, the mean centreline velocity decreases and propagation by inertial waves takes over as the main transport mechanism. The last step is to understand how this mechanism expresses at other wavelengths $k > k_1$. To this end, we first note from figure 10 and 11 that all curves for the displacement of fluctuations of wavenumber k_1 gradually transition away from the pure advection trajectory and converge to the propagative trajectory at $z = z_T$. At this point their displacement velocity matches to the propagation velocity of linear inertial waves. Expressing this property for fluctuations of wavelength k yields the condition (dimensionally)

$$U(z) \simeq V_\phi(k) = \frac{2\Omega}{k}. \tag{4.2}$$

In other words, the transition from advection to propagation for fluctuations of wavelength k takes place when the local, scale-dependent Rossby number $Ro(k, z) = kU(z)/2\Omega$ reaches unity. Another way to express this is that fluctuations are advected at the fastest of the local advection velocity and the group velocity of inertial waves.

To test this criterion on the entire spectrum, we calculate the arrival time of fluctuations for $k \in [0, 40]$, for the values of z displayed on figure 9, using the modified expression of the Lagrangian flow:

$$z(k,t) = \int_0^t \max\left\{\max_x\{\mathbf{u}(x, z(t'), t')) \cdot \mathbf{e}_z\}, v_g(k)\right\} dt'. \tag{4.3}$$

From this expression, we extract the arrival time $\tau(z, k)$ of fluctuations with wavenumber k at height z, which forms the spectral shape of the turbulent front. The results are reported on figure 9, which is representative of all other values of Re_Q we considered. In all cases, the motion of a numerical particle subject to (4.3) matches the actual contours of $E(k, z, t)$ closely for $z/L \geqslant 1.5$. It indeed captures all three regions identified in section cr. This indicates in particular, that in the intermediate region, the arrival time results from an initial advective phase of comparable duration to a second propagative phase, so that the arrival time falls somewhere between a pure advective and a pure propagative time.

5. Conclusion and Discussion

We have analysed the scale-by-scale transport mechanisms in rotating turbulence. The results were obtained by examining the motion of the turbulent front generated during the transient flow of four jets penetrating into or extracted from a rotating vessel of quiescent fluid, and directed along the axis of rotation. In the absence of rotation, the distance from the jet source covered by disturbances evolves (in dimensional variables) as $(z(t)-z_0)/L \simeq 0.377(U_0 t/L)^{0.483}$ (U_0 and L are the jet inlet velocity and the distance between the jets respectively). This law is in good agreement with Long (1978)'s law for the global displacement of a turbulent front, with an offset $z_0 \simeq 0.5-2.0$ cm, incidentally consistent with the values experimentally found by Dickinson & Long (1978) in experiments with an oscillating grid. Additionally, we established that this law is valid at all scales, regardless of their transversal wavenumber k, and of the Reynolds number based on the inlet jet velocity Re_Q. In the presence of rotation, the turbulent front is advected exactly as in the non-rotating case up to a distance $z_T/L \simeq 8.96 Ro_Q^{1/2}$, where the Coriolis force becomes larger than inertia. Past this point, the development of the jet is dominated by the faster propagation of inertial waves. However, since momentum is spread over a larger volume

by inertial waves, it is locally weaker. As a consequence, advection itself is suppressed by rotation.

In the last phase of the jet's evolution, inertial waves reflected on the upper wall of the fluid vessel interfered with inertial waves travelling up, resulting in a suppression of the total transport by inertial waves. This suggests that in confined flows, inertial waves may not be able to transport momentum efficiently. This is particularly relevant in the quasi-two dimensional limit, where our recent experiments showed that they were indeed not driving the dynamics (Brons *et al.* 2019).

The scale-by-scale analysis of the propagation enabled us to answer the questions set out in the introduction:

(i) A clear separation exists between scales advected by inertial waves and by the local mean flow.

(ii) The border between the two regimes is set by the Rossby number based on the transversal wavelength of the scale considered and the local large scale velocity as $Ro_k(k, \mathbf{x}) = kU(\mathbf{x})/2\Omega = 1$. In that sense, this criterion is local both in space, time and scale.

The implication of this phenomenology is that the tranport of turbulent fluctuations as turbulence progresses into the quiescent fluid follows two phases: one purely controlled by local advection for $Ro_k(k, z) > 1$ and one purely controlled by the propagation of inertial waves for $Ro_k(k, z) < 1$. The spectral locality of the transition complement the recent evidence for its spatial locality found by McDermott & Davidson (2019).

In other turbulent flows with more complex flow topology, the same phenomenology would imply that structures may be alternately convected by larger structures and propagated by inertial waves. However, it is worth pointing out that the fact that advection dominates at a given scale does not mean that inertial waves do not exist at that scale. Just like the transversal sweeping of inertial waves in nearly two-dimensional flows (Campagne *et al.* 2015). Axial advection of inertial waves could take place in our setup, but would be shadowed if advection was the fastest mechanism. More generally, our result does not exclude the possibility that inertial waves at small scales may be axially or laterally convected by faster advection too.These remarks apply in particular to non-transient turbulent flows. Indeed, an important feature of the transient problem studied in this paper is the fact that inertial waves are emitted by random fluctuations in a turbulent region where rotation does not dominate. A similar phenomenology may exist in turbulent flows, even when the macroscopic Rossby number remains well below unity, provided random fluctuations also exist at a sufficiently small scale to escape the influence of rotation. Such fluctuations may act as random source of inertial waves competing with local advection to transport momentum. Unlike in transient problems where the displacement of the turbulent front offers a convenient way to track momentum transport, however, the two mechanisms are more difficult to disentangle in a established turbulence, especially if contrary to the jet, momentum is not advected in a preferred direction.

Finally, while the mechanisms found here do not exclude the possibility that nonlinear interactions may participate in the build-up of large quasi-two dimensional structures, they illustrate that linear inertial waves govern transport mechanisms at the large scales, as shown by Davidson *et al.* (2006), but they also dominate down to the level of smaller scales as long as the local balance of Coriolis force and advection favours the former. More generally, it is not unusual that turbulence dynamics be controlled at the scale level by linear processes, as illustrated in magnetohydrodynamic turbulence at low magnetic Reynolds number, where the anisotropy of individual scales is controlled by the balance between inertia and momentum diffusion by the Lorentz force (Sommeria &

Moreau 1982; Pothérat & Klein 2014; Baker *et al.* 2018). Having said this, linear waves themselves can interact nonlinearly and lead to turbulence when they are sufficiently energised, as demonstrated with inertial waves by Duran-Matute *et al.* (2013).

The authors would like to acknowledge support from the Engineering and Physical Sciences Research Council [grant number GR/N64519/01] for the manufacture of the rotating turntable facility and B. Teaca for computational resources used in processing experimental data. AP aknowledges support from the Royal Society under the Wolfson Merit Award Scheme

REFERENCES

Baker, N., Pothérat, A., Davoust, L. & Debray, F. 2018 Inverse and direct energy cascades in three-dimensional magnetohydrodynamic turbulence at low magnetic reynolds number. *Physics Review Letters* **120** (224502).

Bartello, P., Métais, O. & Lesieur, M. 1994 Coherent structures in rotating three-dimensional turbulence. *Journal of Fluid Mechanics* **273**, 129.

Brons, J. A., Pothérat, A. & Thomas, P. J. 2019 Mean flow anisotropy without waves in rotating turbulence. *ArXiv reprint* p. 1902.07984.

Burmann, Fabian & Noir, Jerome 2018 Effects of bottom topography on the spin-up in a cylinder. *Physics of Fluids* **30** (10), 106601, arXiv: https://doi.org/10.1063/1.5051111.

Cambon, C., Mansour, N. N. & Godeferd, F. S. 1997 Energy transfer in rotating turbulence. *Journal of Fluid Mechanics* **337**, 303332.

Cambon, C. & Scott, J.F. 1999 Linear and non-linear models in anisotropic turbulence. *Annual Review of Fluid Mechanics* **31**, 1.

Campagne, A., Gallet, B., Moisy, F. & Cortet, P.P. 2015 Disentangling inertial waves from eddy turbulence in a forced rotating-turbulence experiment. *Physics Review E* **91**, 043016.

Campagne, A., Gallet, B., Moisy, F. & Cortet, P. P. 2014 Direct and inverse energy cascades in a forced rotating turbulence experiment. *Physics of Fluids* **26**, 125112.

Cortet, P.P., Lamriben, C. & Moisy, F. 2010 Viscous spreading of an inertial wave beam in a rotating fluid. *Physics of Fluids* **22**, 086603.

Davidson, P. A. 2013 *Turbulence in Rotating, Stratified and Electrically Conducting Fluids*. Cambridge University Press, Cambridge, England.

Davidson, P. A. 2015 *Turbulence: An Introduction for Scientists and Engineers*. Oxford University Press, Oxford, UK.

Davidson, P. A., Staplehurst, P. J. & Dalziel, B. 2006 On the evolution of eddies in a rapidly rotating system. *Journal of Fluid Mech.* **557**, 135–144.

Dickinson, S.C. & Long, R.R. 1983 Oscillating-grid turbulence including effects of rotation. *Journal of Fluid Mechanics* **126**, 315–333.

Dickinson, S. C. & Long, R. R. 1978 Laboratory study of the growth of a turbulent layer of fluid. *The Physics of Fluids* **21** (10), 1698–1701.

Duran-Matute, M., Flòr, J.-B., Godeferd, F. S. & Jause-Labert, C. 2013 Turbulence and columnar vortex formation through inertial-wave focusing. *Phys. Rev. E* **87**, 041001.

Gallet, B. 2015 Exact two-dimensionalization of rapidly rotating large-reynolds-number flows. *Journal of Fluid Mechanics* **783**, 412447.

Greenspan, H. P. 1968 *The Theory of Rotating Fluids*. Cambridge University Press, Cambridge, England.

Hopfinger, E. J., Browand, F. K. & Gagne, Y. 1982 Turbulence and waves in a rotating tank. *Journal of Fluid Mechanics* **125**, 505534.

Hopfinger, E. J. & Toly, J.-A. 1976 Spatially decaying turbulence and its relation to mixing across density interfaces. *Journal of Fluid Mechanics* **78** (1), 155175.

Kolvin, I., Cohen, K., Vardi, K. & Sharon, E. 2009 Energy transfer by inertial waves during the buildup of turbulence in a rotating system. *Phys.Rev.Let* **102**, 014503.

Long, Robert R. 1978 Theory of turbulence in a homogeneous fluid induced by an oscillating grid. *The Physics of Fluids* **21** (10), 1887–1888.

McDermott, A. D. & Davidson, P.A. 2019 A conjecture for the dipolar-multipolar dynamo transition. *Journal of Fluid Mechanics* **874**, 995–1020.

McEwans, A. D. 1976 Angular momentum diffusion and the formation of cyclones. *Nature* **260**, 126128.

Moore, D.W. & Saffman, P.G. 1969 The flow induced by the transverse motion of a thin disk in its own plane through a contained rapidly rotating viscous liquid. *Journal of Fluid Mechanics* **39** (4), 831–847.

Moore, D. W. & Saffman, P. G. 1968 The rise of a body through a rotating fluid in a container of finite length. *Journal of Fluid Mechanics* **31** (4), 635–642.

Pedlosky, J. 1987 *Geophysical Fluid Dynamics*. Springer, New York.

Pope, S. B. 2000 *Turbulent Flows*. Cambridge University Press, Cambridge, England.

Pothérat, A. 2012 Three-dimensionality in quasi-two dimensional flows: Recirculations and barrel effects. *Europhysics Letters* **98**.

Pothérat, A. & Klein, R. 2014 Why, how and when mhd turbulence at low rm becomes three-dimensional. *Journal of Fluid Mechanics* **761**, 168–205.

Smith, L. M. & Waleffe, F. 1999 Transfer of energy to two-dimensional large scales in forced, rotating three-dimensional turbulence. *Physics of Fluids* **11**, 1608.

Sommeria, J. & Moreau, R. 1982 Why, how and when mhd turbulence becomes two-dimensional. *Journal of Fluid Mechanics* **118**, 507–518.

Staplehurst, P.J, Davidson, P.A. & Dalziel, B. 2008 Structure formation in homogeneous freely decaying rotating turbulence. *Journal of Fluid Mechanics* **598**, 81–105.

Taylor, G.I 1922 The motion of a sphere in a rotating liquid. *Royal Society of London A* **102**, 180.

Thielicke, W. & Stamhuis, E. J. 2014 Pivlab towards user-friendly, affordable and accurate digital particle image velocimetry in matlab. *Journal of Open Research Software* **2**.

Thomson, J. 1868 Letter to lord kelvin (w.thomson). *Glasgow University Library, MS Kelvin T120* .

Vanyo, J. P. 1993 *Rotating Fluids in Engineering Science*. Dover Publications, Mineola, New York, USA.

Yarom, E. & Sharon, E. 2014 Experimental observation of steady inertial wave turbulence in deep rotating flows. *Nature Physics* **10** (7), 510.